The Equation of State and Petrogenesis of Komatiite

Thesis by
Gregory Hale Miller

In Partial Fulfillment of the Requirements
for the Degree of
Doctor of Philosophy

California Institute of Technology
Pasadena, California

1990

(submitted April 27, 1990)

Acknowledgements

I would like to thank Thomas J. Ahrens and Edward M. Stolper for the invaluable guidance, encouragement, support, and opportunities they provided me as my joint thesis advisors. I am also grateful to George R. Rossman, who served as my advisor during my first two years, and who continued to provide encouragement in the subsequent years. David J. Stevenson and William A. Goddard III have also acted as my advisors, and I am grateful for the many ideas and insights they shared with me.

The experimental work presented here would not have been possible without the expert technical assistance of Epaprodito B. Gelle, Michael A. Long, Victor E. Nenow, and Gunther G. Haehn. I am also grateful to Leon F. Young, and Andrew Campbell for their assistance with sample preparation.

I have benefitted greatly from numerous interactions, both on and off campus, with Lynn Abelson, David Bell, Jennifer Blank, the late Tasha Branstrator, Patrick Dobson, Gerrald Fine, Andrew Gaynor, Phillip Ihinger, Glen Mattioli, Lene Miller, Jonathan Nourse, Robert Ripperdan, Catherine Smither, and Bradford White. I also thank my colleages in the shock wave lab, William Anderson, Thomas Duffy, Sally Rigden, Linda Rowan, Douglas Schmitt, and Robert Svendsen.

I am especially thankful for the constant support and encouragement of my wife, Carol Sue, my parents, Diane and Marvin Miller, sister Gail Miller, uncle Roy Miller, and my grandparents, Ednabel and Roy Miller, Gail Dickerson, and the late Colonel Fredrick Dickerson, in whose memory I dedicate this dissertation.

Abstract

(1) Equation of State of Komatiite

The equation of state (EOS) of a molten komatiite (27 wt % MgO) was determined in the 5 to 36 GPa pressure range via shock wave compression from 1550°C and 0 bar. Shock wave velocity, U_S, and particle velocity, U_P, in km/s follow the linear relationship $U_S = 3.13(\pm0.03) + 1.47(\pm0.03)\ U_P$. Based on a calculated density at 1550°C, 0 bar of 2.745±0.005 g/cc, this U_S–U_P relationship gives the isentropic bulk modulus $K_S = 27.0 \pm 0.6$ GPa, and its first and second isentropic pressure derivatives, $K'_S = 4.9 \pm 0.1$ and $K''_S = -0.109 \pm 0.003$ GPa^{-1}.

The calculated liquidus compression curve agrees within error with the static compression results of Agee and Walker [1988a] to 6 GPa. We determine that olivine (Fo_{94}) will be neutrally buoyant in komatiitic melt of the composition we studied near 8.2 GPa. Clinopyroxene would also be neutrally buoyant near this pressure. Liquidus garnet-majorite may be less dense than this komatiitic liquid in the 20-24 GPa interval, however pyropic-garnet and perovskite phases are denser than this komatiitic liquid in their respective liquidus pressure intervals to 36 GPa. Liquidus perovskite may be neutrally buoyant near 70 GPa.

At 40 GPa, the density of shock-compressed molten komatiite would be approximately equal to the calculated density of an equivalent mixture of dense solid oxide components. This observation supports the model of Rigden *et al.* [1989] for compressibilities of liquid oxide components. Using their theoretical EOS for liquid forsterite and fayalite, we calculate the densities of a spectrum of melts from basaltic through peridotitic that are related to the experimentally studied komatiitic liquid by addition or subtraction of olivine. At low pressure, olivine fractionation lowers the density of basic magmas, but above 14 GPa this trend is reversed. All of these basic to ultrabasic liquids are predicted to have similar densities at 14 GPa, and this density is approximately equal to the bulk

(PREM) mantle. This suggests that melts derived from a peridotitic mantle may be inhibited from ascending from depths greater than 400 km.

The EOS of ultrabasic magmas was used to model adiabatic melting in a peridotitic mantle. If komatiites are formed by >15% partial melting of a peridotitic mantle, then komatiites generated by adiabatic melting come from source regions in the lower transition zone (≈500-670 km) or the lower mantle (>670 km). The great depth of incipient melting implied by this model, and the melt density constraint mentioned above, suggest that komatiitic volcanism may be gravitationally hindered. Although komatiitic magmas are thought to separate from their coexisting crystals at a temperature ≈200°C greater than that for modern MORBs, their ultimate sources are predicted to be diapirs that, if adiabatically decompressed from initially solid mantle, were more than 700°C hotter than the sources of MORBs and derived from great depth.

We considered the evolution of an initially molten mantle, *i.e.*, a magma ocean. Our model considers the thermal structure of the magma ocean, density constraints on crystal segregation, and approximate phase relationships for a nominally chondritic mantle. Crystallization will begin at the core-mantle boundary. Perovskite buoyancy at >70 GPa may lead to a compositionally stratified lower mantle with iron-enriched mangesiowüstite content increasing with depth. The upper mantle may be depleted in perovskite components. Olivine neutral buoyancy may lead to the formation of a dunite septum in the upper mantle, partitioning the ocean into upper and lower reservoirs, but this septum must be permeable.

(2) Viscosity Measurement with Shock Waves

We have examined in detail the analytical method for measuring shear viscosity from the decay of perturbations on a corrugated shock front. The relevance of initial conditions, finite shock amplitude, bulk viscosity, and the sensitivity of the measurements to the shock boundary conditions

are discussed. The validity of the viscous perturbation approach is examined by numerically solving the second-order Navier-Stokes equations. These numerical experiments indicate that shock instabilities may occur even when the Kontorovich-D'yakov stability criteria are satisfied. The experimental results for water at 15 GPa are discussed, and it is suggested that the large effective viscosity determined by this method may reflect the existence of ice VII on the Rayleigh path of the Hugoniot. This interpretation reconciles the experimental results with estimates and measurements obtained by other means, and is consistent with the relationship of the Hugoniot with the phase diagram for water. Sound waves are generated at 4.8 MHz at in the water experiments at 15 GPa. The existence of anelastic absorption modes near this frequency would also lead to large effective viscosity estimates.

(3) Equation of State of Molybdenum at 1400°C

Shock compression data to 96 GPa for pure molybdenum, initially heated to 1400°C, are presented. Finite strain analysis of the data gives a bulk modulus at 1400°C, K_{0S}, of 244±2 GPa and its pressure derivative, K'_{0S}, of 4. A fit of shock velocity to particle velocity gives the coefficients of $U_S=c_0+s\,U_P$ to be c_0=4.77±0.06 km/s and s=1.43±0.05. From the zero pressure sound speed, c_0, a bulk modulus of 232±6 GPa is calculated that is consistent with extrapolation of ultrasonic elasticity measurements. The temperature derivative of the bulk modulus at zero pressure, $\partial K_{0S}/\partial T|_P$, is approximately -0.012 GPa/K. A thermodynamic model is used to show that the thermodynamic Grüneisen parameter is proportional to the density and independent of temperature. The Mie-Grüneisen equation of state adequately describes the high temperature behavior of molybdenum under the present range of shock loading conditions.

Table of Contents

List of Tables

Chapter 1:

Chapter 2:

Chapter 3:

List of Figures

Chapter 1:

Chapter 2:

Chapter 3:

Introduction

(1) Melt Densities by Shock Wave Techniques

Ultrasonic sound speed measurements on silicate magmas indicate that they are nearly an order of magnitude more compressible than their crystalline counterparts. This observation, together with the fact that at 1 bar ultrabasic magmas are of comparable density to siliceous crystalline rocks, and only on the order of 10% less dense than ultrabasic rocks, led Stolper *et al.* [1981] to speculate that ultrabasic magmas may become denser than their coexisting crystalline phases at high pressure. If this is true, then silicate magmas generated at sufficiently great depth within the Earth's mantle might be inhibited from rising. In fact, magmas, with their associated heat and incompatible element enrichment, might sink. This phenomenon, if it does occur, would clearly have dramatic and far-reaching consequences for the evolution and chemical stratification of the Earth.

Rigden *et al.* [1984, 1988, 1989] developed a shock wave technique to test dynamically the feasibility of this proposition. They shock-compressed liquids in the system anorthite-diopside, and found that liquids in this system do indeed become denser than their coexisting minerals at pressures greater than 16 GPa. Application of their results to natural basaltic compositions predicted that these magmas would be denser than equilibrium olivine at 7 GPa, and denser than the bulk mantle at 10 GPa. These pressures are much greater than the 1-3 GPa range commonly assumed for the source region of basalts [Presnall *et al.*, 1979; Green *et al.*, 1979; Elthon and Scarfe, 1984], so if this density inversion phenomenon does occur it would be restricted to ultrabasic compositions that are denser, and are thought to originate at greater depth.

Komatiites are amongst the most basic magmas, having MgO contents as high as 33 weight percent. At 1 bar, molten komatiites are denser than the crust upon which they are situated [Nisbet, 1982]. This fact alone indicates the importance of the equation of state in the problem of komatiite petrogenesis. The systematics of sound speeds in silicate liquids [Rivers and Carmichael, 1987] also

predicts that these magmas are highly compressible. Because of their refractory character they are thought to originate at great depth within the mantle [*e.g.*, Takahashi and Scarfe, 1985], thus these magmas are good candidates to exhibit this anomalous density phenomenon. Since komatiitic liquids have erupted on the Earth's surface they could not have been gravitationally hindered from ascending. Nevertheless, it is possible that some komatiitic magmas formed deeper than some critical depth and sank, and those that originated at shallower levels in the mantle ascended. It is also possible that magmas more basic than erupted komatiites are formed within the Earth, but that these denser magmas are prohibited from ascending because of their high density. These possibilities are also connected to the broader issue of the role of melt densities as controlling factors in the eruption of basaltic magmas [Stolper and Walker, 1980; Sparks *et al.*, 1980].

In addition to their high MgO contents, high density, and probable great depth of origin, komatiites are an ancient magma type. Nearly all komatiites are Archaean rocks, with ages in excess of 2500 million years, although younger rocks with komatiitic affinity do exist. The genesis of komatiitic magmas apparently required conditions more common in the Archaean than today. The equation of state of komatiites may provide some constraint on the conditions necessary for the genesis of these unusual magmas, and thereby shed some light on how the Archaean mantle may have differed from the modern mantle.

Another motivation for studying komatiitic magmas is that they may represent very large degrees of partial melting of the mantle [Green, 1975], or even relicts of a wholly molten Earth [Nisbet and Walker, 1982; Agee and Walker, 1988]. It has long been recognized that the young Earth may have been molten [Daly, 1914, pp. 155-173], either as a consequence of fast accretion, core formation, or some other agency. The giant impact scenario, currently a widely accepted model for the formation of the moon, would certainly melt, and likely even vaporize part of the Earth [Cameron and Benz, 1989]. The course of evolution of the Earth from a molten state would

be strongly influenced by the equation of state of ultrabasic magmas.

The experimental measurement of the equation of state of a molten komatiite is presented in Chapter 1. This data is used to model the petrogenesis of komatiites by diapiric processes, and is used as a constraint in a model for the evolution of the Earth from an initially molten state.

(2) Melt Viscosities — Potential Application of Shock Wave Techniques

Equations of state determine the density contrast between coexisting liquids and solids, and hence the magnitude and direction of the gravitational force that drives their segregation. The rate at which this segregation occurs, however, is also largely determined by the liquid viscosity. Models for the genesis of magma and the evolution of large molten bodies, such as those considered in Chapter 1, are sensitive to the viscosity of magmas at high pressure. High-pressure measurements and theoretical models for the viscosity of silica-rich highly polymerized liquids suggest that their viscosity decreases with increasing pressure, and reach a minimum value at some pressure near 25 GPa [Angell *et al.*, 1982]. These pressures are near the limits of conventional large-volume high-pressure techniques, so a special technique is required to measure silicate liquid viscosities in this pressure region. Shock wave techniques have been developed to measure viscosity at high pressure, and the background to one of these shock wave techniques is developed in Chapter 2.

The method considered is based on the observation that nonplanar shock waves have a tendency to flatten as they propagate. Sakharov *et al.* [1965] studied this phenomenon in a variety of substances and found that the approach to planarity in real materials differs from their theory based on the behavior of ideal inviscid liquids. With an analytical method developed by Zaidel' [1967], Sakharov *et al.* [1965] interpreted the observed departure from ideality in terms of viscous behavior, and thereby obtained measurements of the shear viscosity of materials at high pressure. This tech-

nique was subsequently used to study water, mercury, and a variety of solids at high pressure. This technique has not been widely accepted, however, because the viscosities obtained by it are seriously discrepant (by a factor of 10^6 in some cases) with measurements obtained by a variety of other techniques. The reasons for these discrepancies are not known.

In Chapter 2, the analytical method first developed by Zaidel' [1967] is reexamined. Errors are corrected, and some alternative approximations are considered. Whether or not these changes alleviate the discrepancies mentioned above cannot be determined because the original experimental data is not available for reanalysis. It is hoped that this revised analytical method will make possible the use of shock waves to study the rheologic behavior of silicate liquids at high pressure.

(3) Equation of State of Heated Molybdenum by Shock Wave Techniques

The equation of state of molybdenum at high temperature is addressed in Chapter 3. This study was largely motivated by a pragmatic concern: molybdenum is used as a container in the molten silicate experiments. The accuracy with which we can determine the equation of state of silicate liquids is limited in part by our knowledge of the equation of state of molybdenum at high temperature. Molybdenum is also used as a standard in the calibration of the ruby fluorescence pressure scale used in diamond cell experiments [Mao *et al.*, 1978], thus its high temperature equation of state is of more general interest as well.

References

Agee, C.B., and D. Walker, Mass balance and phase density constraints on early differentiation of chondritic mantle, *Earth Planet. Sci. Lett.*, *90*, 144-156, 1988.

Angell, C.A., P.A. Cheeseman, and S. Tamaddon, Pressure enhancement of ion mobilities in liquid silicates from computer simulation studies to 800 kilobars, *Science*, *218*, 885-887, 1982.

Cameron, A.G.W., and W. Benz, Possible scenarios resulting from the giant impact, abstract, *Lunar Planet. Sci. Conf., 20*, 137-138, 1989.

Daly, R.A., *Igneous Rocks and Their Origin*, pp. 563, McGraw-Hill, New York, 1914.

Green, D.H., Genesis of Archean peridotitic magmas and constraints on Archean geothermal gradients and tectonics, *Geology, 3*, 15-18, 1975.

Green, D.H., W.O. Hibberson, and A.L. Jaques, Petrogenesis of mid-ocean basalts, in *The Earth: Its Origin, Structure, and Evolution*, edited by M.W. McElhinney, pp. 256-299, Academic Press, London, 1979.

Elthon, D., and C.M. Scarfe, High-pressure phase equilibria of a high-magnesia basalt and the genesis of primary oceanic basalts, *Am. Mineral., 69*, 1-15, 1984.

Mao, H.K., P.M. Bell, J.W. Shaner, and D.J. Steinberg, Specific volume measurement of Cu, Mo, Pd, and Ag and calibration of the ruby R_1 fluorescence pressure gauge from 0.06 to 1 Mbar, *J. Appl. Phys., 49*, 3276-3283, 1978.

Nisbet, E.G., The tectonic setting and petrogenesis of komatiites, in *Komatiites*, edited by N.T. Arndt and E.G. Nisbet, pp. 501-520, George Allen and Unwin, Boston, 1982.

Nisbet, E.G., and D. Walker, Komatiites and the structure of the Archaean mantle, *Earth Planet. Sci. Lett., 60*, 105-113, 1982.

Presnall, D.C., J.R. Dixon, T.H. O'Donnell, and S.A. Dixon, Generation of mid-ocean ridge tholeiites, *J. Petrol., 20*, 3-35, 1979.

Rigden, S.M., T.J. Ahrens, and E.M. Stolper, Densities of liquid silicates at high pressures, *Science, 226*, 1071-1074, 1984.

Rigden, S.M., T.J. Ahrens, and E.M. Stolper, Shock compression of molten silicate: Results for a model basaltic composition, *J. Geophys. Res., 93*, 367-382, 1988.

Rigden, S.M., T.J. Ahrens, and E.M. Stolper, High-pressure equation of state of molten anorthite and diopside, *J. Geophys. Res., 94*, 9508-9522, 1989.

Rivers, M.L., and I.S.E. Carmichael, Ultrasonic studies of silicate melts, *J. Geophys. Res., 92*, 9247-9270, 1987.

Sakharov, A.D., R.M. Zaidel', V.N. Mineev, and A.G. Oleinik, Experimental investigation of the stability of shock waves and the mechanical properties of substances at high pressures and temperatures, *Sov. Phys. Doklady, 9*, 1091-1094, 1965.

Sparks, R.S.J., P. Meyer, and H. Sigurdsson, Density variation amongst mid-ocean ridge basalts: Implications for magma mixing and the scarcity of primitive lavas, *Earth Planet. Sci. Lett., 46*, 419-430, 1980.

Stolper, E., and D. Walker, Melt density and the average composition of basalt, *Contrib. Mineral. Petrol., 74*, 7-12, 1980.

Stolper, E.M., D. Walker, B.H. Hager, and J.F. Hayes, Melt segregation from partially molten source regions: The importance of melt density and source region size, *J. Geophys. Res., 86*, 6261-6271, 1981.

Takahashi, E., and C.M. Scarfe, Melting of peridotite to 14 GPa and the genesis of komatiite, *Nature, 315*, 566-569, 1985.

Zaidel', R.M., Development of perturbations in plane shock waves, *J. Appl. Mech. Tech. Phys. (Eng. Transl.), 8*, 30-39, 1967.

Chapter 1: The Equation of State of a Molten Komatiite, Komatiite Petrogenesis, and the Evolution of the Hadean Mantle

The equation of state (EOS) of a molten komatiite (27 wt % MgO) was determined in the 5 to 36 GPa pressure range via shock wave compression from 1550°C and 0 bar. Shock wave velocity, U_S, and particle velocity, U_P, in km/s follow the linear relationship $U_S = 3.13(\pm0.03) + 1.47(\pm0.03)\ U_P$. Based on a calculated density at 1550°C, 0 bar of 2.745±0.005 g/cc, this U_S–U_P relationship gives the isentropic bulk modulus $K_S = 27.0 \pm 0.6$ GPa, and its first and second isentropic pressure derivatives, $K'_S = 4.9 \pm 0.1$ and $K''_S = -0.109 \pm 0.003$ GPa^{-1}.

The calculated liquidus compression curve agrees within error with the static compression results of Agee and Walker [1988a] to 6 GPa. We determine that olivine (Fo_{94}) will be neutrally buoyant in komatiitic melt of the composition we studied near 8.2 GPa. Clinopyroxene would also be neutrally buoyant near this pressure. Liquidus garnet-majorite may be less dense than this komatiitic liquid in the 20-24 GPa interval, however pyropic-garnet and perovskite phases are denser than this komatiitic liquid in their respective liquidus pressure intervals to 36 GPa. Liquidus perovskite may be neutrally buoyant near 70 GPa.

At 40 GPa, the density of shock-compressed molten komatiite would be approximately equal to the calculated density of an equivalent mixture of dense solid oxide components. This observation supports the model of Rigden *et al.* [1989] for compressibilities of liquid oxide components. Using their theoretical EOS for liquid forsterite and fayalite, we calculate the densities of a spectrum of melts from basaltic through peridotitic that are related to the experimentally studied komatiitic liquid by addition or subtraction of olivine. At low pressure, olivine fractionation lowers the density of basic magmas, but above 14 GPa this trend is reversed. All of these basic to ultrabasic liquids are predicted to have similar densities at 14 GPa, and this density is approximately equal to the bulk (PREM) mantle. This suggests that melts derived from a peridotitic mantle may be inhibited from ascending from depths greater than 400 km.

The EOS of ultrabasic magmas was used to model adiabatic melting in a peridotitic mantle. If komatiites are formed by >15% partial melting of a peridotitic mantle, then komatiites generated by adiabatic melting come from source regions in the lower transition zone (≈500-670 km) or the lower mantle (>670 km). The great depth of incipient melting implied by this model, and the melt density constraint mentioned above, suggest that komatiitic volcanism may be gravitationally hindered. Although komatiitic magmas are thought to separate from their coexisting crystals at a temperature ≈200°C greater than that for modern MORBs, their ultimate sources are predicted to be diapirs that, if adiabatically decompressed from initially solid mantle, were more than 700°C hotter than the sources of MORBs and derived from great depth.

We considered the evolution of an initially molten mantle, *i.e.*, a magma ocean. Our model considers the thermal structure of the magma ocean, density constraints on crystal segregation, and approximate phase relationships for a nominally chondritic mantle. Crystallization will begin at the core-mantle boundary. Perovskite buoyancy at >70 GPa may lead to a compositionally stratified lower mantle with iron-enriched mangesiowüstite content increasing with depth. The upper mantle may be depleted in perovskite components. Olivine neutral buoyancy may lead to the formation of a dunite septum in the upper mantle, partitioning the ocean into upper and lower reservoirs, but this septum must be permeable.

1. Introduction

The pressure-volume-temperature (PVT) equation of state (EOS) of silicate melts at pressures of several tens to hundreds of kilobars has recently become an area of considerable interest. This interest stems in part from the recognition that magmatic activity extending over much of the depth of the upper mantle and perhaps even the lower mantle may have played a significant role in the

early evolution and differentiation of the Earth. If so, knowledge of the equation of state would be of fundamental importance in setting constraints on the consequences of such deep-seated igneous activity. In particular, it has been suggested [Stolper *et al.*, 1981; Nisbet and Walker, 1982; Rigden *et al.*, 1984; Ohtani, 1985; Takahashi, 1986; Agee and Walker, 1987] that at sufficiently high pressures, silicate melts could become so dense that crystal-melt segregation would be impeded. This could result in a maximum depth from which melts could rise and could have the important consequence of burying heat and incompatible elements that might otherwise have reached the Earth's surface. In extreme cases, silicate melts could be denser than surrounding mantle rocks, resulting in a downward segregation of melts, heat, and heat-producing elements — quite the opposite of most modern shallow igneous activity.

Rigden *et al.* [1984, 1988] determined the EOS of a model basalt to 340 kbar and verified that silicate melts can be of comparable density to mantle minerals and rocks at high pressures. The requisite pressures (≥6 GPa) are, however, much greater than those at which basaltic magmas are generally believed to have formed [Green and Ringwood, 1967]. Melts generated at such high pressures are believed to be more olivine-normative than common basaltic magmas. Komatiitic liquids are examples of magmas that may originate at the high pressures at which silicate magmas may be comparable in density to olivine-rich residual materials. Recent high-pressure melting experiments [Takahashi and Scarfe, 1985; Scarfe and Takahashi, 1986] have demonstrated that liquids similar to komatiitic magmas can be generated by partial melting of garnet lherzolite at pressures of 5 to 7 GPa. At higher pressures, partial melting of garnet lherzolite produces even more olivine-rich magmas, approaching mantle-derived lherzolites in composition at ≈14 GPa [Scarfe and Takahashi, 1986]. Large-scale melting of the mantle may have occurred during accretion [Kaula, 1979; Abe and Matsui, 1986; Matsui and Abe, 1986; Zahnle *et al.*, 1988; Ahrens, 1990] or impact-formation of the moon [Benz *et al.*, 1986, 1987; Cameron and Benz, 1989; Stevenson, 1989], perhaps generating

a komatiitic or peridotitic magma ocean extending to great depth. The equations of state of ultrabasic liquids are critical for evaluating hypotheses for the generation of komatiitic liquids and for quantitative evaluation of early magmatic evolution that may have extended to great depths in the Earth.

Extrapolation of the high-pressure EOS of a model basalt [Rigden *et al.*, 1984, 1988] and simple mineral melts [Rigden *et al.*, 1989] to more olivine-normative compositions involves considerable uncertainty. In particular, liquid olivine components are believed to have a relatively large isentropic bulk modulus (K_S) to 100 kbar but their detailed behavior is unknown (*e.g.*, high K_{0S} and low $\partial K_S/\partial P|_S$ (K'_{0S}) versus low K_{0S} and high K'_{0S}) and can make a big difference in extrapolation of density above a few tens of kilobars [Rivers, 1985; Herzberg, 1987]. Furthermore, although 1 bar bulk moduli of basic and ultrabasic liquids can be modeled with reasonable accuracy [Lange and Carmichael, 1987; Rivers and Carmichael, 1987] their extrapolation to 100 kbar pressures is complicated by the fact that the form of the EOS cannot be anticipated [Rigden *et al.*, 1988].

Direct high-pressure experimentation on ultrabasic liquids is required. One example of the direct measurement of ultrabasic liquid bulk moduli at high pressures are the olivine sink/float bracketing experiments of Agee and Walker [1988a]. The bulk moduli of fayalite-doped komatiitic melts were bracketed by observation of the sinking or floating of olivine spheres to 60 kbar. Extrapolation of these results to end member komatiite suggests flotation of olivine would occur in komatiitic magmas at a pressure of about 80 kbar. The compositional variability (5 to 50 wt % fayalite was added, and equilibrium olivines crystallized out) of these static experiments, however, makes it difficult to generalize their results and to explore the details and specific form of the EOS of komatiitic liquid.

Another direct experimental method for the determination of high-pressure, high-temperature

liquid equations of state is shock wave compression. Shock wave compression has previously been used to measure the EOS of silicate liquids in the system anorthite-diopside to pressures of 400 kbar [Rigden *et al.*, 1984, 1988, 1989]. These results are both consistent with available low-pressure compressibility data and extend these data to lower-mantle pressures through direct measurement. In this paper, we report the results of a study of the equation of state of molten komatiite to 360 kbar using shock wave techniques. This is the first report of the EOS of a complex naturally-occurring melt composition to these pressures. The results of the high-pressure komatiite EOS are used as a basis for evaluating models of the petrogenesis of komatiitic magmas and the early evolution of the mantle.

2. Experimental method

Although the molten silicate shock wave experiment was described by Rigden *et al.* [1988], we have made some modifications to both the experimental procedure and method of data analysis. We therefore will describe the entire experimental and analytical procedure, placing emphasis on those aspects that differ from the earlier work.

A synthetic komatiite (glass plus approximately 10% spinifex olivine) was prepared at Corning Glass Works, Corning N.Y., by Dr. G. Fine. The nominal composition (Table I) was based on a natural komatiite from the Pike Hill area of Munro Township, Ontario [Walker *et al.*, 1977]. Batches of 200 g spectroscopic grade oxides were mixed, then melted at 1650°C for 4 hrs in a Fe-saturated Pt crucible in air. The liquid was then poured onto a 6 by 6 inch cold steel slab to make a patty of appropriate thickness ($\approx$ 0.5 cm) for the shock wave sample assembly. The liquid could not be quenched sufficiently rapidly to prevent growth of spinifex olivines, but by pouring slabs of similar thickness to our sample assembly we were able to ensure that the bulk composition used in our

experiments was similar to the nominal composition listed in Table I despite the chemical stratification of the slab. Cores of 1 cm diameter were cut from the slabs with a water-cooled diamond coring bit. The sample size was determined by a calculation of the mass of melt needed to fill 85-90% of the Mo container (see below) at 1550°C. The measured volume of the Mo sample container, corrected to 1550°C [Touloukian *et al.*, 1970], and the estimated melt density at 1550°C [Lange and Carmichael, 1987] determine the mass of sample needed to fill the container. The 10-15% underfilling was considered necessary to prevent rupturing or distortion of the container. The cores were ground to the desired size with 60 μm alumina.

Two cores, prepared as described above, were used to verify that the core preparation procedure did not bias the sample composition. Thin sections were cut along the axis of the cylindrical cores and analyzed with the Caltech JEOL electron microprobe. Vertical and horizontal transects across the sections were probed at approximately 50 μm intervals. Averages are presented in Table I, column 2.

Molybdenum sample containers were machined of high purity sintered Mo stock (grade ABL-2 from Climax Specialty Metals, Coldwater, Michigan) according to the specifications of Rigden *et al.* [1988]. The inner surfaces of the container were polished to 0.3 μm with alumina to minimize the possibility of bubble adhesion and to provide a smooth and nominally flat metal/liquid interface. Some curvature of the Mo was introduced by the polishing, however, resulting in a slightly concave surface; the thickness of the Mo driver plate (Fig. 1) was found to vary by 10 to 50 μm between the perimeter of the sample well and the center. Other dimensions of the Mo container measured with ±1 μm precision were the thickness of the driver plate outside of the sample well, and the sample well depth and diameter. The density of the Mo container was determined within ±0.02% by the Archimedean method. The measured density agreed with the published density [Straumanis and Shodhan, 1968] within the reported errors, confirming negligible porosity and impurities. A Mo

cover was machined to fit the sample container. The inner surface of the cover was lapped to 0.3 μm, and its thickness was measured to ±1 μm. The lapping produced no measurable curvature. The komatiite cores were placed in the Mo container, the Mo cover was seated in place, and the cover was electron beam welded at 400°C *in vacuo*. The heating under vacuum facilitates the electron beam welding and has the added likely benefit of driving off volatiles adsorbed on the glass. After welding, the sample assembly was measured to ensure that the cap was seated properly. Canting of the cap was checked by measurement of the thickness of the assembly across the cap to ±1 μm. The caps were found to be canted by less than 5 μm across their 1 cm diameter.

The welded sample assembly was hung in a vertical furnace at 1500°C for 15-20 min to verify weld integrity. The liquidus temperature of the sample is approximately 1465°C, so the sample was completely melted. A continuous flow of dry N_2 gas was maintained in the furnace to minimize oxidation of the Mo. The dimensions of the sample container were measured after heating to verify that the cap was not distended from overfilling of the sample container. The loss of thickness owing to Mo loss on oxidation was less than 5 μm. One sample was cut open and examined to verify that the sample had been completely melted. Before heating, the sample consisted of spinifex olivines in a glass matrix. After heating at 1500°C, all of the spinifex olivines were replaced by uniformly distributed ≈10 μm equant skeletal olivine crystals. This textural change indicates complete melting. The sample was also examined to determine whether or not all bubbles had risen to the top of the assembly. Some bubbles persisted at the corners between the cylindrical wall and the flat surfaces of the Mo container, but the majority of the vapor phase had accumulated at the top of the container. This sample was checked for Mo contamination and Fe loss with the Caltech electron probe (Table I, column 3).

The top surfaces of the welded sample assemblies were mirror polished with 0.3 μm alumina. Polishing made the cover measurably concave, with the center depressed up to 20 μm relative to the

Table I: Experimental Komatiite Composition, wt %

Oxide	Nominal	Measured[a]	Measured[a] after heating in Mo container
SiO_2	46.1	45.4	46.5
MgO	27.2	26.6	27.7
FeO[b]	9.7	8.6	8.5
CaO	7.4	7.8	7.7
Al_2O_3	7.6	8.2	8.0
Na_2O	0.9	1.1	0.9
TiO_2	0.4	0.4	0.4
Cr_2O_3	0.4	0.4	0.3
K_2O	0.2	0.3	0.2
MnO	0.1	NA	NA
MoO_2	—	0.0	0.9
Total	100.0	98.8	101.1

[a]average of approximately 100 analyses obtained at 50 μm intervals along horizontal and vertical transects across the sample.
[b]all Fe calculated as FeO

Figure 1: Schematic of shock wave sample assembly. A silicate glass is welded into a Mo sample container. The container is held in a fibrous Al_2O_3 ceramic plate adjacent to a Cu induction coil, used to heat the Mo container and melt the glass. The preheat temperature is monitored with a Pt-Rh thermocouple pressed in a well adjacent to the sample compartment. A metal flyer plate, embedded in a Lexan projectile, is shown in flight just prior to impact. When the impact occurs, a shock will be generated in the sample assembly. First the Mo driver plate is shocked, then the sample, and finally the cover. The arrival of the shock wave on the back (left) surface of the sample assembly is detected by measuring changes in light reflectivity as a function of time. The shock is first detected on the back surface of the driver at approximately the same time that the planar shock wave enters the sample. The shock arrival at the cover is detected with a streak camera. The inset shows the relevant distances: x_c, x_s, and x_d.

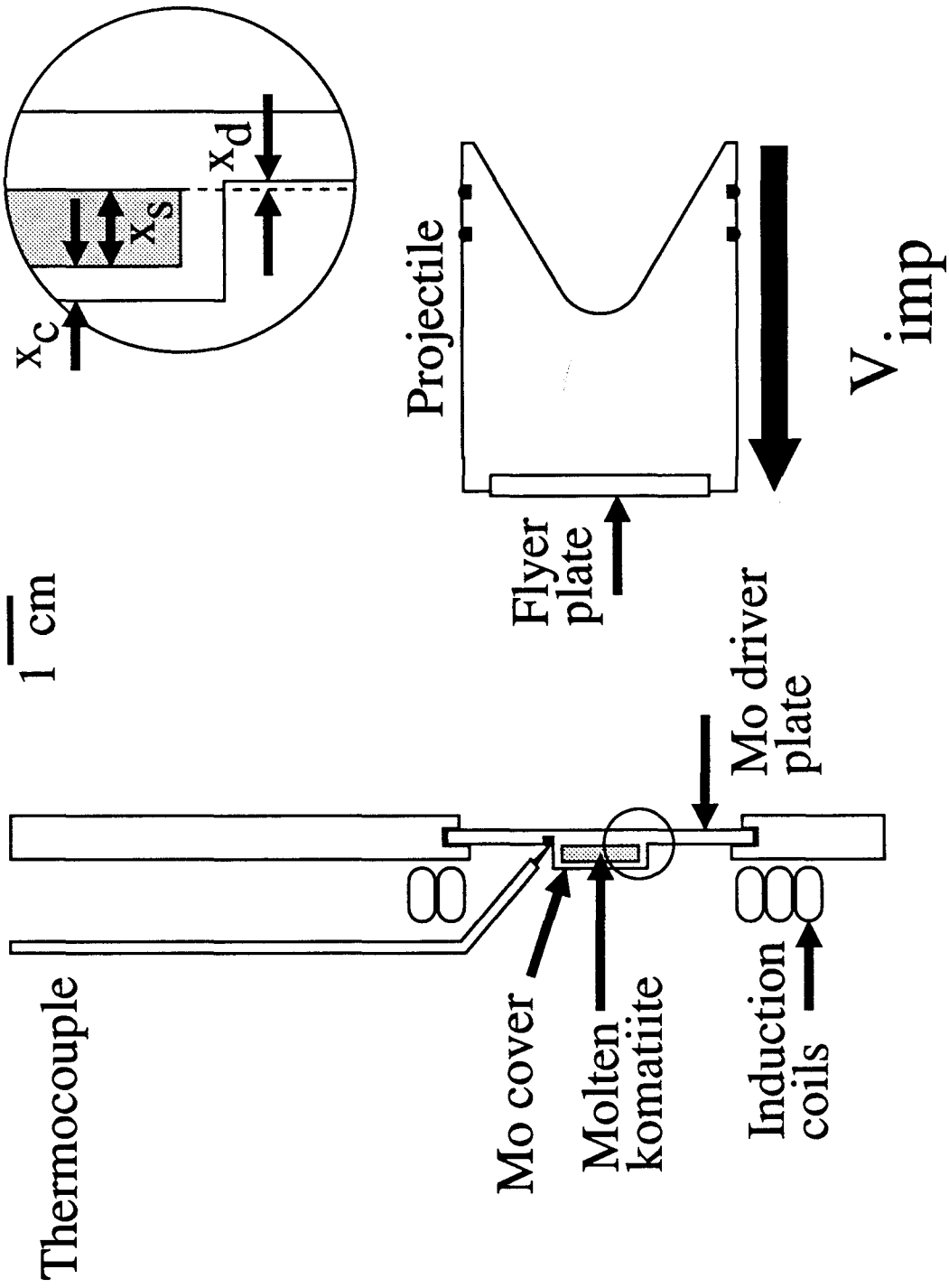
x_c
x_s
x_d
Projectile
V_{imp}
1 cm
Flyer plate
Mo driver plate
Thermocouple
Mo cover
Molten komatiite
Induction coils

Figure 1.

perimeter. The cover and driver plate thicknesses were measured to ±1 μm to determine the concavity and the thickness change during polishing. A 1.4 mm diameter, 1 mm deep well was drilled into the driver plate immediately adjacent to the sample chamber, and a Pt-Rh (type S) thermocouple was pressed into the well. The Mo container was then fitted into a machinable Al_2O_3 ceramic (Zircar) plate and aligned with a water-cooled pie-shaped induction coil made from Cu tubing. The sample assembly and induction coil were then aligned in the sample tank of the Caltech 40 mm propellant gun [Ahrens *et al.*, 1971]. A schematic illustration of the sample assembly and induction coil is shown in Figure 1.

The gun barrel and sample tank were evacuated to below 100 μm Hg, then the Mo sample assembly was induction-heated to 1550°C for ≈1 min. The sample was then allowed to cool to 800°C and the assembly was viewed through a glass port in the tank to verify that the capsule had not ruptured. The sample assembly was subsequently reheated to 1550°C. The sample was maintained at 1550°C for 10 to 20 min until the gun was fired.

The shock experiments consist of impacting the sample assembly with a metallic "flyer plate" attached to a Lexan projectile. The projectile is propelled in the evacuated gun with up to 500 g of nitroglycerine-nitrocellulose propellant to velocities up to 2.5 km/s. The projectile velocity is measured with a double-exposure 30 ns X-ray shadowgraph just prior to impact. Analysis of this X-ray record [*e.g.*, Rigden *et al.*, 1988] determines the projectile velocity to within 2%.

Prior to impact, a xenon flash lamp illuminates the polished surface of the sample assembly. A streak camera is used to measure the intensity of light reflected from the sample assembly along one spatial dimension as a function of time. The spatial axis is normally positioned horizontally across the center of the sample assembly. Its field of view encompasses the Mo cover and the Mo driver plate on either side of the sample well. We use this instrument to record relative shock wave

arrival times between the driver plate surface and the cover surface by detecting when the reflectivity of each surface changes. Free surfaces are empirically found to change their reflectivity when the shock wave arrives. This change could be associated with roughening due to differential rotation of grains on the surface of the polycrystalline material. Unfortunately, the 1550°C Mo surface does not show appreciable roughening by low-pressure shocks. Moreover, the impedance mismatch between Mo and molten silicate attenuates the strength of the shock, and the Mo cap experiences a lower pressure shock than does the Mo driver. Consequently, several of our streak camera records were so difficult to interpret, particularly in the cap region, that these data were rejected.

As noted above, we necessarily had a "bubble" in the sample chamber. Most of the vapor was found to accumulate at the top of the container that was cut open after heating to 1500°C. Aside from cutting open the containers, however, we had no method of determining the location of the bubble at 1550°C in each sample assembly we wished to shock. The possible presence of a bubble in the center of the sample is of great concern since a bubble would delay the shock wave, resulting in an erroneous shock wave velocity measurement. The curvature of the shock wave arrival (discussed below), measured along the centered horizontal slit of the streak camera, could indicate the presence of a bubble in the center of the molten sample. However, the curvature could also be due to edge effects and the concavity of the polished Mo surfaces.

One approach to determining if a bubble rose to the top of the assembly is to try to detect its presence at the top of the sample by using a vertically-positioned streak camera slit. We reasoned that a vertical-slit streak record would be strongly asymmetric if a bubble were present at the top of the assembly. To use a vertical slit it was necessary to rotate the reflected vertical image through 90° with a set of three right angle prisms (Fig. 2) onto the horizontal slit of the stationary streak camera. We conducted 4 experiments with this vertical slit configuration. A schematic illustration

of the vertical-slit streak camera records, and a comparison to horizontal-slit streak records is shown in Figure 3. In all cases a pronounced asymmetry was evident in the vertical-slit records. Furthermore, the vertical extent of the bubble's influence never extended beyond the center of the sample. The absence of bubble-induced delay below the centerline of the vertical-slit experiments strongly suggests that the horizontal slit experiments are free from any bubble influence. The vertical-slit streak records below the centerline were not perfectly flat, but resembled the horizontal slit records. This allowed us to associate the observed curvature of some horizontal streak records with edge effects and the effects of surface curvature.

Interpretation of streak records

The horizontal-slit streak record of shot #753 is reproduced in Figure 4. The time axis is horizontal on the figure, increasing from left to right, and the spatial dimension is vertical. This streak record illustrates a number of features found in some of these experiments and our interpretation of them. The streak record appears in three parts: the left side of the driver plate, the sample cover, and the right side of the driver plate. This separation into parts is a result of poor polishing of the driver next to the sample well. The shock wave arrival at the driver plate free surface is indicated on one side by an apparent increase in reflectivity, and on the other side by a decrease. The apparent increase is probably due to propellant gas that was shock-heated when the shock wave reached the free surface of the molybdenum driver plate. Note that some of the light and dark bands (due to scratches on the surface) can be followed across the shock wave arrival point and into the post-shock region of the record. In some cases these bands are offset along the spatial axis by a slight shearing motion, and in other cases some bands dramatically change in intensity when the shock wave arrives. In cases in which the pre- and post-shock light intensity is nearly equal, the

Figure 2: Prism assembly for rotating the sample image through 90 degrees. Three 2-inch right angle prisms were cemented together to enable the stationary camera (horizontal-slit plane) to view a vertical-slit image of the sample assembly.

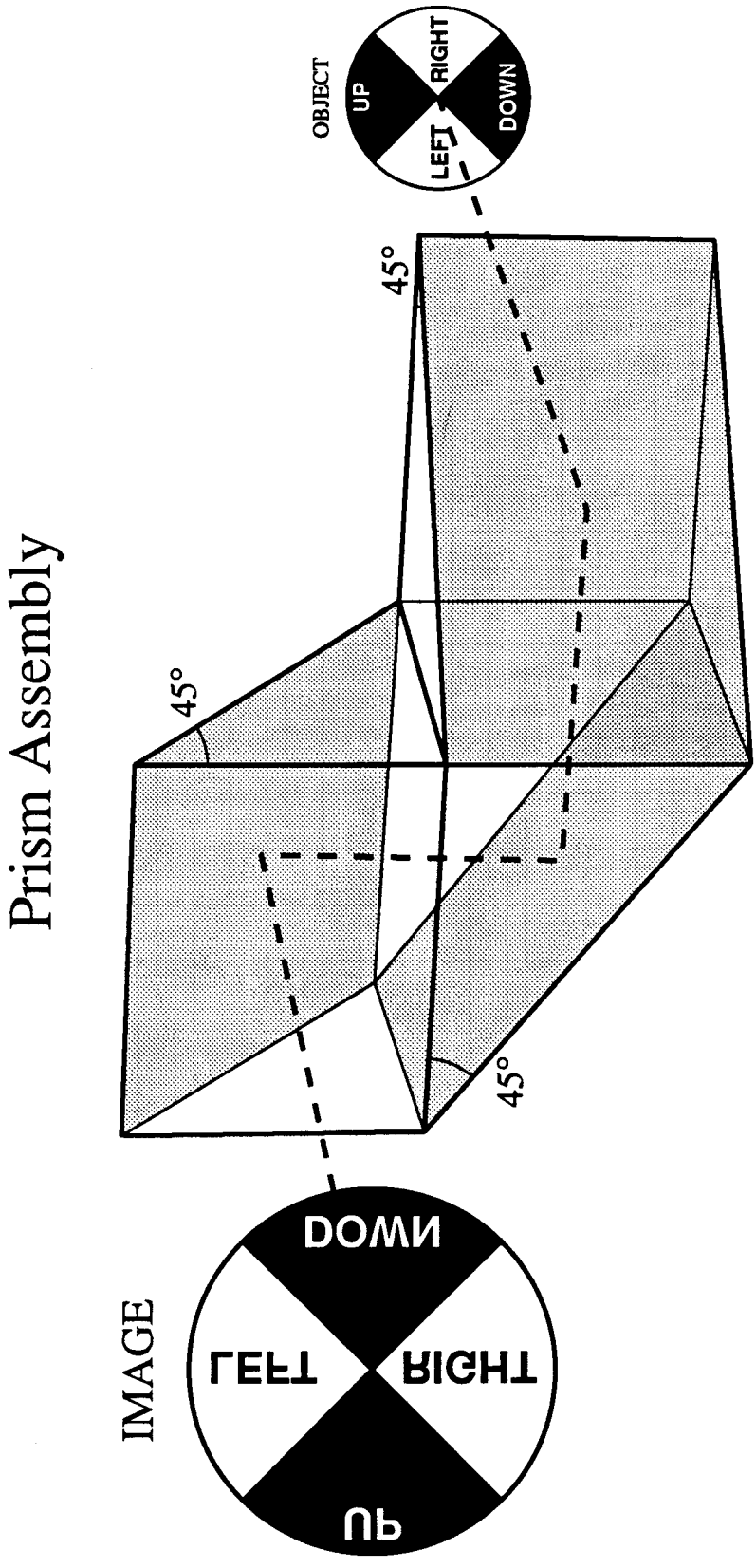
Prism Assembly
OBJECT
UP
RIGHT
DOWN
LEFT
45°
45°
45°
IMAGE
DOWN
LEFT
RIGHT
UP

Figure 2.

Figure 3: Schematic horizontal- and vertical-slit streak camera records. The records show the arrival of the shock wave on the driver plate free surface. After the shock wave has traversed the sample and the cover, the shock wave arrival is seen at the center. Note the presence of edge effects at the edge of the raised sample chamber. The vertical slit streak record is asymmetric because of the bubble, shown at the top of the sample container. The bubble slows the arrival of the shock wave, resulting in a late arrival on the streak camera record. The asymmetry induced by the bubble is easily recognized. The bubble's influence on the shock wave arrival is not detected by the camera below the horizontal centerline.

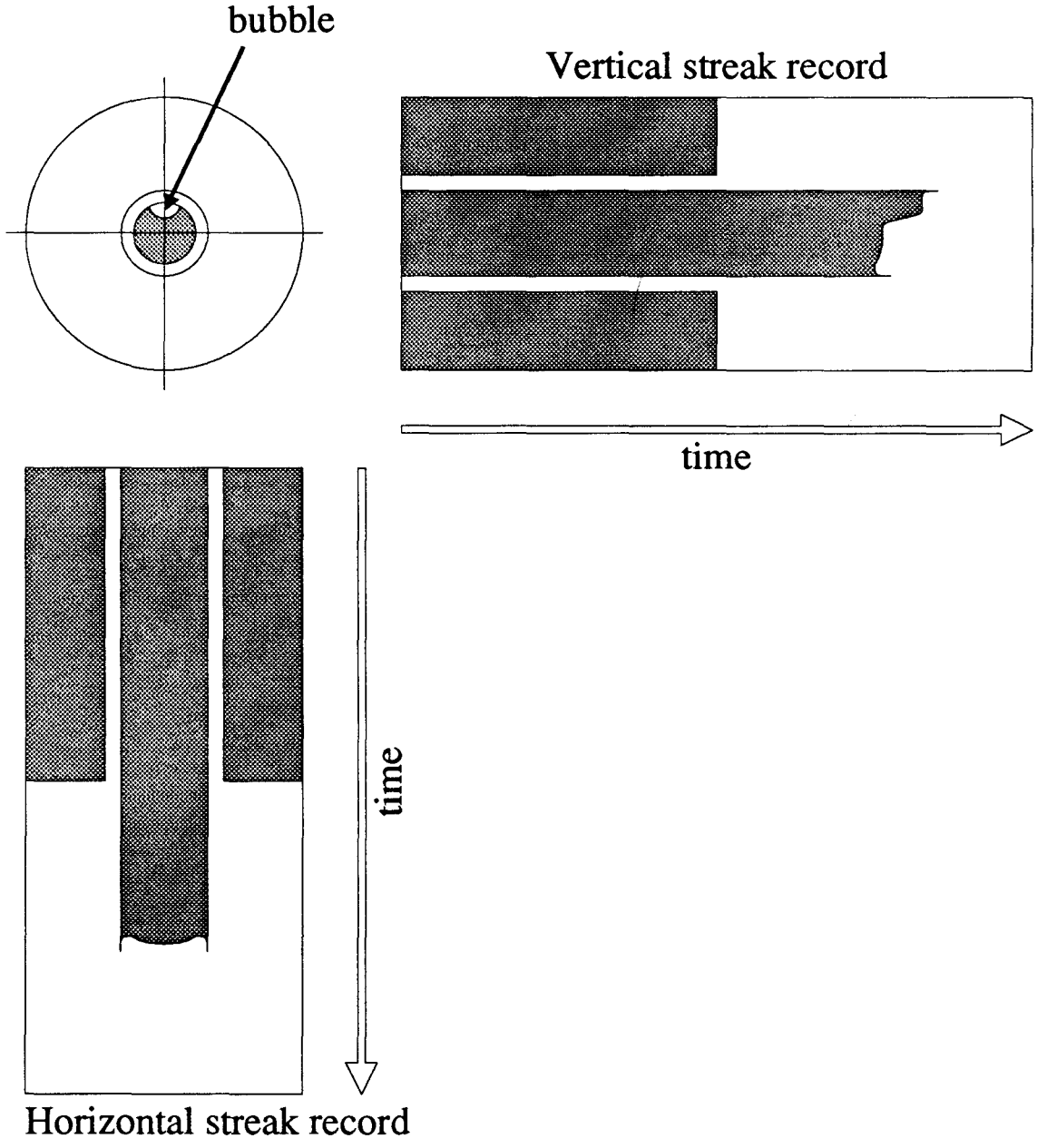
bubble
Vertical streak record
time
time
Horizontal streak record

Figure 3.

changes in these bands are taken as reliable alternative indications of the shock arrival.

The shock wave arrival at the free surface of the cover is often more difficult to interpret than that of the driver because, as noted earlier, the shock wave intensity is lower in the cover than in the driver. In Figure 4, the shock wave appears to arrive much later at the center of the sample than at its perimeter as judged by the sharp cutoff in light intensity. Using the disturbances in light and dark bands to indicate the shock arrival, however, a more uniform shock wave arrival time is indicated. The variation in shock transit times across the cover indicated by the light and dark bands is commensurate with the calculated variation based on the measured curvature of the polished surfaces. Note that the shock wave is the first disturbance to reach the free surface: no elastic precursor waves have been detected in high-temperature Mo [Miller *et al.*, 1988]. Since the shock wave is the first disturbance to reach the free surface, we have in all cases interpreted the first disturbance measured on the streak record as the shock wave arrival; all subsequent features have been interpreted as post-shock effects. Because the change in intensity of the light bands gives a variation in arrival time consistent with the measured surface curvature, and because it occurs prior to any other change in the streak record in the sample region, we take this to be the true shock wave arrival time. A faint parabolic "shadow" can be seen in the region between the shock wave arrival and the cutoff of the reflected light. This parabolic shape is a characteristic post-shock feature of high-temperature Mo [Miller *et al.*, 1988], consistent with our interpretation of this record. Although we chose to illustrate this particular record to show some of the complexities in interpretation, on other streak records the distinction between the shock wave arrival and the post-shock image is as clear as the driver arrival shown in Figure 4.

Figure 4: The horizontal-slit streak camera record from shot #753. Reflected light along the horizontal spatial dimension (vertical axis on the figure) is recorded as a function of time (horizontal axis on figure, time increases from left to right). The shock wave arrival is detected by changes in the reflectivity.

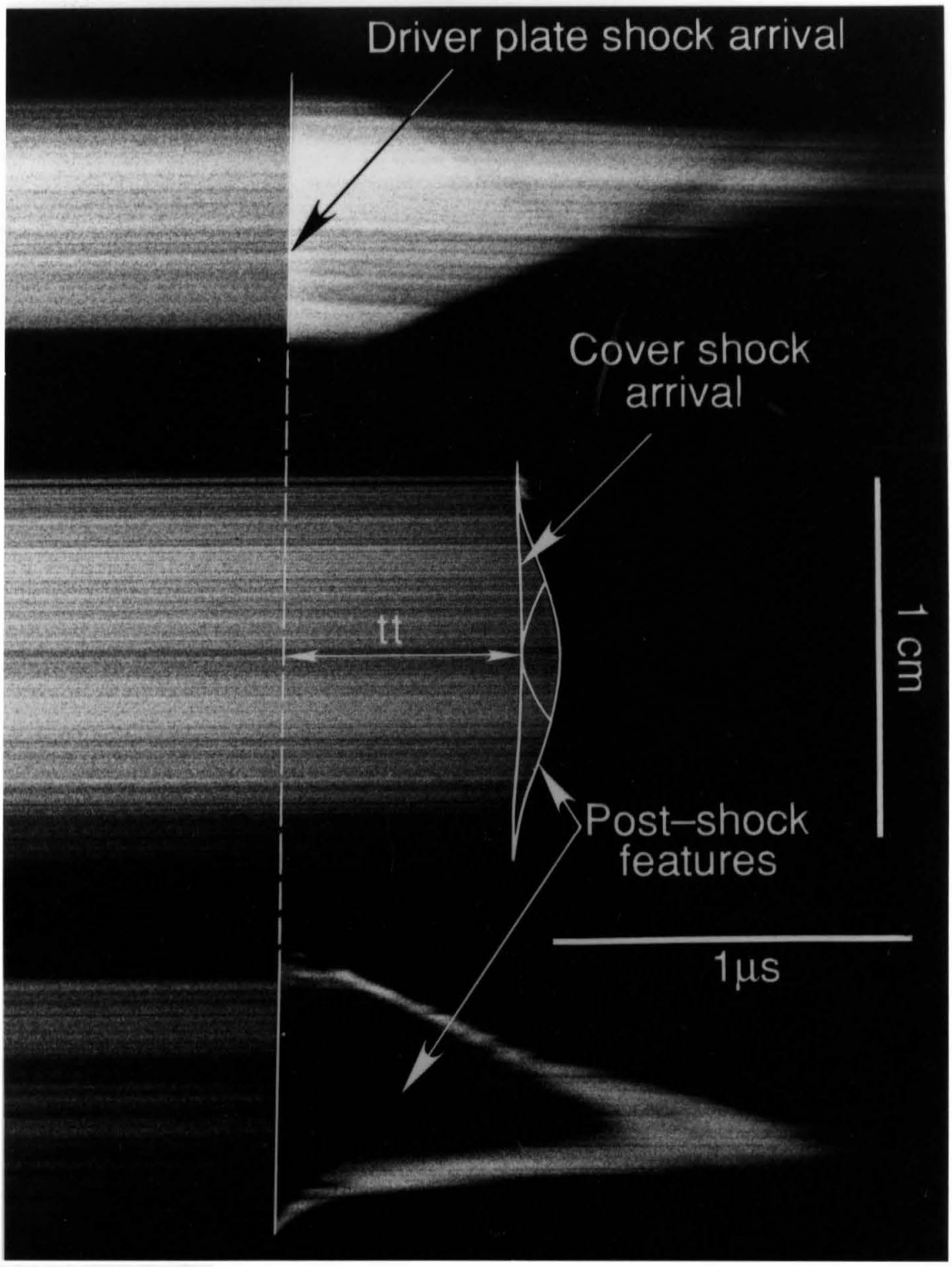
Driver plate shock arrival
Cover shock arrival
tt
1 cm
Post–shock features
1μs

Figure 4.

3. Analytical Procedure

The pressure-density state achieved in the shock experiment can be determined in an idealized experiment from measurement of the shock wave velocity in the sample and the particle velocity of the shocked sample. Neither of these measurements can be made directly in this experiment; both are indirectly determined. The sample shock wave velocity, U_{ss}, and sample particle velocity, U_{ps}, are determined by a coupled set of impedance-match equations for the flyer-driver, driver-sample, and sample-cover interfaces. The known impedance properties of the flyer plate and Mo container, together with the measured projectile velocity and shock wave propagation time, provide the necessary constraints for the impedance-match equations.

The streak camera record gives the transit time interval, tt (Fig. 4), for the shock wave to travel through the sample and the cap. The shock travels at a speed U_{sd} in the Mo driver plate, U_{ss} in the sample, and U_{sc} in the Mo cap:

$$tt = \frac{x_d}{U_{sd}} + \frac{x_s}{U_{ss}} + \frac{x_c}{U_{sc}} , \qquad (1)$$

where the thickness of the sample at 1550°C is x_s, the thickness of the Mo cap is x_c, and the difference in thickness between the driver beneath the sample and the driver outside of the sample assembly is x_d. x_d is nominally zero, however polishing and oxidation of the container make this dimension vary between +120 and -120 μm. x_d is positive when the driver plate extends into the sample well, or negative if the sample well extends into the driver. These measurements are illustrated in the inset to Figure 1. The room temperature value of these thicknesses are determined from the sample container dimensions measured at various points in its preparation, and corrected for temperature with the thermal expansivity of Mo [Touloukian *et al.*, 1970]. Because of the driver plate and cover curvature, the thickness values used were those appropriate for the position on the streak record of the measured transit time. This set of measurements is therefore self-consistent, and

different self-consistent sets give identical results within the propagated errors.

Flyer-driver impedance match

The velocity of the flyer plate, in conjunction with its known shock impedance properties and those of the hot Mo [Miller *et al.*, 1988], suffice to determine the shock velocity in the driver, U_{sd}. The impedance match equation is a statement of stress equality at the flyer/driver interface:

$$P_d = \rho_{0d}U_{pd}(c_{0d} + s_dU_{pd}) = \rho_{0f}(V_{imp} - U_{pd})\left[c_{0f} + s_f(V_{imp} - U_{pd})\right] , \quad (2)$$

where P_d is the shock pressure of the driver, and V_{imp} is the projectile velocity. Eqn. 2 can be solved as a quadratic equation in U_{pd}.

The driver's shock velocity, U_{sd}, and particle velocity U_{pd}, are related by an empirical constitutive equation:

$$U_{sd} = c_{0d} + s_dU_{pd} . \quad (3)$$

Eqn. 3 and an analogous constitutive equation for the flyer plate is implicit in Eqn. 2. The parameters of the constitutive equations, and the initial densities of the driver (ρ_{0d}) and flyer (ρ_{0f}) are given in Table II.

The shock density of the driver, ρ_d, is specified by its initial density and the shock and particle velocities by an equation of mass conservation across the moving shock front:

$$\rho_d = \rho_{0d}\frac{U_{sd}}{U_{sd}-U_{pd}} . \quad (4)$$

Driver-sample impedance match

A similar impedance match can be made to determine the shock and particle velocities of the

Table II: Material Properties

Komatiite at 1550°C					
	ρ_0 [a]	2.745	±	0.005	[g/cc]
	α [a]	8.0×10^{-5}	±	1.7×10^{-5}	[K^{-1}]
	K_T [a]	20.5	±	4.1	[GPa]
	C_p [b]	1.67	±	0.05	[J/g K]
	$(\partial c_0/\partial T)_P$ [c]	-1.4×10^{-3}	±	0.9×10^{-3}	[km/s K]
	η_s [d]	4.3			[poise]
Mo at 1550°C					
	ρ_0 [e]	9.924			[g/cc]
	c_0 [f]	5.008			[km/s]
	s [f]	1.234			[]
	$L_{1550°C}/L_{20°C}$ [g]	1.0098	±	0.0005	[]
2024 Al					
	ρ_0 [h]	2.785			[g/cc]
	c_0 [h]	5.328			[km/s]
	s [h]	1.338			[]
Cu					
	ρ_0 [h]	8.930			[g/cc]
	c_0 [h]	3.940			[km/s]
	s [h]	1.489			[]
Ta					
	ρ_0 [i]	16.654			[g/cc]
	c_0 [i]	3.414			[km/s]
	s [i]	1.200			[]
W					
	ρ_0 [i]	19.224			[g/cc]
	c_0 [i]	4.029			[km/s]
	s [i]	1.237			[]

[a] Lange and Carmichael, 1987.
[b] Stebbins *et al.*, 1984.
[c] Rivers and Carmichael, 1987.
[d] Bottinga and Weill, 1972.
[e] Straumanis and Shodhan, 1968; Touloukian *et al.*, 1970.
[f] Miller *et al.*, 1988.
[g] Linear thermal expansion ratio, Touloukian *et al.*, 1970.
[h] Marsh, 1980.
[i] McQueen *et al.*, 1970.

sample. The following equation is analogous to Eqns. 2 and 3:

$$P_s = \rho_{0s}U_{ss}U_{ps} \approx \rho_{0d}(2U_{pd} - U_{ps})\left[c_{0d} + s_{0d}(2U_{pd} - U_{ps})\right] . \quad (5)$$

The approximations used in this equation will be discussed below. Note that since a relationship between the sample shock velocity, U_{ss}, and the sample particle velocity, U_{ps}, is not yet known (this function is the objective of the experiments), Eqn. 5 will serve as one of several coupled equations to be solved simultaneously for U_{ss} and U_{ps}.

The zero-pressure density of the 1550°C komatiite liquid, ρ_{0s} (given in Table II), is not measured but calculated from the composition and temperature with the partial molar volume data of Lange and Carmichael [1987]. The shocked sample density at pressure P_s, ρ_s, is given by a mass balance equation analogous to Eqn. 4:

$$\rho_s = \rho_{0s}\frac{U_{ss}}{U_{ss}-U_{ps}} . \quad (6)$$

Sample-cover impedance match

The sample-cover impedance match equation is given by:

$$P_c = \rho_{0c}U_{pc}(c_{0c} + s_sU_{pc}) \approx \rho_{0s}(2U_{ps}-U_{pc})\left[c_{0s} + s_s(2U_{ps}-U_{pc})\right] . \quad (7)$$

The approximations used in Eqn. 7 are discussed below. A constitutive equation for the cover,

$$U_{sc} = c_{0c} + s_cU_{pc} , \quad (8)$$

is implicit in the impedance match (Eqn. 7). The shock density of the cover at shock pressure P_c is given by the mass balance equation:

$$\rho_c = \rho_{0c}\frac{U_{sc}}{U_{sc}-U_{pc}} . \quad (9)$$

In our experiments the driver and cap are both Mo and both initially at 1550°C, thus the numeric values of (ρ_{0d}, c_{0d}, s_d) are equal to (ρ_{0c}, c_{0c}, s_c). The shock states, however, are different ($U_{sd} \neq U_{sc}$, $U_{pd} \neq U_{pc}$, $\rho_d \neq \rho_c$, and $P_d \neq P_c$).

Full solution

For each individual experiment, measurements (V_{imp}, x_d, x_s, x_c, and tt) are combined with the assumed shock parameters of the sample (c_{0s} and s_s, assuming a linear U_s–U_p relationship), the known impedance properties of the Mo driver/cap and flyer plate ($\rho_{0d/c}$, $c_{0d/c}$, $s_{0d/c}$, ρ_{0f}, c_{0f}, s_f), and the calculated value ρ_{0s}, to yield calculated values U_{ss} and U_{ps} for the sample. This solution is obtained from simultaneous solution of Eqns. 1-9. For a series of experiments with different flyer plates and/or different impact velocities, a set of calculated U_{ss}-U_{ps} points is obtained. This set of values is then regressed to yield a new set of sample impedance parameters c_{0s} and s_s. The original data for each experiment are then reanalyzed with the new set of impedance parameters, etc..., until convergence is achieved. The final converged values for c_{0s} and s_s are independent of the original assumed values.

The development presented above has presupposed that the experimental relationship between U_{ss} and U_{ps} will be linear. In practice this assumption was not made. Rather, a set of equations analogous to those above was solved with a numeric method that allowed a variety of functional relationships ($U_{ss} = f(U_{ps})$) to be tried, *e.g.*, quadratic and higher-order polynomial forms and piecewise linear functions. A linear relationship fit the data well, as is the usual case for crystalline and some amorphous materials (notable exceptions include fused silica [Marsh, 1980], whose U_s-U_p slope varies continuously, and a liquid anorthite (An) diopside (Di) mixture, $An_{0.36}Di_{0.64}$ [Rigden *et al.*, 1984, 1988], which has two piecewise linear regions that join at approximately 240 kbar).

With the assumption of normally distributed (Gaussian) errors, differential forms of Eqns. 1-9 can be solved simultaneously to determine the uncertainty in U_{ss} and U_{ps} for each individual experiment. This error analysis is presented in Appendix 1. The error analysis is done in conjunction with the determinations of U_{ss} and U_{ps}, and the regression of these values to determine c_{0s} and s_s is done with a weighted least-squares procedure [Bevington, 1969] where each point is weighted by the inverse of its propagated error squared.

One additional assumption has been made in the preceding development. In a composite sample assembly, the flyer-driver interface is solved with the impedance match equations for two (initially) zero-pressure materials. All subsequent impedance matches, however, must describe the interface between a previously shocked material and an initially unshocked material. The impedance match equations for these interfaces require knowledge of the high-pressure impedance properties of the shocked material (*i.e.*, the Hugoniot of the sample centered at the initial Hugoniot state). In our sample assembly we have two interfaces of this type: the driver-sample interface and the sample-cover interface.

At the driver-sample interface the driver plate will isentropically release to the sample shock pressure. This impedance match is rigorously given by a Riemann integral formulation:

$$\int_{U_{pd}}^{U_{ps}} dU_p = -\int_{P_d}^{P_s} dP\left[\rho_d K_{s,d}\right]^{-1/2}, \tag{10}$$

where $K_{s,d}$ is the isentropic bulk modulus of the driver plate at high pressure. This integral expression can be approximated (to second order in U_{ps}) as:

$$P_s = \rho_{0s} U_{ss} U_{ps} = P_d + \rho_d (U_{pd} - U_{ps})\left[c_d^{HP} + s_d^{HP}(U_{pd} - U_{ps})\right] \tag{11}$$

by writing $K_{s,d}$ as $\rho_d (c_d^{HP})^2 + (4s_d^{HP} - 1)(P - P_d)$. This approximate solution of the exact Riemann integral resembles the Rankine-Hugoniot equation (*e.g.*, Eqn. 12) because, to second order in U_p, the

Hugoniot and isentrope are equivalent. At the sample-cover interface the shocked sample will be shocked again to the higher pressure of the shocked cover. Assuming a linear U_s-U_p relationship for the second shock of the sample, this impedance match is given by:

$$P_c = \rho_{0c}U_{pc}(c_{0c} + s_cU_{pc}) = P_s + \rho_s(U_{ps}-U_{pc})\left[c_s^{HP} + s_s^{HP}(U_{ps}-U_{pc})\right] . \quad (12)$$

The HP superscript denotes high-pressure values: c_d^{HP} and s_d^{HP} are the Hugoniot parameters of the driver centered at the high-pressure state P_d, and c_s^{HP} and s_s^{HP} are the Hugoniot parameters of the sample centered at P_s. The flyer-driver impedance match is correct as given in Eqn. 2 since the flyer is at zero pressure prior to impact.

In these cases, the high-pressure impedance properties of the shocked material (c^{HP} and s^{HP}) are not generally known, but they can be calculated from the standard impedance properties (c_0 and s) given knowledge of the thermodynamic Grüneisen parameter, $\gamma \equiv -\partial \ln T/\partial \ln V|_S$, and its isentropic volume derivative, $q \equiv \partial \ln\gamma/\partial \ln V|_S$ [Appendix 2]:

$$(c^{HP})^2 = c_0^2 + 2c_0(2s-1)U_p + [1-s(6+\gamma-5s)]U_p^2 + \frac{s}{c_0}[2+\gamma+s(2s-\gamma-4)]U_p^3 , \quad (13)$$

$$s^{HP} = \frac{16c_0^3s+8c_0^2s(7s-4-\gamma)U_p+4c_0s[4(4s-1)(s-1)+\gamma(2q-\gamma-5s)]U_p^2+12(s-1)s^2[2(s-1)-\gamma]U_p^3}{16c_0[c_0^2+c_0(3s-1)U_p+s(2(s-1)-\gamma)U_p^2]} . \quad (14)$$

A linear U_s-U_p relationship for the principal Hugoniot was assumed.

In the case of the driver-sample impedance match, Eqns. 13 and 14 should be evaluated at P_d, the high-pressure state achieved by the flyer-driver impact. In practice, however, a simplifying assumption is often made for this impedance match. We imagine that a minuscule gap exists between the driver and the sample. If such a gap existed, then the driver would release to zero pressure prior to impact with the sample. If the release were isentropic, then the free surface of the driver would be traveling at twice the particle velocity. This impedance match thus resembles the

flyer-driver impedance match where we substitute $2U_p$ for V_{imp}. The same assumptions were made for the sample-cover impedance match in Eqn. 7. In instances where the free surface velocity is actually measured, this assumption has been found to be good [Jeanloz and Ahrens, 1979], and for solid-solid interfaces, the imaginary gap may in fact exist. In the solid-liquid case, however, the solid surface is wetted by the liquid and no such gap exists. Nevertheless, we tested the validity of this assumption by using the exact form of the impedance match (Eqn. 11 for Eqn. 5, and Eqn. 12 for Eqn. 7, with c^{HP} and s^{HP} evaluated with Eqns. 13 and 14). We assumed that the Grüneisen parameter is independent of temperature, and that it varies with specific volume according to $d\gamma/dV=\gamma/V$ (q=1). Using these assumptions we found that the results are similar whether the more precise equations or the gap approximations are used, so we used the fictitious gap assumption in all our data reduction.

The success of the fictitious gap assumption indicates that the impedance match equations are insensitive to γ, hence the more rigorous analysis cannot be used to constrain γ of molten komatiite in these experiments.

4. Results

U_s–U_p Results

The results of 12 successful molten komatiite shock-wave experiments are listed in Table III and shown in the U_s–U_p plane in Figure 5. The data clearly define a linear trend. A weighted least-squares fit to the data (shown as a solid line in Figure 5) gives a U_s intercept, c_0, of 3.13±0.03 km/s, and a slope, s, of 1.47±0.03. No significant quadratic or higher order terms are present. A linear U_s–U_p trend is observed for most materials [Ruoff, 1967; Jeanloz and Grover, 1988; Jeanloz,

1989] although several notable exceptions exist [*e.g.*, Rigden *et al.*, 1988]. No theoretical justification for the linear function exists, however the absence of 2nd- and higher-order terms implies the absence of 4th- and higher-order terms in the Eulerian finite-strain EOS for typical values of the Grüneisen parameter [Jeanloz and Grover, 1988]. A linear U_s–U_p shock equation therefore often justifies the use of a 3rd-order Birch-Murnaghan EOS to describe isentropic compression.

Each term in a Maclaurin series expansion of the general function $U_s=f(U_p)$ can be related to thermodynamic properties of the sample. Such relationships for the intercept, initial slope, and initial curvature are [Ruoff, 1967; Jeanloz, 1989; Appendix 2]:

$$\lim_{U_p \to 0} U_s = c_0 = \sqrt{K_{0S} V_0}\,, \tag{15}$$

$$\lim_{U_p \to 0} \frac{dU_s}{dU_p} = s = \frac{1}{4}(K'_{0S} + 1)\,, \tag{16}$$

$$\lim_{U_p \to 0} \frac{d^2U_s}{dU_p^2} = 2s' = \frac{8K_{0S}K''_{0S} + (K'_{0S}+1)(7+4\gamma_0-K'_{0S})}{48c_0}\,, \tag{17}$$

where K_{0S} is the isentropic bulk modulus; K'_{0S} is the isentropic pressure derivative of K_{0S}; K''_{0S} is the isentropic pressure derivative of K'_{0S}; V_0 is the specific volume ($1/\rho_0$); c_0 is the bulk sound speed; and γ is the thermodynamic Grüneisen parameter. The zero subscripts denote evaluation at the preshock state; *i.e.*, 0 bar and 1550°C in our experiments.

If we assume that the linear trend defined by our data from $U_p \approx 0.47$ to 2.10 km/s can be extrapolated to $U_p \to 0$, then the coefficients of our best-fit line can be used with Eqns. 15-17 to determine the isentropic bulk modulus of the molten komatiite, and its isentropic pressure derivatives. $K_{0S} = 27.0 \pm 0.6$ GPa from Eqn. 15, and from Eqn. 16 $K'_{0S} = 4.9 \pm 0.1$.

The absence of a quadratic term, s' (Eqn. 17), can be used to constrain K''_{0S} given an estimate of γ_0. The Grüneisen parameter can be calculated from the bulk modulus K_{0S}, specific volume V_0, heat capacity C_{p0}, and thermal expansivity α_0 with:

Table III: Measured and Calculated Experimental Results

Shot #	V_{imp} [km/s]	Flyer	U_s [km/s]	U_p [km/s]	P [GPa]	ρ [g/cc]
754	1.127±0.007	2024 Al	3.85±0.05	0.47±0.01	5.0±0.1	3.13±0.01
785[a]	1.290±0.005	2024 Al	3.91±0.04	0.54±0.01	5.8±0.1	3.19±0.01
780	1.497±0.005	2024 Al	4.07±0.05	0.64±0.01	7.1±0.1	3.25±0.01
784[a]	1.767±0.007	2024 Al	4.26±0.05	0.76±0.01	8.8±0.1	3.34±0.01
782	1.912±0.007	2024 Al	4.31±0.05	0.82±0.01	9.7±0.1	3.39±0.02
777	1.420±0.005	Cu	4.61±0.06	1.02±0.02	12.8±0.2	3.52±0.02
755[a]	1.531±0.007	Cu	4.73±0.13	1.09±0.02	14.2±0.4	3.57±0.04
776	1.628±0.007	Cu	4.88±0.07	1.16±0.02	15.5±0.3	3.60±0.02
775	1.812±0.006	Cu	4.98±0.07	1.29±0.02	17.7±0.3	3.71±0.03
783[a]	1.694±0.007	W	5.47±0.09	1.60±0.02	24.0±0.4	3.88±0.04
781	1.872±0.006	W	5.76±0.10	1.75±0.02	27.7±0.5	3.94±0.04
753	2.496±0.009	Ta	6.21±0.05	2.10±0.02	35.7±0.4	4.15±0.03

[a]vertical slit streak record

Figure 5: Shock velocity (U_s) and particle velocity (U_p) data for 12 molten komatiite experiments. Individual experiments are represented by diamond symbols. The ± 1–σ error bars lie within the symbols if not shown. The solid line is the weighted least-squares best fit to the experimental data, $U_s = 3.13\ (\pm 0.03) + 1.47\ (\pm 0.03)\ U_p$. The shaded band represents the ± 1–σ error bound on the best-fit line. The initial density at 1550°C is 2.745 (±0.005) g/cc [Lange and Carmichael, 1987]. The linear regression coefficients, together with the initial density, give the isentropic bulk modulus, $K_{0S} = 27.0\ (\pm 0.6)$ GPa, and its isentropic pressure derivative $K'_{0S} = 4.9\ (\pm 0.1)$. The circle represents the measured ultrasonic sound speed of a 26.2 wt % komatiitic melt at 1558°C from Manghnani *et al.*, [1989] with a $\pm 1\sigma$ error bar. The square symbol represents the calculated bulk sound speed from the partial-molar properties of Lange and Carmichael [1987] with a $\pm 1\sigma$ error bar, offset for clarity from its 1 bar pressure (U_P=0).

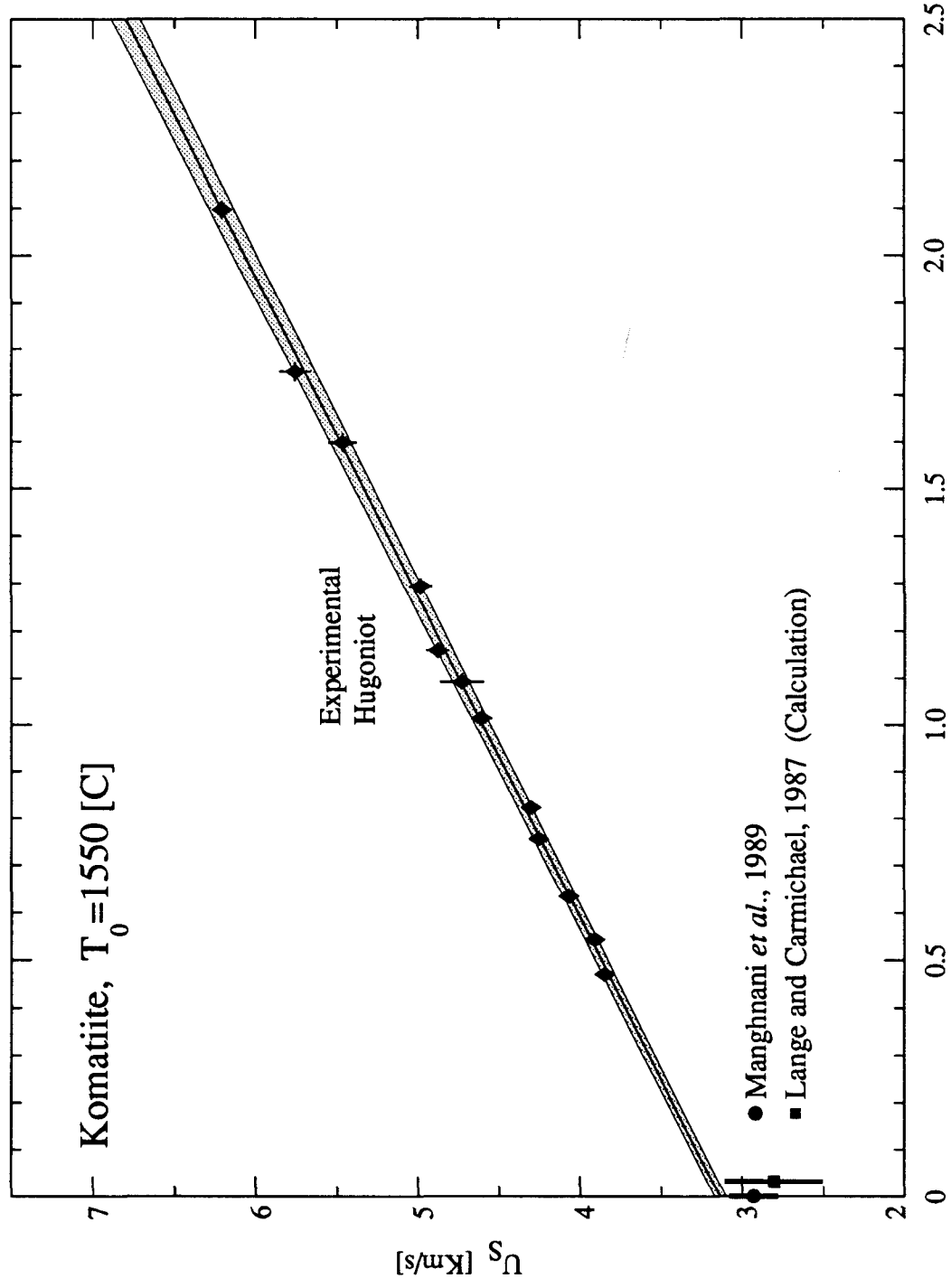
Komatiite, T_0=1550 [C]
Experimental Hugoniot
● Manghnani *et al.*, 1989
■ Lange and Carmichael, 1987 (Calculation)
U_S [Km/s]
U_P [Km/s]
2
3
4
5
6
7
0
0.5
1.0
1.5
2.0
2.5

Figure 5.

$$\gamma_0 \equiv -\left.\frac{\partial \ln T}{\partial \ln V}\right|_S = \frac{\alpha_0 V_0 K_{0S}}{C_{P0}} = \frac{\alpha_0 V_0 K_{0T}}{C_{V0}} . \qquad (18)$$

The heat capacity, 1.67 ± 0.05 J/g° [Stebbins *et al.*, 1984], and thermal expansivity, 8.0×10^{-5} ± 1.7×10^{-5} K^{-1} [Lange and Carmichael, 1987], are calculated from partial-molar properties. With Eqn. 18 the Grüneisen parameter is calculated to be 0.47 ± 0.10 at 1550°C and 1 bar. With s′ = 0, K''_{0S} = -0.109 ± 0.003 GPa^{-1} (Eqn. 17), significantly different from the -0.204 ± 0.014 value implied by a 3rd-order Birch-Murnaghan EOS ($K''_{0S} = [K'_{0S}(7-K'_{0S}) - 143/9]/K_{0S}$). This implies that a 4th- or higher-order finite-strain EOS is required. We note that if volume additivity is assumed for liquid constituents, then an n^{th}-order finite-strain EOS for the end members implies an $(n+1)^{th}$-order finite strain EOS for the ideal mixture. It is not surprising, therefore, to discover high-order terms.

The ultrasonic sound speed of a 26.2 wt % MgO komatiitic liquid was measured by Manghnani *et al.* [1989] to be 2.93 ± 0.15 (1–σ uncertainty) km/s at 1558°C (Fig. 5). This value is very close to our calculated 3.13 km/s, and our extrapolation lies within their ±2–σ error bars. Nevertheless, the difference may be significant. It is possible that the komatiitic liquid is more compressible at low pressure than our extrapolated shock data indicate. If we accept 2.93 km/s as the true 1 bar sound speed (*i.e.*, c_0 = 2.93 km/s ± 0) and regress our data with this as a constraint, we find s = 1.63 ± 0.03 and K'_{0S} = 7.5 ± 0.1. Whether or not the difference between our extrapolated 1 bar sound speed and the ultrasonic measurements is real, it is important to note that the values of K_{0S} and K'_{0S} derived from our data are accurate parameters for characterizing the komatiite EOS in the pressure interval of our experiments.

The partial-molar derivatives $\partial V_i/\partial P|_T$ from Lange and Carmichael [1987] can be used to compute the isothermal bulk modulus, K_{0T} = 20.5 ± 4.1 GPa at 1550°C. The isentropic and isothermal bulk moduli are related by $K_{0S} = K_{0T}(1+\alpha_0\gamma_0 T_0)$, from which a bulk sound speed of 2.82 ± 0.3 km/s is calculated. This calculated value is also shown in Figure 5. The partial-molar calculated

value is about 10% smaller than that inferred from the U_s–U_p fit (c_0 = 3.13 ± 0.03 km/s), but the latter lies completely within the 2-σ bounds of the former. We consider this agreement to be good, especially considering the large uncertainties in α_0 and γ_0, and the fact that compositional extrapolation was required to apply the Lange and Carmichael [1987] coefficients.

A close correspondence between shock wave determinations of c_0 and ultrasonic measurements has also been observed for liquids in the system anorthite-diopside [Rigden *et al.*, 1984, 1988, 1989].

PV Systematics

The U_s–U_p data have been converted to the more familiar PV plane with Eqns. 5 and 6. The PV data are shown in Figure 6 along with the calculated specific volume of our komatiite [Lange and Carmichael, 1987], and the best-fit U_s–U_p line (Fig. 5), converted to a curve in the PV plane. The shock-wave data span a pressure range from 5 to 36 GPa (50 to 360 kbar), and a compression range of 12 to 34%. In terms of depth within the Earth, this pressure range corresponds approximately to 150 to 950 km [Dziewonski and Anderson, 1981].

Rigden *et al.* [1989] proposed a semi-quantitative model for the systematics of melt compression. They noted that oxides like MgO and FeO have similar partial molar volumes in both low-pressure liquid and high-pressure crystalline phases, whereas the oxides SiO_2 and Al_2O_3 are much less dense in a low-pressure melt than in their high-pressure crystalline phases. This difference can be ascribed to the fact that in SiO_2 and Al_2O_3, Si^{+4} and Al^{+3} undergo gradual coordination number changes with O^{-2}, from IV to VI, with increasing pressure. Rigden *et al.* noted that near 40 GPa liquids in the system anorthite-diopside approach the densities of ideal mixtures of dense oxides to within 5-10%. Such a dense-oxide calculation was performed for the komatiite composition (Fig. 6)

using a simplified 5 component model (SiO_2, MgO, FeO, Al_2O_3, and CaO, Table IV). The remaining components are not volumetrically significant, and therefore have little impact on the PV systematics. The dense-oxide PV curve has been adjusted to the calculated shock temperatures of the komatiite (discussed below) to facilitate direct comparison. At 40 GPa the specific volume of the crystalline dense oxide mixture is approximately equal to that of the komatiite, consistent with the prediction of their model. As remarked earlier, the rate of change of the incompressibility of the An-Di system with pressure increases rapidly when the density of the liquid approaches the density of the dense oxide mixture. By analogy, we might expect the komatiite to exhibit this stiffening behavior above ≈ 40 GPa (1000 km).

Shock Temperatures

The shock-wave EOS data specify the internal energy, pressure, and density of the high-pressure molten sample. However, the temperatures achieved in the shocked state have not been measured in these experiments and must be calculated. This temperature calculation relies heavily on the thermodynamic Grüneisen parameter, whose pressure and temperature dependence are poorly constrained. Shock wave experiments using porous samples suggest that γ is a weak function of specific volume and independent of temperature. The functional form usually adopted for γ is:

$$\gamma = \gamma_0 \left[\frac{V}{V_0} \right]^q , \tag{19}$$

where (*cf.* Bassett *et al.*, 1968):

$$q \equiv \left. \frac{\partial \ln \gamma}{\partial \ln V} \right|_S = 1 + \gamma - K'_{0S} - \frac{1}{\alpha K_{0S}} \left. \frac{\partial K_S}{\partial T} \right|_P . \tag{20}$$

Using our shock wave data, values of γ_0 and α_0 discussed above, and using $\partial c_0/\partial T|_P = -1.4\times10^{-3} \pm 0.9\times10^{-3}$ km/s [Rivers and Carmichael, 1987] to calculate the temperature derivative of K_{0S}, we

Table IV: EOS parameters for crystalline oxides[†]

	ρ_0 [g/cc]	K_{0s} [GPa]	K'_{0s}	γ_0
Al_2O_3	3.988	252.7[a]	4.3[a]	1.32[a]
CaO	2.245	112.0[b]	4.8[b]	1.51[b]
FeO	5.864	158[c]	4[c]	1.63[b]
MgO	3.584	162.7[a]	4.27[a]	132[a]
SiO_2	4.290	316.0[d]	4[e]	1.25[e]

[a] Anderson *et al.*, 1968.
[b] Jeanloz and Ahrens, 1980.
[c] Jeanloz and Sato-Sorensen, 1986.
[d] Weidner *et al.*, 1982.
[e] Lyzenga *et al.*, 1982.
[†] q is assumed to be 1.0, and C_V to be 3R/atom for all phases.

Figure 6: Pressure-Volume Hugoniot for molten komatiite. Individual experiments (diamond symbols) are calculated from the experimental U_s and U_p data and the initial density 2.745 (±0.005) g/cc [Lange and Carmichael, 1987]. The ± 1-σ error bars lie within the symbol unless shown. The solid curve which passes through the experimental data is calculated from the best-fit U_s–U_p line. The shaded band represents the ±1–σ error bounds on this fit. The dotted curve is the calculated volume of a solid of komatiitic composition whose EOS is modeled as a mixture of high-pressure, high-temperature, dense oxides. The dense oxide volumes are calculated for the same pressure-temperature curve as the komatiite liquid. The dense oxide calculation assumes volume additivity, and uses the parameters listed in Table IV. Note that the liquid volume and that of the mixed crystalline oxides is approximately equal at 40 GPa.

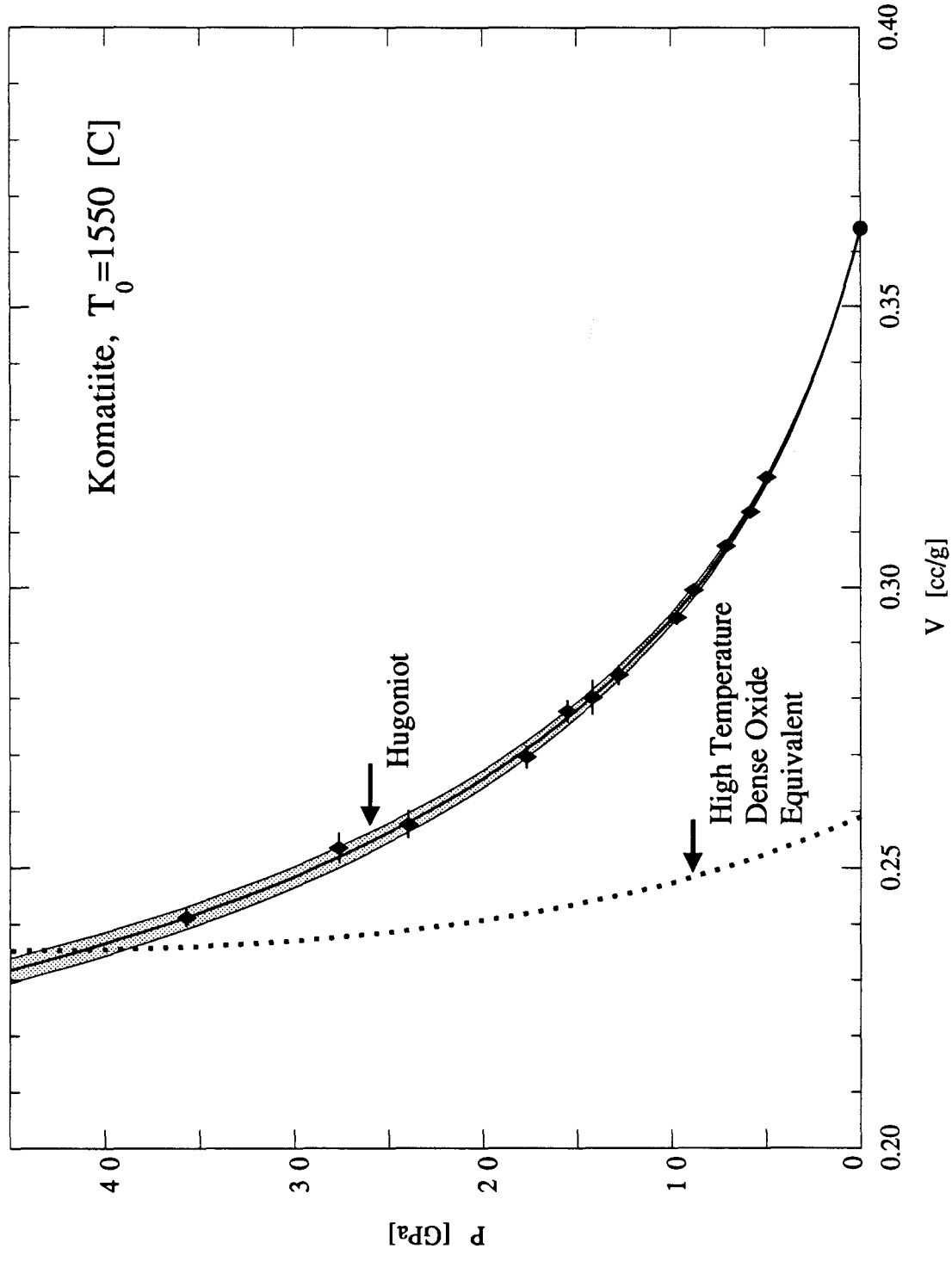
Komatiite, T_0=1550 [C]
Hugoniot
High Temperature
Dense Oxide
Equivalent
P [GPa]
V [cc/g]
0
10
20
30
40
0.20
0.25
0.30
0.35
0.40

Figure 6.

calculate from Eqn. 20 that q = 8.8 ± 7.9 at 0 bar and 1550°C, the principal contribution to the uncertainty coming from α_0 [Lange and Carmichael, 1987]. Given the large error bars on q, we adopt the common assumption that q=1.

An interesting possibility arises in considering how to use q. Porous shock-wave data suggests the form of Eqn. 19. This form may be overly restrictive, however, particularly for liquids. Note that Eqn. 19 prohibits γ from changing sign. If q were indeed large, and if $\partial\gamma/\partial V$ were constant rather than $\partial \ln\gamma/\partial \ln V$, then γ could become negative at high pressure. Some liquids, most notably water, have negative γ in some PT interval. This could be very important for large magma bodies because a negative γ implies a negative α, which in turn means that a barrier to convection will exist.

Shock temperatures are calculated by numerical integration of the differential equation:

$$\left.\frac{\partial T}{\partial V}\right|_{\text{Hugoniot}} = \frac{2\gamma C_P T - V(P-P_0)(1+\alpha\gamma T) + K_S(V_0-V)}{C_P[\gamma(V_0-V) - 2V]} . \qquad (21)$$

The formulation of Walsh and Christian [1955] is a special case of Eqn. 21 for which q=1 and C_V is assumed constant. The remaining terms in Eqn. 21 are evaluated at the appropriate high-pressure state. The high-pressure value of K_S is given by:

$$K_S = \frac{U_s^2}{V_0(1-s\lambda)}\left[(1-\lambda)(1+s\lambda) - \gamma s\lambda^2\right] , \qquad (22)$$

where $\lambda = U_p/U_s$. A C_P or C_V function is required to calculate the temperature. From the 1 bar value of C_P, 1.67 ± 0.05 J/g° from Stebbins *et al.*, [1984], we calculate C_V = 1.56 ± 0.06 J/g°, and assume that C_V remains constant. The calculation of temperature then proceeds as follows: for each volume, γ is calculated from Eqn. 19, then K_S is calculated from Eqn. 22. With the constant value of C_V, α and C_P are calculated from Eqn. 18 and $C_P = C_V(1+\alpha\gamma T)$. The derivative dT/dV is then evaluated (Eqn. 21) from these values of γ, α, K_S, C_P, and V. This derivative is used with the

Bulirsch-Stoer numerical integration algorithm [Press *et al.*, 1988, pp. 582-588] to calculate T along the Hugoniot.

The deviation in P at constant V between the individual experiments and the best-fit curve (Fig. 6) are used to determine the deviation in T at constant V between the individual experiments and the curve obtained by integration of Eqn. 21 with the equation:

$$\left.\frac{\Delta T}{\Delta P}\right|_V \approx \left.\frac{\partial T}{\partial P}\right|_V = \frac{1}{\gamma \rho C_V} . \tag{23}$$

The calculated shock temperatures for the individual experiments and for the best-fit line are shown in Figure 7 with their ± 1-σ errors. For comparison, the isentropic compression temperature, calculated directly from the definition of γ and Eqn. 19, is also shown.

An estimate of the liquidus temperature of komatiite was constructed from available high-pressure melting experiments [Bickle *et al.*, 1977; Takahashi and Scarfe, 1985; Scarfe and Takahashi, 1986; Wei *et al.*, 1990]. According to our calculations the shocked komatiite is probably above its liquidus above 15 GPa and below 1 GPa, but in the 1 to 15 GPa range it is below its liquidus.

At ≈1-15 GPa our calculations suggest that the shock-compressed komatiite is in a field of crystal+liquid stability. Although some crystallization may have occurred below 15 GPa, the overall linearity of the U_s–U_p data is consistent with there being a single (metastable) liquid phase along the Hugoniot in this pressure range. However it is possible that the change in specific volume associated with crystallization is too small to be detected within our ≈ 2% resolution [*e.g.*, Shaner, 1981]. In some systems that undergo a phase change on the Hugoniot, a two-wave shock structure may develop which is manifested in the U_s-U_p data as a discontinuous change in both slope and value. That we have not detected any such discontinuities in our results is consistent with, but does not prove, the idea that crystallization did not occur in our experiments.

Figure 7: Calculated shock and isentropic temperatures for molten komatiite. Shock temperatures are calculated from Eqn. 21. The isentrope temperature is calculated from the definition of the thermodynamic Grüneisen parameter, γ, whose zero-pressure 1550°C value is 0.47 ($\pm$0.10). The ratio γ/V is assumed constant. The shaded band represents the $\pm 1-\sigma$ bounds on the calculated shock temperature. Individual experiments, computed from Eqn. 21 with a Mie-Grüneisen correction term (Eqn. 23), are represented by diamond symbols. The error bounds on the individual experiments include the uncertainty in shock pressure. The liquidus for this composition is estimated from the high-pressure melting experiments of Bickle *et al.* [1977], Takahashi and Scarfe [1985], Scarfe and Takahashi [1986], and Wei *et al.* [1989].

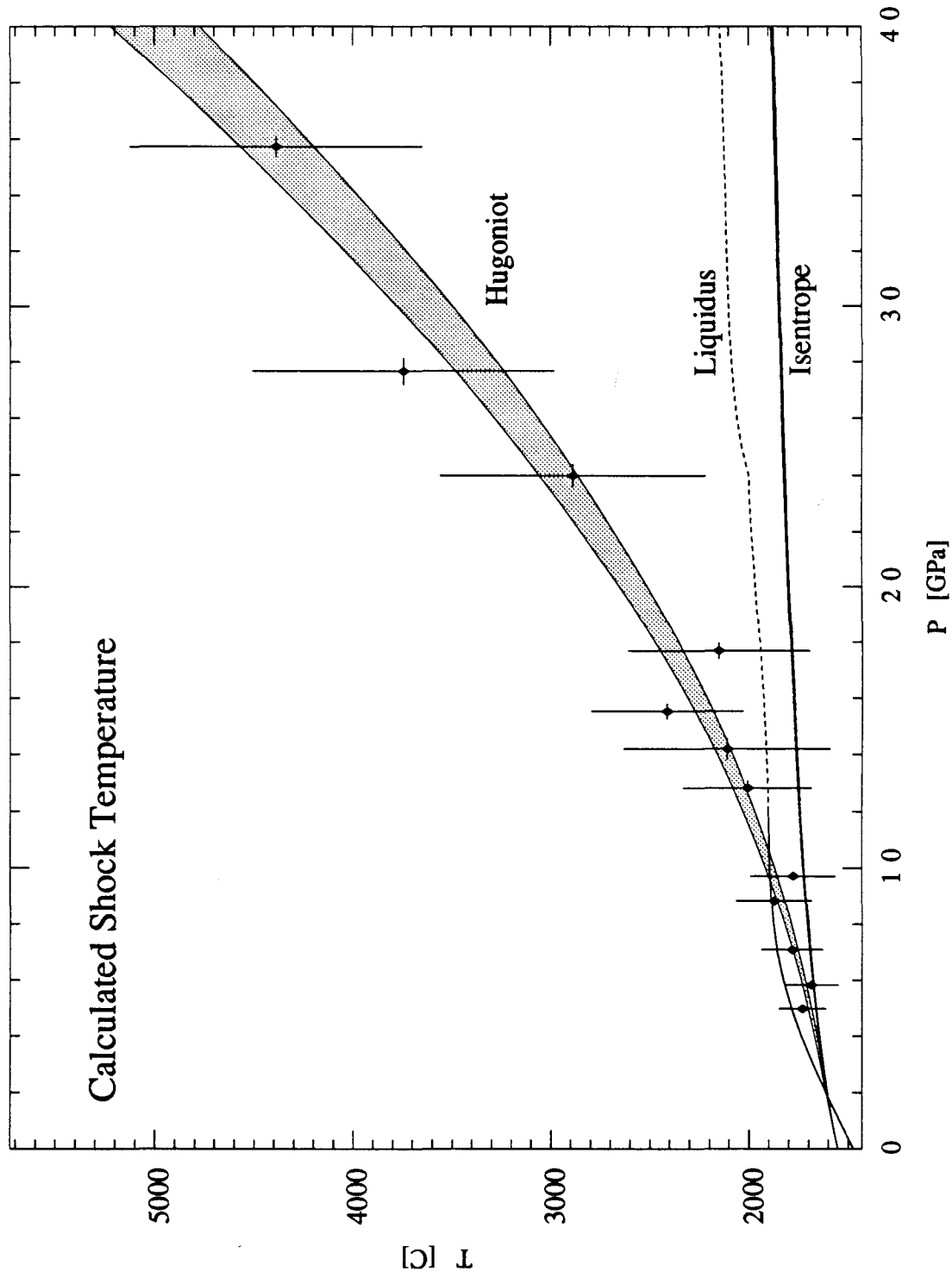
Calculated Shock Temperature
Hugoniot
Liquidus
Isentrope
T [C]
P [GPa]
5000
4000
3000
2000
0
10
20
30
40

Figure 7.

We cannot rule out the possibility that crystallization occurred on the time scale of our experiments, but it seems unlikely. The good agreement shown in Figure 5 between our determination of K_{0S} and the experiments of Manghnani *et al.* [1989] and the calculated value from Lange and Carmichael [1987] supports the interpretation that the lower-pressure Hugoniot states are metastable liquid. Moreover, there is very little time available for crystallization in these experiments. The transit time of the shock wave across the komatiite sample is on the order of 900 ns (x_s/U_{ss}). We estimate the maximum degree of supercooling to be ≈ 120° (Fig. 7), giving an effective quench rate of 1.3×10^8 °/s. Although olivine, the liquidus phase in this region, is well known to crystallize rapidly from ultrabasic melts for quench rates of up to 0.14 °/s [Donaldson, 1976], it has been quenched with a splat quench technique [Williams *et al.*, 1989]. Splat quenching rates of 10^5 to 10^6 °/s were reported for the quenching of monticellite ($CaMgSiO_4$) composition [McMillan, 1984], and McMillan (personal communication) believes that the quench rate for the formation of forsterite glass is similar to within an order of magnitude. If forsterite composition glasses can be quenched at rates of 10^7 °/s, then we consider it unlikely that olivine crystals could have formed during our experiments.

Bethe [1942] attributed a similar argument to J.G. Kirkwood. They suggested that explosions in water do not form ice VII, the equilibrium high-pressure phase, because the shock duration is shorter than the time scale for crystallization. In this case, the Hugoniot would follow the metastable extension of the liquid water curve.

State of Structural Relaxation

The objective of our experiments was to determine the equation of state of our molten komatiite under relaxed conditions. We used shock wave compression to achieve high-pressure states, and

determined the pressure and density with the Rankine-Hugoniot relations. These relations are exact under either of two conditions [Swan *et al.*, 1973]: (1) they are applied across a discontinuous shock interface, or (2) they are applied across a continuous wave with a steady profile. If it can be demonstrated that the shock wave achieved a steady state profile during our experiments, then the Rankine-Hugoniot equations are applicable. As we discuss below, the steady wave condition also assures that the material properties determined from the Rankine-Hugoniot equations refer to a structurally relaxed state.

Bland [1965] investigated the shape of the shock front for viscous solids and determined that the shock profile becomes steady when the shock wave has propagated a distance of about five times its steady state thickness. The shock thickness is proportional to the viscosity, and hence to the relaxation time of the sample [Rivers and Carmichael, 1987; Kress *et al.*, 1989]. The Rankine-Hugoniot equations will be applicable in a given experiment if the distance required for the shock to become steady is less than the sample thickness. Swegle and Grady [1985] defined the dimensionless Bland number, **B**, to be the ratio of the sample thickness to the distance which the wave must travel to reach steady state. If the Bland number is greater than 1 then the shock becomes stable before traversing the sample.

The Bland number can be approximated by [Swegle and Grady, 1985]:

$$\mathbf{B} = \frac{3s^2U_{ps}^2U_{ss}x_s}{16V_0c_0^2\eta_{eff}} \tag{24}$$

for a linear U_s-U_p material, where η_{eff} is an effective viscosity. If all relaxation mechanisms of the sample can be related to viscosity (*e.g.*, by $\eta_s = \tau K_S$ where η_s is the shear viscosity, τ is the relaxation time, and K_S is the isentropic bulk modulus [Rivers and Carmichael, 1987]) then Eqn. 24 will be a valid estimate of the Bland number. If there are relaxation mechanisms with longer time scales than those associated with viscous flow, however, then Eqn. 24 may be inadequate to evaluate the

Bland criterion.

The effective viscosity in Eqn. 24 is defined by dimensional arguments [Jeanloz and Ahrens, 1979] in terms of the shock front strain rate and deviatoric stress. Experimental measurements of the shock profile in water [Harris and Presles, 1981] suggest that this effective viscosity is similar to the shear viscosity. We estimate the effective viscosity of our komatiite to be equal to the 1 bar shear viscosity of 4.3 poise [Bottinga and Weill, 1972]. For an average sample thickness of 3.5 mm, we calculate Bland numbers of 720 at 5 GPa and 26000 at 36 GPa. These numbers are >>1, suggesting that the shocks in our experiments successfully reached steady state. This, in turn, suggests that our experiments probe structurally relaxed, equilibrium states, since the shock can only be steady if the material behind the shock achieves a well-defined, unchanging state. If, however, komatiitic liquids have relaxation mechanisms whose time scales are $\approx 10^2$ times longer than the 16 ps relaxation time implied by the effective viscosity we have chosen, then the Bland criterion may not be satisfied at low shock pressure.

Although satisfaction of the Bland criterion assures the applicability of the Rankine-Hugoniot equations and the sampling of relaxed properties, the finite distance traveled by the shock before it reaches steady state contributes an inaccuracy into our determination of U_s. We experimentally determine the shock wave velocity by calculating the time necessary for the shock to traverse the sample thickness. If the Bland number is greater than 1 then the shock will travel a distance $x_s B^{-1}$ at some average velocity $U_{startup}$ while it is developing its steady profile, and a distance of $x_s(1-B^{-1})$ at its equilibrium velocity U_{eq}. We therefore measure a velocity:

$$U_{measured} \approx \frac{BU_{eq}}{B - 1 + \frac{U_{eq}}{U_{startup}}}, \qquad (25)$$

which will differ from the desired value even though equilibrium is achieved in the experiment. We

use c_0 as a conservative estimate of $U_{startup}$ to find the errors introduced in our measurement of U_s. From Eqn. 25 and the Bland numbers calculated above we determine that our method of measurement introduced errors of 0.03% at 5 GPa and 0.002% at 36 GPa.

The Bland criterion [Swegle and Grady, 1985] differs from the criterion for reaching equilibrium in a shock experiment postulated by Dingwell and Webb [1989]. Dingwell and Webb [1989] suggest that the rise time of the shock front be compared to the relaxation time of the sample to determine whether or not equilibrium is achieved. They reasoned that when the rise time is shorter than the relaxation time, disequilibrium measurements may be made. However, the rise time of the shock is proportional to the viscosity [Bland, 1965; Jeanloz and Ahrens, 1979] which in turn is proportional to the relaxation time [Rivers and Carmichael, 1987; Kress *et al.*, 1989]. The rise of the shock front must be governed by the material's ability to respond to a stress gradient, thus the rise time will be of the same order as the relaxation time. Any gross discrepancies between calculated rise and relaxation times must be due to erroneous model assumptions. The rise time is only relevant in so far as it is related to the time needed for the shock to reach its steady state profile, *i.e.*, if the rise time exceeds the transit time of the shock through the sample, the Rankine-Hugoniot equations will clearly not apply and the experiments will be uninterpretable.

5. Discussion

Comparison to Static Compression Experiments

Agee and Walker [1988a] measured the compressibility of a komatiitic liquid near its liquidus by conducting sink/float bracketing experiments with olivine marker buoys. Liquid densities were bounded by the sink/float measurements and the calculated EOS of the olivine buoy. Experiments

were not conducted on liquid komatiite directly, but rather on komatiitic liquids into which varying amounts of fayalite had been dissolved; this was necessary to achieve olivine flotation in the 6 GPa range of their apparatus. Using a linear P–ρ model, for which $\Delta\rho/\Delta P$ was considered independent of composition, they applied the results of their fayalite-doped komatiites to the end member komatiite. Their end member komatiite composition is essentially the same as our nominal komatiite composition.

We have calculated the EOS of our komatiite on its liquidus from our data using a Mie-Grüneisen thermal pressure correction. This calculation based on our data is compared with the Agee and Walker [1988a] result in Figure 8. The high-pressure komatiite densities predicted by the static and dynamic experiments are identical, within errors, in the 0-6 GPa range of the static experiments. Note, however, that the slopes of the two equations of state, and hence K and K′, are significantly different. Beyond ≈8 GPa the static and dynamic results diverge, with the static linear P–ρ EOS predicting substantially higher densities.

Comparison to Liquidus Phases

The density of molten komatiite, calculated along its liquidus with the dynamic EOS and a Mie-Grüneisen thermal correction, is compared to the calculated high-pressure densities of phases on its liquidus (also at the komatiite liquidus temperature) in Figure 9. These mineral densities are calculated with a Mie-Grüneisen EOS:

$$P = P_S + P_T , \tag{27}$$

where P_S is the isentropic pressure calculated with a 3rd-order Birch-Murnaghan EOS:

$$P_S = \frac{3}{2}K_{0S}\left[\left(\frac{\rho}{\rho_0}\right)^{7/3} - \left(\frac{\rho}{\rho_0}\right)^{5/3}\right]\left[1 - \frac{3}{4}(4-K'_{0S})\left[\left(\frac{\rho}{\rho_0}\right)^{2/3} - 1\right]\right] , \tag{28}$$

Figure 8: A comparison of static and dynamic equations of state for komatiite on its liquidus. The static results of Agee and Walker [1988] are shown as downward-pointing triangles for sinks ($\rho_{ol}>\rho_{liq}$) and upward-pointing triangles for floats. The circle indicates the point at which they predict olivine (Fo_{94}) flotation on the komatiite liquidus. The solid band represents a calculation based on our work and the estimated liquidus shown in Fig. 7. This calculation is done by solving a Mie-Grüneisen EOS for density as a function of pressure and liquidus temperature.

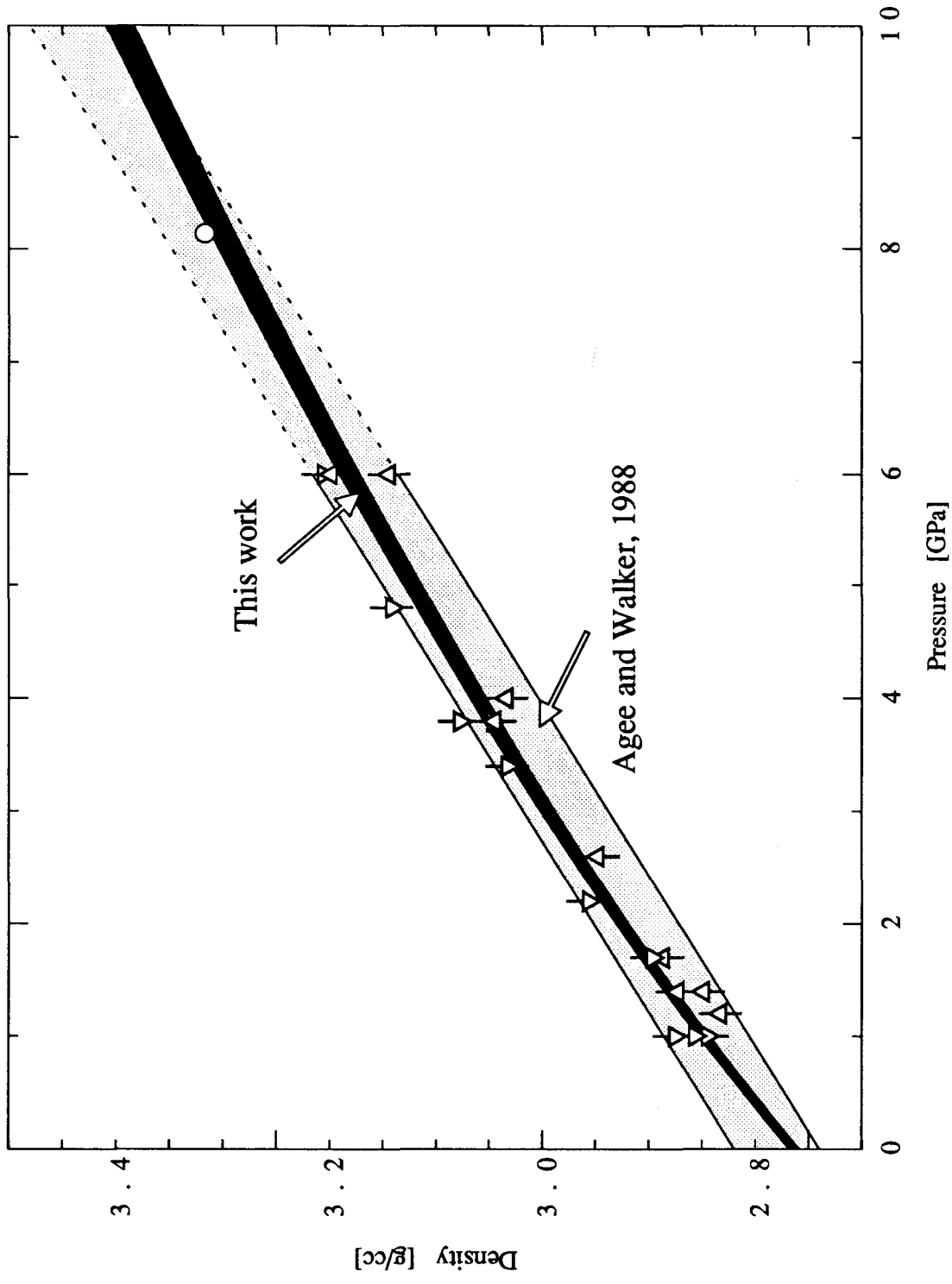
This work
Agee and Walker, 1988
Density [g/cc]
Pressure [GPa]
2.8
3.0
3.2
3.4
0
2
4
6
8
10

Figure 8.

Figure 9: The pressure-density relationships komatiite liquid and its liquidus phases along the high-pressure liquidus. The liquidus temperature is shown in Figure 7. Liquidus phase relationships are taken from Wei *et al.* [1990], with the EOS parameters described in the text and given in Table V. The circle represents the point of olivine neutral density calculated by Agee and Walker [1988a] at 8.1 GPa. Our data suggests that olivine would be neutrally buoyant near 8.2 GPa (252 km), although garnet is the liquidus phase at this pressure for a 25 wt % komatiite.

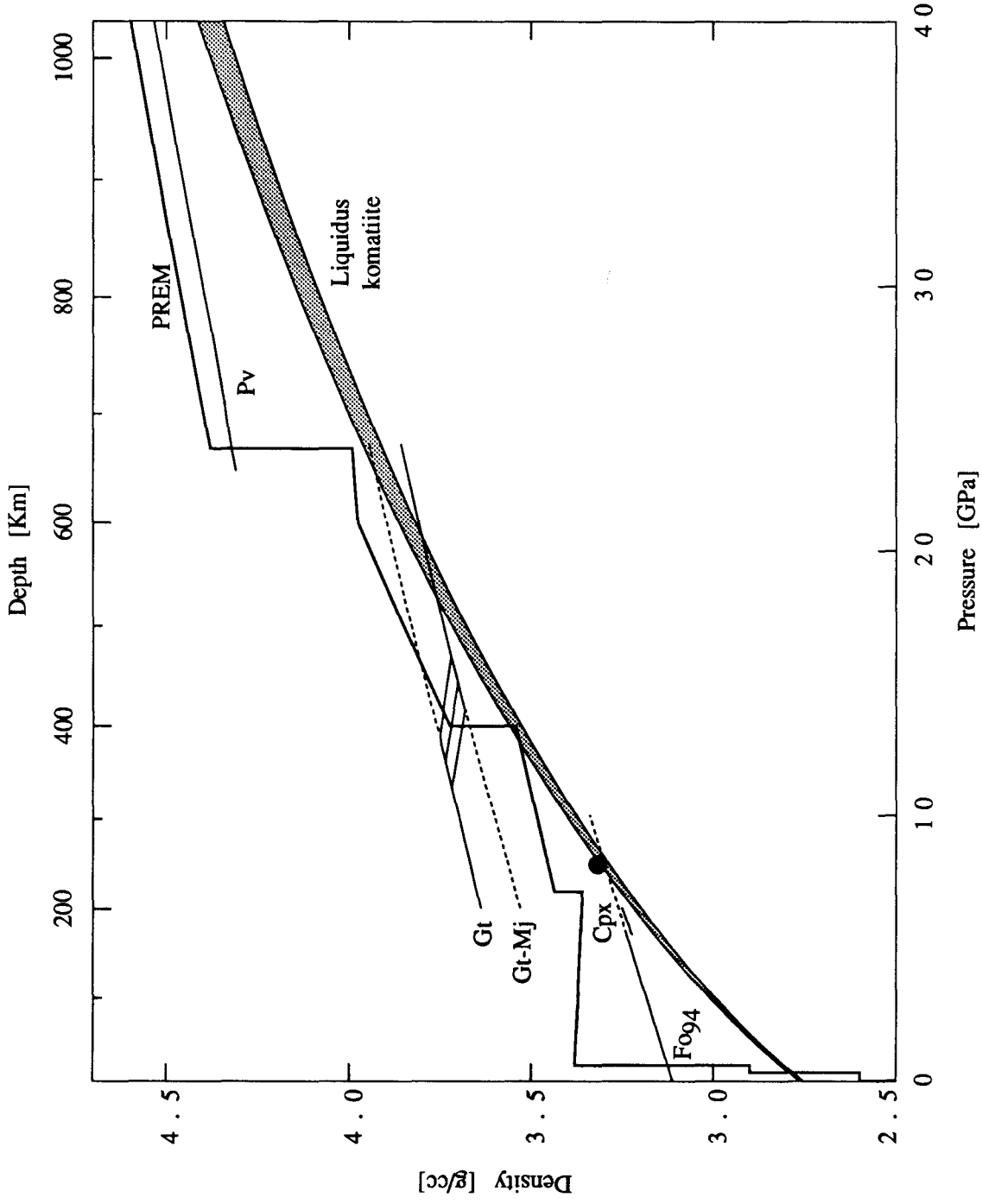
Depth [Km]
200
400
600
800
1000
Pressure [GPa]
0
10
20
30
40
Density [g/cc]
4.5
4.0
3.5
3.0
2.5
PREM
Pv
Liquidus
komatiite
Gt
Gt-Mj
Cpx
Fo94

Figure 9.

Table V: EOS parameters for liquidus phases†

	ρ_0 [g/cc]	K_{0S} [GPa]	K'_{0S}	γ_0
$Fo_{0.94}$	3.311[a]	129.4[a]	5.13[a]	1.15[a]
Di	3.276[b]	108[b]	4.8[b]	1.1[c]
$En_{0.8}Fs_{0.2}$	3.354[d]	103.5[d]	4.8[e]	1.1[c]
En	3.213[f]	107.8[g]	4.8[e]	1.1[c]
Py	3.562[h]	177[i]	4.5[i]	1.1[e]
Alm	4.318[j]	180.1[j]	4.59[j]	1.1[e]
Gr	3.617[k]	171.4[k]	4.25[k]	1.1[e]
Mj (En)	3.518[l]	160[m]	4.0[m]	1.1[e]
Pv ($En_{0.9}Fs_{0.1}$)	4.215[n]	262[o]	3.9[e]	1.7[n]

[a] Kumazawa and Anderson, 1969.
[b] Levien *et al.*, 1979a.
[c] Watanabe, 1982.
[d] Frisillo and Barsch, 1972.
[e] value assumed.
[f] Ohashi and Finger, 1976.
[g] Weidner *et al.*, 1978.
[h] Levien *et al.*, 1979b.
[i] Leitner *et al.*, 1980.
[j] Isaak and Graham, 1976.
[k] Halleck, 1973.
[l] Jeanloz, 1981.
[m] Yagi *et al.*, 1987.
[n] Jeanloz and Knittle, 1989.
[o] isothermal value from Ref n corrected to isentropic value.
† q is assumed to be 1.0, and C_V to be 3R/atom for all phases.

and P_T is the thermal pressure at constant volume:

$$P_T = \gamma\rho C_V(T - T_S) . \quad (29)$$

T_S is the isentropic temperature calculated from the definition of the Grüneisen parameter. Assuming q=1, Eqn. 29 can be rewritten:

$$P_T = \gamma_0\rho_0 C_V\left[T - T_0 e^{[\gamma_0(1-\rho_0/\rho)]}\right] . \quad (30)$$

Equation 27 is solved with a Newton-Raphson technique for density at each PT point.

Olivine is the liquidus phase of ≈25 wt % MgO komatiite to approximately 5.2 GPa [Bickle *et al.*, 1977; Wei *et al.*, 1990]. Taking $K_D = (FeO/MgO)_{olivine}/(FeO/MgO)_{liquid}$ to be 0.30 + 0.02×P (P in GPa) [Takahashi and Kushiro, 1983] to 4 GPa, and 0.38 for higher pressures [Agee and Walker, 1988a], the olivine in equilibrium with our komatiitic liquid changes from Fo_{95} at 1 bar to Fo_{94} above 4 GPa. Since the equilibrium olivine composition is nearly constant, we adopt a single set of physical constants (Table V).

From approximately 5.2 to 6.8 GPa a low-Ca clinopyroxene (Cpx) is the liquidus phase of ≈25 wt % MgO komatiite [Wei *et al.*, 1990]. At 5.5 GPa and 1780°C Wei *et al.* [1990] report a near-liquidus Cpx of composition $Wo_{0.135}En_{0.742}Fs_{0.123}$ (molar). The EOS of this complex composition is calculated by adding volumes of positive quantities of diopside, bronzite ($En_{0.8}Fs_{0.2}$), and enstatite (Table V).

Above 6.8 GPa the liquidus phase of ≈25 wt % komatiite is a garnet [Wei *et al.*, 1990]. Wei *et al.* [1990] report a near-liquidus garnet composition of approximately $Py_{0.791}Alm_{0.110}Gr_{0.099}$ (molar) (Py = pyrope, Alm = almandite, Gr = grossularite) at 10 GPa and 1860°C, although their analyses indicate a small majorite component. The experiments of Ohtani *et al.* [1986] and Irifune [1987] indicate that the majorite content of garnets in equilibrium with peridotitic assemblages increases with pressure to 16 GPa, but that near-liquidus garnets may have lower majorite contents.

We explored the range of probable liquidus garnet compositions by calculating both $Py_{0.791}Alm_{0.110}Gr_{0.099}$ and $Py_{0.316}Alm_{0.044}Gr_{0.040}Mj_{0.600}$ compositions. The EOS of these complex garnets are constructed from the end members (Table V) with the assumption of volume additivity.

Near 24 GPa both the olivine and pyroxene components of the mantle transform into the perovskite structure [Jeanloz and Thompson, 1983]. Ito and Takahashi [1987] found that a Mg-rich perovskite phase is the liquidus phase for a peridotitic composition near 25 GPa. Although high-pressure experiments on komatiitic composition have not been carried out to these extreme pressures, we consider it likely that garnet-majorite will be replaced by perovskite as the first liquidus phase near 24 GPa.

The results presented in Figure 9 indicate that the komatiite composition used in this study is less dense than its assumed liquidus phases at all pressures to 40 GPa, except in the 20-24 GPa interval where majorite-rich garnet may be buoyant in coexisting komatiitic liquid. Thus, if this particular komatiite were formed in the upper mantle it would be buoyant relative to coexisting crystals and would tend to segregate upward. There is, however, substantial chemical variation in natural komatiites and related basalts, with MgO contents ranging from 10 to nearly 40 wt %. To a good first approximation, this variation is controlled by olivine addition or subtraction. As MgO content (and normative olivine) increases, olivine is stabilized on the komatiite liquidus to greater pressures. For example, experiments on a 32 wt % MgO komatiite (Wei *et al.*, 1990) show that such high MgO komatiites can have olivine as the liquidus phase to 9.6 GPa. Would olivine float in such a liquid at this pressure? The key to answering this question is understanding the effects of olivine addition and subtraction on melt density. This issue is addressed in the following section.

Compositional Variation

The compositional systematics of the EOS of multicomponent systems are of fundamental importance to the understanding of natural magmatic systems. As the melt fraction changes, due either to crystallization or melting, compositional changes will take place in the liquid unless the system is at a eutectic. For a ≈25 wt % MgO komatiite, olivine is the first liquidus phase to 5.2 GPa [Wei *et al.*, 1990], and crystallization of komatiite up to this pressure will result in a residual liquid that is more basaltic. A basaltic melt is less dense than a komatiitic melt at low pressure. At high pressure, however, basalt may be more dense than komatiite. This can be understood by considering the behavior of the major oxide components. The partial molar volume of MgO in a silicate melt is similar to that of the high-pressure phase magnesiowüstite, and we anticipate its compressibility to be similar to that of the solid as well [Rigden *et al.*, 1989]. In contrast, although the partial molar volume of SiO_2 in a low pressure melt is substantially greater than that of stishovite, we expect this density difference to diminish with increasing pressure. As the partial molar volume of SiO_2 in the liquid approaches that of stishovite, the densities of more siliceous liquids will begin to overtake those of ultrabasic liquids because the former are far more compressible. This qualitative trend is supported by shock wave data in the system anorthite-diopside [Rigden *et al.*, 1984, 1988, 1989]. When the densities of a liquid basalt analog in this system and liquid komatiite are compared at the same temperature it can be shown that the analog basalt density is similar to the komatiite density near 25 GPa even though the komatiite is far denser at low pressure. Thus, although at lower pressures olivine fractionation leads to dramatic reduction in liquid density [Sparks *et al.*, 1980; Stolper and Walker, 1980], as pressure increases the decrease in density with fractionation decreases, and there may be a pressure beyond which olivine fractionation increases the liquid density. Note that this latter phenomenon will only be observed for liquids sufficiently

olivine normative that olivine remains on the liquidus to very high pressures.

If we adopt the liquid olivine EOS parameters proposed by Rigden *et al.* [1989], then we can calculate komatiite liquidus equations of state for a range of MgO contents. This calculation is presented in Figure 10 for MgO contents ranging from 6.9 to 35.3 wt %. We have approximated the effect of adding (and subtracting) olivine on the liquidus temperature by adding (or subtracting) 20°C per wt % MgO relative to our nominal composition [Nisbet, 1982]. Although this approximation is probably good at near crustal pressures, the experimental data of Wei *et al.* [1990] (for 25 and 31.5 wt % MgO komatiites) indicates that the MgO dependence of the liquidus may be much smaller at high pressure. A more precise calculation of the fusion curves [Walker *et al.*, 1988] is underconstrained by the available data, and would have little effect on the resulting calculations because α is so small. This diagram illustrates three important points: First, near 13.3 GPa the assimilation or fractionation of olivine will not significantly change the density of the melt, *i.e.*, basaltic through peridotitic magmas will have nearly the same density on their 13.3 GPa liquidi. At greater pressure the density of basaltic liquids exceeds that of the peridotitic liquids. This result was anticipated by the calculations of Ohtani [1984] and Rigden *et al.* [1989]. Second, if we use the olivine-clinopyroxene cosaturation point to indicate the probable origin of these ultramafic magmas, then komatiites with MgO >30 wt % will originate under conditions where their liquidus phases (both olivine and clinopyroxene) would float. Third, it is interesting to note that at the 13.3 GPa point where all komatiitic magmas have similar density, their density is approximately equal to that of the bulk mantle [PREM model, Dziewonski and Anderson, 1981].

If substantiated by further experiments the coincidence of all basaltic through peridotitic liquidus equations of state both with each other and with the bulk mantle would imply that it would be difficult for such magmas to ascend from below 400 km. Although komatiitic liquids would be capable of separating (up) from their coexisting crystals, the negligible density contrast between the

Figure 10: Komatiitic liquid liquidus equations of state calculated from our experimental data and the proposed liquid olivine EOS of Rigden *et al* [1989]. The densities of olivine liquid components were calculated from Eqn. 28 using an isothermal rather than an isentropic reference curve. The 1400°C reference isotherms are given by ρ_0 = 2.825/3.718 and α = $1.1\times10^{-4}/1.1\times10^{-4}$ K^{-1} [Lange and Carmichael, 1987], K_{0T} = 24.9/20.5 GPa and K'_T = 10.2/11.2 [Rigden *et al.*, 1989], C_V = 1.92/1.00 J/g° [Stebbins *et al.*, 1984], and γ_0 = .4/.7 (from Eqn. 18) for forsterite/fayalite. We assume q=1. Curves are komatiite with 50 wt % subtracted olivine (6.9% MgO), komatiite (27.2% MgO), and komatiite with 50% added olivine (35.3% MgO). The liquid Fo/Fa component contents of the various liquids were determined by assuming Rayleigh fractionation with K_D=0.38. Liquidus temperatures were adjusted according to the MgO content by adding 20°C per wt % added MgO [Nisbet, 1982]. The curves are open where olivine is the liquidus phase, bold where clinopyroxene is the liquidus phase, and shaded where garnet is the liquidus phase. The equation of state of crystalline olivine is the same as in Figure 8. (a) Calculation in the pressure range of our experiments. (b) Extrapolated to lower mantle conditions.

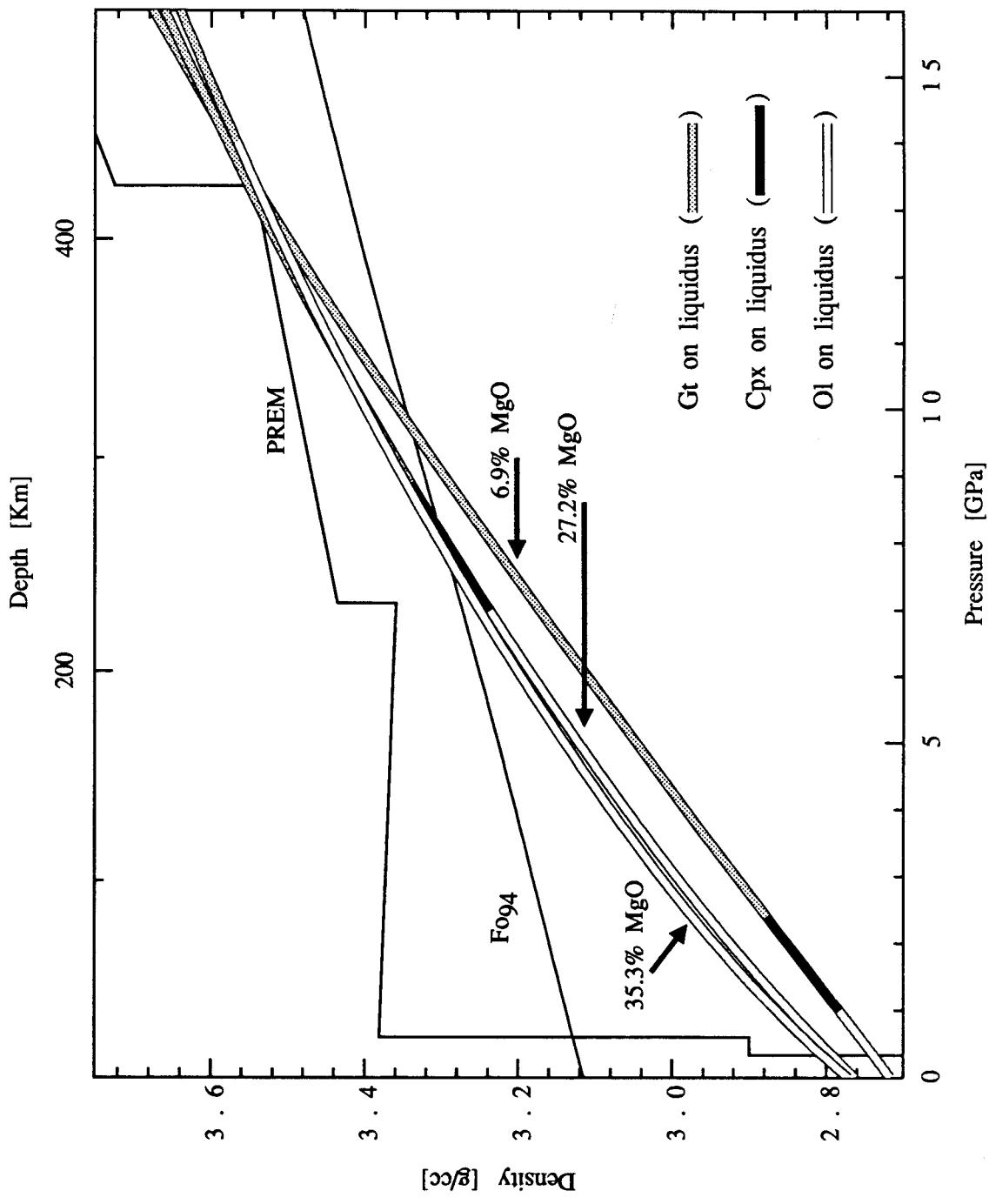
Depth [Km]
200
400
PREM
6.9% MgO
27.2% MgO
35.3% MgO
Fo94
Gt on liquidus
Cpx on liquidus
Ol on liquidus
Density [g/cc]
3.6
3.4
3.2
3.0
2.8
0
5
10
15
Pressure [GPa]

Figure 10a.

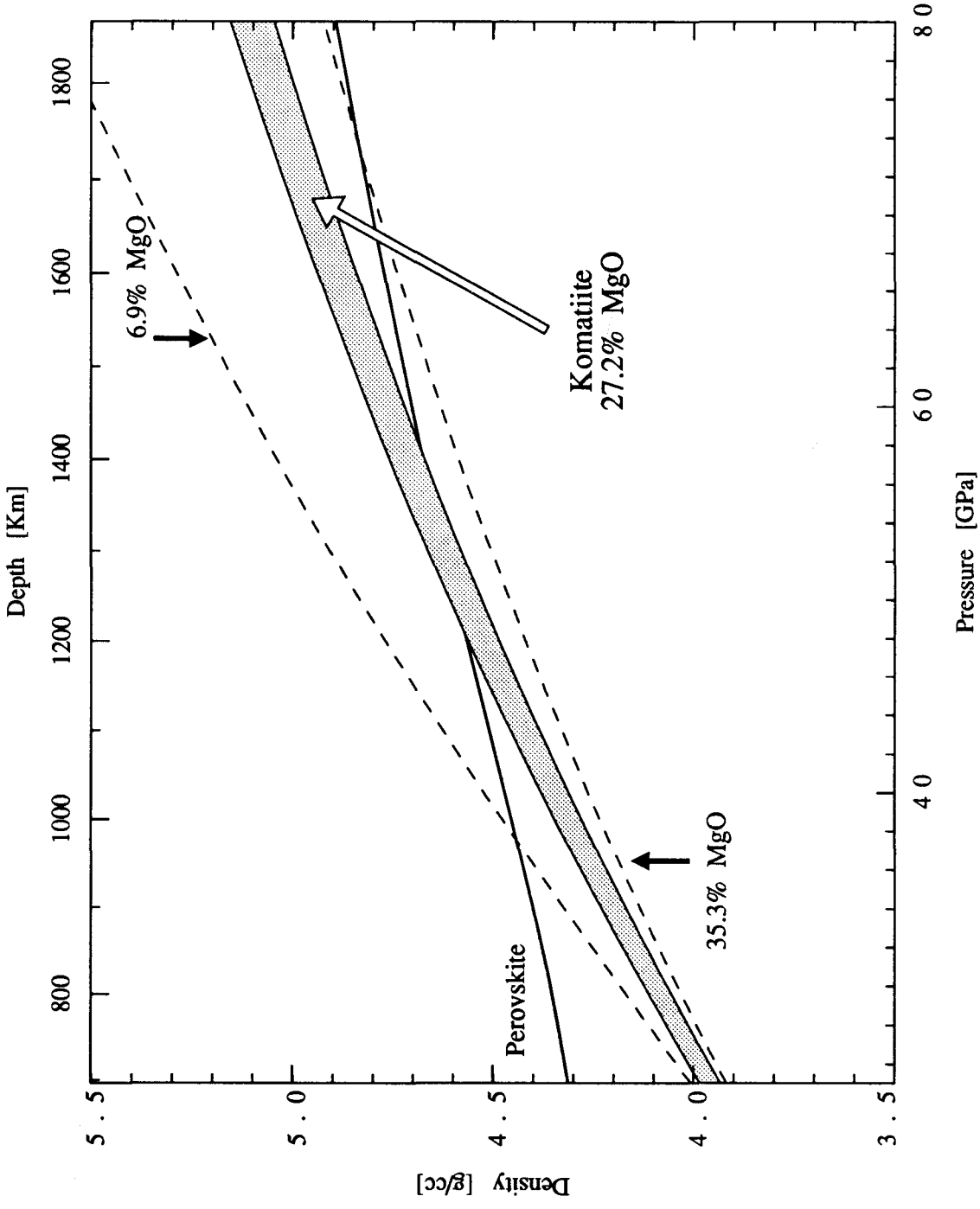
Depth [Km]
800
1000
1200
1400
1600
1800
Density [g/cc]
5.5
5.0
4.5
4.0
3.5
Pressure [GPa]
4 0
6 0
8 0
6.9% MgO
Komatiite
27.2% MgO
35.3% MgO
Perovskite

Figure 10b.

liquid and bulk mantle at this point might inhibit separation of the liquid from its bulk mantle environment. Figure 10 indicates that the spectrum of magma compositions from basaltic through peridotitic are approximately equal in density to the bulk *cold* mantle as represented by the PREM model. If we allow for either a hotter Archaean geotherm, or a thermal aureole surrounding the anomalously hot magma body, then the bulk mantle density near the magma body would likely be lower than the cold PREM estimate. Moreover, increasing temperature shifts the olivine $\rightarrow \beta$ transition to higher pressures by 0.0035 GPa/°C [Suito, 1972; 1977] thereby enlarging the region in which komatiites are negatively buoyant in the bulk mantle by moving the 140 km discontinuity to greater depth. A small positive temperature dependence for the reaction En$\rightarrow$Mj (0.0015 GPa/°C, Irifune, 1987) has less effect on the high-temperature density profile of the transition zone.

In Figure 10b we show this same calculation for lower mantle conditions. The results must be considered speculative since our data have been extrapolated well beyond the 36 GPa limit of our experiments. This calculation indicates that perovskite, ostensibly the densest lower mantle crystalline phase, may be less dense than the range of basic to ultrabasic magma compositions. If this is true then ultrabasic magmas would be incapable of ascending from below ≈1000 km. Ohtani [1983] arrived at the same conclusion, and suggested that downward migration of melts in the lower mantle would transport incompatible and radiogenic elements toward the core. We feel that this is unlikely, even if our calculation is correct, since such melts would likely freeze upon adiabatic compression.

While neutral or negative buoyancy would preclude the upward segregation of a liquid from a static matrix, it might be possible to extract the liquid if the matrix were transported upward in part of a large scale convection system. In this case, both liquid and solid would rise together until the density contrast becomes sufficient for separation to occur. When partial melting is initiated by the adiabatic decompression of upwelling mantle plumes, continued upward transport of the plume may permit escape of the liquid even if it were initially too dense. If chemical equilibrium is maintained

in the source region, however, the chemistry of the liquid will evolve as the upwelling continues. A dense liquid that escapes by this upward transport mechanism would therefore be indistinguishable from a positively buoyant liquid generated at shallower depths if chemical equilibrium is maintained.

6. Application to adiabatic melting and komatiite genesis

Adiabatic gradients

Melting accompanying the adiabatic decompression of mantle diapirs has long been recognized as a possible source of basic and ultrabasic magma [Verhoogen, 1954]. The basic idea is that temperature diminishes more gradually with decreasing pressure in a totally solid system than does the temperature of the anhydrous solidus of typical mantle rocks. An adiabatic diapir may consequently cross the solidus as it rises, thereby undergoing partial fusion. Since the adiabatic gradient of a wholly molten system is solely a function of the EOS of the liquid, and that of a partially molten system is a strong function of the liquid EOS, our komatiitic liquid EOS provides a useful constraint on melting or crystallization under adiabatic conditions for ultrabasic systems. In this section, we develop a semiquantitative formulation of the adiabatic gradient in the melting interval of peridotite and consider its application to diapirism in the mantle and the genesis of komatiites.

An adiabatic process is one in which neither mass nor heat is exchanged with the surroundings. Adiabaticity implies constant entropy under reversible conditions. It can also imply constant enthalpy under irreversible conditions [Waldbaum, 1971], however this reduces to the isentropic case if stress is hydrostatic [Ramberg, 1971]. In this discussion we will equate adiabatic conditions with isentropic conditions.

Several liquid komatiite adiabats are shown in Figure 11. These were calculated using the equation for the adiabatic gradient of a single, homogeneous phase in the absence of phase changes:

$$\left.\frac{\partial T}{\partial P}\right|_S = \frac{\alpha T}{\rho C_P} = \frac{\gamma T}{K_S} . \tag{31}$$

The high-pressure isentropic bulk modulus was determined by differentiation of the Birch-Murnaghan EOS. For adiabats off the principal 1550°C isentrope, we determined K_S from the principal isentrope and applied a Mie-Grüneisen type correction:

$$\left.\frac{\partial K_S}{\partial T}\right|_V = \gamma \rho C_V (1+\gamma-q) . \tag{32}$$

These adiabats are characterized by steep initial slopes but flatten substantially at high pressure. This flattening is due in part to the rapidly increasing bulk modulus and to a lesser extent to our assumption regarding γ, *i.e.*, $\gamma=\gamma_0(V/V_0)^{q=1}$.

In a molten system the adiabatic gradient is wholly specified by the liquid properties, γ_{liq} and $K_{S\ liq}$. Under subsolidus conditions, and in the absence of subsolidus reactions, these terms are evaluated for the appropriate crystalline assemblage. In crossing the solidus, however, the adiabatic gradient is modified by the entropy of fusion. To maintain adiabaticity, the temperature of the diapir must drop sufficiently to accommodate the entropy of fusion. The thermodynamics of this process have been described by Carmichael *et al.* [1974] for one-component systems and by Rumble [1976] for two-component systems. An analogous problem, that of condensation in a multi-component adiabatic atmosphere, has also been studied extensively [*e.g.*, Houghton, 1977]. The meteorological term "wet adiabat" is used to describe the adiabat modified by a phase change, and we will adopt this term here to distinguish this case from the simple adiabat of Eqn. 31.

Figure 11: Several adiabatic gradients for our komatiitic composition. Adiabatic gradients were calculated as described in the text with the assumptions $C_V=3R$ and $q=1$.

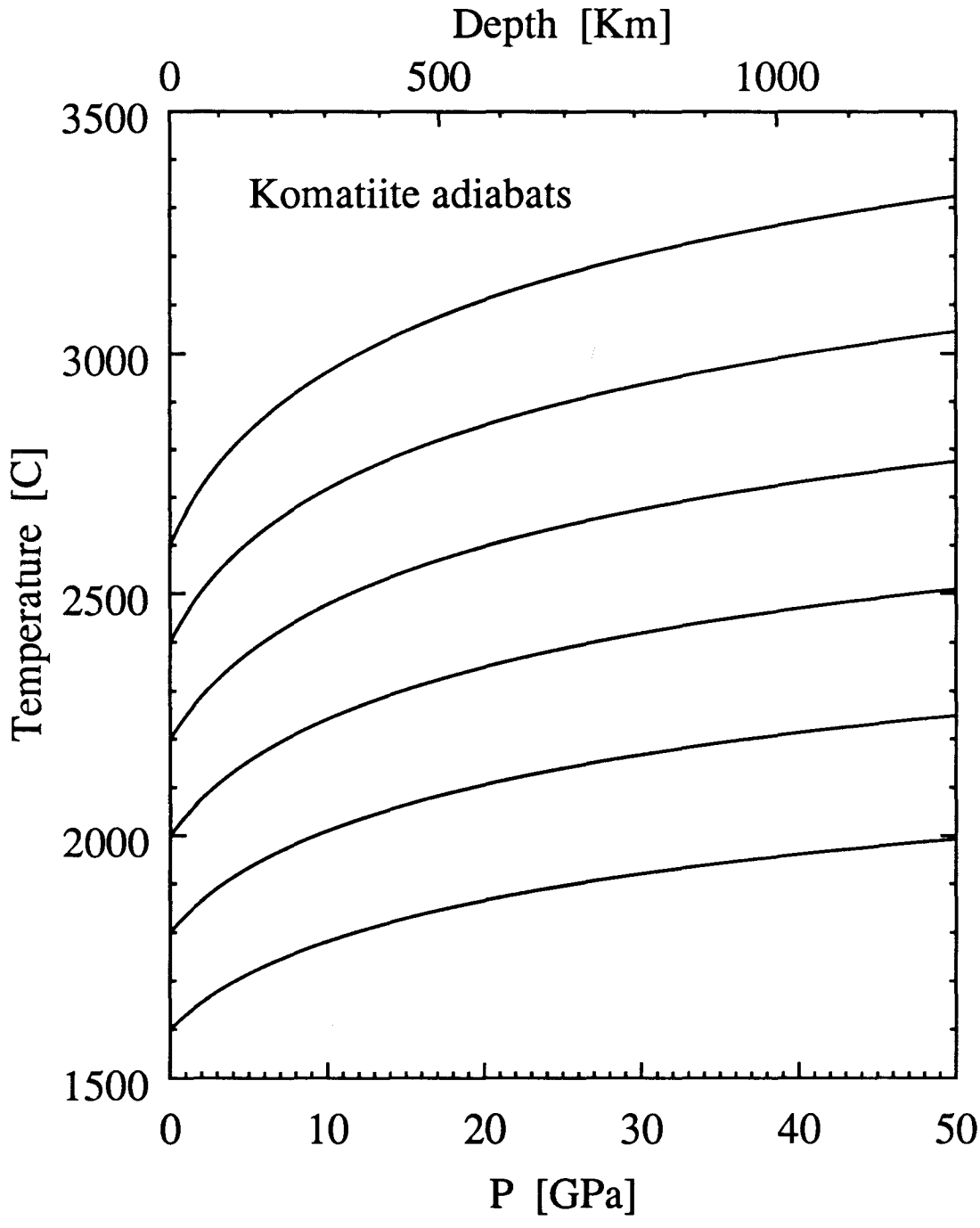
Depth [Km]
0
500
1000
3500
3000
2500
2000
1500
Komatiite adiabats
Temperature [C]
0
10
20
30
40
50
P [GPa]

Figure 11.

We will approach this problem from the limit of complete melting where our data provide the most useful constraints. An expression for the adiabatic gradient can be derived by first writing the specific entropy of a magma, crystals plus liquid:

$$S_{system} = (1-x)S_{liquid} + xS_{crystals} = S_{liquid} - x\Delta S \,, \tag{33}$$

where S_{liquid}, the specific entropy of the liquid, and ΔS, the instantaneous difference in specific entropy between the liquid and coexisting crystals, are functions of the liquid and crystal compositions at crystal mass fraction x as well as temperature and pressure. Differentiating Eqn. 33 then leads to:

$$dS_{system} \approx \left[\frac{C_P}{T} - \Delta S \left.\frac{\partial x}{\partial T}\right|_P\right] dT - \left[\alpha V - \Delta S \left.\frac{\partial x}{\partial T}\right|_P \left.\frac{\partial T}{\partial P}\right|_x\right] dP \,, \tag{34}$$

where we have made the approximation that ΔS is constant, which will be taken to be approximately R/g-atom [Stishov, 1969, 1988; Jeanloz, 1985] and independent of liquid composition and the crystallizing species. Experimental determinations of the entropy of fusion, ΔS_f, for silicates at 1 bar indicate that the first of these approximations is good to better than a few percent for simple ultrabasic systems ($\Delta S_f/R$ is 1.03 for fayalite, 1.01 for enstatite, 1.00 for diopside at their respective 1 bar melting temperatures [Stebbins, *et al.*, 1984]). In a complex liquid the entropy is given by the sum of the entropies of its components and an additional term arising from the permutability of the mixture. This latter term is always positive, hence the entropy of fusion in a polymineralic system will always be greater than ΔS_f for a simple mineral end member. For complex crystalline phases, site mixing also contributes a permutability term to the solid entropy, and there is an analogous contribution to the entropy of fusion but with opposite sign. We anticipate that the greater permutability of the liquid will always favor $\Delta S_f > R$ for ultrabasic systems. The average entropy difference between a wholly molten mantle and a wholly crystalline mantle (at constant T and P) will, therefore, almost certainly be greater than R/g-atom. The specific entropies per atom of several

components of mantle phases (forsterite, enstatite, diopside, jadeite, pyrope, and Tschermack's pyroxene) are all quite similar [Robie *et al.*, 1978]. They differ from one another by less than R/4, thus the instantaneous entropy difference between liquid and coexisting solid (ΔS in Eqn. 3) will probably be $\geq R$ as well. The assumption that ΔS has a constant value of R/g-atom will probably, therefore, lead to an underestimation of the average difference between ultrabasic liquid and crystal entropies. This will lead to conservative conclusions, as will be demonstrated, so we will adopt it for purposes of illustration.

Setting $dS_{system} = 0$ in Eqn. 34 we obtain the slope of the wet adiabat:

$$\left.\frac{\partial T}{\partial P}\right|_{S,\, T_{liquidus} \geq T \geq T_{solidus}} \approx \frac{\left(\frac{\gamma T}{K_S}\right)_{liquid} - \frac{T\Delta S}{C_{P\,liq}} \left.\frac{\partial x}{\partial T}\right|_P \left.\frac{\partial T}{\partial P}\right|_x}{1 - \frac{T\Delta S}{C_{P\,liq}} \left.\frac{\partial x}{\partial T}\right|_P} . \qquad (35)$$

The first term in the numerator is the adiabatic gradient of the crystal-free liquid. Note that when the slope of the constant x contour ($\partial T/\partial P|_x$) is equal to the slope of the crystal-free adiabat ($\partial T/\partial P|_{S,x=0} \equiv \gamma T/K_S$), the wet adiabat will have this same slope. For a given value of ΔS, the steeper the liquidus and solidus are relative to the liquid adiabat, the more rapidly (in terms of pressure or depth) the wet adiabat will cross through the melting interval. If the liquidus and solidus are shallow, as they are believed to be for the deeper upper-mantle, adiabats are slow to pass through the melting interval.

Rigorous evaluation of $\partial x/\partial T|_P$ and $\partial T/\partial P|_x$ requires detailed knowledge of the Gibbs free energy surfaces of the liquid and crystalline phases [Rumble, 1976]. We can make several generalizations without evaluating these terms, however. A constant entropy curve can be constructed for the liquid at all pressures, and a similar curve can be drawn for the crystalline assemblage for the same value of specific entropy. Since the specific entropy of the solid is always less than that of the

liquid at a given temperature and pressure, the solid isentrope must always be at higher temperature (Figure 12). Note that the phases and assemblages described by the isentropes shown in Figure 12 are metastable where the isentrope is shown as a lighter curve. The wet adiabat connects the liquid adiabat at its intersection with the liquidus to the solid adiabat at its intersection with the solidus. While the shape of this wet adiabat curve will depend on the thermodynamics of the phase transition, its intersections at the solidus and liquidus are uniquely specified by knowing the all-liquid and all-solid adiabats (for the same value of specific entropy) and the liquidus and solidus. The points of incipient melting and incipient crystallization under adiabatic conditions can therefore be determined without knowledge of the function x(T).

In going from a completely liquid state to a completely solid state (at constant P) we lower the specific entropy of the system by ≈R/g-atom. In order to bring the entropy of the solid to the same value as the liquid, temperature must be increased. This temperature rise is given by $dT/dx \approx RT/C_P$, so the solid must be hotter than the liquid by $\Delta T \approx T_{liquidus}[\exp(R/C_P)-1]$. Since $C_P \approx 3R$, ΔT is approximately $0.4 \times T_{liquidus}$, or about 800 K in the upper mantle. To the degree that we have underestimated the entropy of fusion by ignoring the permutability of the liquid, we may have also underestimated this change in temperature. For a solid diapir to melt completely upon adiabatic decompression its initial temperature would have to be at least 800 K greater than that of the emergent liquid. The probable phase diagrams for typical peridotitic or chondritic compositions (discussed later) preclude this possibility for solid diapirs that begin to melt in the upper mantle, because the high pressure solidus is not 800 K hotter than the low pressure liquidus anywhere in the pressure range of the upper mantle and transition zone. Consequently, the only way that adiabatic diapirs could become significantly molten (≥50 wt %) in the upper mantle is if they originate in the transition zone or lower mantle or if they were already partially molten (*e.g.*, by heating at a boundary layer) when adiabatic ascent within the upper mantle was initiated.

Figure 12: Cartoon showing that the points of incipient melting and incipient crystallization under adiabatic conditions are determined uniquely by the all-liquid and all-solid adiabats and by the liquidus and solidus. Since the solid has an intrinsically lower specific entropy at constant T and P, it must be hotter than the liquid to have the same specific entropy. The intersection of the liquid adiabat with the liquidus is the point of incipient crystallization, and the intersection of the solid adiabat with the solidus is the point of incipient melting. These intersection points are joined in the two-phase region by the wet adiabat whose shape is a complex function of the Gibbs free energy surfaces. Two possible wet adiabats have been drawn. The straight line (a) corresponds approximately to the case where crystallinity varies linearly with temperature. The curved wet adiabat (b) corresponds to the case where crystallinity changes rapidly near the liquidus and solidus but more slowly in between.

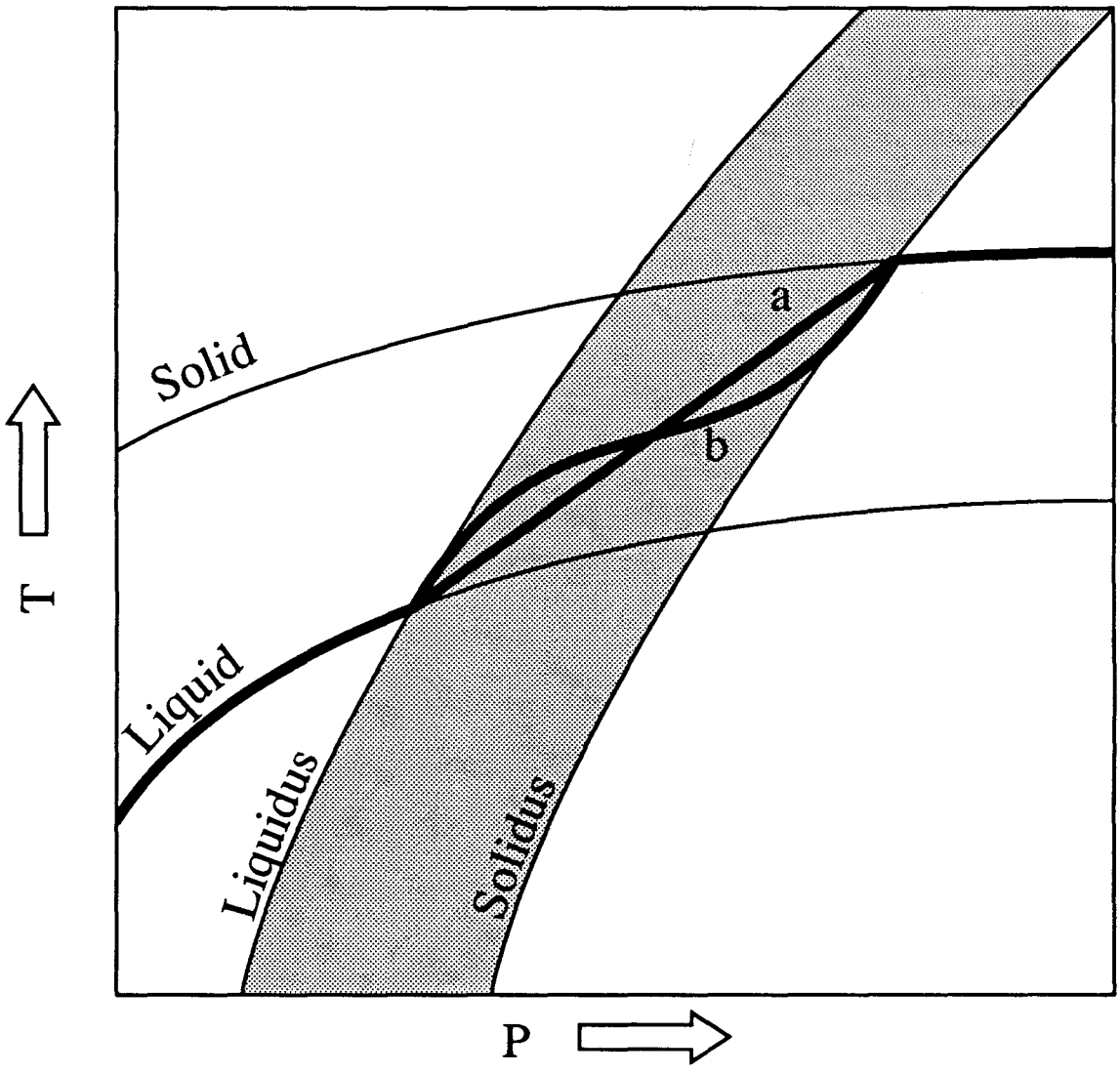

Figure 12.

In order to understand the qualitative features of an adiabatic system in the melting interval, it is necessary to evaluate $\partial x/\partial T|_P$ and $\partial T/\partial P|_x$. To do so we will make another simplifying approximation. A crude estimate of the degree of crystallinity can be made by assuming the crystal mass fraction varies linearly with temperature at constant pressure:

$$x \approx \frac{T_{liquidus}-T}{T_{liquidus}-T_{solidus}} \tag{37}$$

for $T_{liquidus} \geq T \geq T_{solidus}$. Alternatively, we also consider the empirical parameterization of McKenzie and Bickle [1988], who have shown that a cubic polynomial provides a good pressure-independent fit to a variety of experimental x(T) measurements in a garnet peridotite system at low pressure. These two models are shown in Figure 13. We doubt that either of these models accurately describes the details of crystallization, particularly at high pressure (>10 GPa). However, the general features of the resulting calculations are similar regardless of which function is employed, so at least those aspects of the calculations that are not sensitive to the details of x(T) can be evaluated. Again we emphasize that this function only governs the behavior of the adiabat within the melting interval. For a particular value of specific entropy, all functions x(T) will converge at their liquidus and solidus intersection points (Fig. 12).

A phase diagram for an upper mantle comprised of fertile peridotite has been schematically constructed from the high pressure experiments of Takahashi and Scarfe [1985], Takahashi [1986], and Ito and Takahashi [1987] on the KLB-1 spinel lherzolite (Figure 14). The mantle liquidus rises sharply at low pressure but flattens significantly near ≈12 GPa and may even have a maximum [Scarfe and Takahashi, 1986]. With increasing pressure to ≈15 GPa, the melting interval ($T_{liquidus}-T_{solidus}$) also probably decreases [Herzberg, 1983].

Adiabatic gradients through the melting interval have been constructed as described above for the two x(T) functions and are shown in Figure 14. The extent of melting is shown in Figure 15 for

Figure 13: Models for crystallinity (x) as a function of temperature in the melting interval: (a) crystallinity varies linearly in temperature, and (b) the experimentally constrained parameterization of McKenzie and Bickle [1988].

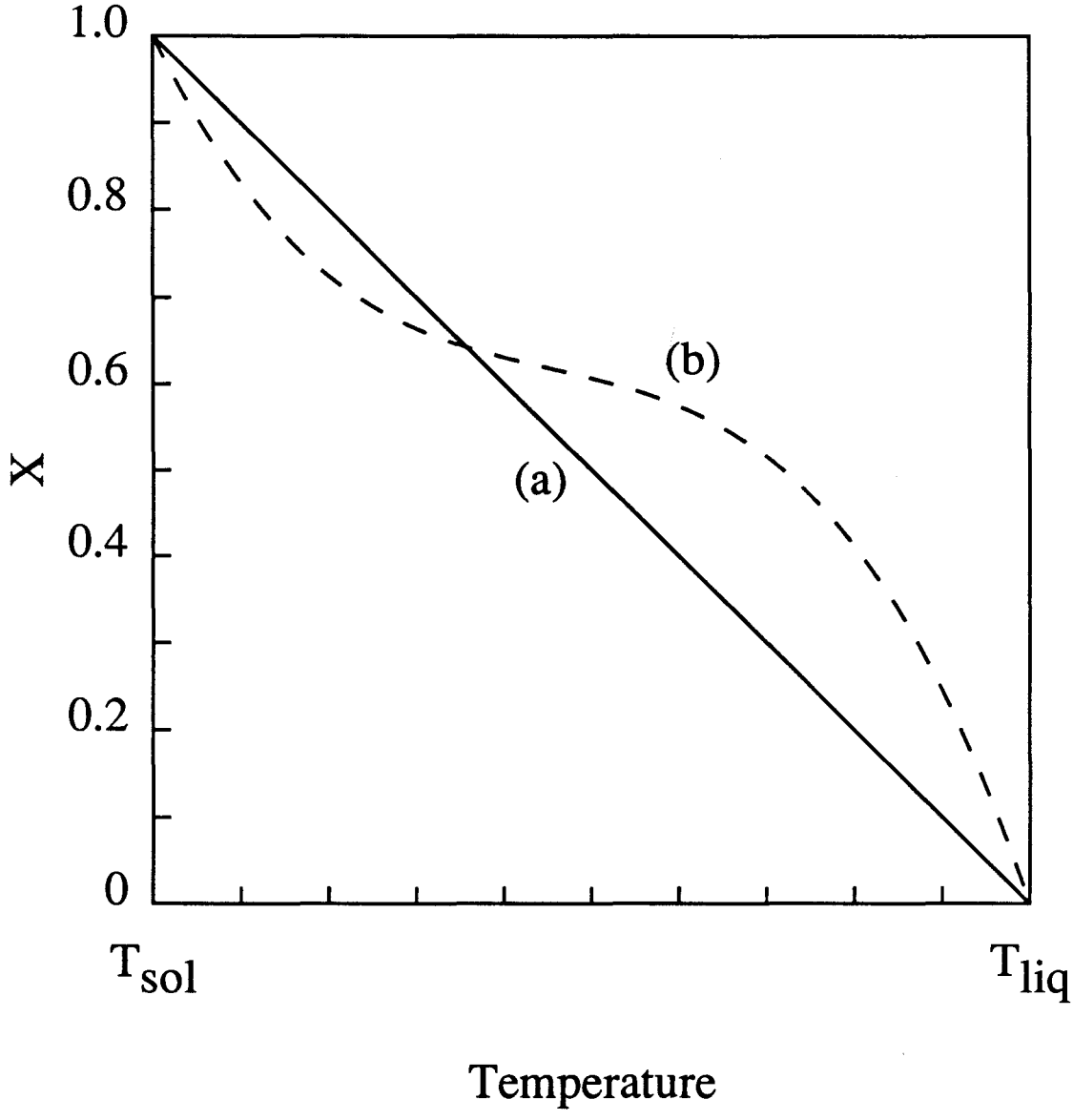

Figure 13.

Figure 14: Model phase diagrams for the upper mantle with superimposed adiabats: (a) linear x(T) relationship, and (b) experimental x(T) relationship from McKenzie and Bickle [1988]. Adiabats are calculated at 50° intervals (at P=0) in each case. The circle represents the olivine-clinopyroxene liquidus cosaturation point for a komatiite broadly similar to the sample we studied [Wei *et al.*, 1990]. The stippled band is the trace of the komatiite liquidus. An estimate of the modern subcontinental mantle geotherm [Mercier and Carter, 1975; Stacey, 1975] is given by the bold dashed line. Changes in entropy associated with subsolidus reactions have been ignored.

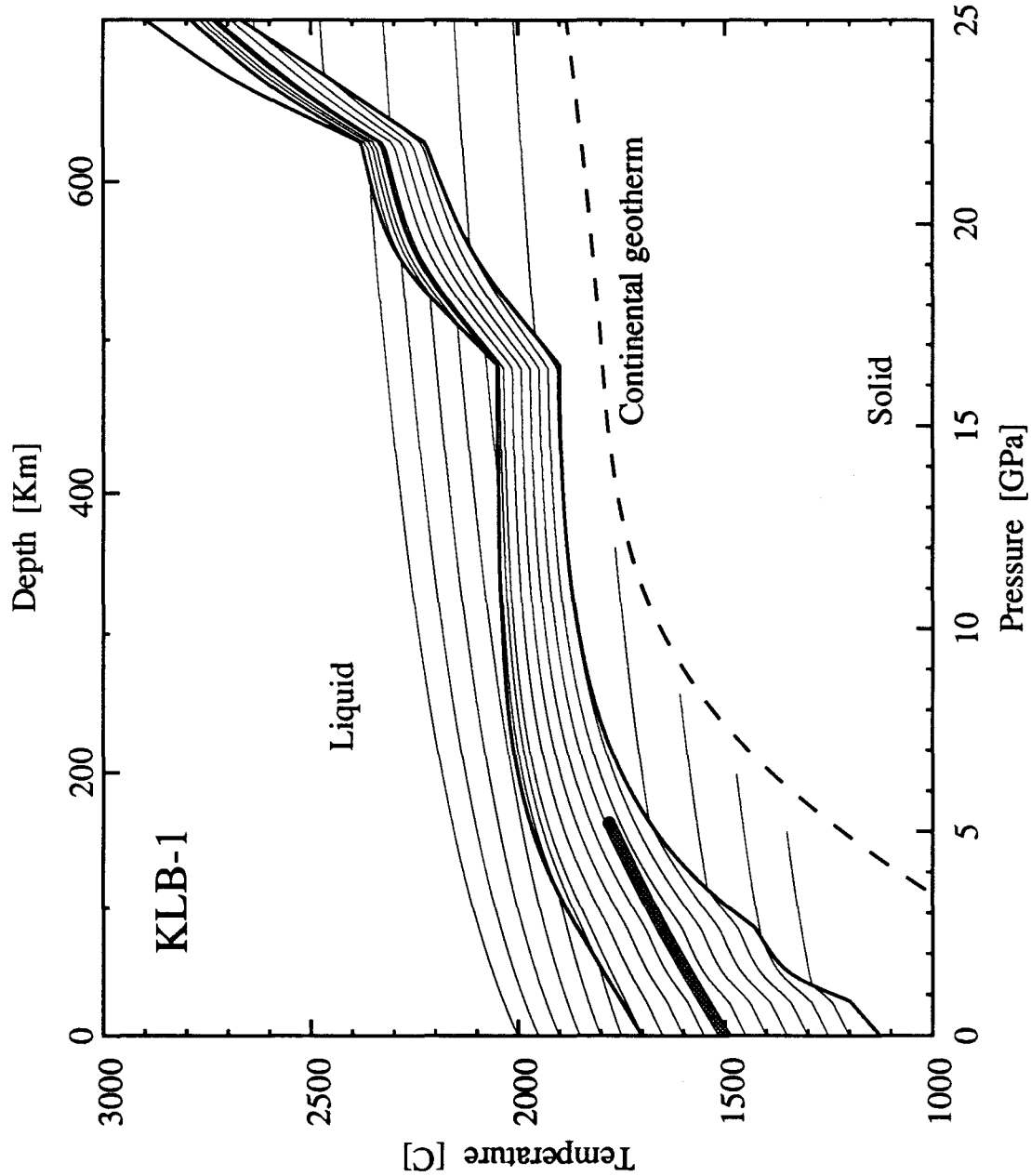
KLB-1
Liquid
Solid
Continental geotherm
Depth [Km]
Pressure [GPa]
Temperature [C]
0
200
400
600
0
5
10
15
20
25
1000
1500
2000
2500
3000

Figure 14a.

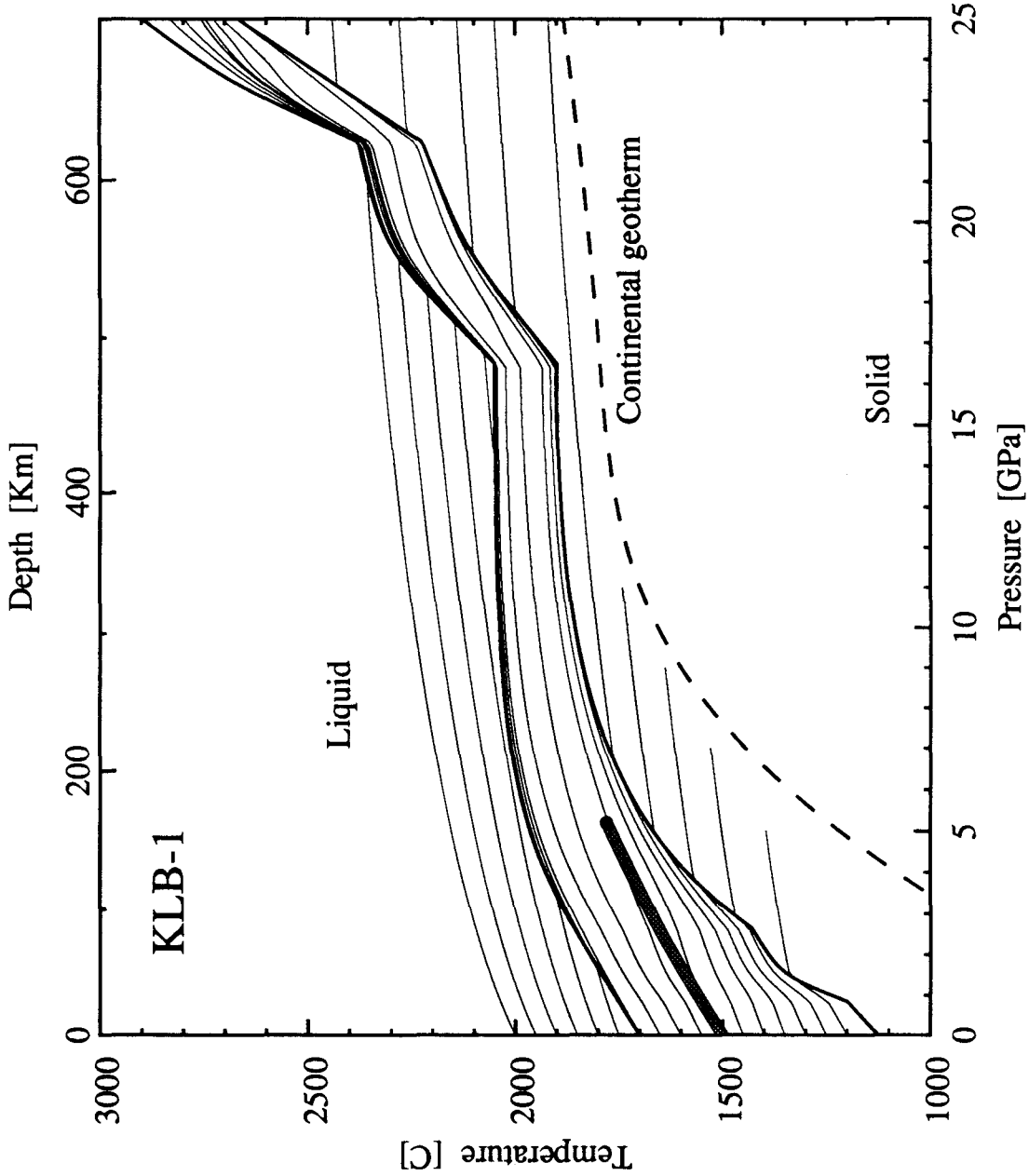
KLB-1
Liquid
Solid
Continental geotherm
Depth [Km]
Pressure [GPa]
Temperature [C]
0
200
400
600
0
5
10
15
20
25
3000
2500
2000
1500
1000

Figure 14b.

the two calculations. We have used the adiabatic gradient from our komatiite as that of the liquid, independent of the extent of fusion, since attempts to account for chemical variation (through addition or subtraction of olivine components) yield similar results. The crystal-free adiabats have roughly the same slope as the liquidus, thus the degree of crystallinity does not vary rapidly with pressure. Note in particular that melt fraction is nearly constant in the 200-400 km interval of the upper mantle (Fig. 15). In no case does an adiabat cross from the liquidus to the solidus in the pressure region of the upper mantle and transition zone, thus, as pointed out above, adiabatic diapirs with very large degrees of partial melting would have to originate in the transition zone or lower mantle. If the permutability contribution to the entropy of fusion were properly accounted for, the depth of incipient melting would probably be even greater for a given degree of partial melting. With a linear x(T) model, melting is distributed evenly between the liquidus and solidus. With the McKenzie and Bickle [1988] parameterization, crystallinity varies rapidly near the solidus and liquidus, but more slowly in between. The adiabats are consequently nearly tangential to the solidus and liquidus curves. With the linear model, up to 50% partial melting is possible if a diapir crossed the solidus at the base of the upper mantle (400 km). Only 40% melting is possible with the parameterization of McKenzie and Bickle [1988] under the same conditions.

In the 0-5 GPa range our calculations predict degrees of partial melting similar to the calculation of McKenzie and Bickle [1988]. We predict melt fractions about 20% smaller than their model (comparing our Figure 15b with Figure 7a of McKenzie and Bickle [1988]). This difference can be attributed in part to different assumptions regarding ΔS; they assumed a value of about 0.63R. In order to generate the amount of melt they consider to be typical of MORB (7 km integrated melt thickness), we require that the mantle be at least 100° hotter than the 1280°C potential temperature (defined as the temperature a mantle parcel would have at 1 bar if it were adiabatically decompressed as a metastable solid) that they advocate.

Figure 15: Weight fraction of liquid generated under adiabatic conditions for (a) linear x(T) model, and (b) MacKenzie and Bickle [1988] parameterization. Each curve represents a single adiabat. The numbers on the curves represent the final 1 bar temperatures of the partially molten diapirs (in degrees Celsius). These curves are the Px projections of the PT adiabats in Figure 14. The circle represents the point of olivine-clinopyroxene cosaturation on a komatiite liquidus [Wei *et al.*, 1990], and the stippled band is the projection of the trace of the komatiite liquidus. Note that melt fractions do not vary significantly in the lower 200 km of the upper mantle.

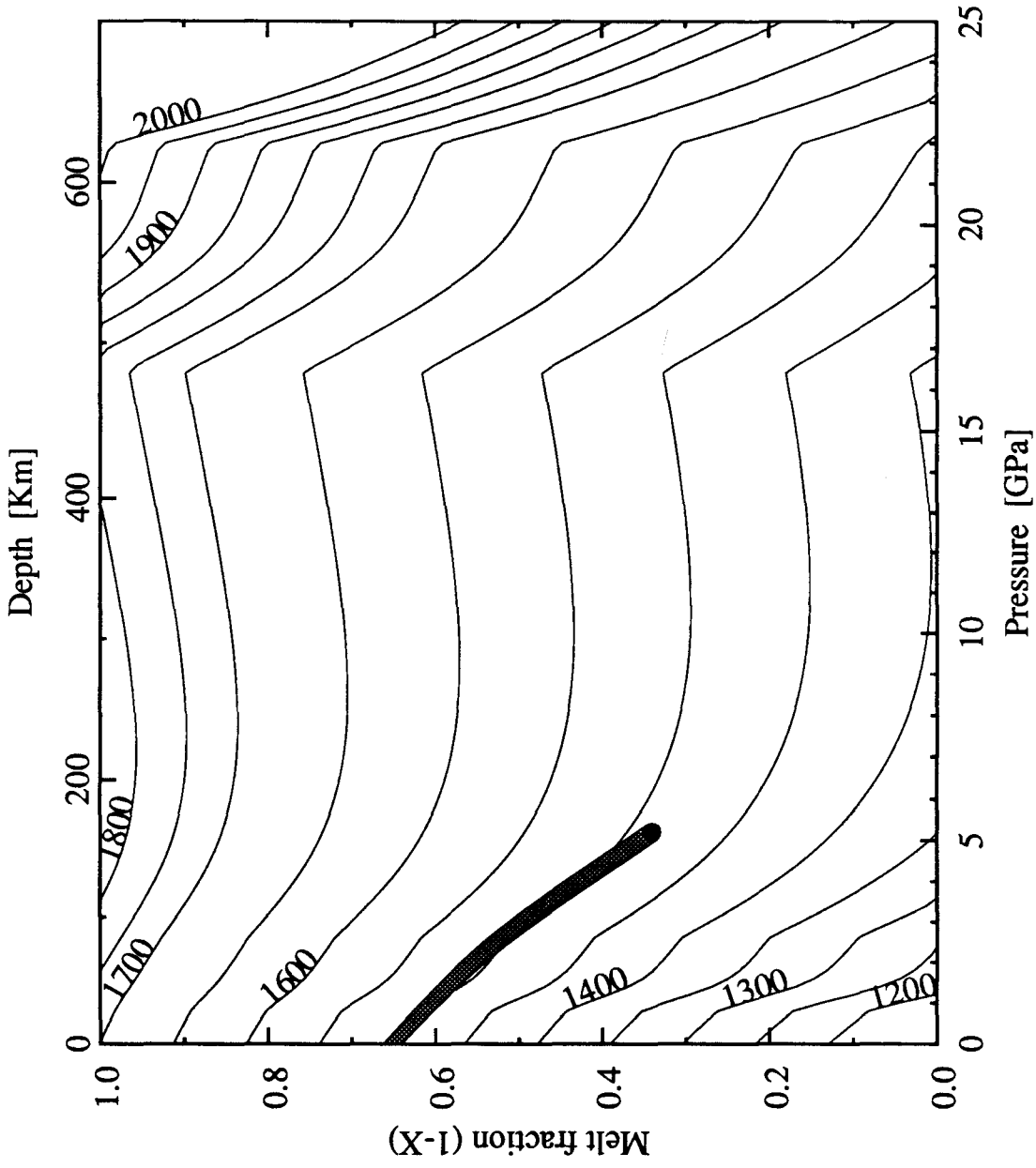
Depth [Km]
0
200
400
600
Pressure [GPa]
0
5
10
15
20
25
Melt fraction (1-X)
1.0
0.8
0.6
0.4
0.2
0.0
2000
1900
1800
1700
1600
1400
1300
1200

Figure 15a.

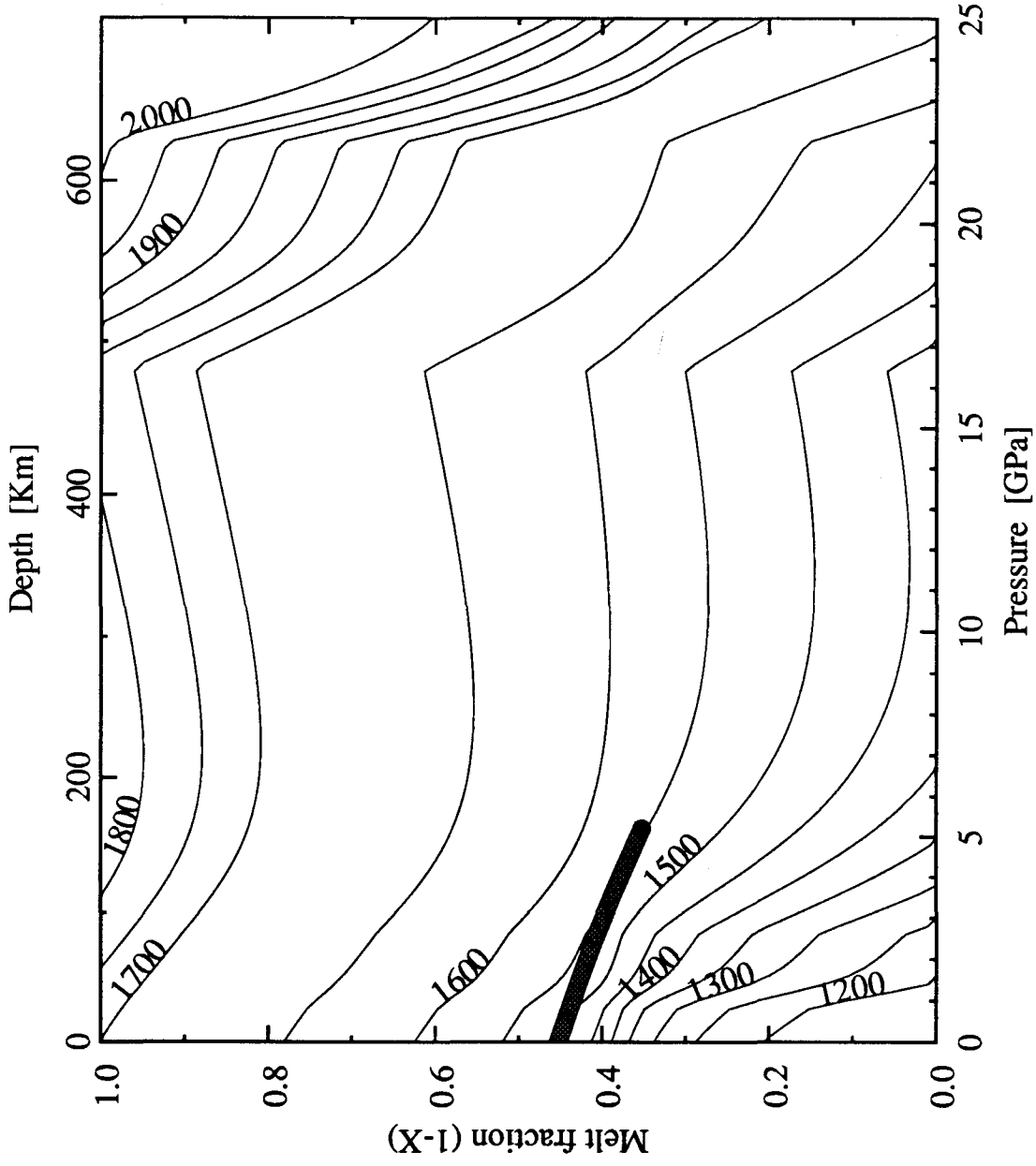
Depth [Km]
0
200
400
600
Pressure [GPa]
0
5
10
15
20
25
Melt fraction (1-X)
1.0
0.8
0.6
0.4
0.2
0.0
2000
1900
1800
1700
1600
1500
1400
1300
1200

Figure 15b.

Diapiric origin of komatiites

Wei *et al.* [1990] determined the phase diagram for a komatiite of broadly similar composition to the one we have studied. This phase diagram is superimposed on the KLB-1 phase diagram (Fig. 14) in Figure 16. Wei *et al.* [1990] suggest that this komatiite could have separated from either an olivine+clinopyroxene residue at 5.2 GPa and 1780°C, or an olivine residue at lower pressure and temperature. The olivine+clinopyroxene cosaturation point for this komatiite is within ≈25°C of the maximum temperature at which olivine+clinopyroxene saturated liquids can be generated by melting of KLB-1 at 5.2 GPa, so the phase equilibria are generally compatible with the idea that a komatiitic liquid of this composition could have been segregated from a KLB-1-like source under these conditions. Wei *et al.* [1990] state that based on a mass balance calculation, such a komatiitic liquid could be formed by 10-30% partial melting of a KLB-1-like source at the cosaturation point. This is similar to the 34-35% melting at 5.2 GPa, 1780°C indicated by our calculations (Fig. 15), which, although dependent on the specific form of the x(T) functions we have used, are thus also compatible with this particular view of komatiite genesis. If komatiitic liquids of this composition were generated by 10-30% partial melting of adiabatic KLB-1-like diapirs, then our calculations suggest that the source region of the diapirs (provided they were initially unmelted) would have to be in the 10-20 GPa range, and that they would have begun to melt between 10 GPa, 1850°C (10%) and 20 GPa, 2150°C (30%). Whether the melt fraction is 10% or 30% makes such a big difference in the minimum depth because melt fraction does not change significantly in the ≈8-16 GPa (≈250-450 km) interval; melt fractions greater than ≈15% require that melting commence in the transition zone.

The Wei *et al.* [1990] phase relations for komatiite and those for KLB-1 peridotite are also compatible with segregation of komatiitic liquid from olivine residue at pressures lower than 5.2

Figure 16: Liquidus and solidus for a 25 wt% MgO komatiite determined by Wei *et al.* [1990]. This komatiite is similar in composition to the one we have studied. This phase diagram is superimposed upon the phase diagram for mantle peridotite (KLB-1, Takahashi [1986]). The appearance of olivine (ol), garnet (gt), clinopyroxene (cpx) and orthopyroxene (opx) are shown for the peridotite. Liquidus appearance of olivine, clinopyroxene, and garnet are indicated on the komatiite liquidus. If this komatiite were formed by the partial fusion of peridotite, then the komatiite would have segregated from residual olivine at pressures less than 5.2 GPa. Higher pressures lead to inconsistencies between the peridotite and komatiite phase equilibria. This diagram also suggests that the komatiite represents ≈35% melting.

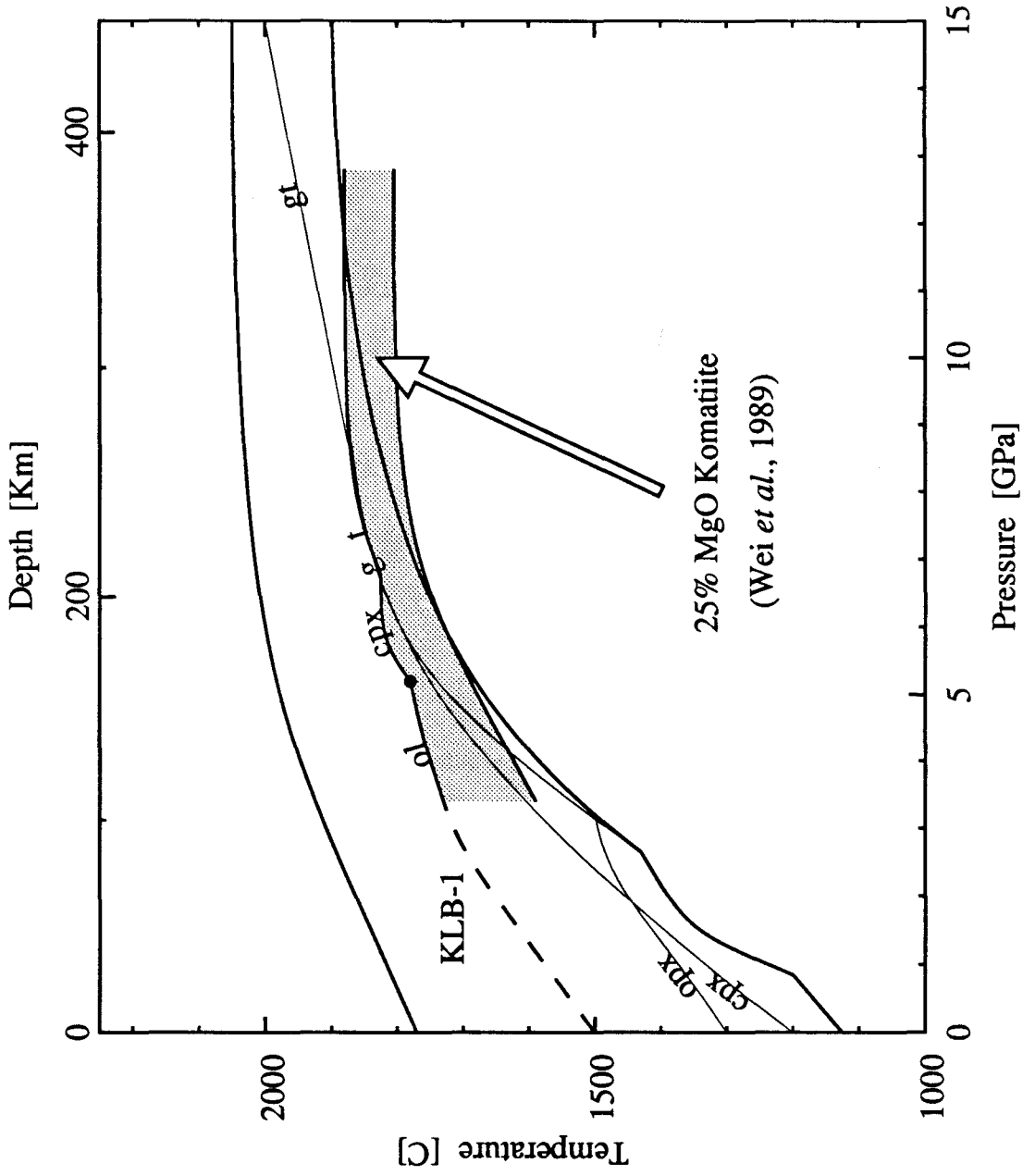
Depth [Km]
0
200
400
Temperature [C]
2000
1500
1000
Pressure [GPa]
0
5
10
15
gt
cpx
gt
ol
KLB-1
25% MgO Komatiite
(Wei et al., 1989)
opx
cpx

Figure 16.

GPa, implying >35% partial melting. Estimates of the degree of partial melting of peridotite required to generate komatiitic liquid plus residual olivine (*e.g.*, Arndt [1977]) are typically on the order of 50-80%. In order to reconcile such high melt fractions with the results of our calculations and the komatiite liquidus given by Wei *et al.* [1990], the komatiitic liquid would have to separate from its olivine residue at pressures of about 1 GPa (for the x(T) function of McKenzie and Bickle [1988]) to 3 GPa (for the linear x(T) function). Subsolidus diapirs that could generate these degrees of partial melting would have to originate below ≈21 GPa in the transition zone with temperatures near 2180°C.

If crystal-liquid segregation is possible in ascending diapirs, then it may be possible to eliminate dense phases, such as garnet-majorite, from them. Olivine is buoyant in komatiitic liquids at pressures above ≈9 GPa, and garnet-majorite is denser at pressures less than about 22 GPa. Mechanisms by which garnet-majorite fractionation could occur under these relatively low melt fraction conditions are not certain, but majorite fractionation trends have been inferred for some South African peridotites [Herzberg *et al.*, 1988], and several authors (*e.g.*, Green [1975], Nesbitt *et al.* [1979], Jahn *et al.* [1982], and Ohtani [1984]) have suggested that garnet fractionation may have been important in the genesis of so-called aluminum-depleted komatiites. We note in particular the suggestion of Ohtani [1984] that the diapirs that generate Al-depleted komatiites originate deeper in the mantle than those that generate Al-undepleted komatiites. As a consequence of their deeper origin, they achieve higher degrees of partial melting, which facilitates garnet fractionation, perhaps aided by the contrasting buoyancy of olivine/pyroxene and garnet in ultrabasic liquids at the relevant pressures. It can be seen in Figures 14 and 15 that small differences in source pressure and temperature at depths >500 km can lead to large differences in melt fraction at high pressure because the KLB-1 solidus and liquidus are steep compared to the all-liquid adiabats in this region. According to our calculations, if garnet fractionation is controlled solely by the melt fraction and density

contrast, then the sources of Al-depleted komatiites could be very similar to the Al-undepleted komatiites, the former requiring as little as about 50° higher initial temperatures.

Several authors have suggested that komatiitic liquids could be generated by pseudoinvariant melting of peridotites at high pressures [Takahashi and Scarfe, 1985; Herzberg and O'Hara, 1985; O'Hara *et al.*, 1975]. Takahashi and Scarfe [1985] reported the formation of a komatiitic liquid as the first partial melt of KLB-1 near 5-7 GPa, although the melt fractions were not determined and may have been rather large given that solid-liquid segregation occurred within their charges. In a similar experiment by Takahashi [1986], also on KLB-1, where both liquid and crystal compositions were reported, the komatiitic liquid generated at 5 GPa and 1700°C (Run 53) represents over 60% partial melting according to mass balance calculations. If komatiitic liquids can indeed be generated by small degrees of partial melting in the 5-7 GPa pressure range, then they must differ from the one studied by Wei *et al.* [1990] if the phase relationships shown in Figure 16 are accurate. In particular, the Wei *et al.* [1990] komatiite liquidus is some 100° higher than the KLB-1 solidus in this pressure range and its solidus is also higher.

In summary, our calculations suggest that mechanisms for komatiite genesis that call for large (>15%) degrees of partial melting by adiabatic decompression require diapirs that begin to melt in the transition zone at pressures in excess of 20 GPa. Mantle potential temperatures in excess of 1750°C are required. These source regions would have to have been anomalously hot with respect to the bulk mantle, unless the entire upper mantle were partially molten [Cawthorn, 1975]. If this were the case, and the entire upper mantle was partially molten, then magmatic activity originating in the mantle would overwhelmingly be controlled by this widely distributed partial melt. The existence of komatiites as a distinct rock type suggests that pervasive mixing with a partially molten mantle did not occur, thus some alternative source of excess heat, such as thermal boundary layers, is suggested. Deep thermal boundary layers that could generate such anomalously hot diapirs might

be between the upper mantle and transition zone [Anderson, 1984; 1989], between the transition zone and lower mantle [Jeanloz and Richter, 1979; Lees *et al.*, 1983; Jeanloz and Knittle, 1989], or even at the core-mantle boundary [Jarvis and Campbell, 1983]. If komatiites can be formed by smaller degrees (<15%) of partial melting, then more modest potential temperatures (1700°C to 1750°C) would be allowed; *e.g.*, if komatiitic liquids can be formed as initial melts in the 5-7 GPa pressure range, then potential temperatures as low as 1600°C are possible. Pyroxene geothermometry indicates that the potential temperature of the mantle beneath continents is about 1600°C [Mercier and Carter, 1975], so if this latter view of the conditions required for production of komatiitic liquids is valid, it might be possible to generate komatiitic liquids in the modern mantle. Whatever the thermal conditions required for komatiite petrogenesis, the existence of paleogene magmas from Gorgona Island, Columbia [Gansser *et al.*, 1979; Echeverria, 1982] that approach komatiites in their chemical composition suggests that the conditions for komatiite formation may not have been restricted to the Archaean.

Figure 17 compares the conditions that have been suggested for the formation of komatiitic liquids to those that have been suggested for the genesis of primary magmas parental to modern MORBs (Presnall *et al.* [1979] *vs.* Green *et al.* [1979] and Elthon and Scarfe [1984]). Note that we have restricted our discussion to a KLB-1 model for mantle source material. More fertile source materials will have lower solidi, thereby allowing greater degrees of melting for a given potential temperature, but depleted sources will have higher solidi and require higher temperatures. The most significant observation is that although the temperatures of melt segregation for komatiitic liquids implied by scenarios that suggest >30% partial melting are only ≈200°C higher than those of modern MORBs, the configuration of the solidus and liquidus of likely source peridotites requires their ultimate sources to be diapirs that, if adiabatically decompressed from initially solid mantle, were more that 700°C hotter than the sources of MORBS and derived from great depth in the

mantle.

7. Application to a Magma Ocean and the Evolution of the Hadean Mantle

Many independent arguments suggest that it is plausible that at least the upper mantle of the Earth was substantially molten in the Hadean. This melting could have resulted from the accretion of the Earth [Kaula, 1979; Abe and Matsui, 1986; Matsui and Abe, 1986; Zahnle *et al.*, 1988; Ahrens, 1990], core formation [Birch, 1965; Solomon, 1978; Shaw, 1979], the impact formation of the moon [Benz *et al.*, 1986, 1987; Cameron and Benz, 1989; Stevenson, 1989], or from some combination of these mechanisms. Recognition of this possibly molten state, together with the idea that ultrabasic liquids may be denser than olivine and other silicate phases at relatively shallow mantle depths, has prompted speculation on the evolution of the upper mantle from a magma ocean [Nisbet and Walker, 1982; Ohtani, 1985; Agee and Walker, 1988b]. The liquidus topologies of several ultrabasic systems including C1 [Ohtani *et al.*, 1986; Ohtani and Sawamoto, 1987], peridotite [Takahashi and Scarfe, 1985; Scarfe and Takahashi, 1986; Ito and Takahashi, 1987], komatiite [Bickle *et al.*, 1977; Wei *et al.*, 1990], and perovskite [Heinz and Jeanloz, 1987; Knittle and Jeanloz, 1989] provide critical constraints on this evolution. Our new data on the equation of state of molten komatiite provides new constraints and allows for more quantitative modeling than was previously possible. In this section we consider applications of the equation of state of a komatiitic liquid to the evolution of the Hadean mantle from an initial wholly molten state.

The following discussions will focus on EOS constraints on the evolution of a molten mantle, but many of these constraints cannot be properly evaluated without fluid dynamical considerations. Density contrasts govern whether or not a crystal would rise or sink in a quiescent liquid, but viscosities, convection velocities, and cooling rates are equally important in determining the ultimate

Figure 17: Phase diagram for KLB-1 [Takahashi, 1986] with fields showing conditions under which komatiite [Wei *et al.*, 1990], MORB (as primitive melt) [Presnall *et al.*, 1979; McKenzie and Bickle, 1988], and picrite (also possible MORB parent) [Green *et al.*, 1979; Elthon and Scarfe, 1984] could have been extracted from their source regions. Adiabatic paths for source material, assuming single stage melting, are indicated by light lines. The komatiite field is based on the phase diagram of Wei *et al.* [1990] for a 25 wt% MgO komatiite. Komatiitic liquids with higher MgO content are anticipated to form under higher PT conditions [Takahashi and Scarfe, 1985; Wei *et al.*, 1990].

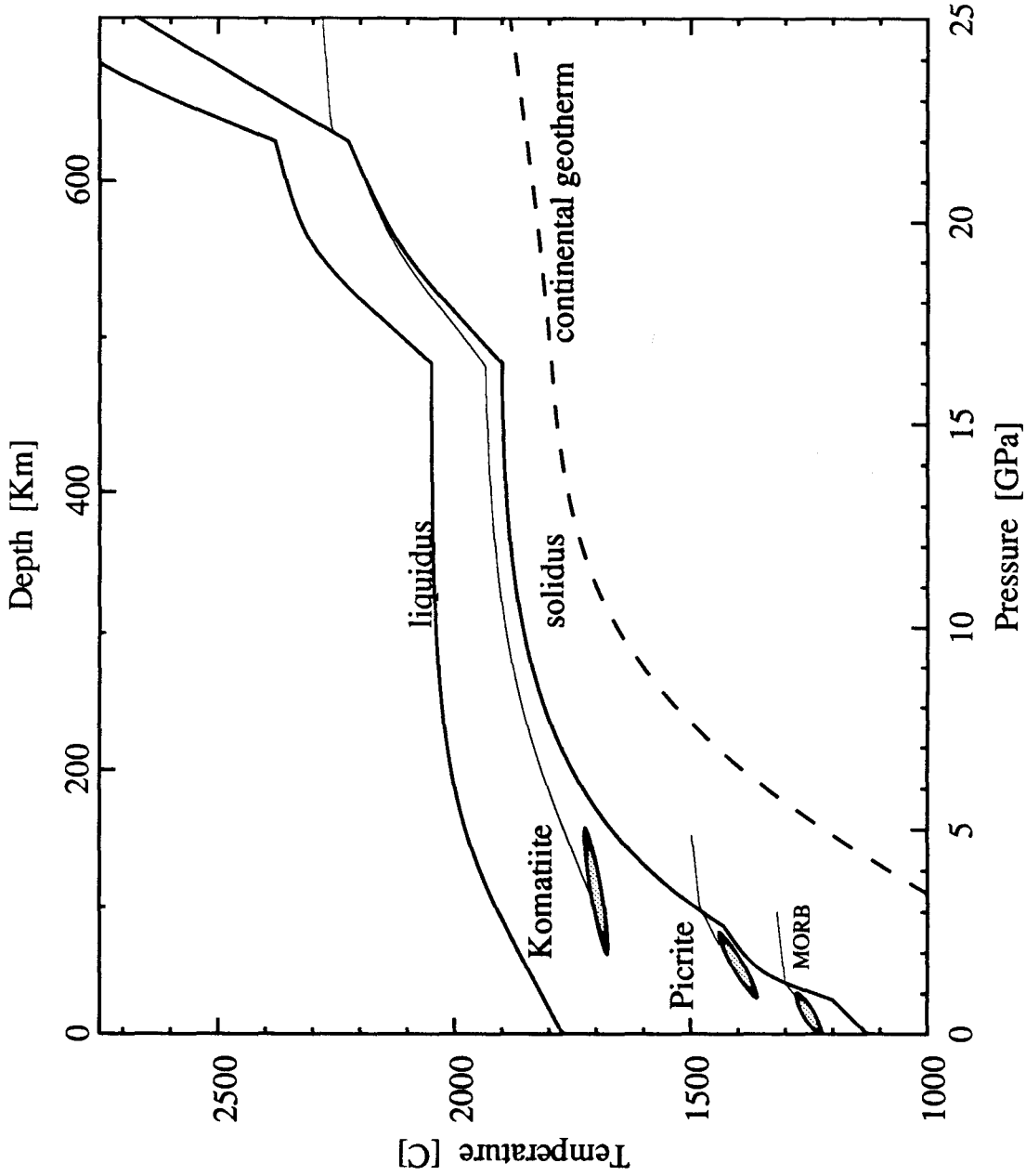
Depth [Km]
0
200
400
600
Temperature [C]
1000
1500
2000
2500
Pressure [GPa]
0
5
10
15
20
25
liquidus
solidus
continental geotherm
Komatiite
Picrite
MORB

Figure 17.

fate of crystals in a convecting magma system. Accordingly, an effort will be made to understand the fluid dynamics of such a system as it evolves.

We will assume that the entire mantle was molten, and that the undifferentiated mantle had an iron-depleted C1 composition [Agee and Walker, 1988b]. For simplicity, we will henceforth refer to this iron-depleted C1 composition simply as C1. Because the mantle is assumed to be liquid, and would have low viscosity, we will also assume that the thermal state of the mantle was approximately adiabatic. As the Earth cools boundary layers may develop, and crystal segregation may occur. Both of these circumstances would make the system nonadiabatic, at least on local length scales. These special circumstances may play important roles in the evolution of the Earth, as will be discussed below. Furthermore, although convection requires some degree of superadiabaticity, we will adopt the adiabatic state as a reference state and follow its development with time.

An approximate fit to the major element chemistry of C1 can be obtained from a mixture of olivine (20.4 wt% of $Fo_{0.98}Fa_{0.02}$ composition), perovskite (38.1 wt % of $En_{0.9}Fs_{0.1}$ composition), and the komatiite we studied (41.5 wt %). From the assumption that liquids mix ideally with respect to volume (*i.e.*, $V=\sum_i x_i V_i$, where V_i is the specific volume of a liquid with the composition of component i and x_i is its mole fraction in the mixture) we can derive the adiabatic gradient of a liquid of C1 composition:

$$\left[\frac{\gamma T}{K_S}\right]_{\text{mixture}} = \frac{\sum_i \left[\frac{x_i V_i C_{Vi}}{V_i K_{Si} - \gamma_i^2 T C_{Vi}} (\gamma_i T)\right]}{\sum_i \left[\frac{x_i V_i C_{Vi}}{V_i K_{Si} - \gamma_i^2 T C_{Vi}} (K_{Si})\right]}, \tag{38}$$

where K_{Si} is the isentropic bulk modulus of a liquid with the composition of component i, C_{Vi} its constant volume heat capacity, and γ_i its Grüneisen parameter. The high-pressure, high-temperature thermodynamic parameters for each liquid end member (V_i, K_{Si}, and γ_i) are calculated from a

Birch-Murnaghan EOS (Eqns. 19 and 28) with Mie-Grüneisen thermal corrections for the pressure (Eqn. 29) and bulk modulus (Eqn. 32). C_V is taken as 3R and q=1 for each component; both C_V and γ are assumed independent of temperature.

The phase diagram for an iron-depleted C1 upper mantle has been investigated by Ohtani *et al.* [1986] and Ohtani and Sawamoto [1987]. Under lower mantle conditions we expect a perovskite+magnesiowüstite subsolidus mineralogy. A representative schematic phase diagram for this system at 100 GPa has been constructed (Fig. 18) assuming ideal mixing of liquid components using the data of Knittle and Jeanloz [1989] as an upper bound for perovskite melting and the calculations of Ohtani [1983] for magnesiowüstite. On the basis of this model calculation we expect that perovskite will be the liquidus phase throughout the lower mantle. Without relying on the details of the perovskite-magnesiowüstite phase diagram, however, two general conclusions can be drawn. First, crystallization of a wholly molten mantle would begin near the core-mantle boundary (Fig. 19). Second, if the upper mantle were wholly molten and the entire mantle were adiabatic, then the lower mantle would be at least partially molten to great depth [*cf.* Agee and Walker, 1988b]. If the mantle were wholly molten to >30 GPa, then our calculations suggest that the zone of partial fusion would extend to the core-mantle boundary (under adiabatic conditions). This can be seen by following the adiabats, which, as described in the previous section, are slow to traverse the melting interval. This conclusion is independent of the details of crystallization (*i.e.*, no knowledge of $\partial T/\partial P|_x$ and $\partial x/\partial T|_P$ is required), but is, of course, sensitive to our assumed lower mantle liquidus and solidus. An adiabatic mantle would therefore not have a crystalline floor initially, but rather a partially molten zone extending to the core. Several adiabatic contours for the partially molten mantle are superimposed on a model C1 phase diagram in Figure 19. The wet (crystal+liquid) adiabats are calculated as discussed in the previous section, with crystal content varying linearly with temperature at constant pressure.

Figure 18: Approximate phase diagram for a chondritic lower mantle at 1 Mbar. The approximate melting temperature of $Mg_{0.9}Fe_{0.1}SiO_3$ perovskite is 3800 K [Knittle and Jeanloz, 1989] and that of $Mg_{0.6}Fe_{0.4}O$ magnesiowüstite is calculated to be ≈6000 K [Ohtani, 1983]. The phase diagram was calculated by assuming that ΔS_f is R/g-atom for each phase with a simple solution model. The solid diagram assumes that the molecular species in the melt phase are given by the mineral formula. The dashed curve assumes one molecular species per oxygen atom, and has been converted to the formula basis in the figure. The arrow indicates the approximate bulk composition of a chondritic mantle. For both models perovskite will be the liquidus phase at ≈3900 K. The solidus is at 3580 K with the formula basis, and 3340 K with the oxygen basis.

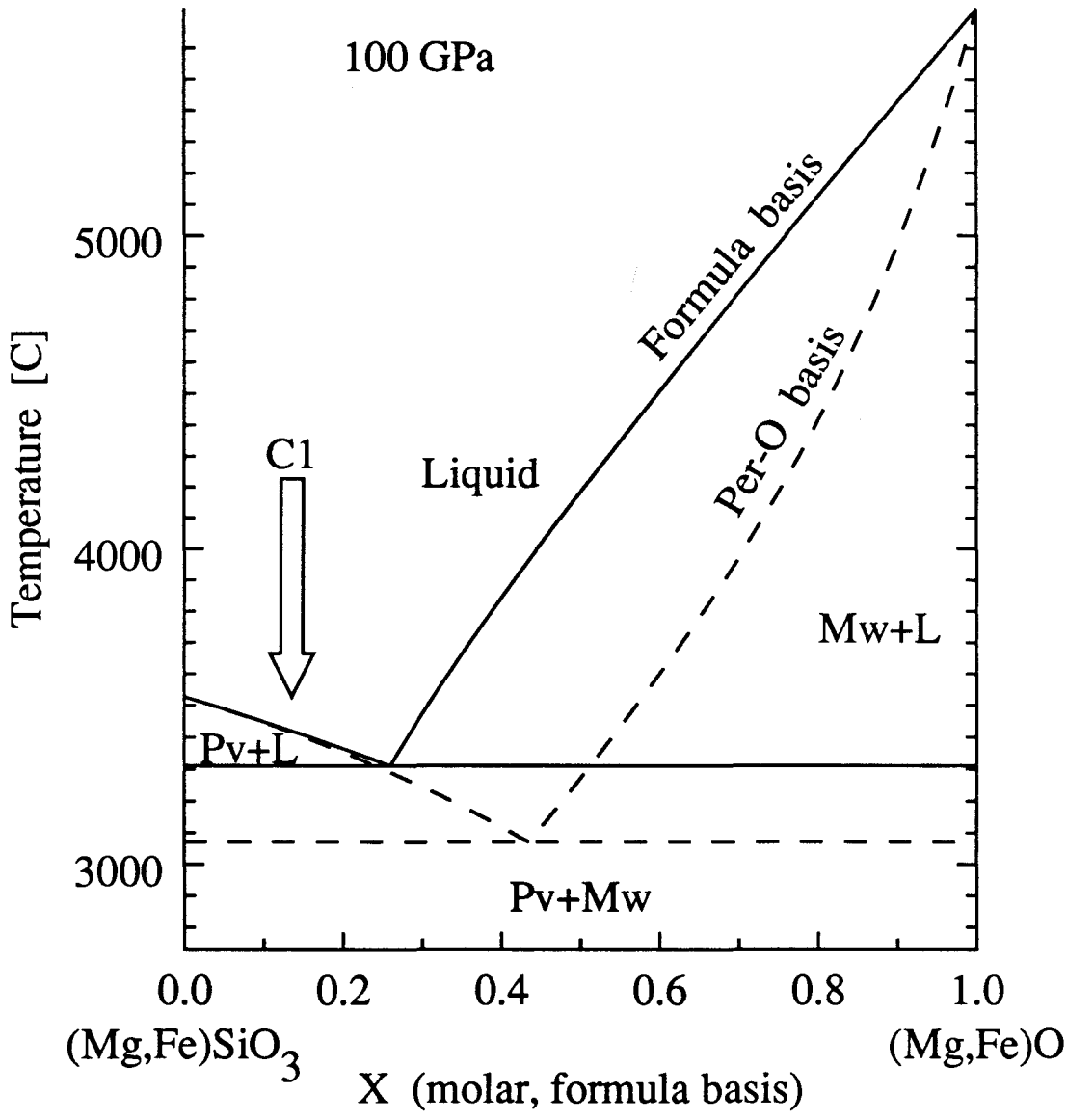
100 GPa
Formula basis
Per-O basis
C1
Liquid
Mw+L
Pv+L
Pv+Mw
5000
4000
3000
Temperature [C]
0.0
0.2
0.4
0.6
0.8
1.0
(Mg,Fe)SiO3
(Mg,Fe)O
X (molar, formula basis)

Figure 18.

If any chemical fractionation (*e.g.*, crystal-liquid segregation) occurs, the phase relations and adiabatic contours described above will not be strictly applicable to the residual liquid. In the following sections we use this model C1 system as an approximation to fractionated systems as well. A more rigorous analysis is not justified given available phase equilibrium data.

The time scale for cooling of a terrestrial magma ocean

Although the lifetime of a magma ocean is not central to our discussion, the extent of chemical fractionations may be limited by the rate at which the mantle cools. For example, in the absence of any atmosphere and crust, the planet might cool so rapidly that little differentiation is possible. At the other extreme, if we allowed an arbitrarily long cooling time, then the molten Earth would be quiescent (non-convecting), and could evolve through fractional crystallization to give a strongly layered body. Accordingly, in this section, we will attempt to constrain the rate of heat loss from the molten Earth. The heat flux from the molten Earth will depend on the surface temperature and on the opacity of the atmosphere, while the surface temperature depends on whether or not a crust could form. In the following subsection we discuss the importance of an atmosphere, and arrive at an approximation for the heat flux as a function of surface temperature. In the subsequent subsection we consider whether or not a crust could form if the upper mantle were a superheated liquid, and what influence this might have on the heat flux from the magma ocean.

(i) *Heat flow through the atmosphere.* The ability of a protoatmosphere to transmit heat from a magma ocean is strongly dependent on the chemical constitution of the atmosphere. The chemical composition of a protoatmosphere will, in turn, depend on the temperature of the Earth's surface. Very high surface temperatures lead to the formation of a metal-oxide (*e.g.*, Na, K, SiO, Mg) atmosphere [Ringwood, 1979]. Lower surface temperatures lead to the formation of a predominately H_2,

CO, H_2O, CO_2, CH_4 atmosphere [Holloway, 1988], and still lower temperatures favor an air, *e.g.*, N_2, atmosphere. Liquid water would not be stable at the Earth's surface if the bulk of the mantle were molten or partially molten. Since such a molten state is the premise of our discussion, we will not consider the latter case.

The potential surface temperature of a totally molten Earth could exceed 3500 K (Fig. 19a). Under such conditions, a metal-oxide vapor atmosphere would form. However, condensation (*i.e.*, the formation of oxide and silicate clouds) would probably limit the effective radiating temperature of the atmosphere to be ≈2000 K [Thompson and Stevenson, 1988]. The radiative black body heat flux corresponding to a temperature of 2000 K is $\sigma T^4 = 0.9$ MW/m^2.

A H_2O, CO, or CO_2 atmosphere that would form at surface temperatures below ≈1500 K could similarly regulate the radiating temperature. The numerical experiments of Zahnle *et al.* [1988] indicate that for surface temperatures below about 1500 K, a water-rich atmosphere would limit the net radiative heat flux to about 150 W/m^2: about 6000 times less than a metal-oxide atmosphere. For surface temperatures above 1500 K, the water-rich atmosphere is transparent to much of the surface radiation, which has significant components in visible and UV wavelengths. Consequently, the radiative properties of the atmosphere in the surface temperature interval of 1500-2000 K would be intermediate between the water-rich and metal-oxide cases.

As a first approximation, we adopt a mean heat flux of 0.9 MW/m^2 when the surface temperature exceeds 2000 K, and a mean heat flux of 150 W/m^2 when the surface temperature drops below 1500 K. If there is no crust on the magma ocean, then the surface temperature will exceed 2000 K when the lower mantle of the Earth is crystallizing (Fig. 19a), and the heat flux regulating fractionation of the lower mantle will be that corresponding to a metal-oxide atmosphere: 0.9 MW/m^2. If no crust exists when the upper mantle crystallizes, then the surface temperature will be between 1500

Figure 19: Estimated C1 phase diagram for the mantle compiled from experimental data of Heinz and Jeanloz [1987], Ito and Takahashi [1987], Knittle and Jeanloz [1989], Ohtani *et al.* [1986], Ohtani and Sawamoto [1987], Scarfe and Takahashi [1986], and Takahashi [1986]. Beyond 25 GPa this phase diagram is highly schematic and based solely on the perovskite liquidus (see Fig. 18). The liquidus phases are olivine to ≈15 GPa followed by majorite to ≈25 GPa and perovskite at higher pressures. Subsolidus reaction boundaries for the sequence plagioclase→spinel→garnet and olivine→β modified spinel→γ spinel→perovskite+mw are also indicated. Superimposed on the phase diagram (Fig. 19a) are adiabatic contours. The entropy of fusion causes subliquidus adiabats to remain in the melting interval over extensive depth intervals. Note that crystallization will begin at the base of a whole Earth magma ocean. The actual temperature profile of a magma ocean will differ from the adiabatic contours wherever boundary layers develop. These boundary layers may form in the lower mantle because of viscosity contrasts, in the upper mantle because of olivine neutral buoyancy, and at the surface where an itinerant crust may form. The difference in energy (in 10^{30} J) between a given wet adiabat and the one above it is written on the adiabat curves. At high temperatures the curves are at $\approx 1.4 \times 10^{30}$ J intervals. At lower temperatures the energy difference increases. Figure 19b is an enlargement of Figure 19a, emphasizing the upper mantle and transition zone. Contours in this figure are at 50° intervals at P=0.

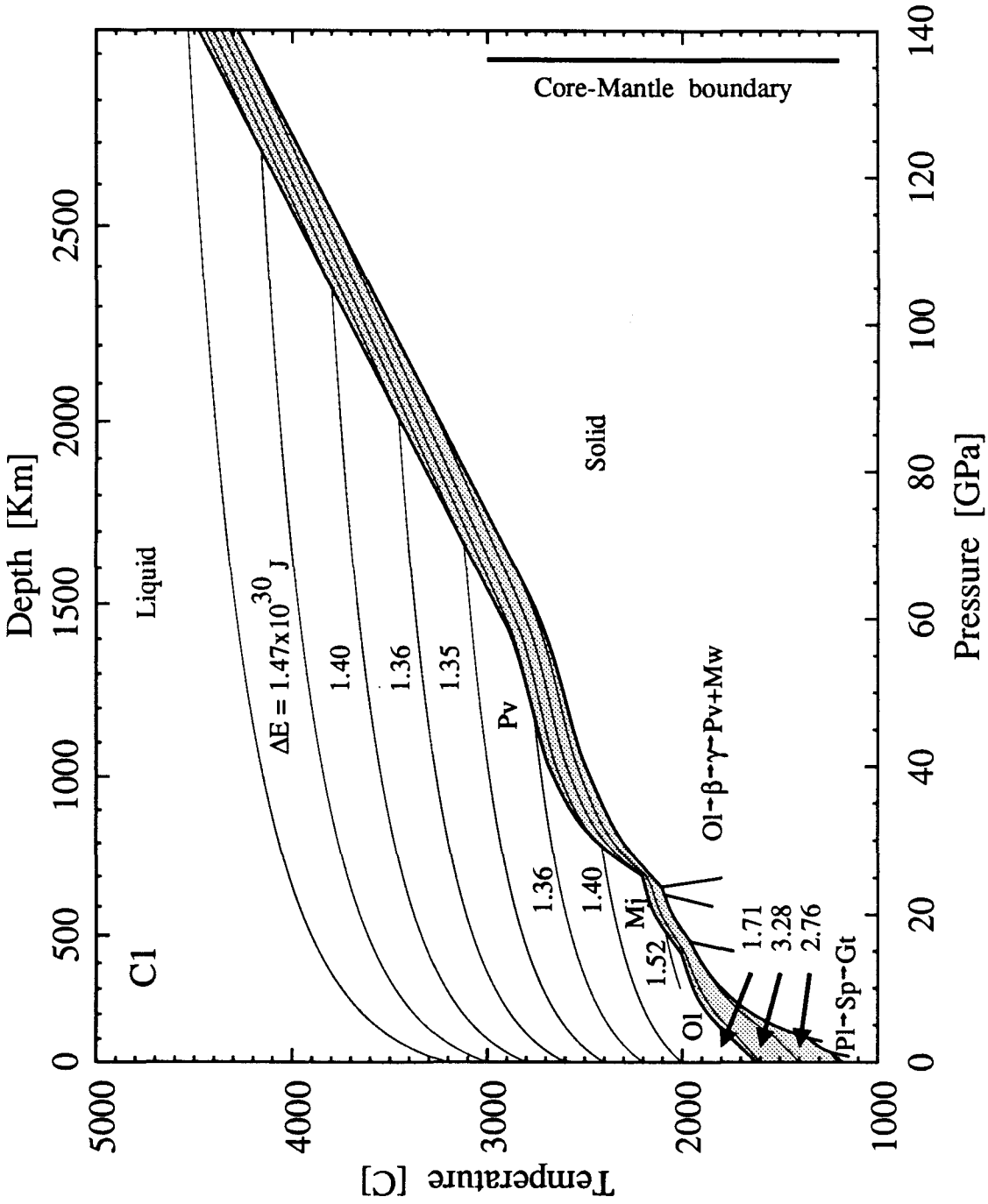
Depth [Km]
0
500
1000
1500
2000
2500
Pressure [GPa]
0
20
40
60
80
100
120
140
Temperature [C]
5000
4000
3000
2000
1000
Core-Mantle boundary
Liquid
Solid
C1
ΔE = 1.47x10^30 J
1.40
1.36
1.35
Pv
1.36
1.40
Mj
1.52
Ol
Ol→β→γ→Pv+Mw
1.71
3.28
2.76
Pl→Sp→Gt

Figure 19a.

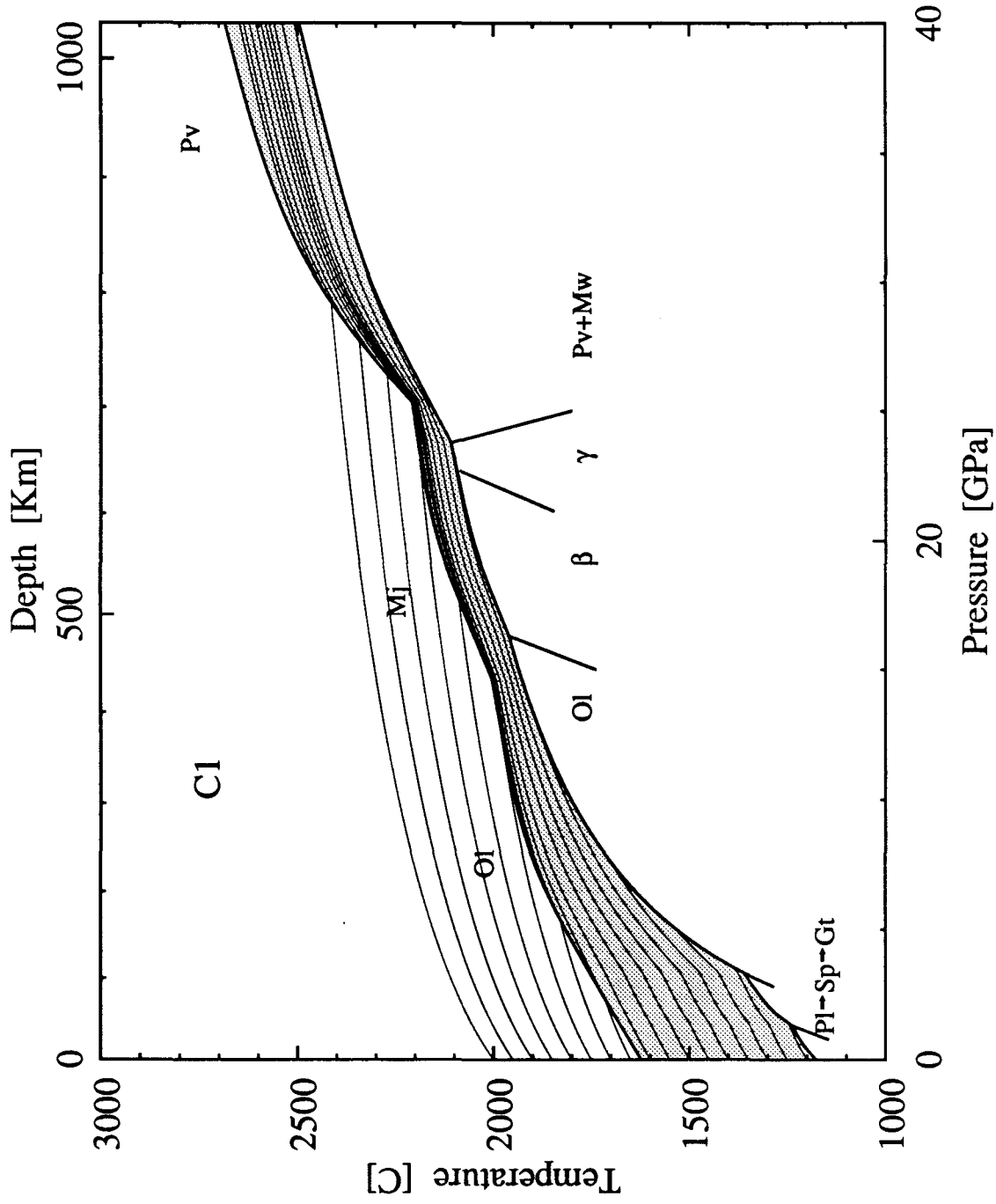
Depth [Km]
0
500
1000
Pressure [GPa]
0
20
40
Temperature [C]
3000
2500
2000
1500
1000
C1
Pv
Mj
Ol
Ol
β
γ
Pv+Mw
Pl→Sp→Gt

Figure 19b.

Figure 20: Cartoon snapshots of the evolution of the mantle from an initial wholly molten state. (a) The first crystals to form will be perovskite. These will form at the base of the lower mantle where the adiabats first cross the liquidus (Fig. 19a). Convection would be so turbulent that individual crystals would not be capable of settling out (up in this case since perovskite could be buoyant at P>70 GPa). Crystal enrichment at the base of the lower mantle could lead to the formation of a viscous boundary layer. In this boundary layer, perovskite crystals might be capable of rising and subsequently become entrained in the turbulent eddies above, leading to perovskite enrichment in the upper liquid region of the mantle. Iron-enriched residual liquid could percolate down toward the core-mantle boundary. (b) When the boundary layer reaches the level of perovskite neutral buoyancy, ≈70GPa, the direction of crystal-liquid segregation will change. In this snapshot, a boundary layer exists in the shallower lower mantle where perovskite crystals may be capable of settling downward. In this shallow region, perovskite-depleted liquid could percolate through the perovskite matrix to be mixed into the convecting liquid above. Below the boundary layer, at the level of perovskite neutral buoyancy, percolating iron-rich perovskite-depleted liquid will sink. The perovskite neutral buoyancy horizon would separate and iron-enriched perovskite-depleted deep lower mantle from a perovskite-enriched iron-depleted shallow lower mantle. Majorite crystals may begin to form near this time, but as they are swept downward in the turbulent eddies they would either dissolve or convert to perovskite. The majorite→perovskite reaction boundary is shallower than the boundary layer at this time. The deep crystalline lower mantle may begin subsolidus convection. (c) When the upper mantle begins to crystallize, a crust may begin to form. The crust would be mechanically unstable and would founder. Olivine crystals larger than 3.5 cm could also segregate from the convecting liquid. The segregated olivine and foundered crust could form pockets of solid debris in

the shallow upper mantle that could resist being entrained in the liquid mantle flows because of their size and relative density. Stagnant boundary layers on the solid debris would allow small (<3.5 cm) olivine crystals to segregate from the magma. Through these three mechanisms (foundered crust, large olivines, and settling of small olivines through stagnant boundary layers), a dunite septum could form in the shallow upper mantle (near ≈9 GPa). In the transition zone majorite continues to crystallize. As eddies carry majorite from the transition zone, they either melt or convert subsolidus to perovskite or clinopyroxene. Majorite segregation is inhibited until the base of the magma ocean (defined as the ≈44% crystallinity boundary layer) reaches the transition zone. The crystalline deep lower mantle is undergoing subsolidus convection. (d) This is a schematic representation of the stratification of the mantle before subsolidus convection and possible rehomogenization takes place. A crust overlies a clinopyroxene- and garnet-rich shallow upper mantle. This layer forms from the upper mantle magma that was depleted in olivine components that sank to form the dunite septum. The dunite septum overlies a transition zone that is also depleted in olivine components. The principal mineralogy of the transition zone would be β-spinel, majorite and garnet. The lower mantle consists of perovskite and magnesiowüstite. This stratification is not gravitationally stable. In particular, the dense garnet-rich shallow upper mantle is denser than the underlying dunite layer. As mentioned earlier, the lower mantle may also be unstably stratified with a dense perovskite-rich layer overlying a less dense magnesiowüstite-rich layer. Also contributing to rehomogenization are late-impacting iron-rich planetesimals (shown as an infalling Fe-rich body). If sufficiently rich in metallic iron, these bodies could sink to the core and substantially enhance subsolidus convection. After the upper mantle undergoes its convective overturn, the crust would overly a peridotitic upper mantle, that in turn would overly a garnet-

majorite-rich transition zone. This stratification would be stable, and could prohibit the Earth from convecting as a single layer. A stratification of this sort has been proposed for the present Earth.

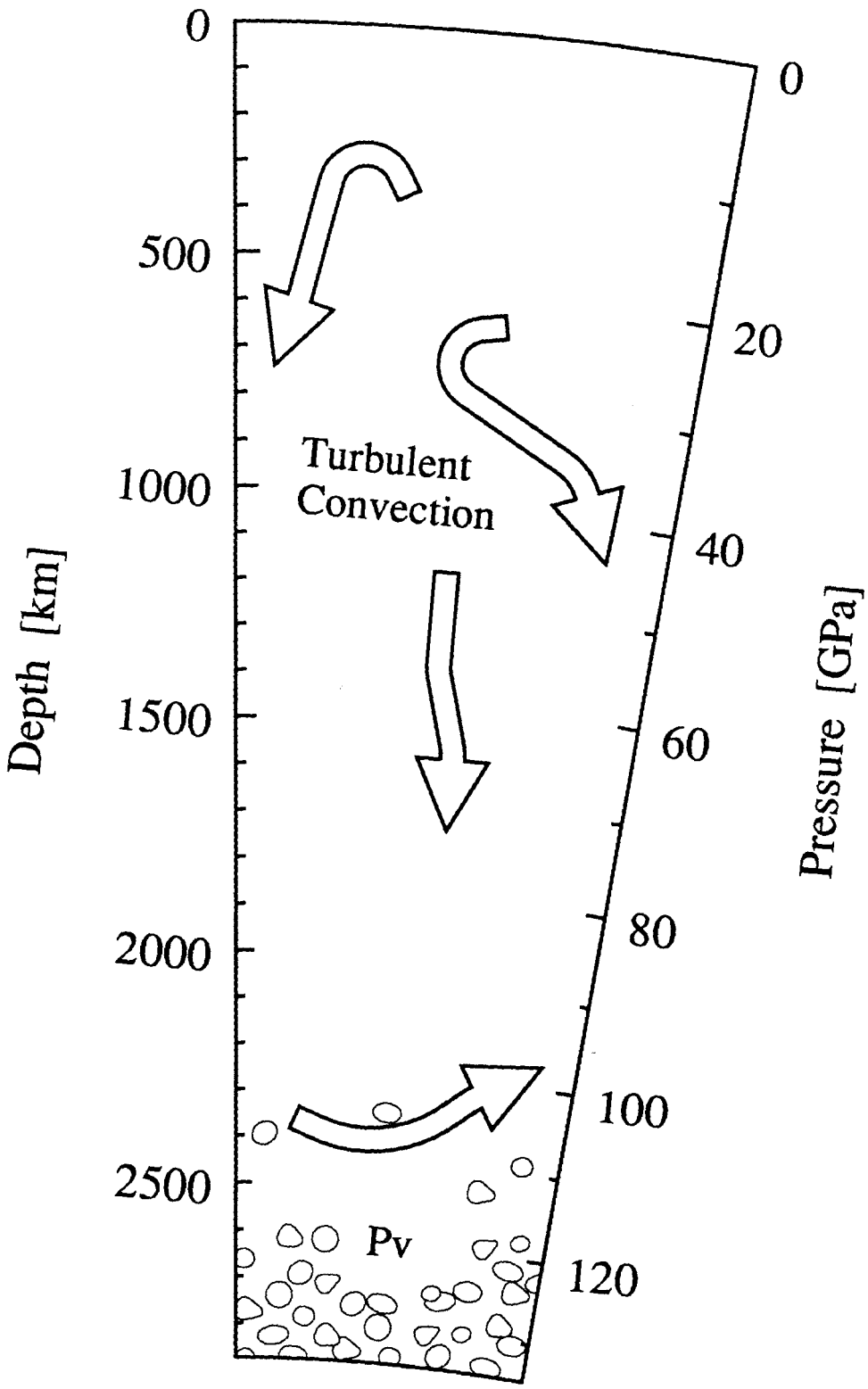
0
500
1000
1500
2000
2500
Depth [km]
0
20
40
60
80
100
120
Pressure [GPa]
Turbulent
Convection
Pv

Figure 20a.

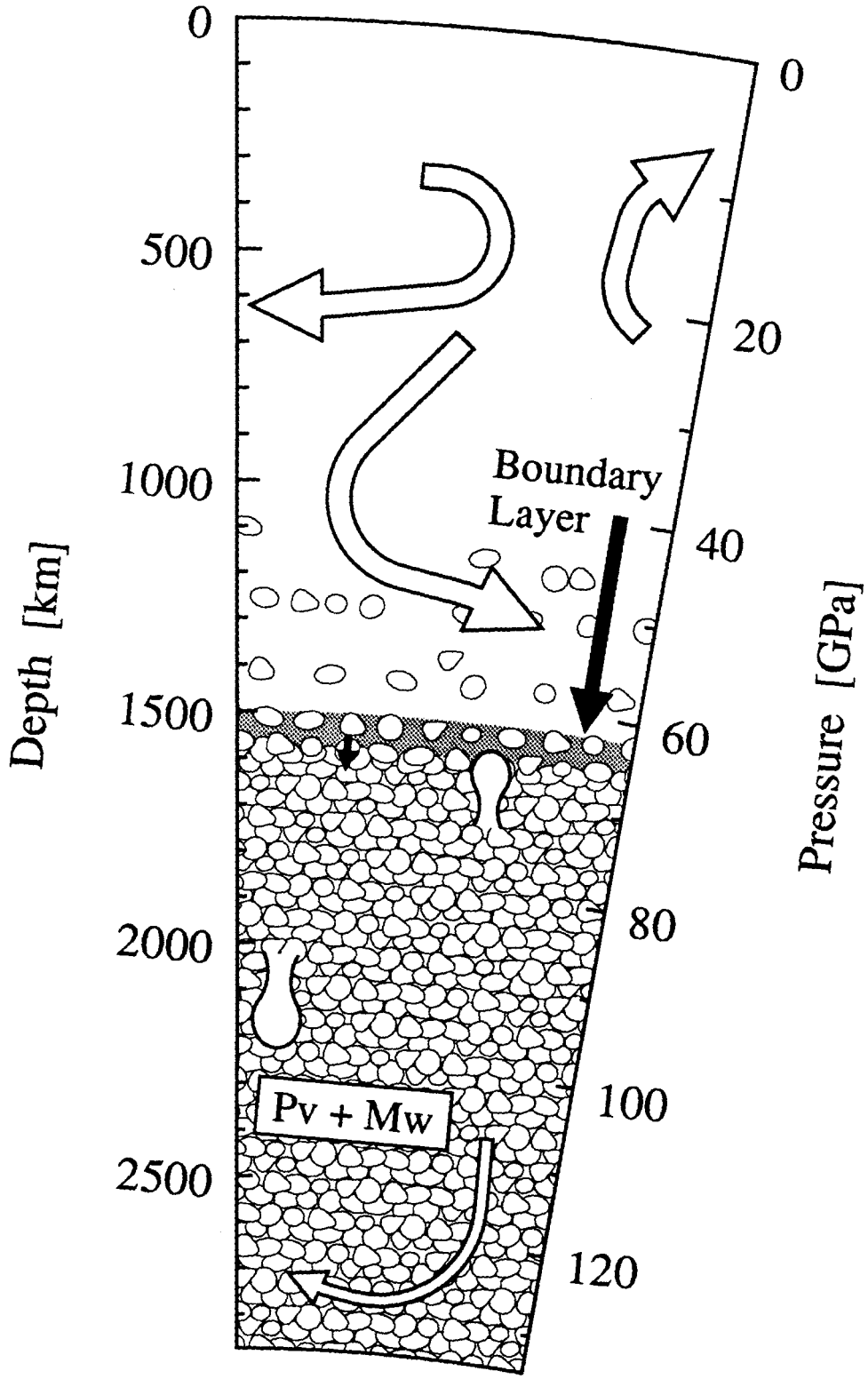
0
500
1000
1500
2000
2500
Depth [km]
0
20
40
60
80
100
120
Pressure [GPa]
Boundary
Layer
Pv + Mw

Figure 20b.

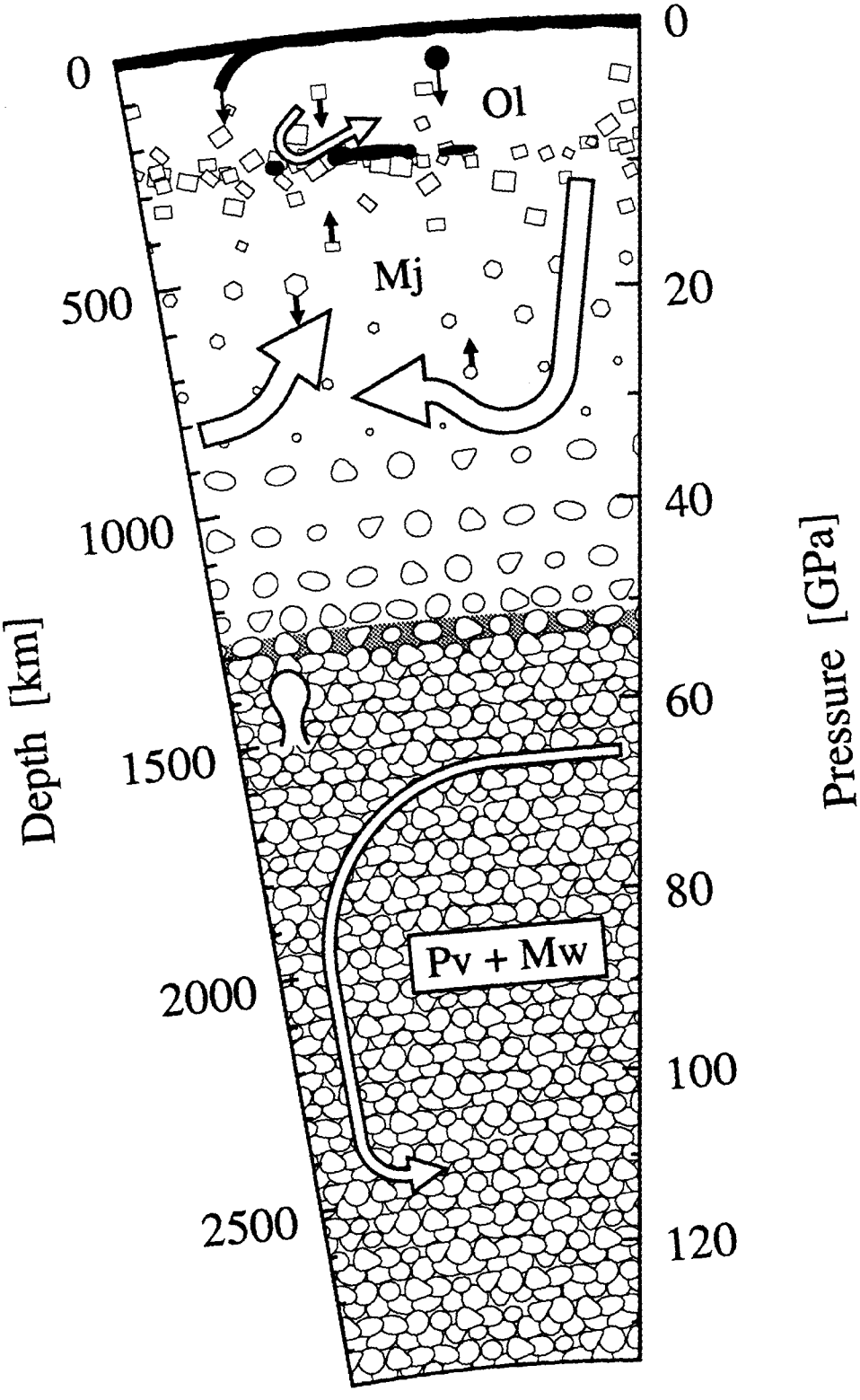
0
500
1000
1500
2000
2500
Depth [km]
0
20
40
60
80
100
120
Pressure [GPa]
Ol
Mj
Pv + Mw

Figure 20c.

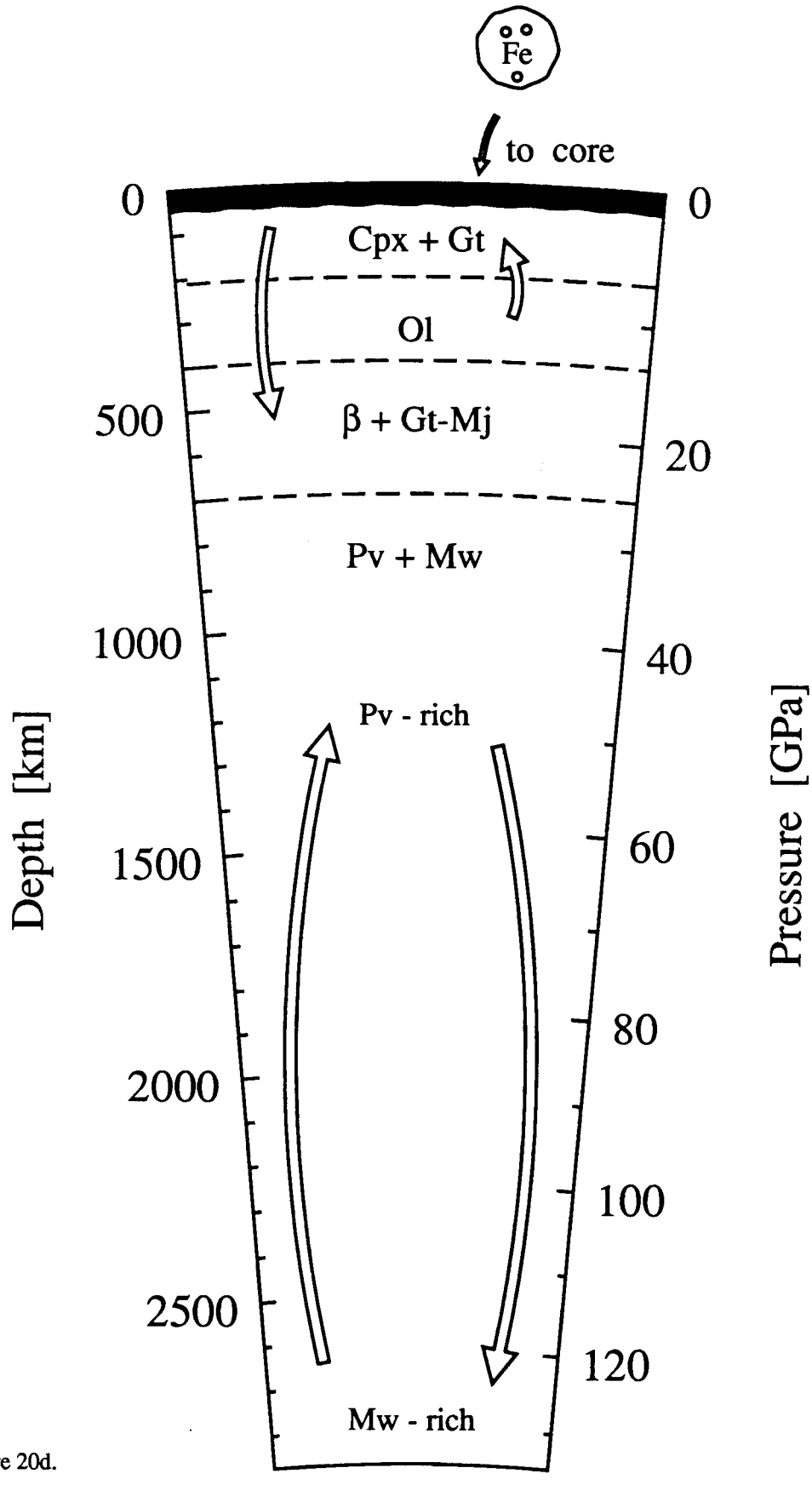
Fe
to core
0
0
Cpx + Gt
Ol
500
β + Gt-Mj
20
Pv + Mw
1000
40
Pv - rich
1500
60
2000
80
100
2500
120
Mw - rich
Depth [km]
Pressure [GPa]

Figure 20d.

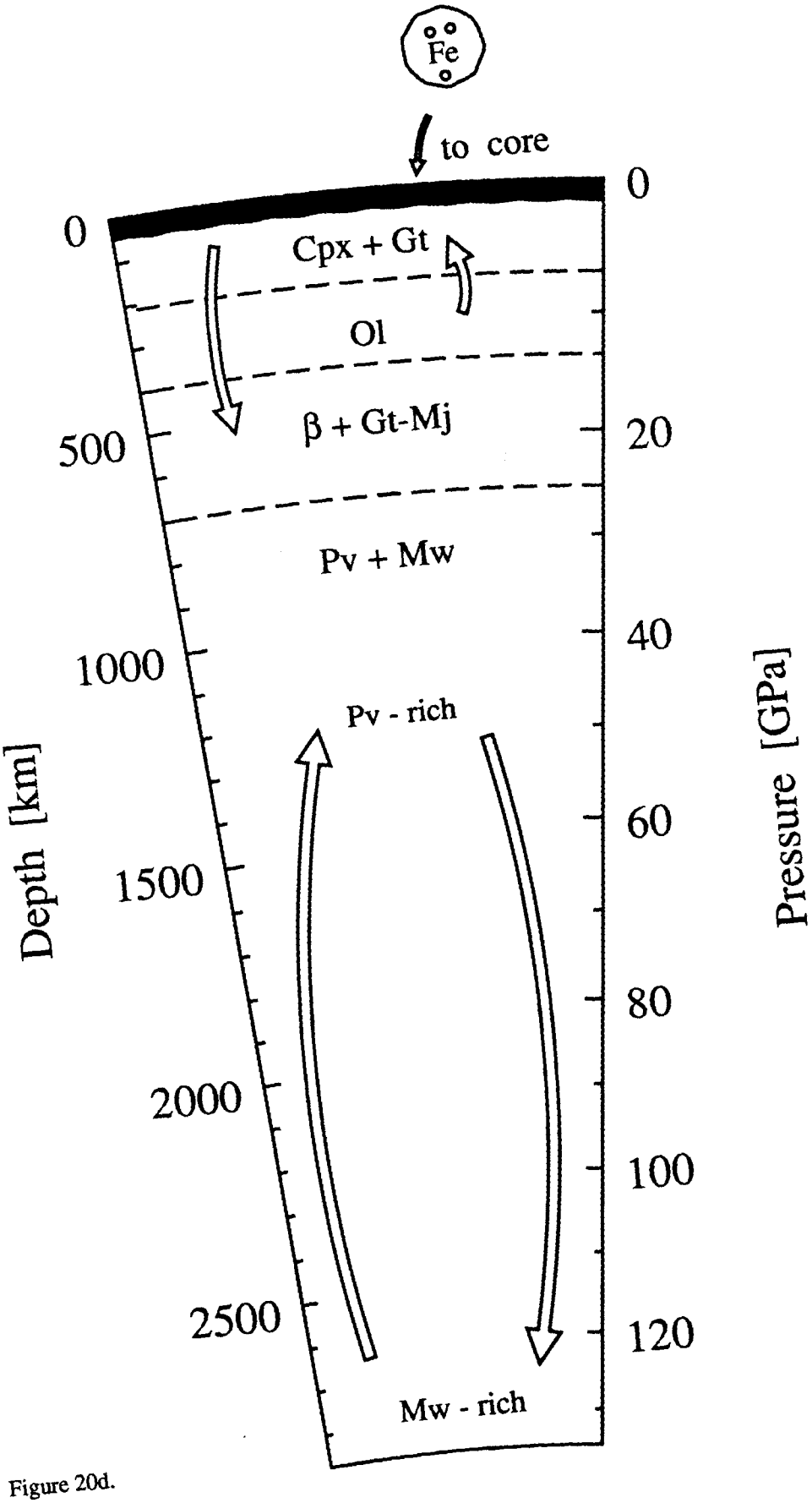
Fe
to core
0
0
Cpx + Gt
Ol
β + Gt-Mj
500
20
Pv + Mw
1000
40
Pv - rich
60
1500
80
2000
100
2500
120
Mw - rich
Depth [km]
Pressure [GPa]

Figure 20d.

and 2500 K (Fig. 19b), and the heat flow will be between 150 W/m^2 and 0.9 MW/m^2. If a crust forms, then the mean surface temperature cannot be greater than the solidus temperature of the crust, ≈1500 K, corresponding to a maximum heat flux of about 150 W/m^2, independent of the temperature of the underlying magma.

The significance of heat flux for chemical fractionation can be shown by considering the energy budget of the molten mantle. From Figure 19a, it can be seen that to generate a crystalline mantle about 1.7×10^{31} J (the sum of the energy differences between adiabatic profiles) must be removed from a wholly molten mantle beginning to crystallize at its base. The surface area of the Earth is about 5×10^{14} m^2. If the Earth cooled at a mean surface temperature greater than 2000 K, *i.e.*, regulated by a metal-oxide atmosphere, then the cooling time would be only 1200 yrs. This case is tantamount to quenching the mantle, and chemical fractionation would be limited. If the mean heat flux were 150 W/m^2, *i.e.*, regulated by a water-rich atmosphere (but no crust), then the cooling time would be 7.2×10^6 yrs. This longer time affords a greater opportunity for chemical fractionation to occur.

(ii) *A crust on a superheated liquid mantle?* The existence of a crust is important for the chemical fractionation of the mantle because it limits the maximum heat flux from the magma ocean to about 150 W/m^2, as discussed in the previous section, and possibly much less since heat transfer might be limited by conduction through the crust. An essential feature of a crust on a magma ocean is that it is not likely to be buoyant. Morse [1987] discussed this problem as it relates to a lunar magma ocean. Another feature of the early evolution of the magma ocean is that the ocean would likely be superheated at low pressure (Fig. 19). A crust would have to support a very steep thermal gradient (at least $(T_{liquidus}-T_{solidus})/\delta$, where δ is the thickness of the crust), and foundered crust would dissolve unless it were thick [Walker and Kiefer, 1985]. Nevertheless, although a crust is not mechanically stable, is seems likely that some glass or crystals would form simply because

convective heat transport may not keep pace locally with the extraordinarily high rate of radiative heat transport. In this subsection we investigate the importance of a crust when the upper mantle is superheated liquid.

Assuming that some crust can be generated, but that it will ultimately sink because of its high density, we consider the possibility of a dynamically maintained crust. As a crude model, we consider a hypothetical pseudo-steady state crust of thickness δ. When it founders, blocks of diameter δ will sink according to Stokes' formula. Let us suppose that most of the radiative heat loss is applied to removing the latent heat of fusion of liquid that regenerates the crust. A crude heat balance is then given by:

$$\frac{\delta^2 \Delta\rho g}{18\eta}\rho\Delta H_f < F \approx \frac{\kappa(T_{liquidus}-T_{surface})}{\delta} \tag{39}$$

in units of energy per time per surface area. Here F is the heat flux from the magma ocean, η is the viscosity of the molten mantle (1 poise), $\Delta\rho$ is the density contrast (200 kg/m^3) between the crust of density ρ (3000 kg/m^3) and the density of the liquid, ΔH_f is the latent heat of fusion (4×10^5 J/kg), and κ is the thermal conductivity (2 J/m K). The surface temperature, $T_{surface}$, must be below the 1 bar liquidus (2000 K) for crystals to form. In the initial stages of the evolution of the magma ocean, *i.e.*, when the lower mantle is crystallizing, we assume the temperature at the bottom of the crust will be approximately equal to the liquidus temperature.

If the heat flux is 150 W/m^2 we find that the crust cannot be thicker than 40 μm. The maximum heat flux, 0.9 MW/m^2, gives a maximum crust thickness of 2.6 mm, but a surface temperature of 830 K that is inconsistent with such a high heat flux. The internally consistent solutions to Eqn. 39 give a crust of negligible thickness. From this exercise we conclude that a dynamically maintained crust is not important from the perspective of heat transfer when the upper mantle is

superheated. The heat flow from the magma ocean would have been controlled entirely by the atmosphere. At later stages of evolution, when the magma ocean may contain crystals at all depths, viscosity below the crust will increase because of the crystal content and lower temperatures of the magma. This viscosity enhancement could stabilize a dynamic crust, allowing it to become an impediment to heat transfer.

Crystal-liquid fractionation in the depth range of the lower mantle

If the whole Earth were molten, then the adiabats shown in Figure 19a indicate that crystallization would have begun at the core-mantle boundary. From Figure 18 we believe that the first phase to crystallize would be perovskite. Any crystal-liquid segregation that occurred during the crystallization of the lower mantle would have perturbed the chemistry of the upper mantle if the liquid portion of the magma ocean were well mixed. Agee and Walker [1988b, 1989] suggest on the basis of a major element mass balance that some perovskite fractionation is required to generate the modern peridotitic upper mantle. Ringwood *et al.* [1987], and Kato *et al.* [1988a, 1988b] argue, however, that perovskite fractionation could not have been important because of the trace element partitioning constraints. We showed earlier that perovskite is probably less dense than a chondritic melt at the conditions of the deepest lower mantle (Fig. 10b); thus perovskite might segregate in a quiescent mantle by flotation at P>70 GPa (d>1680 km), and by settling at P<70 GPa, possibly generating the chemical fractionations inferred by Agee and Walker [1988b, 1989]. In a large convecting magma body, however, the flow regime will ultimately govern the extent to which segregation is possible.

(i) *Perovskite settling/floating in a convecting system.* We assume the condition for segregation in a convecting fluid in the absence of boundary layers is that the settling velocity of the cry-

stals exceeds the convective velocity of the magma. We can estimate the convective velocity of the magma ocean with mixing length theory [Clayton, 1968, pp. 252-259]:

$$v_{conv} \simeq \left[\frac{d\,F}{H_T\,\rho} \right]^{1/3}, \tag{40}$$

where F is the heat flux, d is the depth of the ocean, and H_T is the thermal scale height:

$$H_T = \frac{T}{\rho g \left. \frac{\partial T}{\partial P} \right|_S}, \tag{41}$$

which we calculate to be approximately 2×10^4 km. Note that the convective velocity is weakly dependent on the heat flux. Recall that we have assumed the heat flux to be about 0.9 MW/m^2 during crystallization of the lower mantle. The average convective velocity for a 2900 km deep magma ocean is then about 3 m/s.

For crystal segregation to occur the settling (or rising) velocity must exceed the vertical component of the convective velocity. In a low Reynolds number regime ($\mathrm{Re} \equiv \frac{2rv\rho}{\eta}$ for $\mathrm{Re} \leq 2$, where the Reynolds number, Re, is evaluated for crystals. Here r is the crystal radius, v is the relative crystal-liquid velocity approximated by Eqn. 40, η is the fluid viscosity, g the gravitational acceleration, ρ is the fluid density, and $\Delta\rho$ the density contrast. This is not the Reynolds number characterizing the convective flow of the magma ocean), the settling velocity is well approximated by Stokes' terminal velocity formula. In higher Re regimes a variety of empirical relationships can be used to determine settling velocities [Bird *et al.*, 1960]:

$$r \approx \left[\frac{9\eta v}{2g\Delta\rho}\right]^{1/2} \qquad \mathrm{Re} \leq 2 \qquad (42a)$$

$$r \approx \left[\frac{111\rho v^2}{16g\Delta\rho}\right]^{5/8}\left[\frac{\eta}{2v\rho}\right]^{3/8} \qquad 2 < \mathrm{Re} \leq 500 \qquad (42b)$$

$$r \approx \frac{33\rho v^2}{200g\Delta\rho} \qquad 500 < \mathrm{Re} \leq 2\times10^5\,, \qquad (42c)$$

Note that the viscosity dependence of r is different in each flow regime, and Eqn. 42c is independent of viscosity. The dependence of crystal size on the assumed heat flux is also different in each regime. Comparing Eqn. 40 with Eqns. 42, we see that crystal size is proportional to $F^{1/6}$ (Eqn. 42a), $F^{7/24}$ (Eqn. 42b), or $F^{2/3}$ (Eqn. 42c). We estimate the crystal size by evaluating each of these equations, determining the Reynolds number for each case, and selecting the result that is consistent with the Re conditions. For perovskite in the lower mantle, the maximum crystal-liquid density contrast will be ≈0.25 g/cc. If the viscosity of molten C1 obeys an Arrhenius relationship, independent of pressure, then we would estimate a lower limit for the viscosity to be ≈ 0.01 poise [Bottinga and Weill, 1972]. The combined pressure and temperature dependence of viscosity is unknown for silicate liquids under these conditions so this value for viscosity must be suspect. We estimate that crystals 60 m in diameter would be required if segregation is to occur in such a vigorously convecting system, independent of viscosity (Re is 8×10^8 in this case, outside the bounds of the constitutive relations). If we considered a heat flux 10^3 times smaller, then the velocity would be 30 cm/s, and the required crystal diameter 60 cm. While EOS constraints alone might suggest crystal flotation or settling during lower mantle crystallization, consideration of the flow characteristics in the magma ocean emphatically precludes this possibility.

As the magma ocean cools, a crystal-rich layer will develop at the base of the lower mantle. This crystal enrichment is not a consequence of crystal settling, but simply a result of the wet adiabat approaching the solidus. This crystal enrichment leads to rapidly increasing viscosity, which in

turn could lead to a change in the flow structure of the ocean. According to Roscoe's [1953] criterion, 44% (by volume) of crystals would increase the viscosity over the crystal-free viscosity by a factor of 10, about the maximum viscosity contrast the system can tolerate before forming a boundary layer [Marsh, 1989].

If a boundary layer forms in the lower mantle between crystal-poor magma above and crystal-rich magma below, then chemical fractionation could occur through two mechanisms. First, crystal settling or flotation could occur through this boundary layer, regardless of crystal size, since the moving crystals would not have to oppose convective flow. Second, interstitial liquid could be expelled from the compacting crystal-rich lower zone. If crystals are denser than liquid then intercumulus liquid will be expelled upward, leading to chemical fractionation effects in the upper mantle by upward transport of perovskite-depleted liquid. If crystals are less dense than the liquid, then expelled liquid will segregate downward and the boundary zone will be enriched in crystals. This downward melt segregation would be hidden from the upper mantle, which would be unaffected by this fractionation. If these buoyant crystals become entrained in the convecting liquid above the boundary layer, then chemical fractionation could also occur.

In the lower mantle, our results suggest perovskite would be buoyant in C1-like liquid compositions at pressures ≥70 GPa (1680 km), and more dense than the liquid at lower pressures (Fig. 10b). As the lower mantle crystallizes, the nature of possible chemical fractionation at the boundary layer would therefore change. When the boundary layer exists at greater pressure than the perovskite neutral buoyancy horizon (≈70 GPa), perovskite will tend to float, thereby enriching the magma ocean in perovskite components if boundary layer entrainment can occur. At later times, when the boundary layer is shallower than the perovskite neutral buoyancy horizon, perovskite will tend to settle out from the boundary layer. The combined effect would be to enrich the shallow lower mantle in perovskite components relative to the deep lower mantle. Iron-rich interstitial

liquids in the crystal-rich regions below the boundary layer would also tend to sink at >70 GPa (and perhaps from shallower levels as well, although such liquids might crystallize upon adiabatic compression), perhaps also leading to enrichment of the shallow lower mantle in perovskite components and enrichment of the deep lower mantle in magnesiowüstite components. Such a chemical stratification would be unstable under subsolidus conditions because crystalline perovskite is denser than crystalline magnesiowüstite. The formation of such a stratified lower mantle would therefore give rise to subsequent subsolidus convection.

If crystal-liquid segregation can occur in boundary layers and movement of interstitial liquid below the boundary layer is possible, solidification of the lower mantle initially enriches the overlying magma in perovskite components, and later, when the boundary layer is shallower than ≈70 GPa, depletes the overlying magma in perovskite components. Whether the upper mantle and transition zone would suffer a net enrichment or depletion of perovskite components depends on the relative efficiencies of the initial perovskite flotation and later perovskite settling mechanisms. If these processes were equally efficient, then the upper mantle and transition zone might be expected to be depleted in perovskite because the volume of the perovskite-enriched shallow (P<70 GPa) lower mantle is about 34% greater than the volume of the perovskite-depleted deeper part.

The extent of perovskite fractionation by settling crystals through a boundary layer is difficult to quantify since the crystal content and velocities of turbulent eddies near the boundary layer must be known. Crystal size, which must also be known, depends on the mean residence time of eddies in the subliquidus region of the magma ocean and the kinetics of crystal growth. A simple model for crystal settling in a turbulently convecting magma body was developed by Martin and Nokes [1988]. Their model is based on experimental measurements in the limit of very low crystallinity (≈0.3 volume %). Since the crystal fraction near the boundary layer could be very large, ≈44.0 volume %, their model is not directly applicable in this case. When the crystal fraction in the

boundary layer is large, the viscosity and hence settling rate for individual crystals is strongly dependent on the crystal content. In this limit, the problem of crystal settling through a boundary layer becomes in essence a problem of matrix compaction. Perovskite fractionation by matrix compaction is more easily quantified, and gives a lower limit to the amount of perovskite fractionation that could occur. This mechanism is discussed below.

(ii) *Perovskite fractionation by matrix compaction.* To what extent can matrix compaction lead to fractionation? We are interested in the case where liquid is expelled from a compacting matrix that is undergoing crystallization, and that is growing in vertical extent because of the crystallization of the overlying liquid. This compacting region may also be convecting. To evaluate this mechanism we will first estimate the characteristic velocity of the compacting matrix with the method of Richter and McKenzie [1984] and McKenzie [1984], then compare this velocity to the upward velocity of the solidus in the cooling lower mantle. The characteristic velocity of the compacting matrix is given by [Richter and McKenzie, 1984]:

$$v_c = \frac{k_0}{\eta}(1-\phi_0)\Delta\rho g \,, \tag{43}$$

where k_0 is the permeability, $\Delta\rho$ is the density contrast, and ϕ_0 is the initial volume fraction of the fluid phase. Let us consider the case $\phi_0 = 0.56$, obtained above from Roscoe's criterion for a 10× viscosity increase. Conservative estimates of the remaining terms are $\eta = 1$ poise, $k_0 = 1.7\times10^{-4}$ cm^2 (using the constitutive relationship given by Eqn. 5 of Richter and McKenzie [1984], and assuming a crystal radius of 1 cm), and $\Delta\rho = 0.2$. With these assumptions, the characteristic matrix velocity is 0.5 km/yr, proportional to the crystal size squared.

The time scale for the growth of the crystal-rich layer can be estimated from the heat flux from the magma body. Given the heat flux (0.9 MW/m^2), we calculate the growth of the layer from

the difference in heat and crystal content of the adiabatic profiles (Fig. 19) to be about 2.6 km/yr. Since the liquidus and solidus of the lower mantle are subparallel, the velocity of the solidus will also be ≈2.6 km/yr. Since the velocity of the solidus exceeds the velocity of the compacting matrix by a factor of 5, we infer that matrix compaction may not lead to significant chemical fractionation effects in the lower mantle. This conclusion is not robust, however, since neither the heat flux, viscosity, nor crystal size are well-constrained parameters. In any case, matrix compaction or initial inhomogeneities in initial crystal fractions in the partially molten zones could generate regions of locally high fluid fraction that could ascend rapidly either as diapirs or solitary waves [Richter and McKenzie, 1984; Scott and Stevenson, 1984, 1986, 1988]. Some fractionation by auxiliary diapiric processes or enchanced porous flow as magmons may be possible even if the compaction rate is much smaller than the crystallization rate. We conclude that perovskite fractionation motivated by matrix compaction is possible, but the extent to which it would occur depends strongly on poorly constrained model parameters.

Crystal-liquid fractionation in the depth range of the upper mantle and transition zone

(i) *Garnet-majorite crystallization.* When garnet-majorite begins to crystallize, perovskite crystallization is still incomplete in the lower mantle (Fig. 19), and the floor (>44% crystals) of the magma ocean is deeper (≈40 GPa; ≈1000 km) than the garnet-majorite→perovskite reaction boundary. Thus, if the initially crystallized garnet-majorite were able to sink it would convert to perovskite before reaching the floor of the magma ocean. However, garnet-majorite may begin to crystallize deeper than its ≈22 GPa neutral buoyancy presure with komatiitic liquid (Fig. 9). Thus, when garnet-majorite first crystallizes in the magma ocean it may resist fractionating because of its tendency to float, and might be digested by the overlying superheated liquid. When the floor of the

magma ocean reaches the garnet-majorite→perovskite reaction boundary at about 25 GPa, fractionation of the approximately neutrally buoyant garnet-majorite may be possible. Before this occurs, however, olivine will have begun to crystallize in the upper mantle. As discussed below, and by Agee and Walker [1988b], olivine crystallization could generate a boundary layer in the upper mantle that might isolate the shallow upper mantle from the effects of garnet-majorite fractionation.

(ii) *Olivine crystallization and the formation of a dunite septum.* The prediction that olivine would be less dense than ultrabasic liquid near 8 GPa led Nisbet and Walker [1982], Ohtani [1985], and Agee and Walker [1988b] to suggest that a dunite septum would develop at the depth of olivine neutral-buoyancy. Such a septum would separate the magma ocean into upper and lower regions that could evolve separately. The lower magma reservoir has been suggested by these authors as a source of komatiitic magma. In this subsection we will address the feasibility of this proposition.

The phase diagram (Fig. 19b) suggests that olivine will first begin to crystallize near its neutral buoyancy horizon. Olivine fractionation will therefore probably not be possible initially.

As the mantle continues to cool, olivine will begin to crystallize both above and below the neutral buoyancy horizon. Even when olivine crystals are stable far from the neutral buoyancy horizon, for example at the surface of the magma ocean, crystal settling may not occur. The convective velocity (from the mixing length formula, Eqn. 40, with a heat flux of 150 W/m^2) of the magma ocean will be approximately 10 cm/s. We estimate that the viscosity of crystal-free magma will be ≈1 poise [Bottinga and Weill, 1972]. With these assumptions, a crystal radius of ≥3.5 cm (Eqn. 42b) is required for crystal flotation/settling to occur in the absence of a boundary layer. As discussed previously, this result is weakly dependent on the assumed heat flux (r is proportional to $F^{7/24}$ in this flow regime). Olivine segregation by settling or flotation could occur if ≈3.5 cm crystals could form; this crystal size is proportional to the 3/8 power of viscosity, which could readily be an

order of magnitude higher or lower. Whether crystals of this size could form depends on the kinetics of crystals growth, and on the mean residence time of turbulent eddies in the shallow mantle where olivine is the liquidus phase.

Agee and Walker [1988b] proposed an alternative mechanism for nucleating a septum that circumvents the need for large single crystals. They proposed that meter-sized foundered blocks of crust would sink without dissolving [Walker and Kiefer, 1985], and come to rest near the level of olivine neutral buoyancy. Olivine crystals in the magma could then accumulate above and below the foundered crust through stagnant boundary layers or compaction processes. In this case, the formation of a dunite cumulate layer depends critically on the details of crust formation and crust stability.

When olivine first begins to crystallize, majorite crystallization will be nearly 10% complete in the transition zone, and perovskite crystallization nearly 60% complete in the 25-70 GPa interval. As the upper mantle cools beyond this point, regions both above and below the olivine neutral buoyancy point will begin to crystallize olivine. If a dunite septum develops and grows, it would do so by both olivine settling from above and flotation from below, so the magma reservoirs above and below the septum could both be depleted in olivine and perovskite.

If an olivine septum developed, where would it be situated as the system evolved? Olivine below the neutral density horizon is buoyed up by a force proportional to the density contrast. Olivine above the neutral buoyancy horizon will experience a similar force, but of opposite sign, that pushes the septum downward. The septum will situate itself in a position where these forces are exactly balanced (Archimedes' principle). If crystal accumulation from below were not properly balanced by crystal accumulation from above, then the positive and negative buoyancy forces would not balance. The septum would have to readjust, and this readjustment would necessitate magma

transport through the septum. The "septum" would therefore be permeable. Transport of magma through the permeable septum could transmit chemical fractionations between the upper and lower magma reservoirs, in a direction dependent on the relative crystallization rates of the two reservoirs. It seems likely that the upper, shallow reservoir would crystallize faster. If this were so then downward settling of the dunite septum would force magma from the lower reservoir through the permeable septum to mix with the upper magma reservoir. When the floor of the magma ocean ($\approx$ 44% crystallinity) reaches the level of majorite stability (relative to perovskite), the magma trapped between this floor and the dunite cumulate layer could become depleted in majorite. To the extent that this majorite-depleted magma could traverse the dunite cumulate layer (as this layer sagged downward due to addition of olivine from above faster than from below) and mix with the overlying magma, regions above the dunite septum might develop a majorite-depleted chemical signature. Majorite fractionation in the shallow upper mantle might thus be limited by the development of a dunite cumulate layer, but cannot be entirely excluded.

Post-crystallization rehomogenization processes

The evolution of the Hadean mantle from an initially molten state described above would likely lead to some chemical heterogeneity in the upper mantle. For example, perovskite, majorite, and/or olivine fractionation could have occurred, and, indeed, aspects of the chemistry of mantle rocks and seismic properties of the mantle have been used to infer that they did. However, even if such fractionations occurred, their most extreme manifestations may have been obliterated by subsequent rehomogenization of the mantle by subsolidus convection after most of the mantle crystallized. For example, Ohtani [1985] and Agee and Walker [1988b] noted that the shallow upper mantle, depleted in olivine components by the formation of the dunite cumulate layer, would crystallize

to a denser clinopyroxene and garnet assemblage. Convective overturn might later place the olivine-enriched cumulate at the base of the crust or remix these fractionated components. The extent to which such overturn and rehomogenization could have occurred would depend on the vertical extent of the mantle convection system, and whether the mantle convected in one, two, or many layers. This in turn depends on the extent to which chemical stratification developed during crystallization. However, that the upper and lower mantle and perhaps the transition zone may differ in composition today [*e.g.*, Jeanloz and Knittle, 1989; Anderson, 1989] may suggest that convective rehomogenization was limited to specific regimes within the mantle. On the other hand, convection during the Hadean was far more vigorous than today and would have been facilitated by the generally higher temperature of the mantle.

8. Conclusions

We have measured the Hugoniot of a molten komatiite initially at 1550°C. The data are smooth, indicating that rapid structural reorganization has either not occurred or is too subtle to be detected in the 5-36 GPa range of our experiments. This observation is consistent with Hugoniot measurements on molten diopside and anorthite [Rigden *et al.*, 1989], but differs from molten anorthite+diopside Hugoniot results [Rigden *et al.*, 1988], and possibly molten perovskite diamond cell results [Knittle and Jeanloz, 1989] for which evidence of liquid state structural reorganization is inferred. The isentropic bulk modulus is determined to be 27.0 ± 0.6 GPa, and its isentropic pressure derivative is 4.9±0.1. The pressure-density relationships obtained from these parameters is consistent with the static compression measurements of Agee and Walker [1988a] to 6 GPa.

The 1550°C Hugoniot may cross below the komatiite liquidus at pressures less than 15 GPa. Our data shows no evidence of crystallization or anomalous compression that can be associated with

either crystallization or vitrification. To the extent that shear viscosity is a valid indication of the relaxation time, we believe that our samples were fully relaxed. The kinetics of olivine crystallization support the idea that our samples remained molten, albeit metastably, below 15 GPa.

We confirm the hypothesis that ultrabasic liquids can be more dense than coexisting crystals at upper mantle pressures [Stolper *et al.*, 1981; Ohtani, 1983, 1984]. Olivine and clinopyroxene are neutrally buoyant between 7 and 9 GPa, depending on the specific liquid composition. Garnet-majorite may be buoyant in ultrabasic compositions in the 20-24 GPa interval. Extrapolating our data to 70 GPa, we determine that perovskite could be buoyant in ultrabasic liquids in the lower mantle. Under upper mantle conditions, increasing the normative olivine content of a liquid increases its density. We predict that at higher pressure, olivine addition would diminish the liquid density.

We have applied our komatiite EOS data to the problem of adiabatic melting. We have constructed a simplified model that allows the minimum depth and temperature of a mantle diapir to be constrained given its final melt fraction. This model indicates that an initially unmelted source region for komatiitic lavas would be in the transition zone or the lower mantle if >15% melting is required. Phase diagrams for komatiitic compositions and fertile peridotites are consistent with this interpretation. If this is so, then komatiites may be formed in much the same way as modern basalts and picrites, the difference being that komatiites require substantially hotter (>700°C) diapiric sources.

We have discussed the early stages of the evolution of a magma ocean. Despite the simplicity of our calculations, several conclusions can be drawn: (1) If the mantle were adiabatic, the wholly molten mantle would crystallize from the bottom up. When crystallization begins in the upper mantle, most of the transition zone and lower mantle would still be partially molten. (2) A crust at the

surface of the magma ocean would not have been stable while the crystallization front traversed the lower mantle. The surface temperature of the magma ocean would have been between 1900° and 3200°C, favoring the existence of a metal-oxide atmosphere. (3) Although perovskite would tend to float at depths of ≥1680 km, and sink at shallower depths, convective velocities in a magma ocean this deep would be so high as to prevent crystal-liquid segregation. However, as the system cools, the degree of crystallinity at depth along an adiabat becomes high enough (≥44%) that the less crystalline part of the system above this level and the more crystalline part below begin to convect separately. Matrix compaction in the lower level could lead to expulsion of liquid downward at depths >1680 km, and upwards at depths <1680 km. Diapirism could facilitate this fractionation process. This could lead to effective fractionation of perovskite components in the liquid of the upper mantle. (4) When majorite first begins to crystallize, it would probably tend to float, and the floor of the magma ocean would be deeper than the maximum depth of majorite stability. Majorite would therefore be initially prohibited from fractionating. The later formation of a dunite cumulate layer might limit, but not completely exclude, majorite fractionation effects in the upper mantle. (5) A dunite cumulate layer might form in the upper mantle, either by the settling and/or rising of individual crystals or by the accumulation of crystals around foundered crust. Such a septum would necessarily be permeable; thus, although it could limit subsequent majorite fractionation effects in the region above it, it would not prohibit them altogether in the upper mantle. (6) The formation and evolution of a molten mantle is highly dependent on the accretion scenario, and cannot be modeled on the basis of EOS and phase equilibrium constraints alone. Issues that are difficult to address include (a) the time scale of Earth accretion, (b) the rheological and physical processes that occur in turbulent convection in a deep system without walls, (c) rates of heat transfer through different protoatmospheres that form in response to different rates of planetesimal accretion, (d) the dynamics of crust formation and recycling on a magma ocean, and (e) the dynamics of subsolidus

convection to the extent this governs rehomogenization of the Earth. Future work should address the specific flow structure of the magma ocean, and the specific nature of the coexisting atmosphere.

We are grateful for the komatiite starting materials generously provided by Dr G. Fine at Corning Glass Works, Corning, NY. M. Long and E. Gelle provided invaluable expert assistance in the preparation and execution of the shock experiments. Andrew Campbell (now at University of Chicago) polished and measured the densities of many of the Mo sample containers. We appreciate the use of the 10 kW rf heater provided by L.T. Silver. We are grateful to D.J. Stevenson, D.L. Anderson, and N.T. Arndt (Max-Planck-Institut für Chemie, Mainz) for their thoughtful comments and suggestions. We also thank K. Wei and R.G. Tronnes (University of Alberta) for sharing his unpublished manuscript with us. This work was funded by the National Science Foundation grants EAR-86-18545 and EAR-89-16753. Contribution number 4809, Division of Geological and Planetary Sciences, California Institute of Technology, Pasadena, CA.

References

Abe, Y., and T. Matsui, Early evolution of the Earth: Accretion, atmosphere formation, and thermal history, *J. Geophys. Res., 91*, E291-E302, 1986.

Agee, C.B., and D. Walker, Olivine flotation in a chondritic mantle, *Meteoritics, 22*, 314, 1987.

Agee, C.B., and D. Walker, Static compression and olivine flotation in ultrabasic silicate liquid, *J. Geophys. Res., 93*, 3437-3449, 1988a.

Agee, C.B., and D. Walker, Mass balance and phase density constraints on early differentiation of chondritic mantle, *Earth Planet. Sci. Lett., 90*, 144-156, 1988b.

Agee, C.B., and D. Walker, Comments on "Constraints on element partition coefficients between $MgSiO_3$ perovskite and liquid determined by direct measurements" by T. Kato, A.E. Ringwood, and T. Irifune, *Earth Planet. Sci. Lett., 94*, 160-161, 1989.

Ahrens, T.J., J.H. Lower, and P.L. Lagus, Equation of state of forsterite, *J. Geophys. Res., 76*, 514-528, 1971.

Ahrens, T.J., Earth accretion, in *Origin of the Earth*, edited by J.H. Jones and H.E. Newson, Oxford University Press, New York, 1990 (in press).

Anderson, D.L., Chemical inhomogeneity of mantle above 670 km transition, *Nature, 307*, 114, 1984.

Anderson, D.L., Composition of the Earth, *Science, 243*, 367-370, 1989.

Anderson, O.L., R.C. Schreiber, R.C. Liebermann, and N. Soga, Some elastic constant data on minerals relevant to geophysics, *Rev. Geophys., 6*, 491-524, 1968.

Arndt, N.T., Ultrabasic magmas and high-degree melting of the mantle, *Contrib. Mineral. Petrol., 64*, 205-221, 1977.

Bassett, W.A., T. Takahashi, H.-K. Mao, and J.S. Weaver, Pressure-induced phase transformation in NaCl, *J. Appl. Phys., 39*, 319-325, 1968.

Benz, W., W.L. Slattery, and A.G.W. Cameron, The origin of the moon and the single-impact hypothesis I, *Icarus, 66*, 515-535, 1986.

Benz, W., W.L. Slattery, and A.G.W. Cameron, The origin of the moon and the single-impact hypothesis, II, *Icarus, 71*, 30-45, 1987.

Bethe, H.A., The theory of shock waves for an arbitrary equation of state, *OSRD 545*, pp. 84, 1942.

Bevington, P.R., *Data Reduction and Error Analysis for the Physical Sciences*, pp. 92-118, McGraw-Hill, New York, 1969.

Bickle, M.J., C.E. Ford, and E.G. Nisbet, The petrogenesis of peridotitic komatiites: Evidence from high-pressure melting experiments, *Earth Planet. Sci. Lett., 37*, 97-106, 1977.

Birch, F., Energetics of core formation, *J. Geophys. Res., 70*, 6217-6221, 1965.

Bird, R.B., W.E. Stewart, and E.N. Lightfoot, *Transport Phenomena*, pp. 190-196, Wiley, New York, 1960.

Bland, D.R., On shock structure in a solid, *J. Inst. Math Appl., 1*, 56-75, 1965.

Bottinga, Y., and D.F. Weill, The viscosity of magmatic silicate liquids: A model for calculation. *Am. J. Sci., 272*, 438-475, 1972.

Cameron, A.G.W, and W. Benz, Possible scenarios resulting from the giant impact, abstract, *Lunar Planet. Sci. Conf. 20*, 137-138, 1989.

Carmichael, I.S.E, F.J. Turner, and J. Verhoogen, *Igneous Petrology*, pp. 739, McGraw-Hill, New York, 1974.

Cawthorn, R.G., Degrees of melting in mantle diapirs and the origin of ultrabasic liquids, *Earth Planet. Sci. Lett., 27*, 113-120, 1975.

Clayton, D.D., *Principles of Stellar Evolution and Nucleosynthesis*, pp. 612, McGraw-Hill, New York, 1968.

Dingwell, D.B., and S.L. Webb, Structural relaxation in silicate melts and non-Newtonian melt rheology in geologic processes, *Phys. Chem. Minerals, 16*, 508-516, 1989.

Donaldson, C.H., An experimental investigation of olivine morphology, *Contrib. Mineral. Petrol., 57*, 187-213, 1976.

Dziewonski, A.M., and D.L. Anderson, Preliminary reference Earth model, *Phys. Earth Planet. Iner., 25*, 297-356, 1981.

Echeverria, L.M., Komatiites from Gorgona Island, Colombia, in *Komatiites*, edited by N.T. Arndt and E.G. Nisbet, pp. 199-209, Allen and Unwin, Winchester, 1982.

Elthon, D., and C.M. Scarfe, High-pressure phase equilibria of a high-magnesia basalt and the genesis of primary oceanic basalts, *Am. Mineral., 69*, 1-15, 1984.

Frisillo, A.L., and G.R. Barsch, Measurement of single-crystal elastic constants of bronzite as a function of pressure and temperature, *J. Geophys. Res., 77*, 6360-6384, 1972.

Gansser, A., V.J. Dietrich, and W.E. Cameron, Paleogene komatiites from Gorgona Island, *Nature*,

278, 545-546, 1979.

Green, D.H., and A.E. Ringwood, The genesis of basaltic magmas, *Contrib. Mineral. Petrol., 15*, 103-190, 1967.

Green, D.H., Genesis of Archean peridotitic magmas and constraints on Archean geothermal gradients and tectonics, *Geology, 3*, 15-18, 1975.

Green, D.H., W.O. Hibberson, and A.L. Jaques, Petrogenesis of mid-ocean basalts, in *The Earth: Its Origin, Structure, and Evolution*, edited by M.W. McElhinney, pp. 265-299, Academic Press, London, 1979.

Halleck, P.M., The compression and compressibility of grossular garnet: A comparison of X-ray and ultrasonic methods, Ph.D. thesis, pp. 82, University of Chicago, Ill., 1973.

Harris, P., and H.N. Presles, Reflectivity of a 5.8 kbar shock front in water, *J. Chem. Phys., 74*, 6864-6866, 1981.

Heinz, D.L., and R. Jeanloz, Measurement of the melting curve of $Mg_{0.9}Fe_{0.1}SiO_3$ perovskite at lower mantle conditions and its geophysical implications, *J. Geophys. Res., 92*, 11437-11444, 1987.

Herzberg, C.T., Solidus and liquidus temperatures and mineralogies for anhydrous garnet-lherzolite to 15 GPa, *Phys. Earth Planet. Inter., 32*, 193-202, 1983.

Herzberg, C.T., and M.J. O'Hara, Origin of mantle peridotite and komatiite by partial melting, *Geophys. Res. Lett., 12*, 541-544, 1985.

Herzberg, C.T., Magma density at high pressure Part 1: The effect of composition on the elastic properties of silicate liquids, in*Magmatic Processes: Physiochemical Principles*, edited by B.O. Mysen, pp. 25-46, Geochemical Society, Washington, 1987.

Herzberg, C.T., M. Feigenson, C. Skuba, and E. Ohtani, Majorite fractionation recorded in the geochemistry of peridotites from South Africa, *Nature, 332*, 823-826, 1988.

Holloway, J.R., Planetary atmospheres during accretion: The effect of C-O-H-S equilibria, abstract, *Lunar Planet. Sci. Conf, 19*, 449-500, 1988.

Houghton, J.T., *The Physics of Atmospheres*, Cambridge Univ. Press, Cambridge, 1977.

Irifune, T., An experimental investigation of the pyroxene-garnet transformation in a pyrolite composition and its bearing on the constitution of the mantle, *Phys. Earth Planet. Inter., 45*, 324-336, 1987.

Isaak, D.G, and E.K. Graham, The elastic properties of an almandine-spessartine garnet and elasticity in the garnet solid solution series, *J. Geophys. Res., 81*, 2483-2489, 1976.

Ito, E., and E. Takahashi, Melting of peridotite at uppermost lower-mantle conditions, *Nature, 328*, 514-517, 1987.

Jahn, B.M., G. Gruau, and A.Y. Glikson, Komatiite of the Onverwacht Group, S. Africa: REE geochemistry, Sm/Nd age and mantle evolution, *Contrib. Mineral. Petrol., 80*, 25-40, 1982.

Jarvis, G.T., and I.H. Campbell, Archean komatiites and geotherms: Solution to an apparent contradiction, *Geophys. Res. Lett., 10*, 1133-1136, 1983.

Jeanloz, R., and T.J. Ahrens, Release adiabat measurements on minerals: The effect of viscosity, *J. Geophys. Res., 84*, 7545-7548, 1979.

Jeanloz, R., and F.M. Richter, Convection, composition, and the thermal state of the lower mantle, *J. Geophys. Res., 84*, 5497-5504, 1979.

Jeanloz, R., and T.J. Ahrens, Equations of state of FeO and CaO, *Geophys. J. Roy. Astr. Soc., 62*, 505-528, 1980.

Jeanloz, R., Majorite: Vibrational and compressional properties of a high-pressure phase, *J. Geophys. Res., 86*, 6171-6179, 1981.

Jeanloz, R., and A.B. Thompson, Phase transitions and mantle discontinuities, *Rev. Geophys. Space Phys., 21*, 51-74, 1983.

Jeanloz, R., Thermodynamics of phase transitions, in *Reviews in Mineralogy, 14*, 389-429, edited by S.W. Kieffer and A. Navrotsky, MSA, Washington, D.C., 1985.

Jeanloz, R., and Y. Sato-Sorensen, Hydrostatic compression of $Fe_{1-x}O$ wüstite, *J. Geophys. Res., 91*, 4665-4672, 1986.

Jeanloz, R., and R. Grover, Birch-Murnaghan and U_s–U_p equations of state, in *Proceedings of the American Physical Society Topical Conference on Shock Waves in Condensed Matter, Monterey, CA, 1987*, edited by S.C. Schmidt and N.C. Holmes, pp. 69-72, Plenum, New York, 1988.

Jeanloz, R., Shock wave equation of state and finite strain theory, *J. Geophys. Res., 94*, 5873-5886, 1989.

Jeanloz, R., and E. Knittle, Density and composition of the lower mantle, *Phil. Trans. R. Soc. Lond. A, 328*, 377-389, 1989.

Kato, T., A.E. Ringwood, and T. Irifune, Experimental determination of element partitioning between silicate perovskites, garnets and liquids: Constraints on early differentiation of the mantle, *Earth Planet. Sci. Lett., 89*, 123-145, 1988a.

Kato, T., A.E. Ringwood, and T. Irifune, Constraints on element partition coefficients between $MgSiO_3$ perovskite and liquid determined by direct measurements, *Earth Planet. Sci. Lett.,*

90, 65-68, 1988b.

Kaula, W.M., Thermal evolution of Earth and moon growing by planetesimal impacts, *J. Geophys. Res.*, *84*, 999-1008, 1979.

Knittle, E., and R. Jeanloz, Melting curve of $(Mg,Fe)SiO_3$ perovskite to 96 GPa: Evidence for a structural transition in lower mantle melts, *Geophys. Res. Lett.*, *16*, 421-424, 1989.

Kress, V.C., Q. Williams, and I.S.E. Carmichael, When is a silicate melt not a liquid?, *Geochim. Cosmochim. Acta*, *53*, 1687-1692, 1989.

Kumazawa, M., and O.L. Anderson, Elastic moduli, pressure derivatives, and temperature derivatives of single-crystal olivine and single-crystal forsterite, *J. Geophys. Res.*, *74*, 5961-5972, 1969.

Lange, R.A., and I.S.E. Carmichael, Densities of Na_2O-K_2O-CaO-MgO-FeO-Fe_2O_3-Al_2O_3-TiO_2-SiO_2 liquids: New measurements and derived partial molar properties, *Geochim. Cosmochim. Acta*, *51*, 2931-2946, 1987.

Lees, A.C., M.S.T. Bukowinski, and R. Jeanloz, Reflection properties of phase transition and compositional change models of the 670-km discontinuity, *J. Geophys. Res.*, *88*, 8145-8159, 1983.

Leitner, B.J., D.J. Weidner, and R.C. Liebermann, Elasticity of single crystal pyrope and implications for garnet solid solution series, *Phys. Earth Planet. Inter.*, *22*, 111-121, 1980.

Levien, L., D.J. Weidner, and C.T. Prewitt, Elasticity of diopside, *Phys. Chem. Minerals*, *4*, 105-113, 1979a.

Levien, L., C.T. Prewitt, and D.J. Weidner, Compression of pyrope, *Am. Mineral.*, *64*, 805-808, 1979b.

Lyzenga, G.A., T.J. Ahrens, and A.C. Mitchell, Shock temperatures of SiO_2 and their geophysical implications, *J. Geophys. Res.*, *88*, 2431-2444, 1982.

Manghnani, M.H., R.A. Secco, P. Tao, and T.-C. Liu, Bulk modulus and attenuation in komatiite melts (abstract), *EOS Trans. AGU*, *70*, 1369, 1989.

Marsh, B.D., On convective style and vigor in sheet-like magma chambers, *J. Petrol.*, *30*, 479-530, 1989.

Marsh, S.P., *LASL Shock Hugoniot Data*, pp. 658, University of California Press, Berkeley, 1980.

Martin, D., and R. Nokes, Crystal settling in a vigorously convecting magma chamber, *Nature*, *332*, 534-536, 1988.

Matsui, T., and Y. Abe, Formation of a "magma ocean" on the terrestrial planets due to the blanketing effect of an impact-induced atmosphere, *Earth Moon Planets*, *34*, 223-230, 1986.

McKenzie, D., The generation and compaction of partially molten rock, *J. Petrol., 25*, 713-765, 1984.

McKenzie, D., and M.J. Bickle, The volume and composition of melt generated by extension of the lithosphere, *J. Petrol., 29*, 625-679, 1988.

McQueen, R.G., S.P. Marsh, J.W. Taylor, J.N. Fritz, and W.J. Carter, The equation of state of solids from shock wave studies, in *High-Velocity Impact Phenomena*, edited by R. Kinslow, pp. 294-417, Academic Press, New York, 1970.

Mercier, J.-C., and N.L. Carter, Pyroxene geotherms, *J. Geophys. Res., 80*, 3349-3362, 1975.

Miller, G.H., T.J. Ahrens, and E.M. Stolper, The equation of state of molybdenum at 1400°C, *J. Appl. Phys., 63*, 4469-4475, 1988.

McMillan, P., A Raman spectroscopic study of glasses in the system CaO-MgO-SiO_2, *Am. Mineral., 69*, 645-659, 1984.

Morse, S.A., Origin of earliest planetary crust: role of compositional convection, *Earth Planet. Sci. Lett., 81*, 118-126, 1987.

Nesbitt, R.W., S. Sun, and A.C. Purvis, Komatiites: Geochemistry and genesis, *Canadian Mineral., 17*, 165-186, 1979.

Nisbet, E.G., The tectonic setting and petrogenesis of komatiites, in *Komatiites*, edited by N.T. Arndt and E.G. Nisbet, pp. 501-522, George Allen & Unwin, Boston, 1982.

Nisbet, E.G., and D. Walker, Komatiites and the structure of the Archaean mantle, *Earth Plant. Sci. Lett., 60*, 105-113, 1982.

O'Hara, M.J., M.J. Saunders, and E.P.L. Mercy, Garnet-peridotite, primary basaltic magma and eclogites; interpretation of upper mantle processes in kimberlite, *Phys. Chem. Earth, 9*, 571-604, 1975.

Ohashi, Y., and L.W. Finger, The effects of Ca substitution on the structure of clino-enstatite, *Carnegie Inst. Wash. Year Book, 75*, 743-746, 1976.

Ohtani, E., Melting temperature distribution and fractionation in the lower mantle, *Phys. Earth Planet. Inter., 33*, 12-25, 1983.

Ohtani, E., Generation of komatiite magma and gravitational differentiation in the deep upper mantle, *Earth Planet. Sci. Lett., 67*, 261-272, 1984.

Ohtani, E., The primordial terrestrial magma ocean and its implications for stratification of the mantle, *Phys. Earth Planet. Inter., 38*, 70-80, 1985.

Ohtani, E., T. Kato, and H. Sawamoto, Melting of a model chondritic mantle to 20 GPa, *Nature*,

322, 352-353, 1986.

Ohtani, E., and H. Sawamoto, Melting experiment on a model chondritic mantle composition at 25 GPa, *Geophys. Res. Lett.*, *14*, 733-736, 1987.

Presnall, D.C., J.R. Dixon, T.H. O'Donnell, and S.A. Dixon, Generation of mid-ocean ridge tholeiites, *J. Petrol.*, *20*, 3-35, 1979.

Press, W.H., B.P. Flannery, S.A. Teukolsky, and W.T. Vetterling, *Numerical Recipes in C*, pp. 735, Cambridge University Press, New York, 1988.

Ramberg, H., Temperature changes associated with adiabatic decompression in geological processes, *Nature*, *234*, 539-540, 1971.

Richter, F.M., and D. McKenzie, Dynamical models for melt segregation from a deformable matrix, *J. Geol.*, *92*, 729-740, 1984.

Rigden, S.M., T.J. Ahrens, and E.M. Stolper, Densities of liquid silicates at high pressures, *Science*, *226*, 1071-1074, 1984.

Rigden, S.M., T.J. Ahrens, and E.M. Stolper, Shock compression of molten silicate: Results for a model basaltic composition, *J. Geophys. Res.*, *93*, 367-382, 1988.

Rigden, S.M., T.J. Ahrens, and E.M. Stolper, High-pressure equation of state of molten anorthite and diopside, *J. Geophys. Res.*, *94*, 9508-9522, 1989.

Ringwood, A.E., Origin of the Earth and Moon, pp. 295, Springer-Verlag, New York, 1979.

Ringwood, A.E., T. Kato, and T. Irifune, Minor element partition relationships among high pressure minerals and implications for gross mantle differentiation (abstract), *EOS Trans. AGU*, *68*, 1548, 1987.

Rivers, M.L., and I.S.E. Carmichael, Ultrasonic studies of silicate melts, *J. Geophys. Res.*, *92*, 9247-9270, 1987.

Rivers, M.L., Ultrasonic studies of silicate liquids. Ph.D. Dissertation, University of California, Berkeley, 1985.

Robie, R.A., B.S. Hemmingway, and J.R. Fisher, Thermodynamic properties of minerals and related substances at 298.15 K and 1 bar (10^5 pascals) pressure and at higher temperatures, *U.S. Geol. Survey Bull.*, *142*, 1978.

Roscoe, R., Suspensions, in *Flow properties of disperse systems*, edited by J.J. Hermans, pp. 1-38, North Holland, Amsterdam, 1953.

Rumble, D., The adiabatic gradient and adiabatic compressibility, *Carnegie Inst. Wash. Yearb.*, *75*, 651-655, 1976.

Ruoff, A.L., Linear shock-velocity-particle-velocity relationship, *J. Appl. Phys., 38*, 4976-4980, 1967.

Scarfe, C.M., and E. Takahashi, Melting of garnet peridotite to 13 GPa and the early history of the upper mantle, *Nature, 322*, 354-356, 1986.

Scott, D.R., and D.J. Stevenson, Magma solitons, *Geophys. Res. Lett., 11*, 1161-1164, 1984.

Scott, D.R., and D.J. Stevenson, Magma ascent by porous flow, *J. Geophys. Res., 91*, 9283-9296, 1986.

Scott, D.R., and D.J. Stevenson, The competition between percolation and circulation in a deformable porous medium, *J. Geophys. Res., 93*, 6451-6462, 1988.

Shaner, J.W., New ways of looking for phase transitions at multi-megabar dynamic pressures, in *Physics of Solids Under High Pressure*, edited by J.S. Shilling and R.N. Shelton, pp. 99-108, North-Holland, Amsterdam, 1981.

Shaw, G.H., Core formation in terrestrial planets, *Phys. Earth Planet. Inter., 20*, 42-47, 1979.

Solomon, S.C., Formation, history and energetics of cores in the terrestrial planets, *Phys. Earth Planet. Inter., 15*, 135-145, 1978.

Sparks, R.S.J., P. Meyer, and H. Sigurdsson, Density variation amongst mid-ocean ridge basalts: Implications for magma mixing and the scarcity of primitive lavas, *Earth Planet. Sci. Lett., 46*, 419-430, 1980.

Stacey, F.D., Thermal regime of the Earth's interior, *Nature, 255*, 44-45, 1975.

Stebbins, J.F., I.S.E. Carmichael, and L.K. Moret, Heat capacities and entropies of silicate liquids and glasses, *Contrib. Mineral. Petrol., 86*, 131-148, 1984.

Stevenson, D.J., Formation and early evolution of the Earth, in *Mantle Convection*, edited by W.R. Peltier, pp. 873-873, Gordon and Breach, New York, 1989.

Stishov, S.M., Melting at high pressures, *Sov. Phys. Uspekhi, 11*, 816-830, 1969.

Stishov, S.M., Entropy, disorder, melting, *Sov. Phys. Uspekhi, 31*, 52-67, 1988.

Stolper, E.M., and D. Walker, Melt density and the average composition of basalt, *Contrib. Mineral. Petrol., 74*, 7-12, 1980.

Stolper, E.M., D. Walker, B.H. Hager, and J.F. Hayes, Melt segregation from partially molten source regions: The importance of melt density and source region size, *J. Geophys. Res., 86*, 6261-6271, 1981.

Straumanis, M.E., and R.P. Shodhan, Lattice constants, thermal expansion coefficients, and densities

of molybdenum and the solubility of sulphur, selenium, and tellurium in it at 1100°C, *Z. Metallkde., 59*, 492-495, 1968.

Suito, K., Phase transformations of pure Mg_2SiO_4 into a spinel structure under high pressures and temperatures, *J. Phys. Earth, 20*, 225-243, 1972.

Suito, K., Phase relations of pure Mg_2SiO_4 up to 220 kbar, in *High pressure research: Application in geophysics*, edited by M. Manghnani and S. Akimoto, pp. 255-266, Academic Press, New York, 1977.

Swan, G.W., G.E. Duvall, and C.K. Thornhill, On steady wave profiles in solids, *J. Mech. Phys. Solids, 21*, 215-227, 1973.

Swegle, J.W., and D.E. Grady, Shock viscosity and the prediction of shock wave rise times, *J. Appl. Phys., 58*, 692-701, 1985.

Takahashi, E., and I. Kushiro, Melting of a dry peridotite at high pressures and basalt magma genesis, *Am. Mineral., 68*, 859-879, 1983.

Takahashi, E., and C.M. Scarfe, Melting of peridotite to 14 GPa and the genesis of komatiite, *Nature, 315*, 566-568, 1985.

Takahashi, E., Melting of a dry peridotite KLB-1 up to 14 GPa: Implications on the origin of peridotitic upper mantle, *J. Geophys. Res., 91*, 9367-9382, 1986.

Thompson, C., and D.J. Stevenson, Gravitational instability in two-phase disks and the origin of the moon, *Astrophys. J., 333*, 452-481, 1988.

Touloukian, Y.S., R.K. Kirby, R.E. Taylor, and P.D. Desai, *Thermal expansion of metallic elements and alloys*, pp. 208-218, Plenum, New York, 1970.

Verhoogen, J., Petrological evidence on temperature distribution in the mantle of the Earth, *Trans. Amer. Geophys. U., 35*, 85-92, 1954.

Waldbaum, D.R., Temperature changes associated with adiabatic decompression in geological processes, *Nature, 232*, 545-547, 1971.

Walker, D., R.J. Kirkpatrick, and J.F. Hays, Differentiation of komatiitic lava (abstract), *EOS Trans. AGU, 58*, 527, 1977.

Walker, D., and W.S. Kiefer, Xenolith digestion in large magma bodies, *J. Geophys. Res., 90*, C585-C590, 1985.

Walker, D., C.B. Agee, and Y. Zhang, Fusion curve slope and crystal/liquid buoyancy, *J. Geophys. Res., 93*, 313-323 and 6668, 1988.

Walsh, J.M., and R.H. Christian, Equation of state of metals from shock wave measurements, *Phys.*

Rev., *97*, 1544-1556, 1955.

Watanabe, H. Thermochemical properties of synthetic high-pressure compounds relevant to the Earth's mantle, in *High-Pressure Research in Geophysics*, edited by S. Akimoto and M.H. Manghnani, pp. 441, Center for Academic Publishing, Tokyo, 1982.

Wei, K., R.G. Tronnes, and C.M. Scarfe, Phase relations of aluminum undepleted and aluminum depleted komatiites at 4 to 12 GPa, *J. Geophys. Res.*, in press, 1990.

Weidner, D.J., H. Wang, and J. Ito, Elasticity of orthoenstatite, *Phys. Earth Planet. Inter.*, *17*, P7-P13, 1978.

Weidner, D.J., J.D. Bass, A.E. Ringwood, and W. Sinclair, The single-crystal elastic moduli of stishovite, *J. Geophys. Res.*, *87*, 4740-4746, 1982.

Williams, Q., P. McMillan, and T.F. Cooney, Vibrational spectra of olivine composition glasses: the Mg-Mn join, *Phys. Chem. Minerals*, *16*, 352-359, 1989.

Yagi, T., M. Akaogi, O. Shimomura, H. Tamai, and S. Akimoto, High pressure and high temperature equations of state of majorite, in *High-Pressure Research in Mineral Physics*, edited by M. Manghnani and Y. Syono, pp. 141-147, Terra Scientific Publishing Co., Tokyo, 1987.

Zahnle, K.J., J.F. Kasting, and J.B. Pollack, Evolution of a steam atmosphere during Earth's accretion, *Icarus*, *74*, 62-97, 1988.

Chapter 2: Shock Wave Viscosity Measurement

We have examined in detail the analytical method for measuring shear viscosity from the decay of perturbations on a corrugated shock front. The relevance of initial conditions, finite shock amplitude, bulk viscosity, and the sensitivity of the measurements to the shock boundary conditions are discussed. The validity of the viscous perturbation approach is examined by numerically solving the second-order Navier-Stokes equations. These numerical experiments indicate that shock instabilities may occur even when the Kontorovich-D'yakov stability criteria are satisfied. The experimental results for water at 15 GPa are discussed, and it is suggested that the large effective viscosity determined by this method may reflect the existence of ice VII on the Rayleigh path of the Hugoniot. This interpretation reconciles the experimental results with estimates and measurements obtained by other means, and is consistent with the relationship of the Hugoniot with the phase diagram for water. Sound waves are generated at 4.8 MHz in the water experiments at 15 GPa. The existence of anelastic absorption modes near this frequency would also lead to large effective viscosity estimates.

1. Introduction

The viscosity of high-pressure fluids is one of the fundamental parameters that controls rates of chemical fractionation and heat transport in the Earth. Viscosity can also be used as an indirect probe of the structural configuration of multicomponent liquids [*e.g.*, Kushiro, 1977]. Order of magnitude viscosity changes with temperature [Bottinga and Weill, 1972] and pressure [*e.g.*, Kushiro, 1986] have been detected in silicate liquids. This sensitivity of viscosity to both pressure and temperature demonstrates that extrapolation of low pressure and/or low temperature measurements to high-pressure high-temperature conditions of geophysical interest is subject to very large uncertainties. This is particularly true in silicate systems where liquid state structural changes have been

inferred [*e.g.*, Rigden *et al.*, 1988; Knittle and Jeanloz, 1989]. The systematics of liquid silicate viscosity with pressure are believed to be complex. Molecular dynamics studies on liquid silicates [Woodcock *et al.*, 1976; Angell *et al.*, 1982] predict that viscosity will diminish with increasing pressure to a minimum value in the neighborhood of 25 GPa, and increase thereafter. Static-pressure viscosity measurements to 3 GPa [*e.g.*, Kushiro, 1980] confirm this trend, although the predicted minimum remains experimentally unaccessible by this method.

A variety of methods have been employed to experimentally determine the viscosity of liquids at high pressure. Under static high-pressure conditions, the Stokes drag on falling spheres [Kushiro, 1976, 1977, 1978a,b,c, 1980, 1986; Kushiro *et al.*, 1976; Fujii and Kushiro, 1977a,b; Scarfe *et al.*, 1979; Kanzaki *et al.*, 1987] has been measured to simultaneously determine the density and viscosity of liquids to pressures of 3 GPa. Dynamic high-pressure experiments (shock wave) can be used to access a greater range of pressures and temperatures. These shock wave methods fall into three general categories.

First, the rise time or width of the shock front can be related to some effective viscosity averaged over the range of pressures, temperatures, and compression experienced by the sample in this shock front region [*e.g.*, Bland, 1965]. The rise of the shock front can be experimentally determined with high precision using velocity interferometry techniques, and has been related to viscosity by Swegle and Grady [1985]. Because this method determines the viscosity over the very broad range of conditions experienced in the shock front, and because the strain rates in this region are exceedingly large, this method may be inappropriate for determining the low frequency, *i.e.* relaxed, viscosity of the high-pressure state.

Second, indirect indicators of viscosity have been used to estimate the viscosity of materials at high pressure. These indirect indicators include fluorescence lifetimes in glycerine [Huston *et al.*,

1985], electrical conductivity measurements of weak electrolyte solutions [Hamann and Linton, 1969], and the diffusion-controlled precipitation of sulfur in thiosulphate solutions [Yakusheva *et al.*, 1972]. The fluorescence method is based on the observation that the fluorescence lifetime of the crystal-violet (CV) dye molecule is correlated to the 2/3 power of the viscosity of the glycerine solvent [Förster and Hoffmann, 1971], whether viscosity is varied by changing pressure or temperature [Brey *et al.*, 1977]. This special feature of the CV-glycerine system is critical to the success of this method since pressure and temperature vary simultaneously under shock compression. The conductivity method is based on the theoretical argument, Walden's rule [Walden, 1906], that the product of ionic conductivity and viscosity is a constant for a given system. These methods can, in principle, sample the low frequency viscosity, but they rely critically on the validity of the calibrations that link the measured properties to viscosity. For well-studied systems, where viscosity and conductivity or fluorescence kinetics have been independently measured as functions of pressure and temperature, these indirect indicators can be applied in shock wave experiments. Such methods are inherently suspect outside the pressure/temperature range of static experiments where the validity of the calibrations cannot be assured.

Third, direct measurements of high pressure viscosity are possible by observing induced flows in high pressure materials. These experiments include the measurement of the oscillatory damping of a sinusoidal shock front [Sakharov *et al.*, 1965; Mineev and Savinov, 1967, 1976; Mineev and Zaidel', 1968], and measurement of the viscous drag on an embedded cylinder [Al'tshuler *et al.*, 1977, 1986; Kim, 1984]. These methods require no calibration since they are based on fluid mechanics of viscous flow. In the viscous drag experiment a metal cylinder is embedded in a non-conductive sample, oriented parallel to the plane of the shock. When the sample is shocked the cylinder is accelerated. The initial acceleration is complicated by shock wave interactions, but after a short time the acceleration is controlled by the viscous drag of the sample flowing past the

cylinder. The velocity of the cylinder, measured by detecting electrical current induced by the motion of the metal cylinder in a magnetic field, is recorded as a function of time. This velocity history is analyzed with a simple viscous flow model to give the sample's shear viscosity. Because velocity is detected by measuring electrical currents this technique requires a nonconductive sample. The oscillatory damping experiment works equally well with conductive and nonconductive samples, and is therefore applicable to a greater variety of materials. The oscillatory damping experiment is the subject of this study.

The oscillatory damping experiment is elegant in its simplicity. Figure 1 illustrates the experimental apparatus of Sakharov *et al.* [1965]. An explosive block is used to drive a shock into a disc of sample material in which a series of sinusoidal grooves are cut. When the shock intersects these grooves a sinusoidal perturbation is created on the shock front. This perturbed shock then propagates into a wedge of sample material. The curvature of the shock front generates velocity perturbations in the compressed sample. These velocity perturbations, modified by the sample viscosity, are coupled with the wave front. The shock front fluctuations are therefore direct indicators of the shocked fluid viscosity. The wedge shape of the sample allows the amplitude of the shock front perturbations to be examined as a function of time. The shock profile is detected by recording gas flashes induced by the shock arrival between the top surface of the wedge and the overlying plastic buffer.

In contrast to the simplicity of this experimental design, the analysis of these experiments is very complex, as is evident in the work of Zaidel' [1967]. In the particular case of shocked water, this method gives consistently high values of viscosity relative to other methods (Fig. 2): by a factor of 10^6 relative to the conductivity method, and by a factor of 10^3 relative to the viscous drag method [Al'tshuler *et al.*, 1986]. The former discrepancy may be attributed to the failure of Walden's rule at high pressure [Al'tshuler *et al.*, 1986], but the disagreement with the viscous drag

Figure 1: Schematic of experimental design. An explosive block (a) generates a shock that first enters a sinusoidally grooved sample disc (b). The sinusoidal grooves generate perturbations in the shock front that then propagate into the sample wedge (c). The profile of the shock front is detected as a function of time by the light emitted in the flash gap (d) by the arrival of the shock at the free surface of the wedge. The emitted light is shuttered by the shock induced opacity of a plastic sheet (e), and a mask (f).

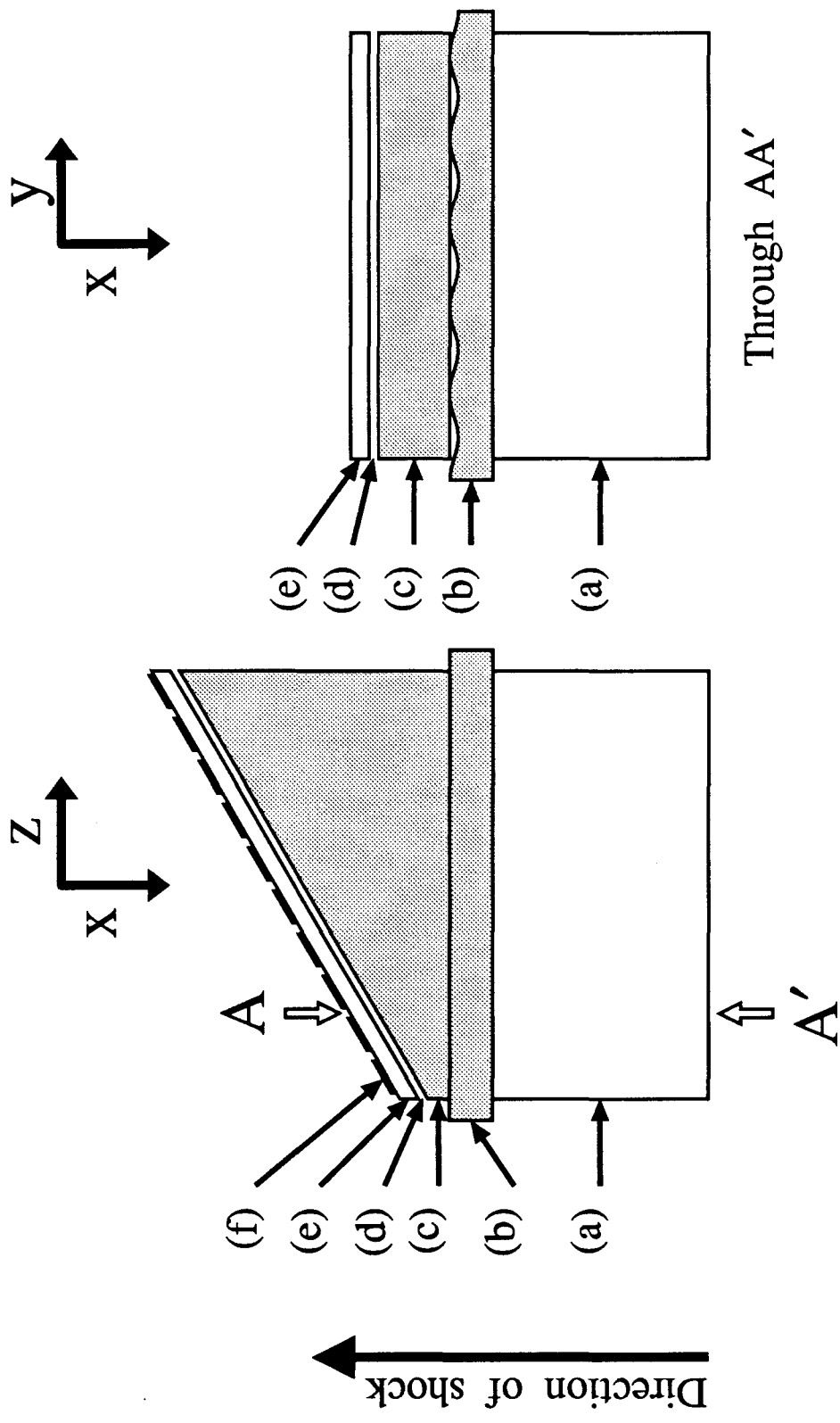

Figure 1.

Figure 2: Summary of shock wave viscosity measurements on water. Data from: Mineev and Zaidel' [1968], (open circles); Mineev and Savinov [1976], (closed circle); Al'tshuler *et al.* [1977], (open squares); Kim [1984], (closed squares); Al'tshuler *et al.* [1986], (open diamonds); and shock thickness measurement of Harris and Presles [1981] (open triangle). Crossed circles indicate our new interpretations of the Mineev and Zaidel' [1968] 15 GPa experiment. (A) corresponds to linearized and second-order calculations without initial conditions or finite amplitude effects. (B) corresponds to calculations with initial condition and finite amplitude effects. The viscosity calculated by Mineev and Zaidel' at 15 GPa lies within the symbol for case B. In all cases it was assumed that $\kappa = \eta$. Symbols with arrows denote upper bounds.

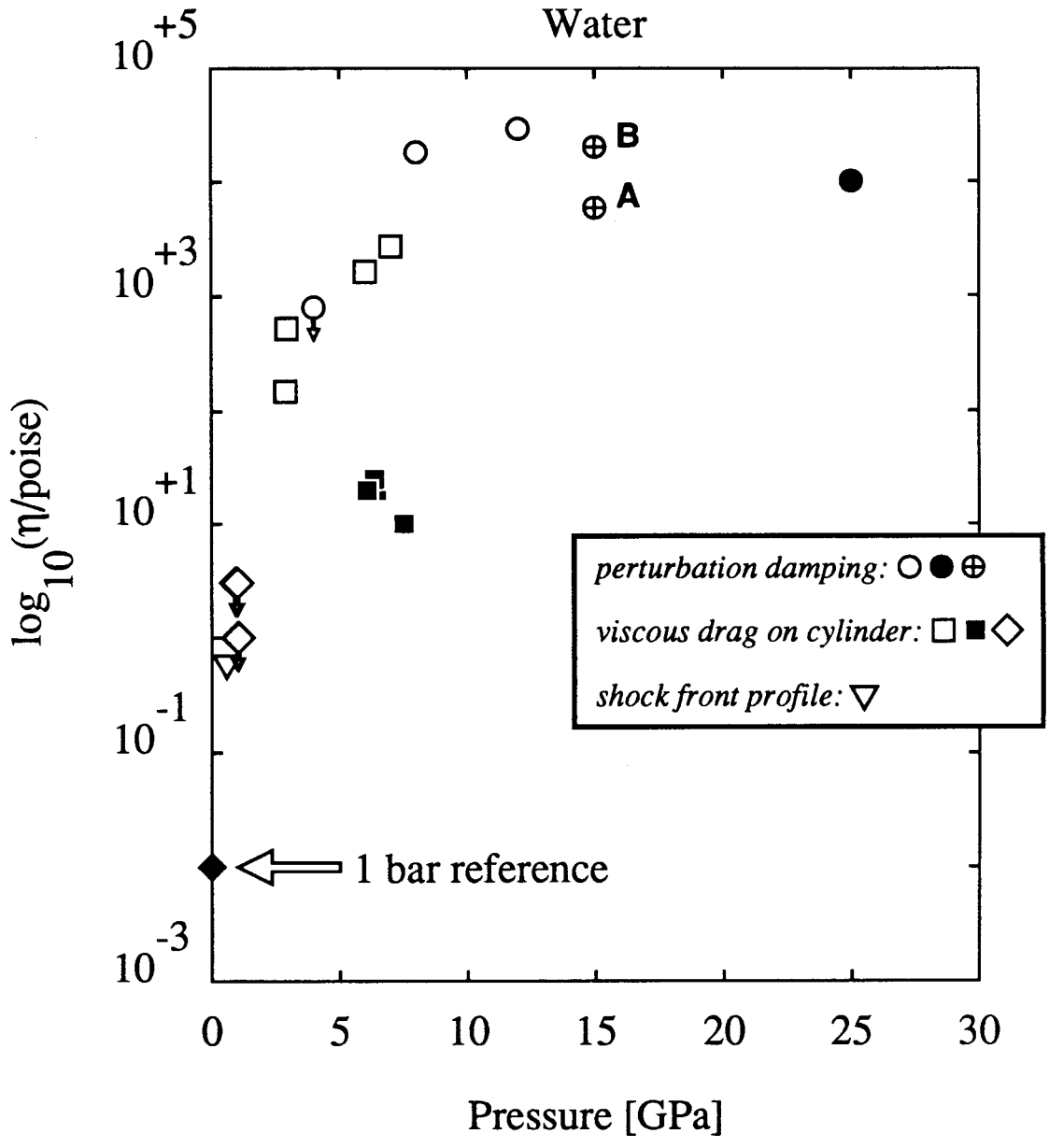
Water
10^{+5}
10^{+3}
10^{+1}
10^{-1}
10^{-3}
$\log_{10}(\eta/\text{poise})$
B
A
perturbation damping:
viscous drag on cylinder:
shock front profile:
1 bar reference
0
5
10
15
20
25
30
Pressure [GPa]

Figure 2.

Figure 3: Schematic geometry of sinusoidally perturbed shock in stationary coordinate frame (a), and co-moving coordinate frame (b). The arrows denote relative senses of motion, but their length is not scaled in proportion to the magnitudes of the velocities.

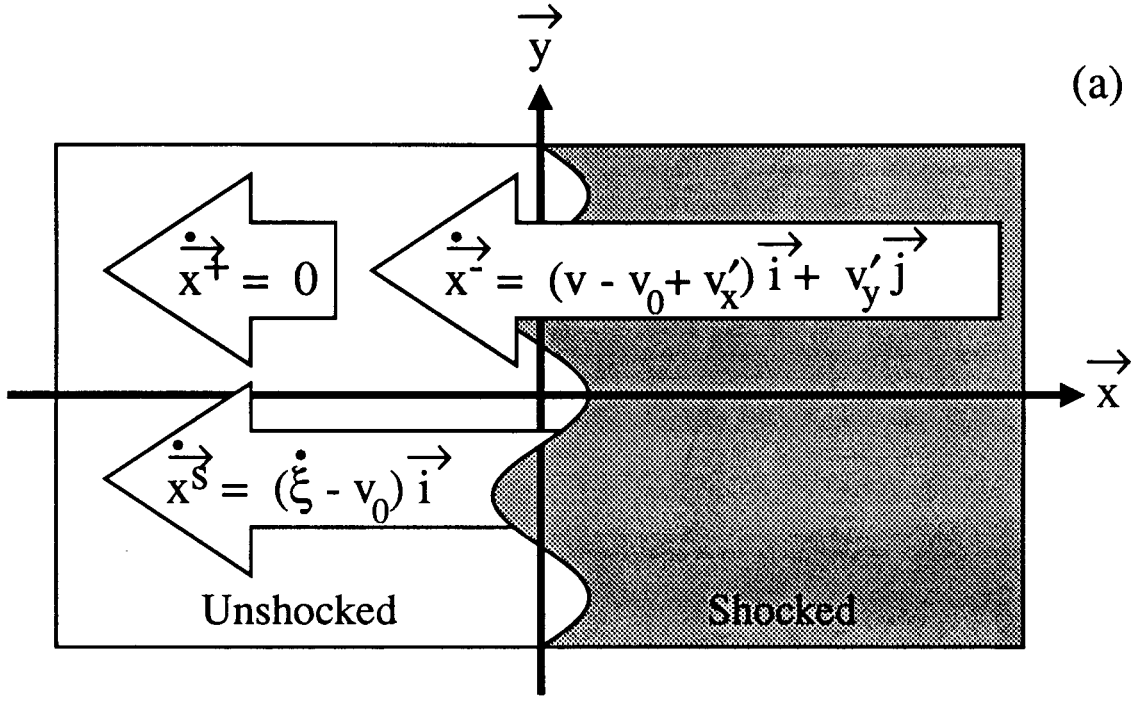

Stationary Coordinate Frame

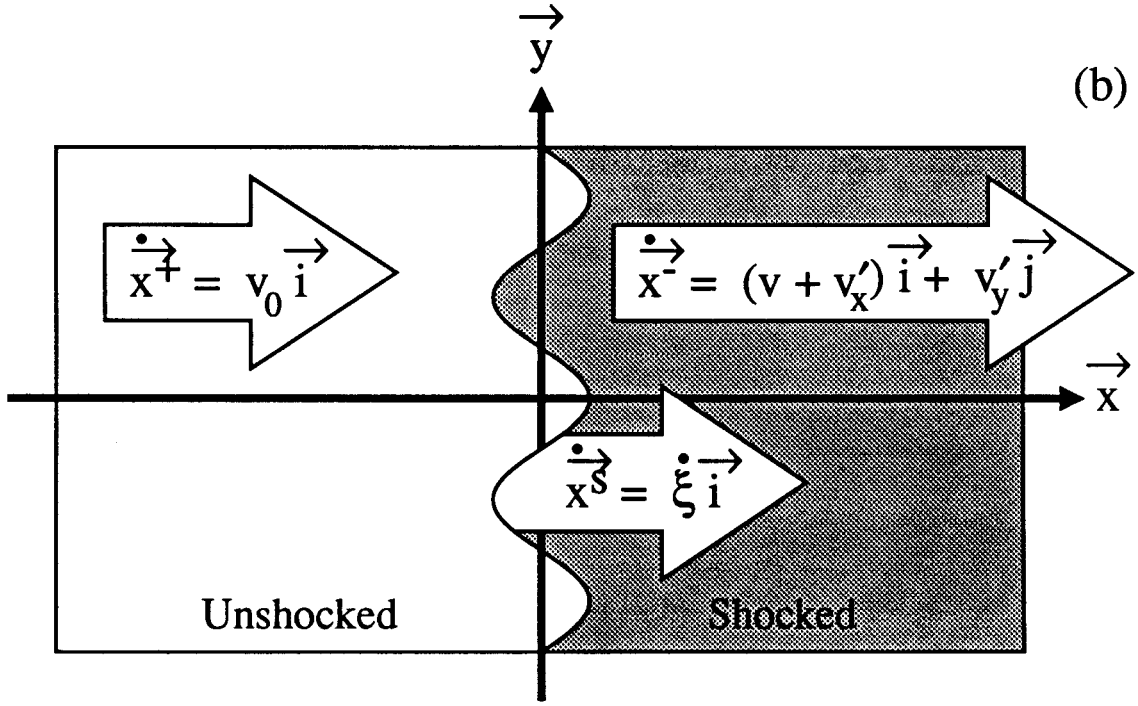

Co-moving Coordinate Frame

Figure 3.

method is less easily explained. It is possible that the analytic method of Zaidel' [1967] is correct, and that water does exhibit a near-solid rheology at high pressure. Alternatively, errors in the analytic method may have led to a misinterpretation of the experiments.

The viscosities of shocked solids determined by this method, however, are in substantially good agreement with estimates obtained through the study of the shock welding phenomenon [Godunov *et al.*, 1971]. Melting points on the Hugoniot have also been detected by associated decreases in viscosity [Mineev and Savinov, 1967] by this method, and are in agreement with independent melting curve measurements.

The purpose of this paper is to examine the analytic method in greater detail, and to augment the treatment of Zaidel' [1967] by considering some alternative approximations. First the boundary conditions (BC) at the shock front are derived in §2. The initial conditions (IC) are discussed briefly in §3. Next, the linearized equations of motion and continuity are developed in §4. The shock perturbation development solution follows in §5 in the inviscid limit. A viscous perturbation follows in §6, and again in §7 with the different set of boundary conditions proposed by Zaidel' [1967].

In §8 a summary of approximations is presented, and their impact is discussed. In §9 and §10 the initial conditions are reexamined and a semiquantitative initial condition model is introduced. In §11 we examine the complete viscous equations to assess the validity of the viscous perturbation method for finite viscosity. Numerical examples are presented that indicate that instabilities may occur for certain ranges of Reynolds number. Finally, in §12 experimental data for water at 15 GPa [Mineev and Zaidel', 1968] is discussed.

It is assumed that the shocked material behaves as a viscoelastic fluid. Anelastic absorption mechanisms are not explicitly considered, although they might be important in some experiments.

The frequency of pressure waves generated by a perturbed shock are inversely proportional to the wavelength of the perturbation. For many materials it is therefore possible, at least in principle, to design an experiment that avoids anelastic phenomena.

2. Boundary Conditions at Shock Front

The boundary conditions at the shock front are readily derived from the generalized Rankine Hugoniot relations. Nevertheless, it seems worthwhile to derive these conditions because the result we obtain differs from that presented by Zaidel' [1967] without derivation. We begin the derivation by specifying the geometry at the shock front. This allows all perturbations to be cast into vector components normal and tangential to the shock front. These vector components are then used with the generalized Rankine Hugoniot relations to obtain the boundary conditions at the shock front. Sign conventions follow Truesdell and Toupin [1960].

In following Zaidel' [1967] we adopt a co-moving coordinate system (Fig. 3) in which the shock front is stationary, nominally the plane x=0. The shocked material travels in the positive x direction at a nominal velocity v ($v=U_S-U_P$, where U_S is the shock velocity, and U_P is the particle velocity), and the unshocked material travels in the positive x direction at a nominal velocity v_0 (U_S). Perturbations are present in the x and y directions, but not in the z direction. The perturbations on the shock front, ξ, are positive when the front is perturbed toward the shocked material.

In the co-moving coordinate system specified above (Fig. 3), a point on the shock front can be given by the generalized coordinate $(x,y) = (\xi(y),y)$, or in vector form by:

$$\vec{x}^S = \xi\vec{i} + y\vec{j}. \tag{1}$$

The tangent to this surface is given by $\partial\vec{x}^S/\partial y$. The normalized, or unit tangent vector is then:

$$\vec{t} = \frac{\xi_y \vec{i} + 1\vec{j}}{\sqrt{1 + \xi_y^2}}, \tag{2}$$

where $\xi_y \equiv \partial\xi/\partial y$, and the unit normal vector is given by:

$$\vec{n} = \frac{1\vec{i} - \xi_y \vec{j}}{\sqrt{1 + \xi_y^2}}. \tag{3}$$

The velocity of the surface point specified by Eqn. 1 is:

$$\dot{\vec{x}}^S = \dot{\xi}\vec{i}. \tag{4}$$

Its normal and tangential components are determined by the dot product of this velocity with the unit direction vectors, Eqns. 2 and 3:

$$\dot{x}_n^S = \frac{\dot{\xi}}{\sqrt{1 + \xi_y^2}} \tag{5}$$

and

$$\dot{x}_t^S = \frac{\xi_y \dot{\xi}}{\sqrt{1 + \xi_y^2}}. \tag{6}$$

The unshocked material ahead of the shock wave is given by the generalized coordinate:

$$\vec{x}^+ = [x + v_0 t]\vec{i} + y\vec{j} \tag{7}$$

with velocity

$$\dot{\vec{x}}^+ = v_0 \vec{i}. \tag{8}$$

This velocity can also be decomposed into normal and tangential components:

$$\dot{x}_n^+ = \frac{v_0}{\sqrt{1 + \xi_y^2}} \tag{9}$$

and

$$\dot{x}_t^+ = \frac{\xi_y v_0}{\sqrt{1 + \xi_y^2}}. \tag{10}$$

Similarly, the compressed material behind the shock front is given by the generalized coordinate:

$$\vec{x}^- = [x + vt + v'_x t]\vec{i} + [y + v'_y t]\vec{j}, \tag{11}$$

where $v\vec{i}$ is the nominal velocity, and primes denote small velocity perturbations ($v'_x\vec{i} + v'_y\vec{j}$). The velocity of the shocked material is:

$$\dot{\vec{x}}^- = (v + v'_x)\vec{i} + v'_y\vec{j}, \tag{12}$$

resolving into normal and tangential components

$$\dot{x}_n^- = \frac{v + v'_x - v'_y\xi_y}{\sqrt{1 + \xi_y^2}} \tag{13}$$

$$\dot{x}_t^- = \frac{v'_y + \xi_y(v + v'_x)}{\sqrt{1 + \xi_y^2}}. \tag{14}$$

In a reference frame moving with the shock front we define the normal velocities $U^{\pm} = \dot{x}_n^S - \dot{x}_n^{\pm}$:

$$U^+ = \frac{\dot{\xi} - v_0}{\sqrt{1 + \xi_y^2}} \tag{15}$$

$$U^- = \frac{\dot{\xi} - v - v'_x + v'_y\xi_y}{\sqrt{1 + \xi_y^2}}. \tag{16}$$

Before evaluating the BC, it is useful to determine the components of the stress tensor in the (n,t) coordinate system. We assume a Newtonian fluid with constant viscosity. The stress tensor in the (x,y) coordinate frame is given by the components:

$$\tau_{xx} = -P + \frac{2}{3}\eta\left[2\frac{\partial v_x}{\partial x} - \frac{\partial v_y}{\partial y}\right] + \kappa\left[\frac{\partial v_x}{\partial x} + \frac{\partial v_y}{\partial y}\right] \tag{17}$$

$$\tau_{xy} = \tau_{yx} = \eta\left[\frac{\partial v_x}{\partial y} + \frac{\partial v_y}{\partial x}\right] \tag{18}$$

$$\tau_{yy} = -P + \frac{2}{3}\eta\left[2\frac{\partial v_y}{\partial y} - \frac{\partial v_x}{\partial x}\right] + \kappa\left[\frac{\partial v_x}{\partial x} + \frac{\partial v_y}{\partial y}\right] \tag{19}$$

where η is the shear viscosity and κ is the bulk viscosity. These components can be cast into normal and tangential stresses with the relationship:

$$\tau_{kl} = \sum_i \sum_j (\vec{i}\cdot\vec{k})(\vec{j}\cdot\vec{l})\tau_{ij} \,. \tag{20}$$

Using the normal and tangent vectors determined above (Eqns. 2 and 3) these sums can be applied to give:

$$\tau_{nn} = \frac{\tau_{xx} - 2\xi_y\tau_{xy} + \xi_y^2\tau_{yy}}{1 + \xi_y^2} \tag{21}$$

$$\tau_{nn} = -P + \kappa\left[\frac{\partial v_x}{\partial x} + \frac{\partial v_y}{\partial y}\right] + \frac{2}{3}\eta\frac{\left[2-\xi_y^2\right]\frac{\partial v'_x}{\partial x} - 3\xi_y\left[\frac{\partial v'_x}{\partial y} + \frac{\partial v'_y}{\partial x}\right] + \left[2\xi_y^2 - 1\right]\frac{\partial v'_y}{\partial y}}{1 + \xi_y^2} \tag{22}$$

$$\tau_{nt} = \frac{\xi_y\tau_{xx} + \left[1-\xi_y^2\right]\tau_{xy} - \xi_y\tau_{yy}}{1 + \xi_y^2} \tag{23}$$

$$\tau_{nt} = \eta\frac{2\xi_y\frac{\partial v'_x}{\partial x} + \left[1-\xi_y^2\right]\left[\frac{\partial v'_x}{\partial y} + \frac{\partial v'_y}{\partial x}\right] - 2\xi_y\frac{\partial v'_y}{\partial y}}{1 + \xi_y^2} \tag{24}$$

We now proceed to develop the BC. One BC at the shock front is the Stokes-Christoffel condition, a conservation of mass equation [Truesdell and Toupin, 1960, pp. 519-523]:

$$\rho^+U^+ - \rho^-U^- \equiv [|\rho U|] = 0 \,. \tag{25}$$

Substituting the quantities determined above, this relation becomes:

$$\rho_0\left[\dot{\xi} - v_0\right] = \rho\left[\dot{\xi} - v - v'_x + v'_y\xi_y\right] \,. \tag{26}$$

A second BC at the shock front is Cauchy's 1st law of motion [Truesdell and Toupin, 1960, pp. 544-548], a stress balance, in the normal direction:

$$[|\tau_{nn}|] + \rho_0 U^+ [|\dot{x}_n|] = 0 \tag{27}$$

$$(P - P_0)\left[1 + \xi_y^2\right] - \frac{2}{3}\eta\left[\left(2-\xi_y^2\right)\frac{\partial v'_x}{\partial x} - 3\xi_y\left[\frac{\partial v'_x}{\partial y} + \frac{\partial v'_y}{\partial x}\right] + \left[2\xi_y^2 - 1\right]\frac{\partial v'_y}{\partial y}\right] \tag{28}$$

$$- \kappa\left[1 + \xi_y^2\right]\left[\frac{\partial v_x}{\partial x} + \frac{\partial v_y}{\partial y}\right] + \rho_0\left[\dot{\xi} - v_0\right]\left[v_0 - v - v'_x + v'_y\xi_y\right] = 0 .$$

The third BC derives from Cauchy's 1st law of motion in the tangential direction:

$$[|\tau_{nt}|] + \rho_0 U^+ [|\dot{x}_t|] = 0 \tag{29}$$

(30)

$$-\eta\left[2\xi_y\frac{\partial v'_x}{\partial x} + \left[1-\xi_y^2\right]\left[\frac{\partial v'_x}{\partial y} + \frac{\partial v'_y}{\partial x}\right] - 2\xi_y\frac{\partial v'_y}{\partial y}\right] + \rho_0\left[\dot{\xi} - v_0\right]\left[\xi_y v_0 - \xi_y(v + v'_x) - v'_y\right] = 0.$$

These BC can be linearized with the approximations:

$$P \rightarrow P + P' , \tag{31}$$

and

$$\frac{1}{\rho} \rightarrow \frac{1}{\rho} - \frac{P'\delta}{\rho^2 v^2} , \tag{32}$$

where

$$\delta \equiv -\rho_0^2 v_0^2 \frac{\partial V}{\partial P}\Big|_{\text{Hugoniot}} \tag{33}$$

is a dimensionless measure of the compressibility on the Hugoniot, evaluated at the nominal shock pressure. Let all perturbations have the form $e^{ik_0 y}$, *i.e.*, suppose that the perturbations vary sinusoidally in the y direction, and collect terms of equal wavenumber. Note that ξ, P', v'_x, and v'_y are all perturbations of wavenumber k_0. Terms of wavenumber 0 (*i.e.*, no perturbations) are

$$\rho_0 v_0 = \rho v , \tag{34}$$

or

$$\rho = \rho_0 \frac{U_S}{U_S - U_P} \tag{35}$$

from Eqn. 26, and

$$P = P_0 + \rho_0(v_0 - v)v_0 , \tag{36}$$

or

$$P = P_0 + \rho_0 U_P U_S \tag{37}$$

from Eqn. 28. Equation 30 gives no information with wavenumber 0. Those terms that are first-order in perturbations, *i.e.*, with wavenumber k_0, are:

$$v'_x + \frac{P'\delta}{\rho v} - \left[\frac{\sigma-1}{\sigma}\right]\dot{\xi} = 0 , \tag{38}$$

$$v'_x + \frac{P'}{\rho v} + \left[\frac{\sigma-1}{\sigma}\right]\dot{\xi} = \frac{2\nu}{3v}\left[2\frac{\partial v'_x}{\partial x} - \frac{\partial v'_y}{\partial y}\right] + \frac{\kappa}{\rho v}\left[\frac{\partial v'_x}{\partial x} + \frac{\partial v'_y}{\partial y}\right] , \tag{39}$$

$$v'_y - v(\sigma-1)\xi_y = \frac{\nu}{v}\left[\frac{\partial v'_x}{\partial y} + \frac{\partial v'_y}{\partial x}\right] . \tag{40}$$

Writing $ik_0 v'_x$ for $\partial v'_x/\partial y$, making similar substitutions for $\partial v'_y/\partial y$ and ξ_y, and taking the Laplace transform, the BC are then given by:

$$\begin{bmatrix} \hat{v}_x \\ i\hat{v}_y \\ \hat{P}/(\rho v) \end{bmatrix}_{x=0} = \begin{bmatrix} -\frac{(\sigma-1)(1+\delta)}{\sigma(1-\delta)}(\xi_0 - s\hat{\xi}) - \frac{2\nu\delta}{3v(1-\delta)}\left[2\frac{\partial \hat{v}_x}{\partial x} - ik_0\hat{v}_y\right] - \frac{\kappa\delta}{\rho v(1-\delta)}\left[\frac{\partial \hat{v}_x}{\partial x} + ik_0\hat{v}_y\right] \\ -k_0 v(\sigma-1)\hat{\xi} + \frac{i\nu}{v}\left[ik_0\hat{v}_x + \frac{\partial \hat{v}_y}{\partial x}\right] \\ \frac{2(\sigma-1)}{\sigma(1-\delta)}(\xi_0 - s\hat{\xi}) + \frac{2\nu}{3v(1-\delta)}\left[2\frac{\partial \hat{v}_x}{\partial x} - ik_0\hat{v}_y\right] + \frac{\kappa}{\rho v(1-\delta)}\left[\frac{\partial \hat{v}_x}{\partial x} + ik_0\hat{v}_y\right] \end{bmatrix}_{x=0} \tag{41}$$

where $\hat{f}(s)$ denotes the Laplace transform of $f(t)$, $\nu = \eta/\rho$ is the kinematic shear viscosity, and

$$\sigma \equiv \frac{\rho}{\rho_0} = \frac{v_0}{v} > 1 \tag{42}$$

is a measure of the strength of the shock.

In the limit of no viscosity, these BC reduce to those of Zaidel' [1967] (his Eqn. 1.9) and D'yakov [1954]. When the viscous terms are retained, Eqn. 40 is the same as Zaidel's Eqn. 2.4a [1967], but the other two viscous BC differ. His BC may be written:

$$\begin{bmatrix} \hat{v}_x \\ i\hat{v}_y \\ \hat{P}/(\rho v) \end{bmatrix}_{x=0} = \begin{bmatrix} -\frac{(\sigma-1)(1+\delta)}{\sigma(1-\delta)}(\xi_0 - s\xi) - \frac{2\nu\beta^2}{3v(1-\beta^2)}\left[2\frac{\partial \hat{v}_x}{\partial x} - ik_0\hat{v}_y\right] \\ -k_0 v(\sigma-1)\xi + \frac{i\nu}{v}\left[ik_0\hat{v}_x + \frac{\partial \hat{v}_y}{\partial x}\right] \\ \frac{2(\sigma-1)}{\sigma(1-\delta)}(\xi_0 - s\xi) + \frac{2\nu}{3v(1-\beta^2)}\left[2\frac{\partial \hat{v}_x}{\partial x} - ik_0\hat{v}_y\right] \end{bmatrix}_{x=0} . \quad (43)$$

The bulk viscosity, κ, is neglected in the Zaidel' analysis. The shear viscosity terms originating in the τ_{nn} component of the stress tensor differ from those of Eqn. 41 by a factors of $\frac{\beta^2(1-\delta)}{\delta(1-\beta^2)}$ for $\hat{v}_{x,x=0}$ and $\frac{(1-\delta)}{(1-\beta^2)}$ for $\hat{P}_{x=0}$. For water at 15 GPa these factors are 1.03 and 1.01 respectively, thus the numerical consequences of these discrepancies are small in this case.

The jump conditions (Eqns. 25, 27, and 29) strictly apply only when the shock front has no structure, *i.e.*, the shock front is an abrupt discontinuity with no width. Lord Rayleigh [1910] demonstrated that a shock in a viscous material will necessarily have finite structure, thereby bringing into question the applicability of the jump relations. If the shock is planar, a steady, unchanging shock with finite width obeys the jump relations [Swan *et al.*, 1973] where the upstream (v^+, P^+) and downstream (v^-, P^-) properties are evaluated in the asymptotic limits $x \rightarrow \pm\infty$. Similarly, if the width of the shock front is sufficiently narrow compared to the radius of curvature of the shock ($r \simeq 4\pi^2/k_0^2\xi$), then the jump conditions may be employed. This condition is readily satisfied in practice since the shock width is generally on the order of tens of nanometers in thickness [*e.g.*, Harris and Presles, 1981], decreasing with increasing shock pressure. A method for expressing the BC given an approximation of the shock front structure is described by Istrakov and Librovich [1966].

3. Initial Conditions

The experiments of Sakharov *et al.* [1965] were designed to generate a perturbed shock wave while producing the least possible disturbance behind the shock front. Sakharov *et al.* [1965] state that the uniformity of the flow behind the shock is disturbed at distances of order ξ_0, the initial shock perturbation amplitude. To the extent that this was true, the approximate IC,

$$v'_x(x,t=0) = v'_y(x,t=0) = P'(x,t=0) = 0 , \tag{44}$$

are applicable everywhere except in the immediate vicinity of the shock front. These IC, used by Zaidel' [1967], assume that the flow field is initially uniform behind the perturbed shock front.

These IC are meant to be compatible with both the differential equations (derived below) and the boundary conditions. In fact, these IC are not compatible with the BC, as can be seen by substituting Eqn. 44 into Eqn. 41. In the inviscid case $i\hat{v}_y = -k_0 v(\sigma-1)\hat{\xi}$, thus a finite shock front perturbation, $\xi \neq 0$, is inconsistent with $\hat{v}_y = 0$ at the shock front $x = 0$. Zaidel' [1967] suggests that for the purpose of a stability analysis the IC can be neglected. While this may be true, it remains to be shown that the IC are unimportant for the purpose of modeling actual experiments.

In §5, §6, and §7, where we follow the derivation of Zaidel' [1967], the IC will be neglected (*i.e.*, we use Eqn. 44). In §9 and §10 the IC will be reexamined and it will be shown that these IC do have a strong influence over the resulting perturbation development.

4. Equations of Motion and Continuity

The differential equations governing the compressible flow in the shocked sample are the standard equations of motion and continuity. For completeness, these equations will be presented and cast into the form used by Zaidel' [1967].

Noting that there is no z variation in any quantity, the equations of motion can be written as:

$$\frac{\partial v_x}{\partial t} + v_x\frac{\partial v_x}{\partial x} + v_y\frac{\partial v_x}{\partial y} = \frac{1}{\rho}\left[\frac{\partial \tau_{xx}}{\partial x} + \frac{\partial \tau_{yx}}{\partial y}\right] \tag{45a}$$

$$\frac{\partial v_y}{\partial t} + v_x\frac{\partial v_y}{\partial x} + v_y\frac{\partial v_y}{\partial y} = \frac{1}{\rho}\left[\frac{\partial \tau_{xy}}{\partial x} + \frac{\partial \tau_{yy}}{\partial y}\right] . \tag{45b}$$

Next, we substitute the Newtonian viscosity form of the stress tensor (Eqns. 17, 18, and 19) and linearize the equations. This linearization is accomplished by writing the velocities and pressure in terms of their nominal values plus a perturbation. Only those terms that are first order in the perturbations are retained. The perturbation quantities are denoted by primes:

$$v_x \rightarrow v + v'_x \tag{46}$$

$$v_y \rightarrow v'_y \tag{47}$$

$$P \rightarrow P + P' . \tag{48}$$

The resulting equations of motion are:

$$\frac{\partial v'_x}{\partial t} + v\frac{\partial v'_x}{\partial x} + \frac{1}{\rho}\frac{\partial P'}{\partial x} = \nu\left[\frac{4}{3}\frac{\partial^2 v'_x}{\partial x^2} + \frac{\partial^2 v'_x}{\partial y^2} + \frac{1}{3}\frac{\partial^2 v'_y}{\partial x \partial y}\right] + \frac{\kappa}{\rho}\left[\frac{\partial^2 v'_x}{\partial x^2} + \frac{\partial^2 v'_y}{\partial x \partial y}\right] , \tag{49a}$$

$$\frac{\partial v'_y}{\partial t} + v\frac{\partial v'_y}{\partial x} + \frac{1}{\rho}\frac{\partial P'}{\partial y} = \nu\left[\frac{1}{3}\frac{\partial^2 v'_x}{\partial x \partial y} + \frac{\partial^2 v'_y}{\partial x^2} + \frac{4}{3}\frac{\partial^2 v'_y}{\partial y^2}\right] + \frac{\kappa}{\rho}\left[\frac{\partial^2 v'_x}{\partial x \partial y} + \frac{\partial^2 v'_y}{\partial y^2}\right] . \tag{49b}$$

The equation of continuity is:

$$\frac{\partial \rho}{\partial t} + \frac{\partial}{\partial x}(\rho v_x) + \frac{\partial}{\partial y}(\rho v_y) = 0 . \tag{50}$$

This equation is linearized with the adiabatic approximation:

$$\frac{1}{\rho} \rightarrow \frac{1}{\rho} - \frac{P'}{\rho^2 c^2} , \tag{51}$$

resulting in the equation

$$\frac{\partial P'}{\partial t} + v\frac{\partial P'}{\partial x} + \rho c^2\left[\frac{\partial v'_x}{\partial x} + \frac{\partial v'_y}{\partial y}\right] = 0 . \tag{52}$$

The complete differential equations (Eqns. 49a, 49b, and 52) are solvable in principle. The algebraic complexity of the system is formidable, however, so a perturbation method is adopted. First the equations are solved in the inviscid limit. The role of viscosity is then examined by considering viscous effects to be the result of small perturbations on the inviscid solution. The complete equations will be readdressed in §11.

Dropping the primes on the perturbed quantities in the linearized equations of motion and continuity, taking their Laplace transform, and letting all perturbed quantities depend on y as $e^{ik_0 y}$, these equations can be expressed in matrix form:

$$\frac{\partial \vec{u}}{\partial x} = A\vec{u} + \vec{g} , \tag{53a}$$

where

$$\vec{u} \equiv \begin{bmatrix} \hat{v}_x \\ i\hat{v}_y \\ \hat{P}/(\rho v) \end{bmatrix} , \tag{53b}$$

$$A \equiv \begin{bmatrix} \dfrac{\beta^2 k_0 z}{1-\beta^2} & \dfrac{-k_0}{1-\beta^2} & \dfrac{-\beta^2 k_0 z}{1-\beta^2} \\ 0 & -k_0 z & k_0 \\ \dfrac{-k_0 z}{1-\beta^2} & \dfrac{k_0}{1-\beta^2} & \dfrac{\beta^2 k_0 z}{1-\beta^2} \end{bmatrix} , \tag{53c}$$

and

$$\vec{g} \equiv \begin{bmatrix} \frac{\beta^2}{v(1-\beta^2)}\left[\frac{P(0)}{\rho v} - v_x(0)\right] \\ \frac{iv_y(0)}{v} \\ \frac{1}{v(1-\beta^2)}\left[v_x(0) - \beta^2\frac{P(0)}{\rho v}\right] \end{bmatrix} + \tag{53d}$$

$$\begin{bmatrix} -\frac{\beta^2}{v(1-\beta^2)}\left[\nu\left[\frac{4}{3}\frac{\partial^2\hat{v}_x}{\partial x^2} - k_0{}^2\hat{v}_x + \frac{ik_0}{3}\frac{\partial\hat{v}_y}{\partial x}\right] + \frac{\kappa}{\rho}\left[\frac{\partial^2\hat{v}_x}{\partial x^2} + ik_0\frac{\partial\hat{v}_y}{\partial x}\right]\right] \\ \frac{i}{v}\left[\nu\left[\frac{ik_0}{3}\frac{\partial\hat{v}_x}{\partial x} + \frac{\partial^2 y}{\partial x^2} - \frac{4k_0{}^2}{3}\hat{v}_y\right] + \frac{\kappa}{\rho}\left[ik_0\frac{\partial\hat{v}_x}{\partial x} - k_0{}^2\hat{v}_y\right]\right] \\ \frac{1}{v(1-\beta^2)}\left[\nu\left[\frac{4}{3}\frac{\partial^2\hat{v}_x}{\partial x^2} - k_0{}^2\hat{v}_x + \frac{ik_0}{3}\frac{\partial\hat{v}_y}{\partial x}\right] + \frac{\kappa}{\rho}\left[\frac{\partial^2\hat{v}_x}{\partial x^2} + ik_0\frac{\partial\hat{v}_y}{\partial x}\right]\right] \end{bmatrix}.$$

The factor e^{ik_0y} has been omitted for clarity.

$$\beta \equiv \frac{v}{c} \tag{54}$$

is the Mach number of the shocked sample with respect to the high pressure sound speed c, and

$$z \equiv \frac{s}{k_0 v} \tag{55}$$

is a dimensionless form of the Laplace transform variable s.

Supposing the inviscid solution of Eqn. 53 has the form:

$$\vec{u} = \vec{u}_{x=0}e^{\lambda x} \tag{56}$$

leads to a characteristic equation for the eigenvalues λ. From the characteristic equation we get 3 eigenvalues and 3 corresponding left eigenvectors ($\psi A = \lambda\psi$):

$$\lambda_1 = -k_0 z \qquad \lambda_2 = \frac{k_0(\beta^2 z - \omega)}{1-\beta^2} \qquad \lambda_3 = \frac{k_0(\beta^2 z + \omega)}{1-\beta^2} \tag{57}$$

$$\psi_1 = \begin{bmatrix} -1 \\ z \\ -1 \end{bmatrix}^t \qquad \psi_2 = \begin{bmatrix} z \\ -1 \\ \omega \end{bmatrix}^t \qquad \psi_3 = \begin{bmatrix} z \\ -1 \\ -\omega \end{bmatrix}^t \tag{58}$$

where

$$\omega \equiv \sqrt{\beta^2 z^2 + 1 - \beta^2}\,. \tag{59}$$

It is convenient to decompose the matrix of Eqn. 53 into the form

$$\mathbf{A} = \mathbf{S}^{-1}\mathbf{\Lambda}\mathbf{S} \tag{60}$$

where S is the matrix whose rows are the left eigenvectors, and $\mathbf{\Lambda}$ is the diagonal matrix of eigenvalues:

$$\begin{bmatrix} \frac{\beta^2 k_0 z}{1-\beta^2} & \frac{-k_0}{1-\beta^2} & \frac{-\beta^2 k_0 z}{1-\beta^2} \\ 0 & -k_0 z & k_0 \\ \frac{-k_0 z}{1-\beta^2} & \frac{k_0}{1-\beta^2} & \frac{\beta^2 k_0 z}{1-\beta^2} \end{bmatrix} = \begin{bmatrix} \frac{1}{z^2-1} & \frac{\omega z+1}{2\omega(z^2-1)} & \frac{\omega z-1}{2\omega(z^2-1)} \\ \frac{z}{z^2-1} & \frac{\omega+z}{2\omega(z^2-1)} & \frac{\omega-z}{2\omega(z^2-1)} \\ 0 & \frac{1}{2\omega} & \frac{-1}{2\omega} \end{bmatrix} \begin{bmatrix} -zk_0 & 0 & 0 \\ 0 & \frac{k_0(\beta^2 z-\omega)}{1-\beta^2} & 0 \\ 0 & 0 & \frac{k_0(\beta^2 z+\omega)}{1-\beta^2} \end{bmatrix} \begin{bmatrix} -1 & z & -1 \\ z & -1 & \omega \\ z & -1 & -\omega \end{bmatrix}. \tag{61}$$

The differential equations Eqn. 53 can then be solved as:

$$\frac{\partial}{\partial x}\vec{u} = \mathbf{S}^{-1}\mathbf{\Lambda}\mathbf{S}\vec{u} + \vec{g} \tag{62}$$

$$\frac{\partial}{\partial x}(\mathbf{S}\vec{u}) = \mathbf{\Lambda}(\mathbf{S}\vec{u}) + (\mathbf{S}\vec{g}) \tag{63}$$

$$(\mathbf{S}\vec{u}) = e^{\mathbf{\Lambda}x}\left[(\mathbf{S}\vec{u})_{x=0} + \int_0^x e^{-\mathbf{\Lambda}\chi}(\mathbf{S}\vec{g})\partial\chi\right] \tag{64}$$

$$\vec{u} = \mathbf{S}^{-1}e^{\mathbf{\Lambda}x}\left[(\mathbf{S}\vec{u})_{x=0} + \int_0^x e^{-\mathbf{\Lambda}\chi}(\mathbf{S}\vec{g})\partial\chi\right] \tag{65}$$

when the viscous terms in $\vec{g}$ and $\vec{u}_{x=0}$ are considered as small perturbations.

5. Solution in the Inviscid Limit

Note that there are 3 BC that determine the solution $\vec{u}$ for an arbitrary forcing function $\vec{\xi}$. Since we are interested in determining this function, we require an additional constraint. The approach that Zaidel' [1967] adopted was to consider the long-time behavior of the solution. Requiring all quantities to be bounded, λ must be negative for some real positive s. λ_3 violates this constraint. The solution is therefore given by setting the third component of the vector $\mathbf{S}\vec{u}$, the

coefficient of λ_3, equal to zero. In a real experiment, there may be some boundary at a finite distance from the shock front where perturbations must go to zero. Such a boundary could be a driver plate - sample interface, for example. A finite boundary condition of this type would allow all three eigenvectors to participate in the solution, although the contribution of the third would have to approach zero as the boundary moves farther from the shock front.

Adopting this approximation we can write

$$(S\vec{u})_{x=0} = \begin{bmatrix} -\frac{(\sigma-1)}{\sigma}[k_0 v\hat{\xi}(\sigma-1)z+\xi_0] \\ \frac{(\sigma-1)}{\sigma(1-\delta)}\left[k_0 v\hat{\xi}[(1+\delta)z^2-2\omega z+\sigma(1-\delta)] - \xi_0[(1+\delta)z-2\omega]\right] \\ \frac{(\sigma-1)}{\sigma(1-\delta)}\left[k_0 v\hat{\xi}[(1+\delta)z^2+2\omega z+\sigma(1-\delta)] - \xi_0[(1+\delta)z+2\omega]\right] \end{bmatrix} \tag{66}$$

by multiplying the vector of BC, $\vec{u}_{x=0}$ (Eqn. 41) in the inviscid limit, by the matrix S given in Eqn. 61. The IC contribution to Eqn. 65 is given by:

$$\int_0^x \partial\chi e^{-\Lambda\chi}(S\vec{g}) = \int_0^x \partial\chi \begin{bmatrix} e^{-\lambda_1\chi}\frac{iv_y(0) - v_x(0)}{v} \\ e^{-\lambda_2\chi}\frac{\beta^2(z-\omega)\left[\frac{P(0)}{\rho v}\right] - (\beta^2 z-\omega)v_x(0) - i(1-\beta^2)v_y(0)}{v(1-\beta^2)} \\ e^{-\lambda_3\chi}\frac{\beta^2(z+\omega)\left[\frac{P(0)}{\rho v}\right] - (\beta^2 z+\omega)v_x(0) - i(1-\beta^2)v_y(0)}{v(1-\beta^2)} \end{bmatrix}. \tag{67}$$

In the limit $x\to\infty$ we require all perturbations to vanish, and the solution is therefore determined by setting the sum of the third components of the vectors given by Eqns. 66 and 67 to zero. The dimensionless amplitude of the shock front corrugation, $\phi \equiv \xi/\xi_0$, can then be written as:

$$\hat{\phi} \equiv \frac{\xi}{\xi_0} = \frac{1}{k_0 v} \frac{(1+\delta)z + 2\omega}{(1+\delta)z^2 + 2\omega z + \sigma(1-\delta)} \tag{68a}$$

$$- \frac{1}{k_0 v} \frac{\sigma(1-\delta)}{\xi_0(\sigma-1)v(1-\beta^2)} \frac{\int_0^\infty \partial\chi e^{-\lambda_3\chi}\left[\beta^2(z+\omega)\left[\frac{P(0)}{\rho v}\right] - (\beta^2 z+\omega)v_x(0) - i(1-\beta^2)v_y(0)\right]}{(1+\delta)z^2 + 2\omega z + \sigma(1-\delta)} \tag{68b}$$

Zaidel' [1967] noted that the second term containing the IC will always be finite. He reasoned that it is therefore sufficient, for the purpose of a stability analysis, to neglect this term (*i.e.*, use the IC of Eqn. 44). This is reasonable, but may be insufficient for the modeling of real experiments. For the purpose of reproducing his results, we will accept this approximation for now. The IC will be reexamined in §9.

To invert Eqn. 68a, it is convenient to transform variables according to:

$$\varepsilon \equiv \frac{1-\beta^2}{\beta^2} \tag{69}$$

$$\mu \equiv \sqrt{\varepsilon} \tag{70}$$

$$T \equiv \mu\tau = k_0 ct\sqrt{1-\beta^2} = k_0 v\mu t \tag{71}$$

$$z = \frac{\mu}{2}\left[W - \frac{1}{W}\right] \tag{72}$$

$$\omega = \frac{\beta\mu}{2}\left[W + \frac{1}{W}\right] \tag{73}$$

to give the result:

$$\phi \equiv \frac{\xi}{\xi_0} = \frac{1}{2\pi i}\int e^{\frac{1}{2}T\left(W-\frac{1}{W}\right)} dW \left[W+\frac{1}{W}\right] \frac{W^2(1+\delta+2\beta) - (1+\delta-2\beta)}{W^4(1+\delta+2\beta) + W^2\left[\frac{4\sigma}{\varepsilon}(1-\delta) - 2(1+\delta)\right] + (1+\delta-2\beta)} . \tag{74}$$

This expression is similar to Zaidel's [1967] Eqns. 1.16 and 1.17 (he is missing the term $W+\frac{1}{W}$, probably a typographic error).

With this transformation, the branch $+\sqrt{\beta^2 z^2 + 1 - \beta^2}$ in the complex z plane is mapped onto the right half of the complex W plane (Re[W] > 0). On this half-plane, Re[z] will be negative when $|W| < 1$, and positive when $|W| > 1$. If the poles of Eqn. 74 lie outside the unit circle, $|W| = 1$, then a pole in the z plane will exist with Re[z] > 0, and the solution will consequently be unbounded as $t \to \infty$. It is easily shown that all singularities of the integrand lie within the unit circle $|W| = 1$ when:

$$\frac{\sigma-\varepsilon}{\sigma+\varepsilon} < \delta < 1 . \tag{75}$$

When these inequalities are satisfied the solution will be bounded and the shock will be stable. These inequalities are identical to Kontorovich's [1957] requirements for the stability of a shock wave (correcting D'yakov's [1954] earlier work). The inequality $\delta < 1$ is satisfied when the shock velocity increases with increasing particle velocity, *i.e.*, $\partial U_S/\partial U_P > 0$. The second inequality, $\delta > (\sigma-\varepsilon)/(\sigma+\varepsilon)$, is satisfied when the high pressure isentropic bulk modulus, K_S, is greater than both $(P-P_0)/(\sigma-1)$ and $(P-P_0)(1+\gamma)$, assuming γ, the thermodynamic Grüneisen parameter, is less than $2/(\sigma-1)$. A discussion of the relationship between these stability criteria and the conditions for shock splitting is given by Fowles and Houwing [1984].

Assuming the singularities lie within the unit circle, we can let the contour of integration be a counterclockwise unit circle:

$$W = e^{2\pi i y} \tag{76}$$

$$\phi = 2\int_{\delta}^{1} e^{iT\sin(2\pi y)} dy \cos(2\pi y) \frac{e^{6\pi i y}(1+\delta+2\beta) - e^{2\pi i y}(1+\delta-2\beta)}{e^{8\pi i y}(1+\delta+2\beta) + e^{4\pi i y}\left[\frac{4\sigma}{\varepsilon}(1-\delta)-2(1+\delta)\right] + (1+\delta-2\beta)} . \tag{77}$$

Multipling through by the complex conjugate of the denominator, making another change of variables,

$$X = \sin(2\pi y) \tag{78}$$

and using symmetry to eliminate terms gives:

$$\phi = \frac{4\beta\varepsilon\sigma(1-\delta)}{\pi}\int_0^1 \frac{\cos(TX)\sqrt{1-X^2}\,\partial X}{\varepsilon^2X^4\left[(1+\delta)^2-4\beta^2\right] + 2\varepsilon X^2\left[2(1-\beta^2)-\sigma(1-\delta^2)\right] + \sigma^2(1-\delta)^2} \tag{79}$$

This is the final expression for the amplitude of the shock front perturbation in the inviscid limit when the IC are neglected (Fig. 4). Note that the initial time derivative of Eqn. 79, $\dot{\phi}_0$, is zero ($\dot{\phi}$ is a function of sin(TX), which is zero at T=0). This result is similar to Zaidel's [1967] Eqns. 1.20 and 1.21, but he is missing the $4\beta^2$ term in the denominator (probably a typographic error).

By substituting the solution, Eqn. 68a, into the BC, Eqn. 41, we can solve Eqn. 65 for the inviscid velocity and pressure perturbations:

$$\hat{v}_x = \frac{\xi_0(\sigma-1)}{1-z^2}\,\frac{[(1+\delta)z^2+2\omega z+(1-\delta)]e^{\lambda_1 x} - 2(1+\omega z)e^{\lambda_2 x}}{(1+\delta)z^2 + 2\omega z + \sigma(1-\delta)} \tag{80a}$$

$$i\hat{v}_y = \frac{\xi_0(\sigma-1)}{1-z^2}\,\frac{z[(1+\delta)z^2+2\omega z+(1-\delta)]e^{\lambda_1 x} - 2(\omega+z)e^{\lambda_2 x}}{(1+\delta)z^2 + 2\omega z + \sigma(1-\delta)} \tag{80b}$$

$$\frac{\hat{P}}{\rho v} = 2\xi_0(\sigma-1)\frac{e^{\lambda_2 x}}{(1+\delta)z^2 + 2\omega z + \sigma(1-\delta)} \tag{80c}$$

D'yakov [1954] found that a perturbed shock front generates two types of motion. The first type, in which entropy changes while pressure remains constant, he calls entropy-vortex waves. This motion is related to the eigenvalue λ_1. The second type of motion, in which entropy is constant while pressure changes, is sound waves. The eigenvalues λ_2 and λ_3 are related to these waves.

The existence of the two wave types suggests competing roles for the bulk and shear viscosity. Incompressible flow, entropy-vortex waves in this case, is independent of the bulk viscosity. Sound waves, in which compression does occur, are dependent on both the shear and bulk viscosities [*e.g.*, Landau and Lifshitz, 1959, pp. 298-302].

Figure 4: Development of corrugated shock perturbations in an inviscid fluid. Calculated with Eqn. 79 with the parameters listed in Table III.

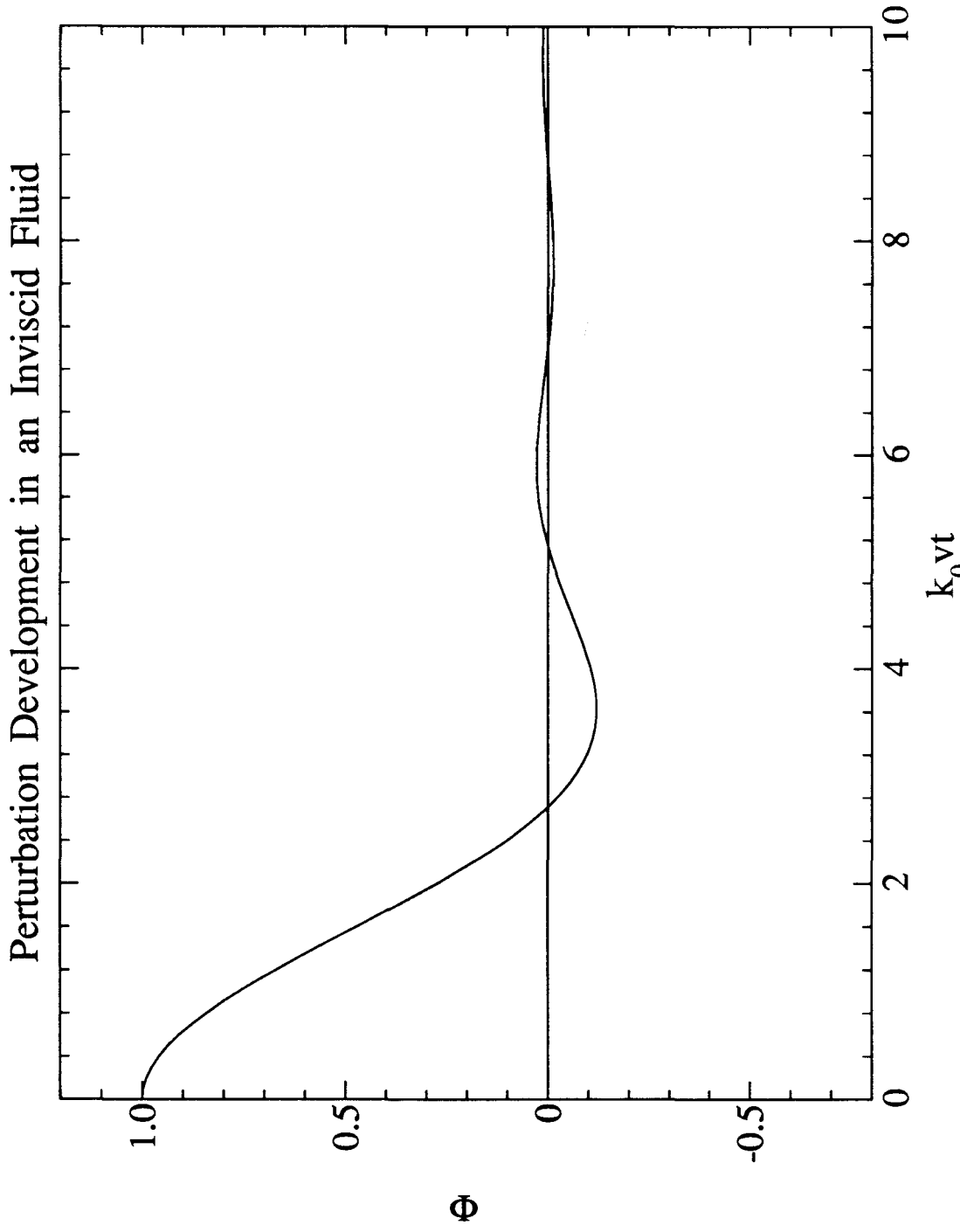
Perturbation Development in an Inviscid Fluid
1.0
0.5
0
-0.5
Φ
0
2
4
6
8
10
k_0vt

Figure 4.

For future reference, note that when the transformations (Eqns. 69-73, 76, and 78), are applicable, a single transformation can be employed:

$$z \rightarrow i\mu X \tag{81a}$$

$$\omega \rightarrow \mu\beta\sqrt{1-X^2} \tag{81b}$$

6. Viscous Perturbations

The essence of the perturbation treatment is to evaluate the viscous stresses given the inviscid solution. The method of solution follows from Eqns. 62-65, but now the viscous terms in the BC, $\vec{u}_{x=0}$, and the vector $\vec{g}$ are evaluated from the inviscid solution, Eqn. 80. Now, as before, we require the solution to be finite for all values of x. Since the third eigenvalue leads to exponential growth of the perturbations, the part of the solution (Eqn. 64) that is weighted by this eigenvalue must be identically zero. This constraint gives the result:

$$k_0 v\hat{\phi} = \frac{(1+\delta)z + 2\omega}{(1+\delta)z^2 + 2\omega z + \sigma(1-\delta)} + \tag{82a}$$

(82b)

$$+ \frac{\sigma}{R_s} \frac{z^2[(1+\delta)^2+4\beta^2] + 4\omega z(1+\delta) + [4(2-\beta^2)-(1+\delta)^2]}{\left[(1+\delta)z^2 + 2\omega z + \sigma(1-\delta)\right]^2}$$

$$- \frac{2\sigma}{\varepsilon R_b} \frac{(z-\omega)(\delta z+\omega)}{\left[(1+\delta)z^2 + 2\omega z + \sigma(1-\delta)\right]^2} \tag{82c}$$

$$- \frac{\sigma(1-\delta)}{R_s} \frac{z^2(1+\delta) + 2\omega z + (1-\delta)}{\left[(1+\delta)z^2 + 2\omega z + \sigma(1-\delta)\right]^2} \tag{82d}$$

$$+ \frac{\sigma(1-\delta)}{\varepsilon R_b} \frac{(z-\omega)(\omega^2+1)}{\omega\left[(1+\delta)z^2 + 2\omega z + \sigma(1-\delta)\right]^2}, \tag{82e}$$

where the shear Reynolds number is defined as

$$R_s \equiv \frac{v}{k_0 \nu} = \frac{v\rho}{k_0 \eta}, \tag{83}$$

and, by analogy, the bulk Reynolds number is defined as

$$R_b \equiv \frac{v\rho}{k_0\left[\frac{4}{3}\eta + \kappa\right]} . \tag{84}$$

The first term (Eqn. 82a) is the Laplace transform of the inviscid solution, and the remaining terms are the viscous perturbations. Equations 82b and 82c arise from the surface (*i.e.*, the BC), and Eqns. 82d and 82e arise from the volume of the shocked fluid.

Since the poles of Eqns. 82b, 82c, and 82d are identical to those of the inviscid solution, Eqn. 82a, the transformations of Eqn. 81 can be applied in the inverse Laplace transformation of these terms. The ω in the denominator of Eqn. 82e introduces a singularity at the branch point $W = \pm i$, thus the transformation, Eqn. 81, alone is not applicable for the inversion of this term. To invert this term we use the convolution theorem:

$$\frac{1}{\omega}\hat{f}(z) \rightarrow \frac{1}{\beta\mu}\int_0^T \partial u\, f(u)\, J_0(T-u) , \tag{85}$$

where $J_0(T)$ is the zero-order Bessel function of the first kind.

The complete viscous solution may then be written as:

(86a)

$$\phi = \frac{4\beta\varepsilon\sigma(1-\delta)}{\pi}\int_0^1 \partial X \frac{\cos(TX)\sqrt{1-X^2}}{\varepsilon^2X^4\left[(1+\delta)^2-4\beta^2\right] + 2\varepsilon X^2\left[2(1-\beta^2)-\sigma(1-\delta^2)\right] + \sigma^2(1-\delta)^2}$$

(86b)

$$+ \frac{4\sigma\beta\mu}{\pi R_b}\int_0^1 \partial X\, X\sqrt{1-X^2}\sin(TX)\frac{\varepsilon^2X^4[8\beta^2+(1+\delta)(1-4\delta-\delta^2)]-2\varepsilon X^2[4(1-\beta^2)+\sigma[2(1+\beta^2)-(1+\delta)^2]]+\sigma(1-\delta)[4(1-\beta^2)+\sigma(1-\delta)^2]}{\left[\varepsilon^2X^4[(1+\delta)^2-4\beta^2] + 2\varepsilon X^2[2(1-\beta^2)-\sigma(1-\delta^2)] + \sigma^2(1-\delta)^2\right]^2}$$

(86c)

$$- \frac{8\sigma\beta\mu\varepsilon(1-\delta)}{3\pi R_s}\int_0^1 \partial X\, X\sqrt{1-X^2}\sin(TX)\frac{\varepsilon X^2[(3+\delta)(1+\delta)-\sigma[(1+\delta)^2-4\beta^2]]-\sigma[4(2-\beta^2)-(1+\delta)^2-\sigma(1-\delta^2)]}{\left[\varepsilon^2X^4[(1+\delta)^2-4\beta^2] + 2\varepsilon X^2[2(1-\beta^2)-\sigma(1-\delta^2)] + \sigma^2(1-\delta)^2\right]^2}$$

(86d)

$$-\frac{2\sigma\beta\mu(1-\delta)}{\pi R_b}\int_0^1 \partial X\, X\sqrt{1-X^2}\sin(TX)\frac{\varepsilon^2X^4[(1+\delta)^2+4\beta^2(2+\delta)]-2\varepsilon X^2[2(3+2\delta)-2\beta^2(2+\delta)+\sigma(1-\delta)(1+\delta+2\beta^2)]+\sigma(1-\delta)[8-4\beta^2+\sigma(1-\delta)]}{\left[\varepsilon^2X^4[(1+\delta)^2-4\beta^2]+2\varepsilon X^2[2(1-\beta^2)-\sigma(1-\delta^2)]+\sigma^2(1-\delta)^2\right]^2}$$

(86e)

$$-\frac{8\sigma(1-\delta)}{\pi R_b}\int_0^1 \partial X\, X^2\sqrt{1-X^2}\,\Xi_C(T,X)\frac{\varepsilon X^2(1+\delta)-\sigma(1-\delta)}{\left[\varepsilon^2X^4[(1+\delta)^2-4\beta^2)]+2\varepsilon X^2[2(1-\beta^2)-\sigma(1-\delta)^2]+\sigma^2(1-\delta)^2\right]^2}$$

(86f)

$$-\frac{12\sigma\beta\mu\varepsilon(1-\delta)}{3\pi R_s}\int_0^1 \partial X\, X\sqrt{1-X^2}\sin(TX)\frac{\varepsilon^2X^4[(1+\delta)^2-4\beta^2]+2\varepsilon X^2[1+\delta^2-2\beta^2]+\sigma(2-\sigma)(1-\delta)^2}{\left[\varepsilon^2X^4[(1+\delta)^2-4\beta^2)]+2\varepsilon X^2[2(1-\beta^2)-\sigma(1-\delta)^2]+\sigma^2(1-\delta)^2\right]^2},$$

where

$$\Xi_C(T,X) \equiv \int_0^T \partial u\, \cos(uX)J_0(T-u)\,. \tag{87}$$

Equation 86a is the inviscid solution, Eqns. 86b and 86c are viscous terms that arise from the BC, and Eqns. 86d, 86e, and 86f are viscous terms that arise from the volume (Fig. 5). Those terms containing R_b have their origin in sound waves, while those viscous terms independent of R_b originate from the entropy-vortex waves.

This result differs significantly from that given by Zaidel's [1967] Eqn. 2.8. This is not surprising, however, considering that our BC differ. Using his BC, however, we also arrive at a different result than he presents. The solution obtained from his BC is presented in the following section.

The initial slopes of the viscous perturbations can be determined from:

$$\lim_{t\to 0}\phi = \lim_{\omega\to\beta z,\, z\to\infty}(k_0vz)^2\hat{\phi} = \frac{2k_0v\sigma(\beta+\delta)}{R_s(1+\delta+2\beta)} - \frac{k_0v\sigma(1-\beta)[\beta(1+\delta)+2\delta]}{R_b\varepsilon(1+\delta+2\beta)^2} \tag{88}$$

where we use the fact that the initial value of the viscous perturbations is zero. For all well-behaved systems, *i.e.*, $\delta>0$, that part of the solution dependent on shear viscosity has a positive ini-

Figure 5: Viscous perturbations. (a) Shear and bulk viscous perturbations from surface and volume sources (Eqn. 86), and (b) shock corrugations amplitude for $R_s = 4.23$ and $\kappa = \eta$ calculated with perturbation method (Eqn. 86) compared to inviscid solution (Eqn. 79) for parameters listed in Table III.

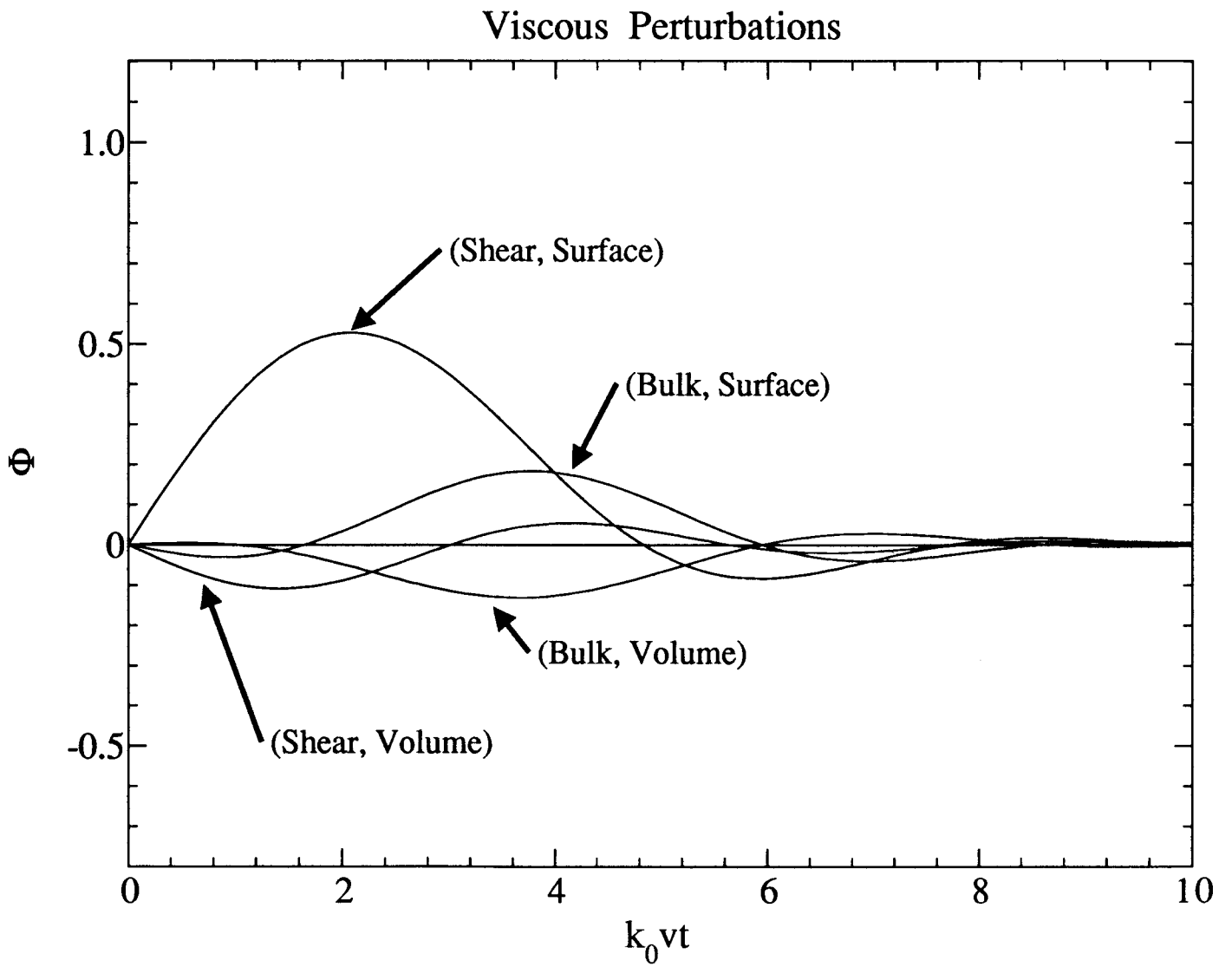
Viscous Perturbations
1.0
0.5
0
-0.5
Φ
(Shear, Surface)
(Bulk, Surface)
(Bulk, Volume)
(Shear, Volume)
0
2
4
6
8
10
k0vt

Figure 5a.

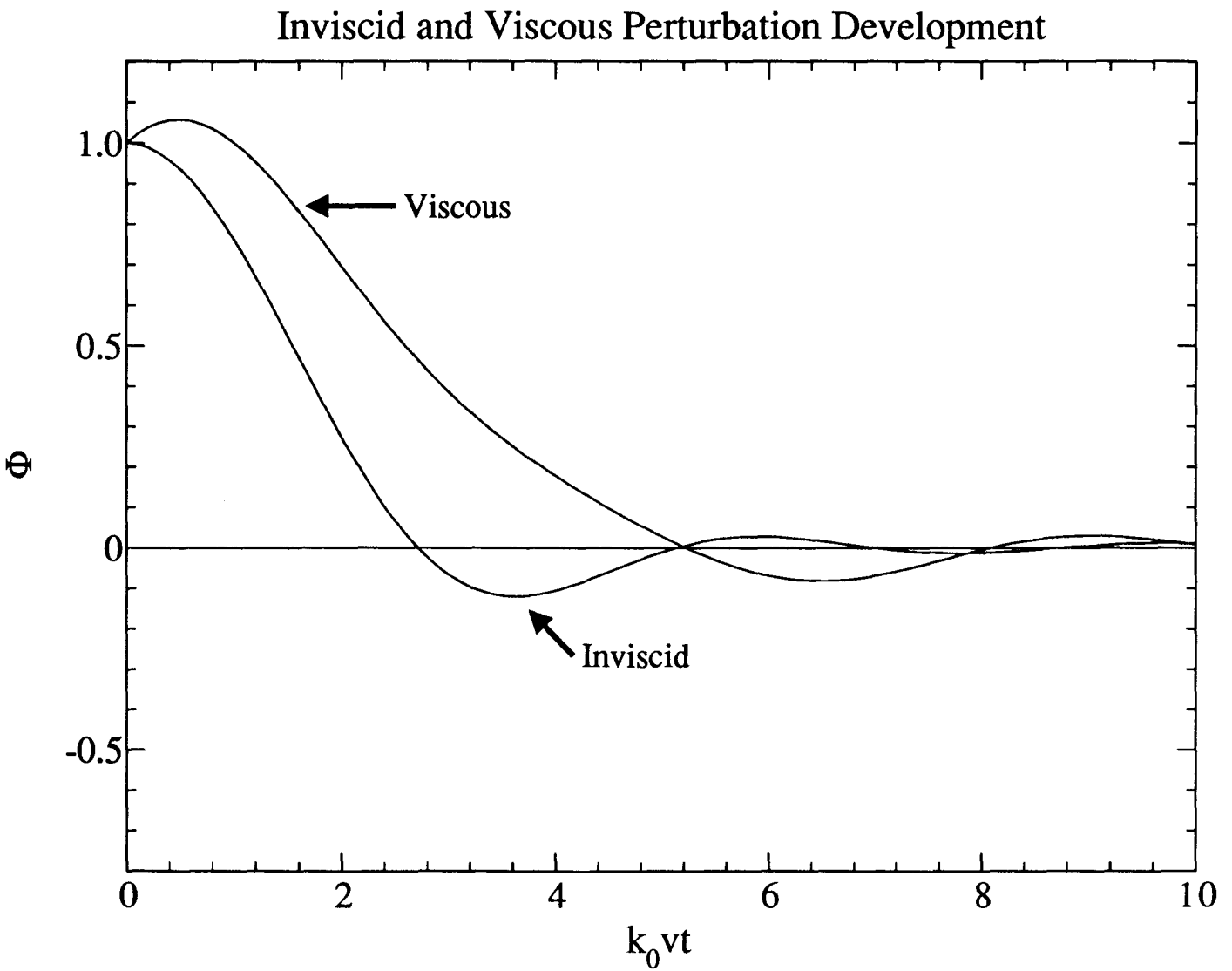
Inviscid and Viscous Perturbation Development
1.0
0.5
0
-0.5
Φ
Viscous
Inviscid
0
2
4
6
8
10
k_0vt

Figure 5b.

tial slope. Conversely, the bulk viscosity contribution is initially negative. This limit predicts, therefore, that shear viscosity will initially amplify the shock perturbations rather than dampen them. That this is contrary to the behavior reported by Sakharov *et al.*, [1965] may indicate the importance of the bulk viscosity in their experiments.

7. Viscous Perturbation with the BC of Zaidel' [1967]

For the purpose of comparison with Zaidel' [1967], we will derive the viscous perturbation term from the BC that he proposes. His BC (his Eqn. 2.4) are given by Eqn. 43, and neglect the bulk viscosity. Using these BC, and solving for the shock perturbation amplitude as before, we obtain the solution:

$$k_0 v\hat{\phi} = \frac{(1+\delta)z + 2\omega}{(1+\delta)z^2 + 2\omega z + \sigma(1-\delta)} \tag{89a}$$

(89b)

$$+ \frac{\sigma(1-\delta)}{3R_s(1-\beta^2)} \frac{z^2[12\beta^2 + 3(1+\beta^2)(1+\delta)] + 2\omega z[(3-\beta^2) + 3(1+\delta)] + [8+13(1-\beta^2)+3\delta(1-\beta^2)]}{\left[(1+\delta)z^2 + 2\omega z + \sigma(1-\delta)\right]^2}$$

$$+ \frac{\sigma(1-\delta)}{3R_s(1-\beta^2)} \frac{4\beta^2(z-\omega)(\omega^2+1) - 3\omega(1-\beta^2)[z^2(1+\delta)+2\omega z+(1-\delta)]}{\omega\left[(1+\delta)z^2 + 2\omega z + \sigma(1-\delta)\right]^2}, \tag{89c}$$

again breaking up into the inviscid component, Eqn. 89a, and viscous perturbations, Eqns. 89b and 89c. Equation 89b arises from the BC, and Eqn. 89c arises from the volume. The inverse Laplace transforms are obtained as described previously:

$$\phi = \frac{4\beta\varepsilon\sigma(1-\delta)}{\pi} \int_0^1 \frac{\cos(TX)\sqrt{1-X^2}\,\partial X}{\varepsilon^2X^4\left[(1+\delta)^2-4\beta^2\right] + 2\varepsilon X^2\left[2(1-\beta^2)-\sigma(1-\delta^2)\right] + \sigma^2(1-\delta)^2} \tag{90a}$$

(90b)

$$-\frac{2\sigma\mu(1-\delta)}{3\pi R_s\beta}\int_0^1 \partial X\, X\sqrt{1-X^2}\sin(TX)\frac{A\varepsilon^2X^4+B\varepsilon X^2+C}{\left[\varepsilon^2X^4[(1+\delta)^2-4\beta^2]+2\varepsilon X^2[2(1-\beta^2)-\sigma(1-\delta^2)]+\sigma^2(1-\delta)^2\right]^2}$$

(90c)

$$-\frac{32\mu\sigma(1-\delta)}{3\pi R_s}\int_0^1 \partial X\, X^2\sqrt{1-X^2}\Xi_C(T,X)\frac{\varepsilon X^2(1+\delta)-\sigma(1-\delta)}{\left[\varepsilon^2X^4[(1+\delta)^2-4\beta^2]+2\varepsilon X^2[2(1-\beta^2)-\sigma(1-\delta^2)]+\sigma^2(1-\delta)^2\right]^2},$$

where

$$A = 2\left[3(1+\delta)^3+8\beta^4(3+\delta)-4\beta^2(1-\delta)(5+2\delta)\right] \tag{91a}$$

$$B = 3(1+5\delta^2)-\beta^2(1-\delta)-9\beta^2\delta(1+\delta)-54\beta^2(1-\beta^2)+16\beta^4\delta - \sigma(1-\delta)\left[3(1+\delta)^2-4\beta^2(2-\delta-4\beta^2)\right] \tag{91b}$$

$$C = -2\sigma(1-\delta)\left[8\beta^4+12(1-\beta^2)(3+\delta)-\sigma(1-\delta)\left[3(1+\delta)+4\beta^2\right]\right] \tag{91c}$$

In Zaidel's Eqn. 2.8 [1967], the viscous perturbation has the form of Eqn. 90b but with different coefficients, and no term with the form of Eqn. 90c.

8. Summary of Approximations

The approximations used in the previous sections, and in the Zaidel' [1967] development, are:

- Initial conditions. The initial conditions, Eqn. 44, are clearly inexact, although they may suffice for the case $k_0\xi_0 \ll 1$. They call for a well-established smooth shock to be instantaneously perturbed without affecting the flow field behind the shock. In any real experiment the creation of a perturbed shock front will necessarily generate perturbations behind the front. This approximation is appropriate for the purposes of a stability analysis, but is inappropriate for the modeling of any real experiment.

- Small amplitude perturbations. This approximation manifests itself in two ways. First, the boundary condition at the shock front applies at $x=\xi$ and not $x=0$. We have used the latter, and have therefore implicitly required ξ to be small. Second, we have assumed that long wavelength perturbations greatly exceed shorter wavelength perturbations. When $k_0\xi_0$ is large, these shorter wavelength perturbation terms cannot be ignored. This assumption is not restrictive since we can solve for other, shorter wavelength, Fourier components of the solution.

- Far-field boundary conditions. To determine the function ξ as a function of time, an additional boundary condition is required. Zaidel' [1967] imagines a boundary infinitely far behind the shock front, and requires that all perturbations vanish at this point. In a real experiment there may be such a boundary at a finite distance behind the front, *e.g.*, at the interface between the sample and the explosive, or the sample and the projectile in a gun experiment. The influence of the position of this boundary must be determined to assess the applicability of his approach. A test of this assumption can be made by comparing the results calculated above with the results for a corrugated shock generated by the motion of a corrugated piston against a fluid sample. Freeman [1955] and Zaidel' [1958] considered the latter problem and derived solutions for an inviscid fluid.

- Negligible viscosity. By treating viscosity as a perturbation to an inviscid solution, we restrict the form of the solution to linear combinations of the inviscid eigenvectors. It is not immediately apparent that these eigenvectors adequately describe the flow field in the viscous case. If the inviscid eigenvectors are demonstrably appropriate, then successively higher-order viscous perturbations could be used to get increasingly more accurate estimates of the full viscous solution.

- Bulk viscosity. The bulk viscosity of water is greater than its shear viscosity at 1 bar [Lieber-

mann, 1949]. In Zaidel's [1967] analysis the bulk viscosity was neglected. According to the theory of absorption of sound [Landau and Lifshitz, 1959, pp. 298-302], the bulk viscosity and shear viscosity have approximately equal importance. If at high pressure the bulk and shear viscosities are similar in magnitude, this neglect could lead to factor of 2 errors, but not the several order of magnitude discrepancies described previously.

- Narrow shock width. As discussed in §2, the jump conditions employed in formulating the BC are exact only in the limit of a strictly discontinuous shock. The application of these conditions to viscous materials requires that the shock front width be very small compared to the radius of curvature of the shock. This condition is readily satisfied in practice.

- Linearizations. Linearizing approximations include the adiabatic ρ'—P' relationship, and the Newtonian viscosity approximations. These approximations are probably adequate when the strain rates and pressure perturbations are small, *i.e.*, $k_0\xi \ll 1$.

Qualitatively, the solutions obtained thus far are inconsistent with the published experimental data [Sakharov *et al.*, 1965; Mineev and Savinov, 1967]. In particular, the initial slope ($\dot{\phi}_0$) is negative in the experiments but positive, or slightly negative if $\kappa \gg \eta$, in the theory. The reason for this discrepancy will be shown to be a consequence of the initial conditions in §9 and §10.

Whether the viscosities calculated by the viscous perturbation method are reasonable depends in part on the validity of the viscous perturbation method for small but finite viscosity. This question is examined in §11.

9. Effect of Finite Perturbation Amplitude and Initial Conditions

Finite amplitude and initial conditions are intimately related since as amplitude increases the initial perturbations must also increase. Finite amplitude and initial conditions are coupled in a

second way as well. The solution, Eqn. 65, can be written:

$$\vec{u} = S^{-1}e^{\Lambda x}\left[e^{-\Lambda\xi}(S\vec{u})_{x=\xi} + \int_{\xi}^{x} e^{-\Lambda\chi}(S\vec{g})\partial\chi\right], \tag{92}$$

where we now specify the boundary conditions at the surface $x=\xi$, the true shock interface, rather than the approximation $x=0$. As before, we require that the perturbations vanish as $x\rightarrow\infty$, so the third component of the bracketed vector must vanish. When the initial conditions and viscosity are neglected, this reduces to the case where the third component of $S\vec{u}_{x=0}$ is zero, as before. When these terms are included, however, the integral expression in Eqn. 92 gives a second finite amplitude contribution.

The initial conditions are increasingly important as the product $k_0\xi_0$ becomes nonnegligible (*i.e.*, when the amplitude ξ_0 is comparable to or greater than the perturbation wavelength $\frac{2\pi}{k_0}$). An indication of the importance of these initial conditions can be gained by estimating an initial condition that is compatible with the boundary conditions. A simple family of solutions will be derived that is characterized by two adjustable parameters. The quantity α indicates how rapidly the initial perturbations decay away from the shock front, and the quantity S is the initial time decay of the shock front. A dimensional derivation of these quantities is presented in the next section.

Suppose that the initial flow parameters are of the form:

$$v_x(t=0,x) = f_x(x)e^{ik_0y} = f_x^0 e^{k_0(iy-\alpha x)} \tag{93a}$$

$$iv_y(t=0,x) = f_y(x)e^{ik_0y} = f_y^0 e^{k_0(iy-\alpha x)} \tag{93b}$$

$$\frac{P(t=0,x)}{\rho v} = f_p(x)e^{ik_0y} = f_p^0 e^{k_0(iy-\alpha x)}. \tag{93c}$$

From the inviscid boundary conditions, Eqn. 41, it can be shown that:

$$f_x^0 = \frac{(\sigma-1)(1+\delta)}{\sigma(1-\delta)}\dot{\xi}_0 \tag{94a}$$

$$f_y^0 = -k_0v(\sigma-1)\xi_0 \tag{94b}$$

$$f_p^0 = \frac{-2(\sigma-1)}{\sigma(1-\delta)}\dot{\xi}_0 \,. \tag{94c}$$

Defining the quantity

$$S \equiv \frac{\dot{\xi}_0}{k_0 v \xi_0} \,, \tag{95}$$

the IC contribution, Eqn. 68b, becomes:

$$k_0 v \hat{\phi}_{IC} = \frac{\beta^2(3+\delta)Sz + (1+\delta+2\beta^2)S\omega - \sigma(1-\delta)(1-\beta^2)}{[\beta^2 z + \omega + \alpha(1-\beta^2)][(1+\delta)z^2 + 2\omega z + \sigma(1-\delta)]} \,, \tag{96}$$

which can be inverted via the transformation Eqn. 81 into:

(97)

$$\phi_{IC} = \frac{2\beta\varepsilon}{\pi}\int_0^1 \frac{\partial X \sqrt{1-X^2}\left[\left[A_1\varepsilon^2X^4 + B_1\varepsilon X^2 + C_1\right]\cos TX - \mu X\left[D_1\varepsilon X^2 + E_1\right]\sin TX\right]}{\left[\beta^4\varepsilon^2X^4 - 2\beta^2\varepsilon X^2[1-\alpha^2(1+\beta^2)] + [1-\alpha^2(1-\beta^2)]^2\right]\left[\varepsilon^2X^4[(1+\delta)^2-4\beta^2] + 2\varepsilon X^2[2(1-\beta^2)-\sigma(1-\delta^2)] + \sigma^2(1-\delta)^2\right]} \,,$$

where:

$$A_1 = -\beta^2\left[S\alpha[(1+\delta)^2-4\beta^2] + \sigma(1-\delta)(1+\delta+2\beta^2)\right] \tag{98a}$$

(98b)

$$B_1 = S\alpha\left[(1+\delta)^2 + 4\beta^2(\delta+2\beta^2) + \beta^2\sigma(1-\delta)(1+\delta-2\beta^2) - \alpha^2(1-\beta^2)[(1+\delta)^2-4\beta^2] + \sigma(1-\delta)(1+\delta+2\beta^2)\right]$$
$$- \alpha^2\sigma(1-\delta)(1-\beta^2)(1+\delta-2\beta^2) + \beta^2\sigma^2(1-\delta)^2$$

$$C_1 = -\sigma(1-\delta)[1-\alpha^2(1-\beta^2)]\left[S\alpha(1+\delta+2\beta^2) + \sigma(1-\delta)\right] \tag{98c}$$

$$D_1 = 2\beta^2\left[S(1+\delta+2\beta^2) - S\beta^2\sigma(1-\delta) + S\alpha^2[(1+\delta)^2-4\beta^2] + \alpha\sigma(1-\delta)(2+\delta+\beta^2)\right] \tag{98d}$$

$$E_1 = -2\Big[S\left[(1+\delta+2\beta^2) - \alpha^2(1+\delta) - \alpha^2\beta^2(1-\delta-2\beta^2) - \beta^2\sigma(1-\delta) + \alpha^2\beta^2\sigma(1-\delta)(2+\delta+\beta^2)\right] \tag{98e}$$
$$+ \alpha\sigma(1-\delta)\left[(1-\beta^2) + \beta^2\sigma(1-\delta) - \alpha^2(1-\beta^2)^2\right]\Big] \,.$$

The transformation Eqn. 81 is valid, *i.e.*, the poles of Eqn. 96 lie within the unit circle $|W| < 1$, when Eqn. 75 is satisfied and

$$|\beta\mu\alpha| < 1 \,. \tag{99}$$

If this condition is violated, *i.e.*, if initial perturbations are attenuated more rapidly than

$\exp[-(\beta\mu)^{-1}k_0x]$, an instability will develop.

Now Eqn. 79 together with Eqn. 97 gives an estimate of the shock front perturbation in the inviscid limit subject to the initial conditions of Eqn. 93. The finite amplitude of the shock front has not yet been considered. To account for the finite amplitude as a perturbation to the linear result we use Eqn. 92. Requiring the solution to be finite as $x\to\infty$, we discover that ξ is given by the sum of Eqn. 79 and the product $\exp(-\alpha k_0\xi)$ times Eqn. 97, where the sum of Eqns. 79 and 97 is used in the exponential multiplier ξ':

$$\phi = \frac{4\beta\varepsilon\sigma(1-\delta)}{\pi}\int_0^1 \frac{\cos(Tx)\sqrt{1-x^2}\,dx}{\varepsilon^2x^4\left[(1+\delta)^2-4\beta^2\right] + 2\varepsilon x^2\left[2(1-\beta^2)-\sigma(1-\delta^2)\right] + \sigma^2(1-\delta)^2} + \tag{100}$$

$$\frac{2\beta\varepsilon\exp(-k_0\alpha\xi')}{\pi}\int_0^1 \frac{\partial X\sqrt{1-X^2}\left[(A_1\varepsilon^2X^4 + B_1\varepsilon X^2 + C_1)\cos TX - \mu X(D_1\varepsilon X^2 + E_1)\sin TX\right]}{\left[\beta^4\varepsilon^2X^4 - 2\beta^2\varepsilon X^2[1-\alpha^2(1+\beta^2)] + [1-\alpha^2(1-\beta^2)]^2\right]\left[\varepsilon^2X^4[(1+\delta)^2-4\beta^2] + 2\varepsilon X^2[2(1-\beta^2)-\sigma(1-\delta^2)] + \sigma^2(1-\delta)^2\right]}.$$

This correction, and the effect of the approximate initial conditions, is shown in Figure 6.

A viscous perturbation to this solution can be obtained by using this result to estimate the shear stresses in the inviscid case. Using these estimates, a new viscous perturbation can be derived that takes account of the finite initial conditions.

The viscous perturbation that arises from these initial conditions is:

$$k_0v\hat{\phi}_{visc} = \frac{2}{R_s(1-\delta)}\frac{\sum_{i=0}^{5}A_iz^i + \omega\sum_{i=0}^{4}B_iz^i}{\left[\beta^2z+\omega+\alpha(1-\beta^2)\right]^3\left[(1+\delta)z^2+2\omega z+\sigma(1-\delta)\right]^2} \tag{101a}$$

$$+ \frac{1}{2R_b(1-\delta)}\frac{\sum_{i=0}^{5}C_iz^i + \omega\sum_{i=0}^{4}D_iz^i}{\left[\beta^2z+\omega+\alpha(1-\beta^2)\right]^3\left[(1+\delta)z^2+2\omega z+\sigma(1-\delta)\right]^2} \tag{101b}$$

$$- \frac{(1-\beta^2)}{2R_b}\frac{E_0 + zE_1}{\omega\left[\beta^2z+\omega+\alpha(1-\beta^2)\right]^3\left[(1+\delta)z^2+2\omega z+\sigma(1-\delta)\right]^2} \tag{101c}$$

where the coefficients A_i, B_i, C_i, D_i, and E_i are given in Table I. For simplicity, both the surface

Figure 6: Effect of approximate initial conditions (Eqn. 97) on the inviscid solution, with and without finite amplitude correction (Eqn. 100), compared to inviscid solution without initial conditions (Eqn. 79). Evaluated with parameters listed in Table III.

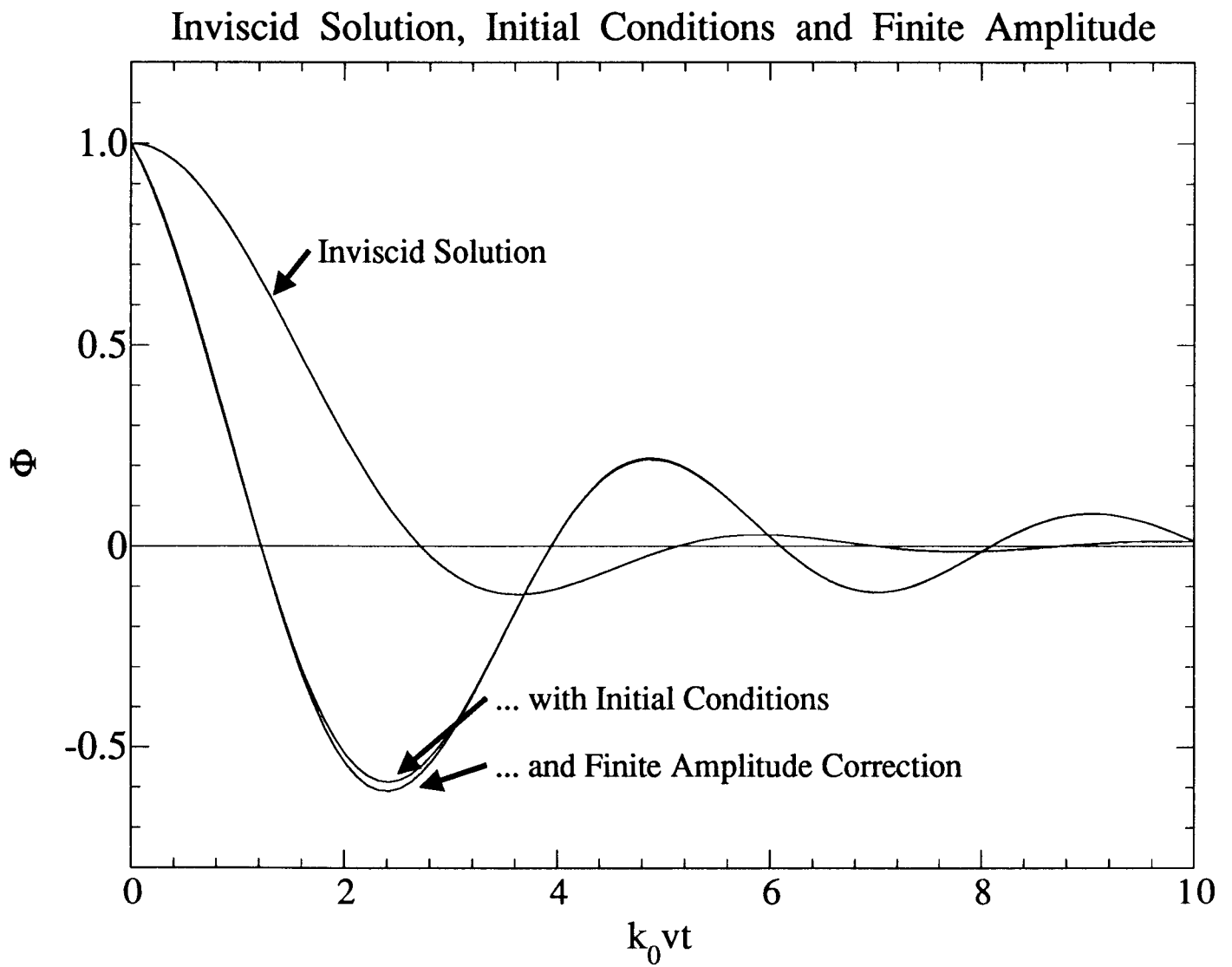
Inviscid Solution, Initial Conditions and Finite Amplitude
1.0
0.5
0
-0.5
Φ
Inviscid Solution
... with Initial Conditions
... and Finite Amplitude Correction
0
2
4
6
8
10
k0vt

Figure 6.

and volume contributions have been combined. The initial slope due to viscous terms, $\dot{\phi}_{visc}$, is determined to be:

$$\lim_{t\to 0}\dot{\phi}_{visc} = \frac{2k_0v\sigma(\beta+\delta)}{R_s(1+\delta+2\beta)} \tag{102}$$

$$-\frac{\beta k_0 v}{2R_b}\frac{S\alpha\left[(1+\delta)(1+6\delta+\delta^2+8\beta^2)+2\beta(1+3\delta)(3+\delta)\right]+\sigma(1-\delta)\left[(1+6\delta+\delta^2)+2\beta[3(1+\delta)+2\beta]\right]}{(1+\beta)(1-\delta)(1+\delta+2\beta)^2}$$

When $S<0$, $\alpha>0$, and $0<\delta<1$, the initial slope will be positive. The influence of viscosity is again to initially amplify the shock front perturbation relative to the inviscid case.

Defining

$$A_{even}(X) \equiv \sum_{i=0}(-\varepsilon)^i A_{2i}X^{2i} = A_0 - \varepsilon A_2X^2 + \varepsilon^2 A_2X^4 \tag{103a}$$

$$A_{odd}(X) \equiv \mu\sum_{i=1}(-\varepsilon)^{(i-1)}A_{2i-1}X^{2i-1} = \mu A_1X - \mu\varepsilon A_3X^3 + \mu\varepsilon A_5X^5\,, \tag{103b}$$

and similar even and odd polynomials for the coefficients B_i, C_i, and D_i, the integrals become:

(104a)

$$\phi_{visc} = -\frac{4\beta\varepsilon}{\pi R_s(1-\delta)(1-\beta^2)^3}\int_0^1 \partial X\,\sqrt{1-X^2}\times$$

$$\frac{\cos(TX)\left[A_{even}G_{even}-A_{odd}G_{odd}+B_{even}F_{even}-B_{odd}F_{odd}\right]-\sin(TX)\left[A_{even}G_{odd}+A_{odd}G_{even}+B_{even}F_{odd}+B_{odd}F_{even}\right]}{\left[\varepsilon^2X^4[(1+\delta)^2-4\beta^2]+2\varepsilon X^2[2(1-\beta^2)-\sigma(1-\delta^2)]+\sigma^2(1-\delta)^2\right]^2\left[\beta^4\varepsilon^2X^4-2\beta^2\varepsilon X^2[1-\alpha^2(1+\beta^2)]+[1-\alpha^2(1-\beta^2)]^2\right]^3}$$

(104b)

$$-\frac{\beta\varepsilon}{\pi R_b(1-\delta)(1-\beta^2)^3}\int_0^1 \partial X\,\sqrt{1-X^2}\times$$

$$\frac{\cos(TX)\left[C_{even}G_{even}-C_{odd}G_{odd}+D_{even}F_{even}-D_{odd}F_{odd}\right]-\sin(TX)\left[C_{even}G_{odd}+C_{odd}G_{even}+D_{even}F_{odd}+D_{odd}F_{even}\right]}{\left[\varepsilon^2X^4[(1+\delta)^2-4\beta^2]+2\varepsilon X^2[2(1-\beta^2)-\sigma(1-\delta^2)]+\sigma^2(1-\delta)^2\right]^2\left[\beta^4\varepsilon^2X^4-2\beta^2\varepsilon X^2[1-\alpha^2(1+\beta^2)]+[1-\alpha^2(1-\beta^2)]^2\right]^3}$$

Table I

$$A_0 = \sigma(1-\delta)(1-\beta^2)^2\Big[S[1+\alpha^2(1-\beta^2)](1+\delta+2\beta^2)+\alpha[3+\alpha^2(1-\beta^2)](3-\delta^2-2\beta^2)-2\alpha\sigma(1-\delta)(1-\beta^2)\Big]$$

$$A_1 = -(1-\beta^2)\Big[2S\alpha(1-\beta^2)(1-\delta^2)(1+\delta+2\beta^2)-\sigma(1-\delta)\Big[(2+3\delta-\delta^2)+\beta^2(7-3\delta-2\delta^2)-6\beta^4+2S\alpha(1-\beta^2)\Big[\delta(1+\delta)+4\beta^2(1+\delta)+2\beta^4\Big]$$
$$+\alpha^2(1-\beta^2)\Big[(4+9\delta-\delta^2)+\beta^2(1-2\delta)(5+\delta)-6\beta^4\Big]\Big]+\sigma^2(1-\delta)^2(1-\beta^2)\Big[\delta+2\beta^2+\alpha^2\delta(1-\beta^2)\Big]\Big]$$

$$A_2 = -(1-\beta^2)\Big[S\beta^2(1-\delta^2)\Big[(5+4\beta^2+3\delta)+\alpha^2(1-\beta^2)(3+\delta)\Big]-\sigma(1-\delta)\Big[S\beta^2\Big[(1+3\delta)(2+\delta)+\beta^2(11+7\delta)+2\beta^4\Big]+\alpha\Big[3\delta(1+\delta)$$
$$+\beta^2(23-8\delta)(1+\delta)-\beta^4(11+18\delta+\delta^2)-6\beta^6\Big]+S\alpha^2\beta^2(1-\beta^2)[1+4\delta+\delta^2+2\beta^2]+\alpha^3(1-\beta^2)^2[\delta(1+\delta)+2\beta^2]\Big]$$
$$+2\alpha\beta^2\sigma^2(1-\delta)^2(1-\beta^2)(1+\delta)\Big]$$

$$A_3 = -\beta^2\Big[2S\alpha(1-\beta^2)(1-\delta^2)[1+\delta+\beta^2(5+\delta)]-\sigma(1-\delta)\Big[(3+9\delta+2\delta^2)+2\beta^2(8-3\delta^2)-\beta^4(13+9\delta)-2\beta^6+2S\alpha(1-\beta^2)\Big[\delta(1+\delta)+\beta^2(4+7\delta+\delta^2)$$
$$+2\beta^4\Big]+3\alpha^2(1-\beta^2)^2[1+4\delta+\delta^2+2\beta^2]\Big]+\sigma^2(1-\delta)^2(1-\beta^2)\Big[\delta+\beta^2(2+\delta)\Big]\Big]$$

$$A_4 = -\beta^2\Big[S\beta^2(1-\delta^2)[5+3\delta+\beta^2(7+\delta)]-\sigma(1-\delta)\Big[3\alpha(1-\beta^2)\Big[\delta(1+\delta)+\beta^2(4+7\delta+\delta^2)+2\beta^4\Big]+S\beta^2\Big[(1+6\delta+3\delta^2)+\beta^2(1+\delta)(9+\delta)+2\beta^4\Big]\Big]\Big]$$

$$A_5 = \beta^4\sigma(1-\delta)\Big[(1+6\delta+3\delta^2)+\beta^2(1+\delta)(9+\delta)+2\beta^4\Big]$$

$$B_0 = \sigma(1-\delta)(1-\beta^2)\Big[(3-\delta^2-2\beta^2)+2S\alpha(1-\beta^2)(1+\delta+2\beta^2)+3\alpha^2(1-\beta^2)(3-\delta^2-2\beta^2)-\sigma(1-\delta)(1-\beta^2)[1+\alpha^2(1-\beta^2)]\Big]$$

$$B_1 = -(1-\beta^2)\Big[S(1-\delta^2)[1+\alpha^2(1-\beta^2)](1+2\beta^2+\delta)-\sigma(1-\delta)\Big[S\Big[\delta(1+\delta)+5\beta^2(1+\delta)+4\beta^4\Big]+\alpha\Big[(5-\delta)(1+2\delta)+\beta^2(1-\delta)(13+4\delta)-12\beta^4\Big]$$
$$+S\alpha^2(1-\beta^2)(1+\delta)(3\beta^2+\delta)+\alpha^3(1-\beta^2)^2(1+3\delta)\Big]+2\alpha\sigma^2(1-\delta)^2(1-\beta^2)(\beta^2+\delta)\Big]$$

$$B_2 = -4S\alpha\beta^2(1-\beta^2)(1-\delta^2)(2+\delta+\beta^2)+\sigma(1-\delta)\Big[\delta(1+\delta)+2\beta^2(5+4\delta-2\delta^2)-\beta^4\delta(9+\delta)-6\beta^6+2S\alpha\beta^2(1-\beta^2)\Big[(1+5\delta+2\delta^2)+\beta^2(5+3\delta)\Big]$$
$$+3\alpha^2(1-\beta^2)^2(1+\delta)(3\beta^2+\delta)\Big]-\beta^2\sigma^2(1-\delta)^2(1-\beta^2)(1+2\delta+\beta^2)$$

$$B_3 = -\beta^2\Big[S(1-\delta^2)\Big((1+\delta)+3\beta^2(3+\delta)+2\beta^4\Big) -\sigma(1-\delta)\Big[S\Big(\delta(1+\delta)+\beta^4(7+3\delta)+\beta^2(5+12\delta+3\delta^2)\Big) +3\alpha(1-\beta^2)\Big((1+5\delta+2\delta^2)+\beta^2(5+3\delta)\Big)\Big]\Big]$$

$$B_4 = \beta^2\sigma(1-\delta)\Big[\delta(1+\delta)+\beta^2(5+12\delta+3\delta^2)+\beta^4(7+3\delta)\Big]$$

$$C_0 = -\beta^2\sigma(1-\delta)(1-\beta^2)\Big[4S\delta(1-\beta^2)-2\alpha[3+\alpha^2(1-\beta^2)][2\delta-\beta^2(1+\delta)]+S\alpha^2\Big(4\delta(4+\delta)-\beta^2(1+\delta)(11+\delta)+2\beta^4(1+\delta)\Big) +\alpha\sigma(1-\delta)[4\delta-\beta^2(3+\delta)]\Big]$$

$$C_1 = -\beta^2\Big[2S\alpha(1-\beta^2)\Big(6\delta(3+\delta)-\beta^2(7+14\delta+3\delta^2)-2\beta^4(1-\delta)-2\alpha^2(1-\beta^2)(3+\delta)(\beta^2-\delta)\Big) -\sigma(1-\delta)\Big[2\beta^2\Big((1+5\delta)-3\beta^2(1+\delta)\Big) -S\alpha\Big(2\delta(7+\delta) +\beta^2(5-\delta)(1-\delta)-\beta^4(3+\delta)(5+\delta)+4\beta^6(1+\delta)\Big) +4\alpha^2\beta^2(1-\beta^2)^2(2+\delta)+2S\alpha^3(1-\beta^2)(3+\delta)(\beta^2-\delta)\Big] +\sigma^2(1-\delta)^2\Big[2\delta+\beta^2(1+\delta)-\beta^4(3+\delta) -2\alpha^2(1-\beta^2)(\beta^2-\delta)\Big]\Big]$$

$$C_2 = -\beta^2\Big[S\Big[2\Big(2\delta(3+\delta)+\beta^2(5+2\delta+\delta^2)-\beta^4(3+\delta)^2-2\beta^6(1-\delta)\Big) +\alpha^2(1-\beta^2)\Big(4\delta(3+\delta)(4+\delta)-\beta^2(19+19\delta+9\delta^2+\delta^3)-4\beta^4(5+3\delta)\Big)\Big] +\sigma(1-\delta)\Big[2S\beta^2\Big(+2(1+3\delta)+\beta^2(1-7\delta)-\beta^4(1+\delta)\Big) +\alpha(1-\beta^2)\Big(4\delta(6+\delta)-\beta^2(15+24\delta+\delta^2)-2\beta^4(5+\delta)\Big) +S\alpha^2\beta^2\Big((7+24\delta+5\delta^2) -\beta^2(21+18\delta+\delta^2)+2\beta^4(1+\delta)\Big) +2\alpha^3(1-\beta^2)^2[2\delta-\beta^2(1+\delta)]\Big] +\alpha\beta^2\sigma^2(1-\delta)^2\Big[(3+5\delta)-\beta^2(7+\delta)\Big]\Big]$$

$$C_3 = -\beta^2\Big[S\alpha\Big(2\delta(1+\delta)(3+\delta)+\beta^2(31+87\delta+25\delta^2+\delta^3)-\beta^4(37+83\delta+23\delta^2+\delta^3)-4\beta^6(3+\delta)-2\alpha^2(1-\beta^2)(3+\delta)(\beta^2-\delta)(1+\delta+2\beta^2)\Big) +\sigma(1-\delta)\Big[2\delta(3+\delta)+\beta^2(7+12\delta+\delta^2)-\beta^4(17+22\delta+\delta^2)-4\beta^6+S\alpha\beta^2\Big((1+14\delta+\delta^2)+\beta^2(13+10\delta+\delta^2)-4\beta^4(1+\delta)\Big) +2\alpha^2(1-\beta^2)\Big(\delta(3+\delta) +\beta^2(1+\delta)-2\beta^4(2+\delta)\Big)\Big] +\beta^2\sigma^2(1-\delta)^2[1+\delta+\beta^2(5+\delta)]\Big]$$

$$C_4 = -\beta^4\Big[S\Big[2\Big((1+6\delta+\delta^2)+\beta^2(3+\delta)(5+\delta)+2\beta^4(1-\delta)\Big) +\alpha^2\Big((7+51\delta+33\delta^2+5\delta^3)-\beta^2(23+27\delta+13\delta^2+\delta^3)-4\beta^4(5+3\delta)\Big)\Big] +\sigma(1-\delta)\Big[2S\beta^2[1+5\delta+\beta^2(1+\delta)]+\alpha\Big((9+30\delta+5\delta^2)-\beta^2(11+20\delta+\delta^2)-2\beta^4(5+\delta)\Big)\Big]\Big]$$

$$C_5 = -\beta^4\Big[S\alpha\Big((1+\delta)(1+6\delta+\delta^2)+\beta^2(3+\delta)(7+16\delta+\delta^2)+8\beta^4(1+\delta)\Big) +\sigma(1-\delta)\Big[(1+6\delta+\delta^2)+\beta^2(1+\delta)(17+\delta)+4\beta^4\Big]\Big]$$

$$D_0 = S\alpha(1-\beta^2)(1-\delta)\left[(1-\delta^2)+8\beta^2\right]-\sigma(1-\delta)\left[(1-\delta^2)+\beta^2(1-6\delta+\delta^2)+2\beta^4(1+\delta)+S\alpha\beta^2\left\{(1+12\delta+3\delta^2)-\beta^2(9+14\delta+\delta^2)+2\beta^4(1+3\delta)\right\}\right.$$
$$\left.-2\alpha^2(1-\beta^2)^2\left\{(1-\delta)+3\beta^2(1+\delta)\right\}-2S\alpha^3\beta^2(1-\beta^2)(3+\delta)(\beta^2-\delta)\right]+\beta^2\sigma^2(1-\delta)^2\left[(1-3\delta)+\beta^2(1+\delta)+2\alpha^2(1-\beta^2)(\beta^2-\delta)\right]$$

$$D_1 = S\left[2\beta^2\left\{(1-6\delta-3\delta^2)+\beta^2(1+\delta)(3+\delta)+2\beta^4(1-\delta)\right\}+\alpha^2(1-\beta^2)\left\{(1-\delta)(1+\delta)^2-4\beta^2(1+8\delta+3\delta^2)+4\beta^4(2+\delta)(3+\delta)\right\}\right]-\sigma(1-\delta)\left[2S\beta^2\left\{2\delta\right.\right.$$
$$\left.+\beta^2(3-\delta)-\beta^4(1+3\delta)\right\}-\alpha(1-\beta^2)\left\{(1-\delta^2)+4\beta^2(1-\delta)+2\beta^4(7+5\delta)\right\}+S\alpha^2\beta^2\left\{(1+16\delta+3\delta^2)-\beta^2(3+6\delta-\delta^2)-2\beta^4(5+\delta)\right\}$$
$$\left.+2\alpha^3\beta^2(1-\beta^2)^2(1-\delta)\right]-\alpha\beta^2\sigma^2(1-\delta)^2\left[(1+3\delta)-\beta^2(1-\delta)-4\beta^4\right]$$

$$D_2 = -\beta^2\left[S\alpha\left\{(1+41\delta+19\delta^2+3\delta^3)+\beta^2(1-\delta)(17+6\delta+\delta^2)-4\beta^4(3+\delta)^2-2\alpha^2(1-\beta^2)(3+\delta)^2(\beta^2-\delta)\right\}-\sigma(1-\delta)\left[(1-10\delta-3\delta^2)\right.\right.$$
$$\left.\left.+\beta^2(5+10\delta+\delta^2)+4\beta^4(2+\delta)-2S\alpha\beta^2\left\{(5+14\delta+\delta^2)-4\beta^2\delta\right\}-2\alpha^2(1-\beta^2)\left\{(1+8\delta+\delta^2)-2\beta^2(2+3\delta)\right\}\right]+2\beta^2\sigma^2(1-\delta)^2[2+\delta+\beta^2]\right]$$

$$D_3 = -\beta^2\left[S\left\{\alpha^2\left\{(1+\delta)(1+12\delta+3\delta^2)+\beta^2(7+\delta)(1+6\delta+\delta^2)-4\beta^4(11+11\delta+2\delta^2)\right\}+4\beta^2\left\{(4+7\delta+\delta^2)+\beta^2(5-\delta)\right\}\right\}\right.$$
$$\left.+\sigma(1-\delta)\left\{4S\beta^2[\delta+\beta^2(1+2\delta)]+\alpha\left\{(1+12\delta+3\delta^2)+\beta^2(1+\delta)(11+\delta)-8\beta^4(3+2\delta)\right\}\right\}\right]$$

$$D_4 = -2\beta^4\left[S\alpha\left\{(4+17\delta+10\delta^2+\delta^3)+\beta^2(11+18\delta+3\delta^2)\right\}+\sigma(1-\delta)\left\{(4+9\delta+\delta^2)+\beta^2(7+3\delta)\right\}\right]$$

$$E_0 = S\alpha(1-\beta^2)\left\{(1-\delta^2)+8\beta^2\right\}-\sigma(1-\delta)\left[(1+\delta)+\beta^2(1-\delta)+S\alpha\beta^2\left\{(1-\delta)-4\beta^2\right\}-2\alpha^2(1-\beta^2)(1+2\beta^2)\right]+\beta^2\sigma^2(1-\delta)^2$$

$$E_1 = S\left[2\beta^2(1+\delta+2\beta^2)+\alpha^2(1-\beta^2)((1+\delta)^2-4\beta^2)\right]-\sigma(1-\delta)\left[2S\beta^4-\alpha\left\{(1+\delta)+\beta^2(3-\delta)+2\beta^4\right\}+S\alpha^2\beta^2(1+\delta+2\beta^2)+2\alpha^3\beta^2(1-\beta^2)\right]$$
$$-\alpha\beta^2\sigma^2(1-\delta)^2$$

Table II

$$F_{even}(X) = \alpha\sigma^2(1-\delta)^2(1-\beta^2)^2\left[3+\alpha^2(1-\beta^2)\right]\left[1-\alpha^2(1-\beta^2)\right]^3$$

$$-2\varepsilon X^2\alpha(1-\beta^2)\left[1-\alpha^2(1-\beta^2)\right]\left[2\left[3+\alpha^2(1-\beta^2)\right](1-\beta^2)^2\left[1-\alpha^2(1-\beta^2)\right]^2+\sigma(1-\delta)(1-\beta^2)\left[1-\alpha^2(1-\beta^2)\right]\left[3(1+\delta+8\beta^2)\right.\right.$$
$$\left.\left.-2\alpha^2(1-\beta^2)(1+\delta-12\beta^2)-\alpha^4(1-\beta^2)^2(1+\delta)\right]+6\beta^2\sigma^2(1-\delta)^2\left[(1+\beta^2)-\alpha^2(1-3\beta^2)(1-\beta^2)\right]\right]$$

$$+\varepsilon^2X^4\alpha\left[(1-\beta^2)^2\left[1-\alpha^2(1-\beta^2)\right]\left[3\left[(1+\delta)^2+4\beta^2(9+4\delta)+16\beta^4\right]-\alpha^2(1-\beta^2)\left[5(1+\delta)^2+68\beta^2-144\beta^4\right]+\alpha^4(1-\beta^2)^2\left[(1+\delta)^2\right.\right.$$
$$\left.-4\beta^2(11+12\delta)\right]+\alpha^6(1-\beta^2)^3\left[(1+\delta)^2+4\beta^2\right]\Big]+8\beta^2\sigma(1-\delta)(1-\beta^2)\left[3\left[(1+\delta)+\beta^2(9+\delta)-2\beta^4\right]-2\alpha^2(1-\beta^2)\left[3(1+\delta)+3\beta^2(2-\delta)\right.\right.$$
$$\left.-14\beta^4\right]+3\alpha^4(1-\beta^2)^2\left[(1+\delta)-\beta^2(7+3\delta)-2\beta^4\right]+6\alpha^6\beta^2(1-\beta^2)^3\Big]+6\beta^4\sigma^2(1-\delta)^2\left[(3+6\beta^2-5\beta^4)-4\alpha^2(1-\beta^2)(1-2\beta^2-\beta^4)\right.$$
$$\left.+\alpha^4(1-\beta^2)^2(1-6\beta^2+\beta^4)\right]\Big]$$

$$-4\varepsilon^3X^6\alpha\beta^2\left[(1-\beta^2)\left[3\left[(1+\delta)^2+\beta^2(27+18\delta+\delta^2)+4\beta^4(3-\delta)-10\beta^6\right]-2\alpha^2(1-\beta^2)\left[3(1+\delta)^2+3\beta^2(13+4\delta-\delta^2)-4\beta^4(16+7\delta)-12\beta^6\right]\right.\right.$$
$$+3\alpha^4(1-\beta^2)^2\left[(1+\delta)^2-\beta^2(5+14\delta+3\delta^2)-4\beta^4(7+\delta)+2\beta^6\right]+12\alpha^6\beta^2(1-\beta^2)^3(1+\delta)\Big]+\beta^2\sigma(1-\delta)\left[3\left[3(1+\delta)+6\beta^2(5+\delta)-\beta^4(17+5\delta)\right.\right.$$
$$\left.\left.-4\beta^6\right]-4\alpha^2(1-\beta^2)\left[3(1+\delta)+3\beta^2(1-2\delta)-\beta^4(31+3\delta)+3\beta^6\right]+3\alpha^4(1-\beta^2)^2\left[(1+\delta)-\beta^4(3-\delta)-2\beta^2(5+3\delta)\right]\right]$$
$$\left.+\beta^4\sigma^2(1-\delta)^2\left[3(1+4\beta^2-\beta^4)-2\alpha^2(1+\beta^2)(1-4\beta^2+\beta^4)\right]\right]$$

$$+\varepsilon^4X^8\alpha\beta^4\left[2\left[3\left[3(1+\delta)^2+2\beta^2(37+30\delta+3\delta^2)+\beta^4(19-34\delta-5\delta^2)-4\beta^6(17+2\delta)+8\beta^8\right]-4\alpha^2(1-\beta^2)\left[3(1+\delta)^2+2\beta^2(14+3\delta-3\delta^2)\right.\right.\right.$$
$$\left.\left.-\beta^4(5+3\delta)(19+\delta)-6\beta^6(3-\delta)+4\beta^8\right]+3\alpha^4(1-\beta^2)^2\left[(1+\delta)^2-2\beta^2(5+10\delta+3\delta^2)-\beta^4(31+6\delta-\delta^2)+4\beta^6\right]\right]$$
$$+8\beta^2\sigma(1-\delta)\left[3\left[(1+\delta)+4\beta^2(3+\delta)+\beta^4(1-\delta)-2\beta^6\right]-2\alpha^2\left[(1+\delta)-3\beta^2\delta-\beta^4(17+3\delta)+\beta^6(4+\delta)\right]\right]+3\beta^4\sigma^2(1-\delta)^2(1+6\beta^2+\beta^4)\Big]$$

$$-2\varepsilon^5X^{10}\alpha\beta^6\left[2\left[3\left[(1+\delta)^2+\beta^2(25+24\delta+4\delta^2)+\beta^4(6-\delta)(4+\delta)-\beta^6(13+4\delta)-\beta^8\right]-2\alpha^2\left[(1+\delta)^2+\beta^2(7-3\delta^2)-\beta^4(43+34\delta+3\delta^2)\right.\right.\right.$$
$$\left.\left.\left.-\beta^6(5-8\delta-\delta^2)+4\beta^8\right]\right]+3\beta^2\sigma(1-\delta)\left[(1+\delta)+2\beta^2(7+3\delta)+\beta^4(9+\delta)\right]\Big]$$

$$+3\varepsilon^6X^{12}\alpha\beta^8\left[(1+\delta)^2+2\beta^2(13+14\delta+3\delta^2)+\beta^4(41+18\delta+\delta^2)+4\beta^6\right]$$

$$F_{odd}(X) = \mu X(1-\beta^2)\left[1-\alpha^2(1-\beta^2)\right]^2\sigma(1-\delta)\left[4(1-\beta^2)\left[1+3\alpha^2(1-\beta^2)\right]\left[1-\alpha^2(1-\beta^2)\right]+3\beta^2\sigma(1-\delta)\left[1+6\alpha^2(1-\beta^2)+\alpha^4(1-\beta^2)^2\right]\right]$$

$$-2\mu\varepsilon X^3\left[2(1-\beta^2)^2\left[1-\alpha^2(1-\beta^2)\right]^2\left[(1+\delta+3\beta^2)+2\alpha^2(1-\beta^2)(1+\delta+9\beta^2)-3\alpha^4(1-\beta^2)^2(1+\delta-\beta^2)\right]+\beta^2\sigma(1-\delta)(1-\beta^2)\left[1-\alpha^2(1-\beta^2)\right]\times\right.$$
$$\left.\left[(13+3\delta)+\alpha^2(1-\beta^2)[5(5+3\delta)+72\beta^2]-\alpha^4(1-\beta^2)^2(41+15\delta-24\beta^2)+3\alpha^6(1-\beta^2)^3(1-\delta)\right]+2\beta^4\sigma^2(1-\delta)^2\left[(3-2\beta^2)+3\alpha^2(1-\beta^2)(3+2\beta^2)\right.\right.$$
$$\left.\left.-3\alpha^4(5-2\beta^2)(1-\beta^2)^2+\alpha^6(3-2\beta^2)(1-\beta^2)^3\right]\right]$$

$$+\beta^2\mu\varepsilon^2X^5\left[(1-\beta^2)\left[(1+\delta)(23+3\delta)+60\beta^2-32\beta^4+12\alpha^2(1-\beta^2)\left[(1+\delta)^2+4\beta^2(7+3\delta)+8\beta^4\right]-6\alpha^4(1-\beta^2)^2\left[(1+\delta)(17+5\delta)\right.\right.\right.$$
$$\left.\left.+4\beta^2(19+4\delta)-16\beta^4\right]+4\alpha^6(1-\beta^2)^3\left[(1+\delta)(19+3\delta)+12\beta^2(1-\delta)-8\beta^4\right]-3\alpha^8(1-\beta^2)^4\left[(3-\delta)(1+\delta)-4\beta^2\right]\right]+8\beta^2\sigma(1-\delta)\left[(8+3\delta)\right.$$
$$\left.-2\beta^2(1+\delta)-3\beta^4+3\alpha^2(1-\beta^2)\left[3(1+\delta)+2\beta^2(10+\delta)-4\beta^4\right]-3\alpha^4(1-\beta^2)^2\left[(8+5\delta)+2\beta^2(3-\delta)-5\beta^4\right]\right.$$
$$\left.+\alpha^6(1-\beta^2)^3\left[(7+3\delta)-2\beta^2(4+\delta)\right]\right]+6\beta^4\sigma^2(1-\delta)^2\left[(3-\beta^2)+2\alpha^2(3+4\beta^2-3\beta^4)-\alpha^4(1-\beta^2)^2(5+\beta^2)\right]\right]$$

$$-4\beta^4\mu\varepsilon^3X^7\left[(1+\delta)(13+3\delta)+2\beta^2(14-2\delta-\delta^2)-2\beta^4(19+3\delta)+6\beta^6+3\alpha^2(1-\beta^2)\left[3(1+\delta)^2+2\beta^2(31+20\delta+\delta^2)+8\beta^4(2-\delta)-12\beta^6\right]\right.$$
$$\left.-3\alpha^4(1-\beta^2)^2\left[(1+\delta)(11+5\delta)+2\beta^2(22+6\delta-\delta^2)-2\beta^4(13+5\delta)-2\beta^6\right]+\alpha^6(1-\beta^2)^3\left[(1+\delta)(11+3\delta)-2\beta^2(1+8\delta+\delta^2)-8\beta^4\right]\right.$$
$$\left.+\beta^2\sigma(1-\delta)\left[(19+9\delta)+\beta^2(7-3\delta)-8\beta^4+6\alpha^2\left[3(1+\delta)+2\beta^2(11+2\delta)-\beta^4(11+3\delta)-2\beta^6\right]-3\alpha^4(1-\beta^2)^2[7+5\delta+\beta^2(11+\delta)]\right]\right.$$
$$\left.+3\beta^4\sigma^2(1-\delta)^2[1+\alpha^2(1+3\beta^2)]\right]$$

$$+\beta^6\mu\varepsilon^4X^9\left[2\left[(1+\delta)(29+9\delta)+\beta^2(77+14\delta-3\delta^2)-4\beta^4(13+4\delta)+6\alpha^2\left[3(1+\delta)^2+4\beta^2(14+11\delta+\delta^2)+\beta^4(5-22\delta-3\delta^2)-4\beta^6(7+\delta)\right]\right.\right.$$
$$\left.\left.-3\alpha^4(1-\beta^2)^2\left[(1+\delta)(9+5\delta)+\beta^2(41+22\delta+\delta^2)+4\beta^4\right]\right]+4\beta^2\sigma(1-\delta)\left[(11+6\delta)+10\beta^2-3\beta^4+6\alpha^2\left[(1+\delta)+3\beta^2(3+\delta)+2\beta^4\right]\right]\right.$$
$$\left.+\beta^4\sigma^2(1-\delta)^2(3+\beta^2)\right]$$

$$-2\beta^8\mu\varepsilon^5X^{11}\left[2\left[(8+3\delta+\beta^2)\left[(1+\delta)+3\beta^2-\beta^4\right]+3\alpha^2\left[(1+\delta)^2+4\beta^4(4+\delta)+\beta^2(19+18\delta+3\delta^2)\right]\right]+\beta^2\sigma(1-\delta)[5+3\delta+\beta^2(7+\delta)]\right]$$

$$+\beta^{10}\mu\varepsilon^6X^{13}\left[(1+\delta)(7+3\delta)+\beta^2(25+14\delta+\delta^2)+4\beta^4\right]$$

$$G_{even}(X) = -\sigma^2(1-\delta)^2(1-\beta^2)\left[1+3\alpha^2(1-\beta^2)\right]\left[1-\alpha^2(1-\beta^2)\right]^3$$
$$+2\varepsilon X^2\left[2(1-\beta^2)^2\left[1+3\alpha^2(1-\beta^2)\right]\left[1-\alpha^2(1-\beta^2)\right]^3+\sigma(1-\delta)(1-\beta^2)\left[1-\alpha^2(1-\beta^2)\right]^2\left[(1+\delta)+6\beta^2+2\alpha^2(1-\beta^2)(1+\delta+18\beta^2)\right.\right.$$
$$\left.\left.-3\alpha^4(1-\beta^2)^2(1+\delta-2\beta^2)\right]+2\beta^2\sigma^2(1-\delta)^2\left[1-\alpha^2(1-\beta^2)\right]\left[1+\alpha^2(1+9\beta^2)(1-\beta^2)-\alpha^4(2-3\beta^2)(1-\beta^2)^2\right]\right]$$

$$-\varepsilon^2X^4\Big[(1-\beta^2)\Big[1-\alpha^2(1-\beta^2)\Big]\Big[(1+\delta)^2+4\beta^2(8+3\delta)+\alpha^2(1-\beta^2)\Big((1+\delta)^2+20\beta^2(4+3\delta)+144\beta^4\Big]-\alpha^4(1-\beta^2)^2\Big[5(1+\delta)^2+4\beta^2(28+15\delta)$$
$$-48\beta^4\Big]+3\alpha^6(1-\beta^2)^3[(1+\delta)^2-4\delta\beta^2]\Big]+8\beta^2\sigma(1-\delta)\Big[[1+\delta+2\beta^2(3-2\beta^2)]+3\alpha^2\beta^2(1-\beta^2)[3(3+\delta)+4\beta^2]$$
$$-3\alpha^4(1-\beta^2)^2\Big[(1+\delta)+2\beta^2(6+\delta)-4\beta^4\Big]+\alpha^6(1-\beta^2)^3\Big[2(1+\delta)+3\beta^2(1-\delta)-4\beta^4\Big]\Big]+6\beta^4\sigma^2(1-\delta)^2\Big[(1+\beta^2)+4\alpha^2\beta^2(3-\beta^2)$$
$$-\alpha^4(1-\beta^2)^2(1+5\beta^2)\Big]\Big]$$

$$+4\varepsilon^3X^6\beta^2\Big[(1+\delta)^2+2\beta^2(11+6\delta)-8\beta^4(1+\delta)-6\beta^6+3\alpha^2\beta^2(1-\beta^2)\Big[3(1+\delta)(5+\delta)+4\beta^2(11+2\delta)-8\beta^4\Big]-3\alpha^4(1-\beta^2)^2\Big[(1+\delta)^2$$
$$+2\beta^2(14+12\delta+\delta^2)+8\beta^4(1-\delta)-10\beta^6\Big]+\alpha^6(1-\beta^2)^3\Big[2(1+\delta)^2+\beta^2(17+6\delta-3\delta^2)-4\beta^4(5+2\delta)\Big]+3\beta^2\sigma(1-\delta)\Big[(1+\delta)+\beta^2(7+\delta)$$
$$-2\beta^4+4\alpha^2\beta^2\Big[3(2+\delta)+\beta^2(3-\delta)-3\beta^4\Big]-\alpha^4(1-\beta^2)^2\Big[(1+\delta)+2\beta^4+5\beta^2(3+\delta)\Big]\Big]+\beta^4\sigma^2(1-\delta)^2\Big[1+2\beta^2+3\alpha^2\beta^2(3+\beta^2)\Big]\Big]$$

$$-\varepsilon^4X^8\beta^4\Big[2\Big[3(1+\delta)^2+\beta^2(59+42\delta+3\delta^2)+4\beta^4(2-3\delta)-16\beta^6+12\alpha^2\beta^2\Big[3(1+\delta)(3+\delta)+\beta^2(25+6\delta-\delta^2)-2\beta^4(7+3\delta)-2\beta^6\Big]$$
$$-3\alpha^4(1-\beta^2)^2\Big[(1+\delta)^2+\beta^2(29+30\delta+5\delta^2)+4\beta^4(6+\delta)\Big]\Big]+8\beta^2\sigma(1-\delta)\Big[(1+\delta)+2\beta^2(4+\delta)+3\alpha^2\beta^2\Big[(5+3\delta)+\beta^2(7+\delta)\Big]\Big]$$
$$+\beta^4\sigma^2(1-\delta)^2(1+3\beta^2)\Big]$$

$$+2\varepsilon^5X^{10}\beta^6\Big[2\Big[(1+\delta)^2+\beta^2(19+16\delta+2\delta^2)+10\beta^4-3\beta^6+3\alpha^2\beta^2\Big[(1+\delta)(7+3\delta)+\beta^2(25+14\delta+\delta^2)+4\beta^4\Big]\Big]$$
$$+\beta^2\sigma(1-\delta)\Big[(1+\delta)+3\beta^2(3+\delta)+2\beta^4\Big]\Big]$$

$$-\beta^8\varepsilon^6X^{12}\Big[(1+\delta)^2+\beta^2(19+18\delta+3\delta^2)+4\beta^4(4+\delta)\Big]$$

$$G_{odd}(X) = -4\mu X\alpha\sigma(1-\delta)(1-\beta^2)\Big[1-\alpha^2(1-\beta^2)\Big]^2\Big[\Big[3+\alpha^2(1-\beta^2)\Big](1-\beta^2)\Big[1-\alpha^2(1-\beta^2)\Big]+3\beta^2\sigma(1-\delta)\Big[1+\alpha^2(1-\beta^2)\Big]\Big]$$
$$+4\mu\varepsilon X^3\alpha\Big[(1-\beta^2)^2\Big[1-\alpha^2(1-\beta^2)\Big]^2\Big[3(1+\delta+4\beta^2)-2\alpha^2(1-\beta^2)(1+\delta-6\beta^2)-\alpha^4(1-\beta^2)^2(1+\delta)\Big]+6\beta^2\sigma(1-\delta)(1-\beta^2)\Big[1-\alpha^2(1-\beta^2)\Big]\times$$
$$\Big[(3+\delta+2\beta^2)-2\alpha^2(1-3\beta^2)(1-\beta^2)-\alpha^4(1-\beta^2)^2(1+\delta)\Big]+\beta^4\sigma^2(1-\delta)^2\Big[3(3-\beta^2)-2\alpha^2(1-\beta^2)(3-7\beta^2)-3\alpha^4(1-\beta^2)^2(1+\beta^2)\Big]\Big]$$

$$-4\mu\varepsilon^2X^5\beta^2\alpha\Big[(1-\beta^2)\Big[3\Big[(1+\delta)(5+\delta)+4\beta^2(5+\delta)-4\beta^4\Big]-\alpha^2(1-\beta^2)\Big[3(1+\delta)(9+\delta)+12\beta^2(1-2\delta)-56\beta^4\Big]+3\alpha^4(1-\beta^2)^2\Big[(3-\delta)(1+\delta)$$
$$-4\beta^2(5+3\delta)-4\beta^4\Big]+3\alpha^6(1-\beta^2)^3\Big[(1+\delta)^2+4\beta^2\Big]\Big]+2\beta^2\sigma(1-\delta)\Big[3\Big[3(2+\delta)+\beta^2(5-\delta)-5\beta^4\Big]-2\alpha^2(1-\beta^2)\Big[3(3+\delta)-\beta^2(19+7\delta)$$
$$-6\beta^4\Big]-3\alpha^4(1-\beta^2)^2\Big[\delta+\beta^2(7+\delta)-\beta^4\Big]\Big]+\beta^4\sigma^2(1-\delta)^2\Big[3(3+\beta^2)-\alpha^2(3-14\beta^2+3\beta^4)\Big]\Big]$$

$$+4\mu\varepsilon^3X^7\alpha\beta^4\Big[3\Big[3(1+\delta)(3+\delta)+\beta^2(35+10\delta-\delta^2)-2\beta^4(11+5\delta)-4\beta^6\Big]-2\alpha^2(1-\beta^2)\Big[3(1+\delta)(5+\delta)-\beta^2(13+38\delta+7\delta^2)-4\beta^4(17+3\delta)$$
$$+6\beta^6\Big]+3\alpha^4(1-\beta^2)^2\Big[(1-\delta^2)-\beta^2(17+14\delta+\delta^2)-2\beta^4(1-\delta)\Big]+2\beta^2\sigma(1-\delta)\Big[3\Big[(5+3\delta)+\beta^2(9+\delta)-2\beta^4\Big]-\alpha^2\Big[(7+3\delta)-2\beta^2(13+7\delta)$$
$$-3\beta^4(3-\delta)+4\beta^6\Big]\Big]+3\beta^4\sigma^2(1-\delta)^2(1+\beta^2)\Big]$$

$$-4\mu\varepsilon^4X^9\alpha\beta^6\Big[3\Big[(1+\delta)(7+3\delta)+\beta^2(33+18\delta+\delta^2)-4\beta^4\delta-4\beta^6\Big]-\alpha^2\Big[(1+\delta)(11+3\delta)-2\beta^2(13+26\delta+7\delta^2)-\beta^4(77+18\delta-3\delta^2)+4\beta^6(5+2\delta)\Big]$$
$$+3\beta^2\sigma(1-\delta)\Big[(3+2\delta)+2\beta^2(4+\delta)+\beta^4\Big]\Big]$$

$$+12\alpha\beta^8\mu\varepsilon^5X^{11}(2+\delta+\beta^2)[1+\delta+\beta^2(5+\delta)]$$

(104c)

$$+\frac{\mu}{\pi R_b(1-\beta^2)^2}\int_0^1 \partial X\,\sqrt{1-X^2}\times$$

$$\frac{\Xi_C(T,X)\left[F_0G_{even}-\mu F_1 X\,G_{odd}\right]-\Xi_S(T,X)\left[F_0G_{odd}+\mu F_1 X_{odd}G_{even}\right]}{\left[\varepsilon^2X^4[(1+\delta)^2-4\beta^2]+2\varepsilon X^2[2(1-\beta^2)-\sigma(1-\delta^2)]+\sigma^2(1-\delta)^2\right]^2\left[\beta^4\varepsilon^2X^4-2\beta^2\varepsilon X^2[1-\alpha^2(1+\beta^2)]+[1-\alpha^2(1-\beta^2)]^2\right]^3},$$

where

$$\Xi_S(T,X) \equiv \int_0^T \partial u\,\sin(uX)\,J_0(T-u) \tag{105}$$

by analogy to the function $\Xi_C(T,X)$ defined by Eqn. 87, and the polynomials $F_{even}(X)$, $F_{odd}(X)$, $G_{even}(X)$, and $G_{odd}(X)$ are given in Table II. This viscous perturbation is shown in Figure 7.

10. Dimensional Analysis of the Quantities α and S

A simple dimensional argument can be made for the semiquantitative estimation of the parameters α and S that we hypothesize to characterize the initial shock perturbation structure. First recall the specific experimental geometry of Sakharov *et al.* [1965] (Figs. 1, 3 and 4). A section of sample material has a set of sinusoidal grooves cut in its upper surface. The planar surface of a wedge of identical sample material is then placed over these sinusoidal grooves. For fluid samples, thin metal or plastic containers were used to reproduce this geometry [Mineev and Zaidel', 1968]. The containers themselves are assumed to have negligible impact on the perturbation development. A shock is initiated in the first, grooved, sample. When the shock front reaches the grooves, the shocked specimen will begin to release adiabatically to ambient pressure. 180° out of phase with these releasing regions, the shock will continue unperturbed to approach the upper sample wedge (Fig. 4b). In the limit $k_0 \to 0$ the "normal" regions 180° out of phase with the releasing regions will be unaffected by this release process.

Figure 7: Viscous perturbation calculation (Eqns. 100 and 104) compared to inviscid calculation (Eqn. 100), both with approximate initial conditions and finite amplitude correction. Evaluated with parameters listed in Table III, $R_s = 4.32$, and $\kappa = \eta$.

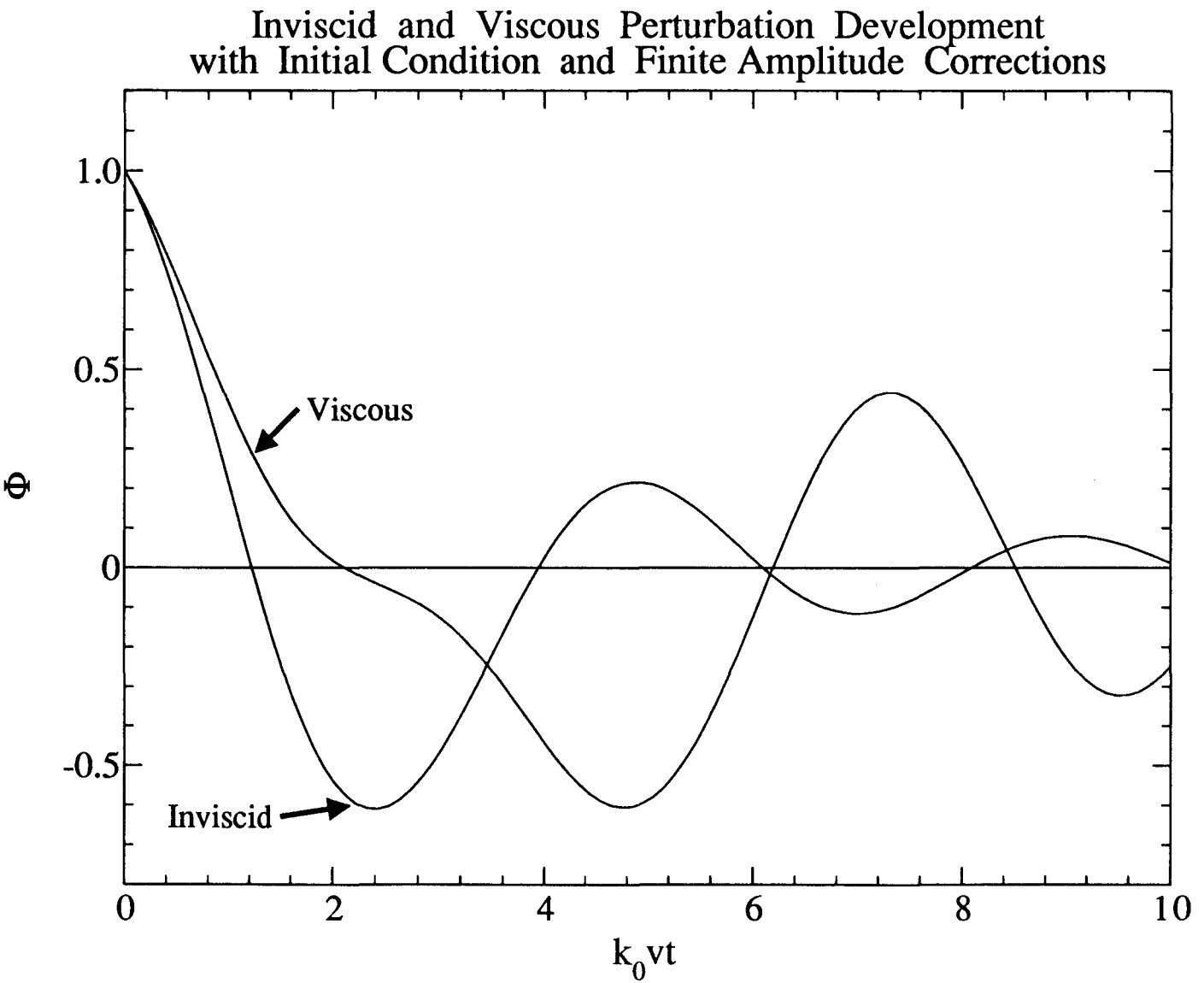
Inviscid and Viscous Perturbation Development
with Initial Condition and Finite Amplitude Corrections
1.0
0.5
0
-0.5
Φ
Viscous
Inviscid
0
2
4
6
8
10
k0vt

Figure 7.

Figure 8: Schematic of the development of perturbations in the shock front. When the shock first reaches the grooves in the sample disc (a), the sample will begin to release to ambient pressure. A release wave propagates backward into the shocked material as the shock wave progresses forward where the shock has not intersected the grooves (b). When the grooves are closed a sinusoidally perturbed shock front will have been generated (c), and a perturbed region will exist behind this shock front.

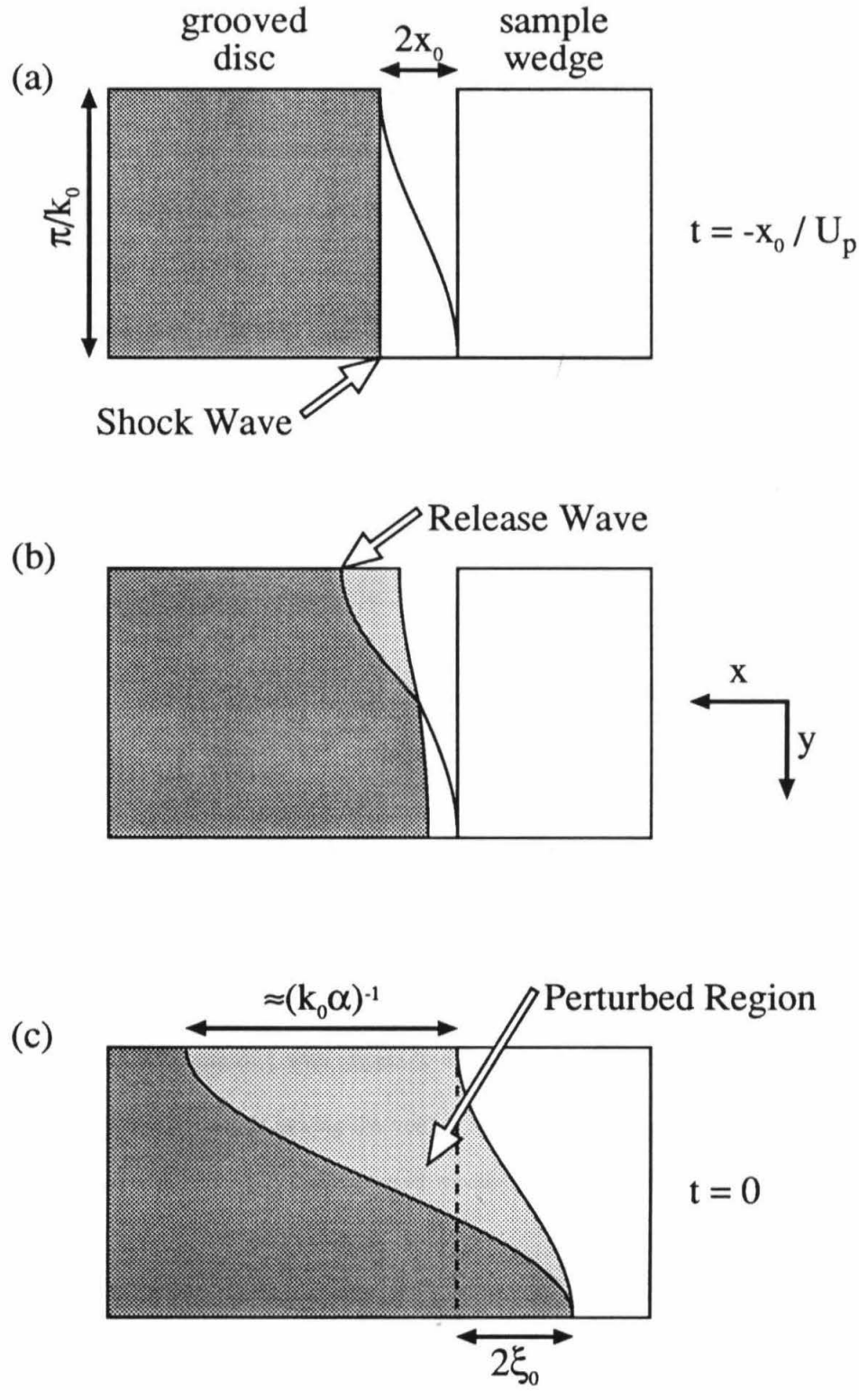
(a)
grooved disc
$2x_0$
sample wedge
π/k_0
$t = -x_0 / U_p$
Shock Wave
(b)
Release Wave
x
y
(c)
$\approx(k_0\alpha)^{-1}$
Perturbed Region
$t = 0$
$2\xi_0$

Figure 8.

In the regions where release commences, the free surface will travel with velocity $\approx 2U_P$. In the "normal" region, the shock travels at a velocity U_S. In the weak shock limit, $\sigma<2$, $U_S > 2U_P$ and the shock will reach the wedged sample before the released surface does. In this case, ξ_0 will be positive where the grooves were cut, and negative where the sample material is continuous. ξ_0 will have the opposite phase if the shock is strong, $\sigma>2$.

If the initial depth of the grooves is $2x_0$, *i.e.*, the groove depth varies as $x_0[1-\cos(k_0 y)]$, then the initially released material will reach the wedge at a time

$$t_{close} = \frac{x_0}{U_P}, \tag{106}$$

the time necessary to close the sinusoidal void. In this same time, the shock wave will have traveled a distance

$$\frac{x_0 U_S}{U_P}, \tag{107}$$

or a distance

$$\frac{x_0(U_S-2U_P)}{U_P} \tag{108}$$

into the wedge (Fig. 4c). This is twice the initial amplitude of the shock wave perturbation:

$$\xi_0 = \frac{x_0(U_S - 2U_P)}{2U_P} = \frac{x_0 |2-\sigma|}{2(\sigma-1)}. \tag{109}$$

The initial amplitude ξ_0 is taken to be positive, so we use the absolute value $|2-\sigma|$. The sign of $(2-\sigma)$ determines the phase of ξ with respect to the grooves.

While the free surface is closing the void, a release wave is traveling in the opposite direction into the shocked material. This release wave travels at a velocity $(c - U_P)$, and will travel a distance

$$\frac{x_0(c - U_P)}{U_P} \tag{110}$$

away from the point of initial release, or a distance of

$$\frac{x_0(c + U_P)}{U_P} \tag{111}$$

relative to the first surface of the wedge at time t_{close}. The characteristic length scale of this initial disturbance is thus

$$\frac{1}{k_0\alpha} \approx \frac{x_0(c + U_P)}{U_P} = \frac{2[1 + \beta(\sigma-1)]\xi_0}{\beta|2-\sigma|} , \tag{112}$$

or

$$\alpha \approx \frac{\beta|2-\sigma|}{2k_0\xi_0[1 + \beta(\sigma-1)]} . \tag{113}$$

Sakharov *et al.* [1965] suggest that the length scale for the initial velocity perturbations will be on the order of ξ_0. According to this approximate analysis, the length scale will be approximately $1/(k_0\alpha) \approx 20\times\xi_0$ for water at 15 GPa.

When the void first closes a velocity perturbation will exist. Where a void had existed material will have a velocity of $2\,U_P$, and where no void had existed material will have a velocity of U_P. In the coordinate frame of Zaidel' [1967], the initial velocity perturbation will be

$$2v'_x = -U_P = -v(\sigma-1) . \tag{114}$$

From Eqns. 94a and 95 we then have:

$$S = -\frac{\sigma(1-\delta)}{2(1+\delta)k_0\xi_0} . \tag{115}$$

The initial time derivative of ξ will therefore be negative for all stable shocks $\delta < 1$.

At the level of approximation considered here, both α and S are functions of the product $k_0\xi_0$. The impact of these "nonlinear" parameters may be experimentally assessed, independently of viscous effects, by using different values of $k_0\xi_0$ and, independently, k_0 or ξ_0 [Sakharov *et al.*, 1965].

This approximate analysis gives approximate values of α and S that qualitatively reproduce the observed short-time behavior of the shock front oscillations. It would be useful to derive more exact expressions for the initial shock and flow structure.

11. Complete Viscous Solution

We noted in §8 that the perturbation approach may be overly restrictive in that only the inviscid eigenmodes of the system are considered. In going from the inviscid solution to a viscous solution, the governing differential equations change from first- to second-order, and the solution becomes correspondingly more complex. In the case of viscous flow, it is commonly observed that instabilities occur for certain critical Reynolds numbers. These so-called Tollmien-Schlichting instabilities [Schlichting, 1979] are most commonly associated with viscous boundary layers, since it is in this context that viscosity is most commonly encountered, but the phenomena may be relevant to the issue of shock stability as well.

The complete second-order differential equations that govern this problem may be solved to give a Laplace transform solution for the shock front corrugation amplitude. This solution will be presented below. The solution, $\hat{\phi}$, is algebraically complex, however, and is not as easy to interpret as was the inviscid solution. Because of this complexity, we resort to numerical solution methods. By way of some numerical examples, it will be shown that the complete second order equations do indeed exhibit instabilities.

The second-order equations may be written as a set of five first-order equations by introducing the variables:

$$q \equiv \frac{1}{k_0} \frac{\partial v_x}{\partial x} , \tag{116}$$

and

$$r \equiv \frac{1}{k_0}\frac{\partial v_y}{\partial x} . \tag{117}$$

Using these new variables, the Laplace transformed equations of motion and continuity can be written as:

(118)

$$\frac{\partial}{\partial x}\begin{bmatrix} \hat{v}_x \\ i\hat{v}_y \\ \hat{P} \\ \rho v \\ \hat{q} \\ i\hat{r} \end{bmatrix} = k_0 \begin{bmatrix} 0 & 0 & 0 & 1 & 0 \\ 0 & 0 & 0 & 0 & 1 \\ 0 & -(1+\epsilon) & -z & -(1+\epsilon) & 0 \\ \frac{R_b}{R_s}(1+R_s z) & -R_b(1+\epsilon) & -R_b z & -R_b\epsilon & \frac{(R_b-R_s)}{R_s} \\ 0 & \frac{R_s}{R_b}(1+R_b z) & -R_s & \frac{(R_s-R_b)}{R_b} & R_s \end{bmatrix} \begin{bmatrix} \hat{v}_x \\ i\hat{v}_y \\ \hat{P} \\ \rho v \\ \hat{q} \\ i\hat{r} \end{bmatrix} + \begin{bmatrix} 0 \\ 0 \\ \frac{P}{\rho v^2} \\ R_b\left[\frac{P}{\rho v^2} - \frac{v_x}{v}\right] \\ -\frac{iR_s v_y}{v} \end{bmatrix}_{t=0} .$$

For simplicity, we will neglect the initial conditions in the following development.

As before, we seek an eigenvalue expansion for this matrix equation. The characteristic equation obtained from this expansion factors into two parts. The first is dependent only upon the pure shear viscosity:

$$\lambda^2 - k_0 R_s \lambda - k_0^2(1+R_s z) = 0 , \tag{119}$$

giving eigenvalues:

$$\lambda_1 = \frac{k_0}{2}\left[R_s - \sqrt{R_s^2 + 4(1+R_s z)}\right] \tag{120a}$$

and

$$\lambda_2 = \frac{k_0}{2}\left[R_s + \sqrt{R_s^2 + 4(1+R_s z)}\right] . \tag{120b}$$

The first eigenvalue, λ_1, leads to decay of the perturbations for any real positive z, whereas the second solution will lead to exponential growth. In the inviscid limit, this part of the characteristic equation gave the single root λ_1 of Eqn. 57.

The second factor of the characteristic equation is dependent solely on the viscosity accompanying compression without shear:

$$\lambda^3 + k_0\lambda^2(R_b\varepsilon+z) - k_0^2\lambda(1+2R_bz) - k_0^3[R_b(1+\varepsilon+z^2)+z] = 0 . \tag{121}$$

The roots of this cubic equation are algebraically complex:

$$\frac{\lambda_3}{k_0} = -2\sqrt{a}\cos(\frac{\theta}{3}) - \frac{(R_b\varepsilon+z)}{3} \tag{122a}$$

$$\frac{\lambda_4}{k_0} = -2\sqrt{a}\cos(\frac{\theta+2\pi}{3}) - \frac{(R_b\varepsilon+z)}{3} \tag{122b}$$

$$\frac{\lambda_5}{k_0} = -2\sqrt{a}\cos(\frac{\theta+4\pi}{3}) - \frac{(R_b\varepsilon+z)}{3} \tag{122c}$$

where

$$a \equiv \frac{(R_b\varepsilon+z)^2 + 3(1+2R_bz)}{9} \tag{123a}$$

$$b \equiv \frac{2(R_b\varepsilon+z)^3 + 9(R_b\varepsilon+z)(1+2R_bz) - 27[R_b(1+\varepsilon+z^2) + z]}{54} \tag{123b}$$

and

$$\theta \equiv \text{Arccos}\,\frac{b}{\sqrt{a^3}} \tag{123c}$$

The root λ_4 is positive for real positive values of z, and will therefore lead to instability. Both λ_3 and λ_5 are negative for real positive z, and might therefore be acceptable solutions. For complex z, however, the phase of λ_3 indicates that it corresponds to waves incident upon the shock whereas λ_5 corresponds to waves emitted by the shock. λ_3 might therefore be excluded on the grounds that it is unphysical. In the inviscid limit, the two eigenvalues associated with these acoustic modes were λ_2 and λ_3 of Eqn. 57.

The complete boundary conditions at the shock front may be written as:

(124)

$$u_{x=0} \equiv \begin{bmatrix} \hat{v}_x \\ i\hat{v}_y \\ \hat{P}/(\rho v) \\ \hat{q} \\ i\hat{r} \end{bmatrix}_{x=0} = \begin{bmatrix} \dfrac{-\xi_0(\sigma-1)(1+\delta)R_bR_s^2 + \hat{\xi}k_0v(\sigma-1)R_s[zR_bR_s(1+\delta)-\sigma\delta(2R_b-R_s)] - R_s^2\sigma\delta\hat{q} + \sigma\delta(2R_b-R_s)i\hat{r}}{\sigma\left[R_bR_s^2(1-\delta) + \delta(2R_b-R_s)\right]} \\ \dfrac{\xi_0(\sigma-1)(1+\delta)R_bR_s - \hat{\xi}k_0v(\sigma-1)R_bR_s[z(1+\delta)+R_s\sigma(1-\delta)] + R_s\sigma\delta\hat{q} + \sigma(1-\delta)R_bR_si\hat{r}}{\sigma\left[R_bR_s^2(1-\delta) + \delta(2R_b-R_s)\right]} \\ \dfrac{-\xi_0(\sigma-1)[2R_b(1-R_s^2)-R_s] + \hat{\xi}k_0v(\sigma-1)[z(2R_b(1-R_s^2)-R_s)+\sigma R_s(2R_b-R_s)] + \sigma R_s^2\hat{q} - \sigma(2R_b-R_s)i\hat{r}}{\sigma\left[R_bR_s^2(1-\delta) + \delta(2R_b-R_s)\right]} \\ \hat{q} \\ i\hat{r} \end{bmatrix}_{x=0}$$

Recall that the boundary conditions in the inviscid case are underspecified, *i.e.*, $\hat{v}_{x,x=0}$, $\hat{v}_{y,x=0}$, and $\hat{P}_{x=0}$ are not uniquely defined, but are functions of $\hat{\xi}$. By omitting one eigenmode from the solution, we acquired an additional constraint, and it became possible to determine $\hat{\xi}$. In the present case, our boundary conditions are underspecified to a greater extent: we have the three boundary values $\hat{\xi}$, $\hat{q}_{x=0}$, and $\hat{r}_{x=0}$ that are undetermined. By omitting three of the five eigenmodes from the solution, we satisfy the necessary constraints. Applying the methodology described previously, we may determine the behavior of the shock front by simultaneously solving:

$$^l\psi_2 \cdot u_{x=0} = 0 \tag{125a}$$

$$^l\psi_3 \cdot u_{x=0} = 0 \tag{125b}$$

$$^l\psi_4 \cdot u_{x=0} = 0 \tag{125c}$$

for the three unknowns $\hat{q}_{x=0}$, $\hat{r}_{x=0}$, and $\hat{\xi}$, where $^l\psi_n$ is the left eigenvector corresponding to λ_n.

An alternative formulation of the solution is to expand the velocity and pressure perturbations in terms of the right eigenvectors:

$$u = C_1{}^r\psi_1 + C_5{}^r\psi_5 , \tag{126}$$

where $^r\psi_n$ is the right eigenvector corresponding to eigenvalue λ_n. This alternative approach, formally identical to the earlier method, is somewhat less awkward in this case.

We begin by taking appropriate linear combinations of the boundary conditions to obtain:

$$k_0v\hat{\xi}(\sigma-1)z = (\sigma-1)\xi_0 + \sigma\left[\hat{v}_x + \delta\frac{\hat{P}}{\rho v}\right] \tag{127a}$$

$$R_s\hat{q} = 2R_bR_s\hat{v}_x + (2R_b-R_s)i\hat{v}_y + R_bR_s(1+\delta)\frac{\hat{P}}{\rho v} \tag{127b}$$

and

$$iz\hat{r} = R_s(\sigma-1)\xi_0 + (R_s\sigma+z)\hat{v}_x + R_szi\hat{v}_y + R_s\sigma\delta\frac{\hat{P}}{\rho v} \tag{127c}$$

at x=0. The last two conditions, in conjunction with Eqn. 126, may be used to determine the coefficients C_1 and C_5. Defining:

$$\vec{\Phi}_1 = \begin{bmatrix} 2R_bR_s \\ 2R_b-R_s \\ R_bR_s(1+\delta) \\ -R_s \\ 0 \end{bmatrix} \quad \text{and} \quad \vec{\Phi}_2 = \begin{bmatrix} R_s\sigma+z \\ R_sz \\ R_s\sigma\delta \\ 0 \\ -z \end{bmatrix}, \tag{128}$$

we write:

$$M \equiv \begin{bmatrix} {}^r\psi_1\cdot\Phi_1 & {}^r\psi_5\cdot\Phi_1 \\ {}^r\psi_1\cdot\Phi_2 & {}^r\psi_5\cdot\Phi_2 \end{bmatrix} \tag{129a}$$

$$M\begin{bmatrix} C_1 \\ C_5 \end{bmatrix} = \begin{bmatrix} 0 \\ -R_s(\sigma-1)\xi_0 \end{bmatrix} \tag{129b}$$

to determine the coefficients C_1 and C_5. These coefficients, together with Eqn. 126, serve to determine $\hat{v}_x$ and $\hat{P}/(\rho v)$, which may be used to solve for $\hat{\xi}$ with Eqn. 127a.

The right eigenvectors are:

$${}^r\psi_1 = \begin{bmatrix} 1 \\ -\lambda'_1 \\ 0 \\ \lambda'_1 \\ -\lambda'^2_1 \end{bmatrix} \quad \text{and} \quad {}^r\psi_5 = \begin{bmatrix} -\lambda'_5(\lambda'_5+z) \\ (\lambda'_5+z) \\ -(1+\varepsilon)(1-\lambda'^2_5) \\ -\lambda'^2_5(\lambda'_5+z) \\ \lambda'_5(\lambda'_5+z) \end{bmatrix}, \tag{130}$$

leading to the solution:

$$k_0v\hat{\phi} = -\frac{R_b\left[(\lambda'_5+z)\left[4(1+R_sz-\lambda'_5\lambda'_1) + 2R_s(\lambda'_1-R_s+z) + R_s(R_sz-2)(z-\lambda'_5)\right] - R_s\delta(1+\varepsilon)(1-\lambda'^2_5)(R_sz+2)\right]}{\det(M)}, \tag{131}$$

where

$$\det(M) = -R_b\Big[R_s\delta(1+\varepsilon)(1-\lambda'^2_5)\Big[R_s(\sigma-z^2) - 2(\lambda'_1\sigma+z)\Big] \tag{132}$$
$$+ (\lambda'_5+z)\Big[2(1+R_sz-\lambda'_5\lambda'_1)(R_s\sigma+2z) + 2R_sz(\lambda'_1-R_s+z) + R_s(z-\lambda'_5)(R_sz^2-2z-R_s\sigma)\Big]\Big] ,$$

and λ'_i is λ_i/k_0.

In the inviscid limit, $R_s \to \infty$ and $R_b \to \infty$, the eigenvalues correspond to those derived in the previous section (*i.e.*, Eqn. 57). The solution, $\hat{\phi}$, is also identical to the inviscid solution, Eqn. 68a, obtained in the previous sections. The D'yakov-Kontorovich stability criteria are therefore applicable in this case.

If we seek a approximate solutions for λ_1 and λ_5 in the form of power series expansions, *e.g.*,

$$\lambda_1 \approx -k_0z - \frac{k_0(1-z^2)}{R_s} + O(R_s^{-2}) \tag{133a}$$

and

$$\lambda_5 \approx \frac{k_0(\beta^2z - \omega)}{(1-\beta^2)} + \frac{k_0\beta^4(z-\omega)^3}{2R_b(1-\beta^2)^3\omega} + O(R_b^{-2}) , \tag{133b}$$

and write a Taylor series expansion for $\hat{\phi}$:

$$\hat{\phi} \approx \lim_{R_s\to\infty,\, R_b\to\infty} \hat{\phi} + R_s^{-1} \lim_{R_s\to\infty,\, R_b\to\infty} \left[\frac{\partial\hat{\phi}}{\partial R_s^{-1}}\right] + R_b^{-1} \lim_{R_s\to\infty,\, R_b\to\infty} \left[\frac{\partial\hat{\phi}}{\partial R_b^{-1}}\right] \tag{134}$$

then we arrive at the same solution, Eqn. 82, obtained by the perturbation method of Zaidel' [1967], valid in the limit of negligible viscosity.

The limit of infinite viscosity may also be obtained from Eqn. 131. In the limit $R_s \to 0$, the characteristic equation, Eqn. 119, gives the two solutions:

$$\lambda = \pm k_0 , \tag{135}$$

where the negative solution is the stable one. When $R_b \to 0$, the acoustic characteristic equation, Eqn. 121, gives the three solutions:

$$\lambda = -k_0 z, \pm k_0 . \tag{136}$$

The two negative roots are unconditionally stable, however only the root $\lambda = -k_0 z$ gives an eigenvector that is linearly independent of the entropy waves.

The shock front perturbation in this limit is

$$\lim_{R_s \to 0,\, R_b \to 0} k_0 v \hat{\phi} = \frac{1}{z} , \tag{137}$$

thus the shock front perturbation amplitude is a unit step function:

$$\lim_{R_s \to 0,\, R_b \to 0} \phi = 1 \text{ for } t > 0 , \tag{138}$$

the amplitude will neither grow nor diminish with time, and is therefore unconditionally stable. This limiting behavior is very different from that indicated by the linearized perturbation method, and indicates the limitations of that method for large but finite viscosity.

To study the solution for finite viscosity requires that the inverse Laplace transform of Eqn. 131 be found. Because of the complexity of this equation, we employ the Legendre polynomial quadrature method of Bellman *et al.* [1966] to numerically invert Eqn. 131. This inversion is shown in Figure 9 for several values of R_s, with R_b determined by specifying $\kappa = \eta$. When R_s is large, *i.e.*, 128 or larger, the solution approaches the inviscid solution (without initial conditions or finite amplitude corrections). When R_s is 4, the solution is approximately critically damped: the oscillations of ϕ about zero are greatly reduced. Smaller shear Reynolds numbers lead to qualitatively different behavior. As R_s approaches zero (not shown), the amplitude tends to remain constant at $\phi = 1$, but ultimately become unstable as for the case $R_s = 1$ shown in Figure 9. All of the numerical experiments conducted so far with $0 < R_s < 4$ ultimately exhibit instabilities.

Viscosity can usually be considered as a stabilizing factor, as in the case of flow through a pipe. When the Reynolds number is larger than some critical value, or, equivalently, the viscosity is too small, turbulence develops. Small Reynolds numbers, or large viscosities, give laminar flow.

Figure 9: Numerical inversion of second-order equation (Eqn. 131) for $\kappa = \eta$, and R_s=1, 2, 4, 8, 16, 32, 64, and 128, with parameters listed in Table III. The squares represent the points calculated by the twentieth-order shifted Lagrange polynomial quadrature method [Bellman *et al.*, 1966], and the curves are fit to the points with cubic splines. Shear Reynolds numbers smaller than 4 appear to give unstable solutions. Large shear Reynolds number solutions approach the inviscid solution given by Eqn. 79, Figure 4.

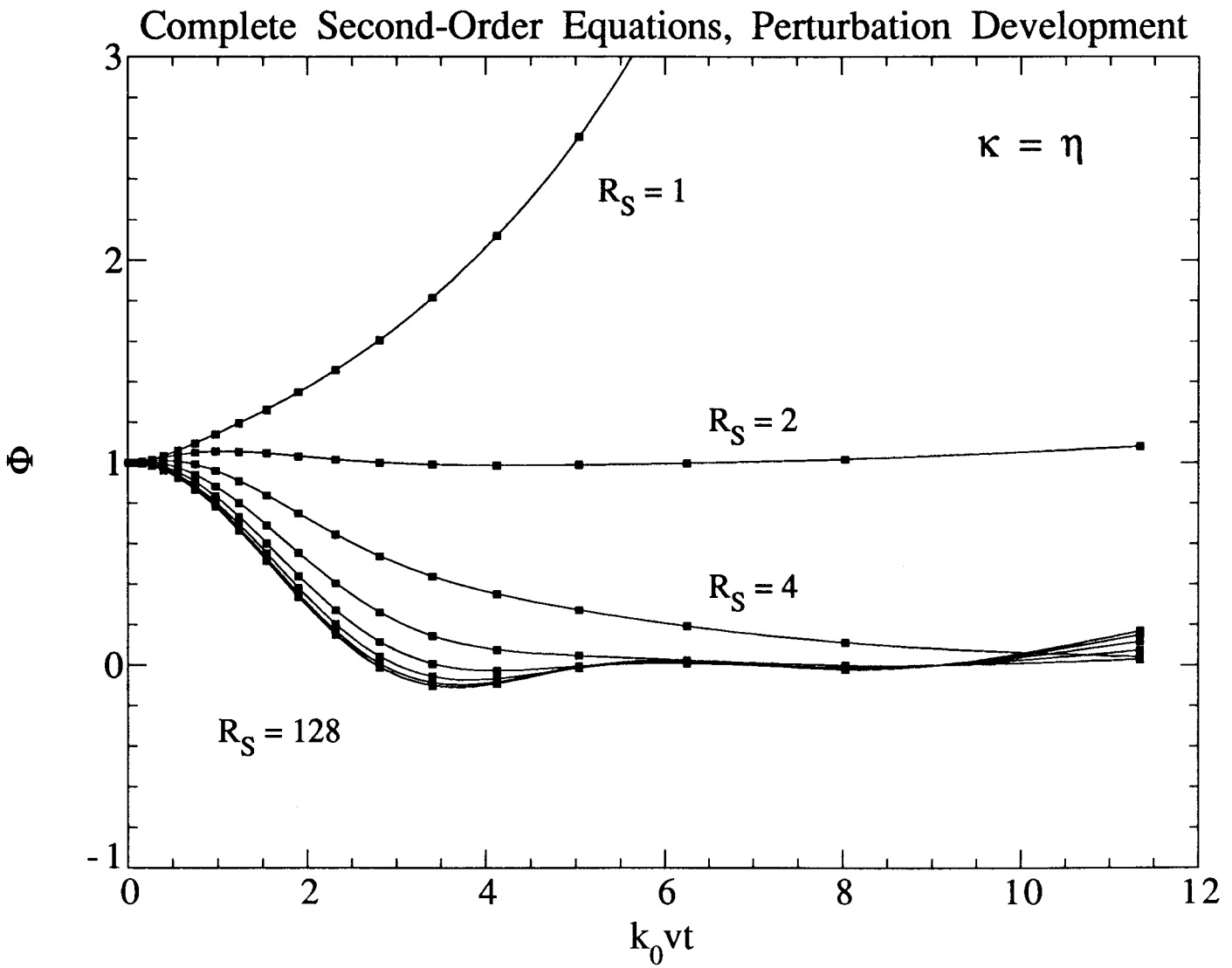
Complete Second-Order Equations, Perturbation Development
κ = η
R_S = 1
R_S = 2
R_S = 4
R_S = 128
Φ
k_0vt
3
2
1
0
-1
0
2
4
6
8
10
12

Figure 9.

The opposite behavior is exhibited in this corrugated shock problem. One interpretation of this behavior comes from the analysis of Freeman [1955] of a related problem: that of a shock driven by a corrugated piston in an inviscid fluid. He identified the mechanism of shock perturbation decay as the interference of pressure (sound) waves at the shock front. If these pressure waves were strongly attenuated, as in a highly viscous fluid, then the damping mechanism would be ineffective.

These instabilities are kinetic in origin, and as such are fundamentally different from those that arise from violation of the Kontorovich-D'yakov criteria. The latter, which are thermodynamic in origin, lead to shock-splitting. We infer, by analogy to Tollmein-Schlichting instability theory, that these low Reynolds number instabilities lead to turbulence at the shock front. Since there is a wavelength for any viscous material such that R_e will be less than 4, these calculations predict that turbulence may occur commonly in shock experiments. Whether such turbulence is detectable would depend on the wavelength of the perturbation and the magnitude of the viscosity, in addition to the thermodynamic parameters that characterize the system. The possible existence of such turbulence at the shock front offers a new interpretation for the rapid dynamic mixing that is observed in shock-induced chemical reactions [*e.g.*, Boslough, 1989, 1990].

12. Review of Experiments on Water

As an example, we will examine the experimental results for water shocked to 15 GPa, the maximum shock pressure achieved in the viscosity measurement experiments of Mineev and Zaidel' [1968]. The Hugoniot is given by ρ_0 = 0.998 [g/cc], c_0 = 2.393 [km/s], and s = 1.333 ($U_S = c_0 + s U_P$) [Mitchell and Nellis, 1982], valid in the range $1.5 < U_P < 7.1$ [km/s]. At a peak shock pressure of 15 GPa, the linear U_S–U_P relation gives U_S = 5.383 [km/s] and U_P = 2.243 [km/s]. v is then 3.140, and v_0 is 5.383.

The Hugoniot bulk modulus can be determined from the U_S-U_P shock equation of state:

$$K_H \equiv -V \frac{\partial P}{\partial V}\Big|_{Hugoniot} = \frac{U_S}{V_0}(U_S - U_P)\left[\frac{U_S + U_P U_S'}{U_S - U_P U_S'}\right], \tag{139}$$

where U_S' is $\partial U_S/\partial U_P$, or s for a linear (*i.e.*, $U_S = c_0 + s U_P$) material. This relationship allows δ, Eqn. 33, to be calculated from:

$$\delta = \frac{U_S - U_P U_S'}{U_S + U_P U_S'} = \frac{\sigma - s(\sigma-1)}{\sigma + s(\sigma-1)}, \tag{140}$$

from which we calculate $\delta = 0.287$ at 15 GPa.

The high pressure isentropic bulk modulus is calculated from the thermodynamic identity:

$$K_S = \rho c^2 = K_H\left[1 - \frac{\gamma}{2}(\sigma-1)\right] + \frac{\gamma}{2}(P - P_0), \tag{141}$$

where γ is the thermodynamic Grüneisen parameter. From Eqn. 141 the parameter β, Eqn. 54, is found to be:

$$\beta = \sqrt{\frac{\delta}{1 - \tfrac{1}{2}\gamma(\sigma-1)(1-\delta)}}. \tag{142}$$

Using the experimental value of $\gamma = 1.5$ [Mitchell and Nellis, 1982] at high pressure obtained from a Mie-Grüneisen model, Eqn. 142 gives $\beta = 0.682$. Bakanova *et al.* [1976] measured the sound speed of shock compressed water, and a value of 5.8 km/s is given by their results at 15 GPa. Using this experimentally constrained sound speed, β is found to be 0.541. Since water is not well described by the Mie-Grüneisen equation of state, we will use the value $\beta = 0.541$.

The initial amplitude of the perturbations is reported to be in the range $k_0\xi_0 = 0.19$ to 1.13. From Eqn. 113 we then estimate α to be in the range 0.34 to 0.06, and from Eqn. 115 S is in the range -2.50 to -0.42.

Mineev and Zaidel' [1968] calculate a viscosity of 2.2×10^4 poise with perturbation wavelengths of 1 and 2 cm. The shear Reynolds number (R_s) that characterizes this problem, Eqn.

83, is then 4.23 ($2\pi/k_0$ = 1 cm) or 8.46 ($2\pi/k_0$ = 2 cm). Note that the viscous perturbation method is valid in the limit $R_s, R_b \rightarrow \infty$.

The conditions, Eqns. 75 and 99, for the transformation contours are satisfied.

Viscosities were obtained from the Sakharov *et al.* [1965] type experiments by conducting two experiments with different Reynolds numbers, and measuring the difference in normalized time of the first zero crossing of ϕ. Doubling the Reynolds number for water at 15 GPa shifted the zero crossing by by $k_0 v \Delta t = 0.59$ (Mineev and Zaidel' [1968] report $\frac{k_0 v_0 \Delta t}{2\pi} = 0.16$). Figure 10 shows the calculated shift in zero crossing times for a doubling of the Reynolds number as a function of R_s^{-1}. When initial conditions are neglected, the perturbation theory predicts $R_s^{-1} = 0.078$ (Fig. 10a), assuming $\kappa = \eta$, from which η is found to be 6700 poise ($k_0 = 2\pi$). With these same assumptions, the second-order analysis predicts η = 5800 poise (Fig. 10d). The perturbation method gives essentially the same result, within an order of magnitude, as the more exact second-order equations. The effect of the approximate initial conditions is to predict somewhat larger viscosities; 19000 poise without the finite amplitude correction (Fig. 10b), and 20000 poise with the finite amplitude correction (Fig. 10c). These results are summarized in Table IV. For all model calculations, increasing κ/η predicts a slight decrease in η.

These large calculated values of viscosity appears to be robust in the sense that different levels of approximation give similar values to within an order of magnitude. While the addition of an IC model reconciles the shape of $\phi(T)$ with the experimental data (assumed to be qualitatively similar to the published results for aluminum [Sakharov *et al.*, 1965; Mineev and Savinov, 1967]), its impact on the resulting viscosity calculation is unimportant in this case.

The good agreement between our calculations and the results of Mineev and Zaidel' [1968] demonstrates that the differences between our formulae and Zaidel's [1967] are minor, yet the

Table III: Water parameters at 15 GPa to model Mineev and Zaidel' [1968]

Parameter	Eqn.	Value
v_0		5.383 km/s
v		3.140 km/s
c		5.8 km/s
σ	42	1.714
β	54	0.541
δ	140	0.287
ε	69	1.153
μ	70	1.074
k_0		2π cm^{-1}
$k_0\xi_{s0}$		1
α	113	0.056
S	115	-0.47

Table IV: Calculated shear viscosities for water at 15 GPa

Method	Shear Viscosity [poise]
Mineev and Zaidel' [1968] with viscous perturbation method of Zaidel' [1967]	22000
Viscous perturbation (Eqn. 86, Fig. 10a)	6700[a]
Viscous perturbation with approximate initial conditions (Eqns. 97 and 104, Fig. 10b)	19000[a]
Viscous perturbation with initial conditions and finite amplitude correction (Eqns. 100 and 104, Fig. 10c)	20000[a]
Second-order solution without initial conditions (Eqn. 131, Fig. 10d)	5800[a]

[a] $\kappa = \eta$ is assumed.

Figure 10: Shift in time of first zero crossing for a doubling of the shear Reynolds number as a function of $1/R_s$ for $\kappa = 0$, η, 2η, 3η, and 4η, for (a) viscous perturbation method without initial conditions, (b) perturbation method with approximate initial conditions, (c) perturbation method with approximate initial conditions and finite amplitude correction, and (d) second-order equation without initial conditions. Curves are calculated for water at 15 GPa, with $k_0\xi_0 = 1$, $k_0 = 2\pi$ cm^{-1}, and parameters listed in Table III. Large arrows illustrate the calculation of shear Reynolds number from a set of experiments. Doubling the Reynolds number by doubling the perturbation wavelength shifts the first zero crossing of ϕ in dimensionless time (k_0vt). For water at 15 GPa, this shift is 0.59. Assuming $\kappa = \eta$, the shear Reynolds number is 12.8 (Fig. 10a), corresponding to a shear viscosity of 6700 poise (with parameters of Table III).

Figure 10a.

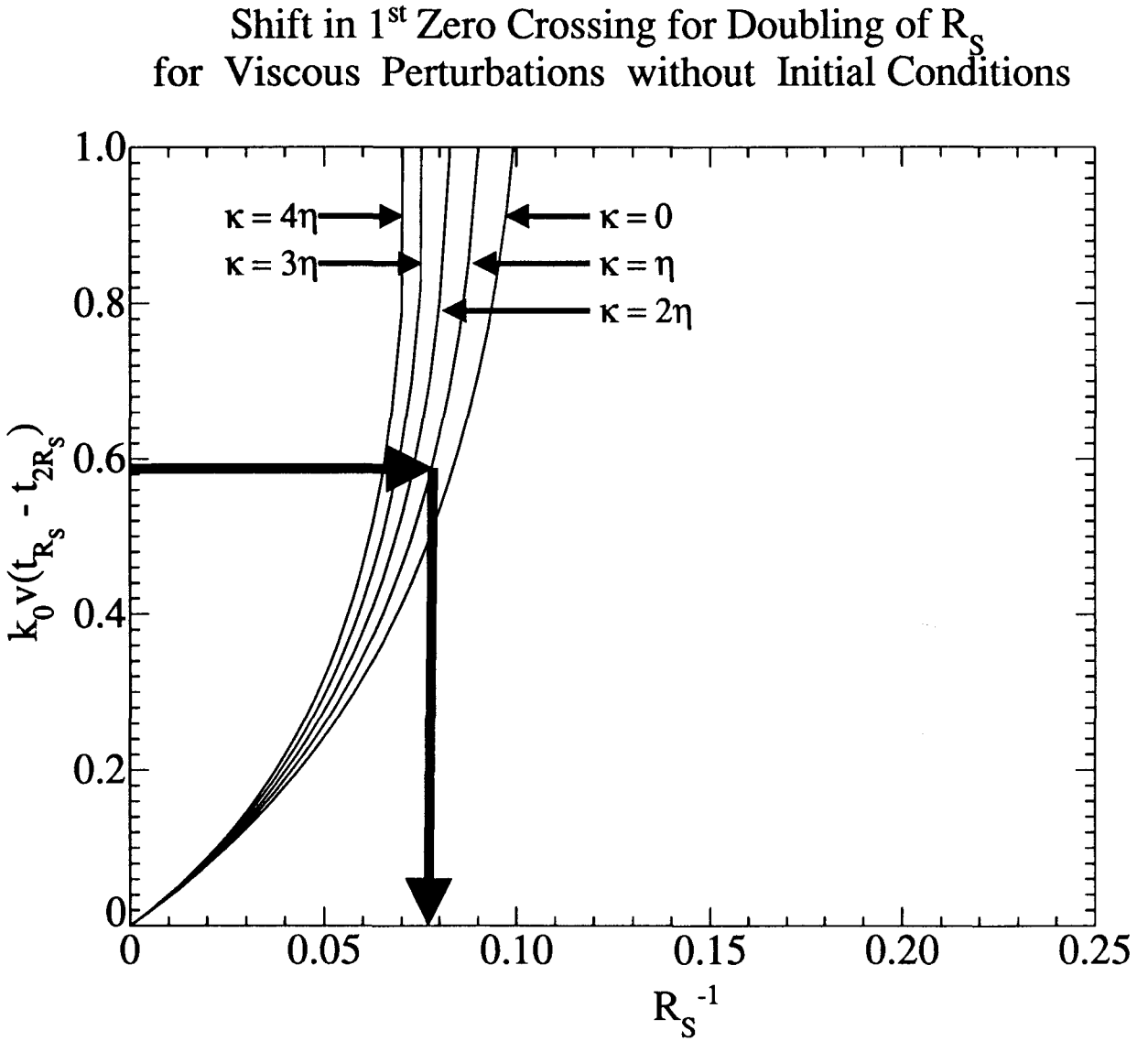
Shift in 1st Zero Crossing for Doubling of R_S
for Viscous Perturbations without Initial Conditions
$\kappa = 4\eta$
$\kappa = 3\eta$
$\kappa = 0$
$\kappa = \eta$
$\kappa = 2\eta$
$k_0 v(t_{R_S} - t_{2R_S})$
R_S^{-1}
1.0
0.8
0.6
0.4
0.2
0
0
0.05
0.10
0.15
0.20
0.25

Figure 10b.

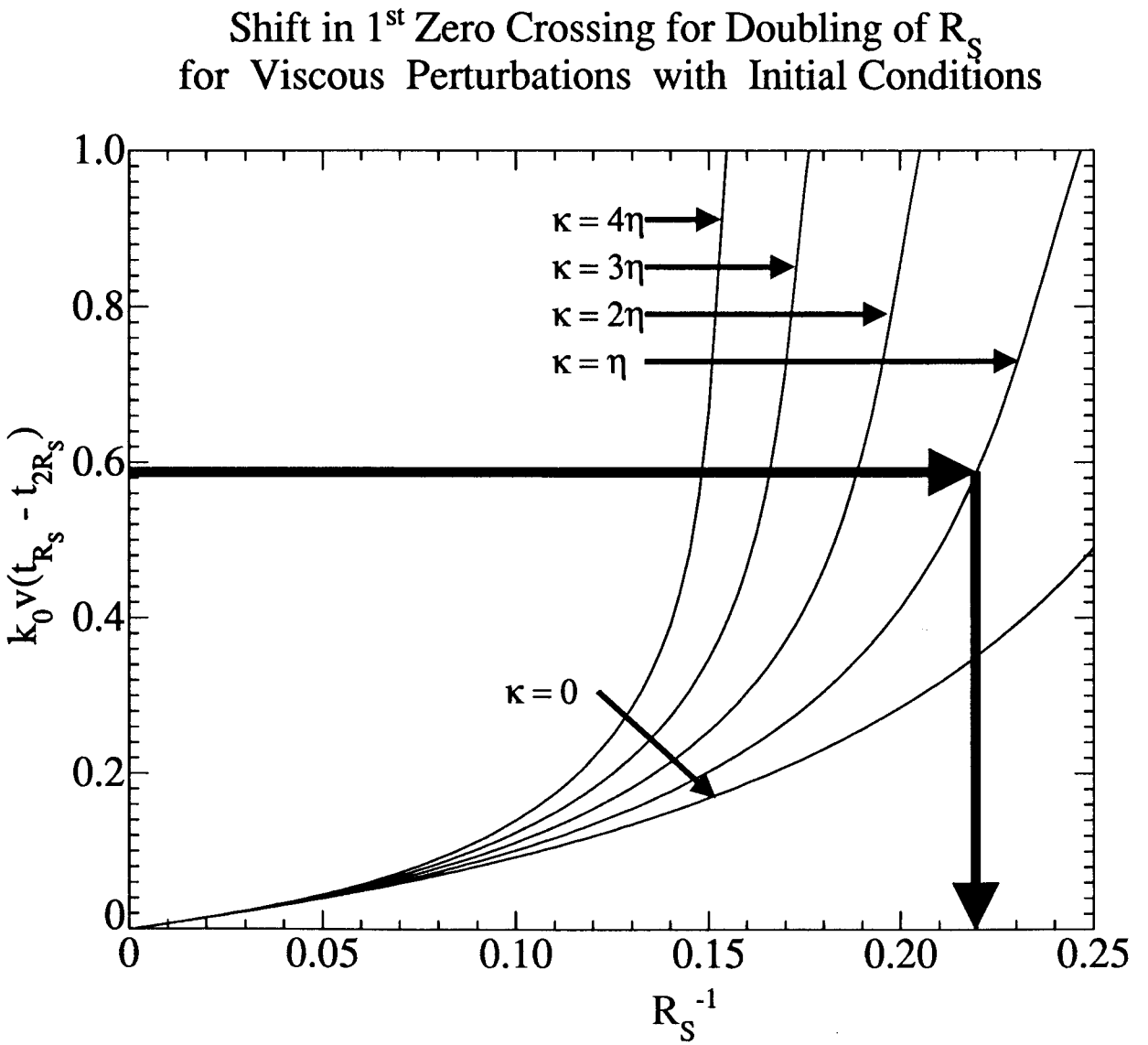
Shift in 1st Zero Crossing for Doubling of R_S
for Viscous Perturbations with Initial Conditions
$\kappa = 4\eta$
$\kappa = 3\eta$
$\kappa = 2\eta$
$\kappa = \eta$
$\kappa = 0$
$k_0 v(t_{R_S} - t_{2R_S})$
R_S^{-1}
0
0.2
0.4
0.6
0.8
1.0
0.05
0.10
0.15
0.20
0.25

Figure 10c.

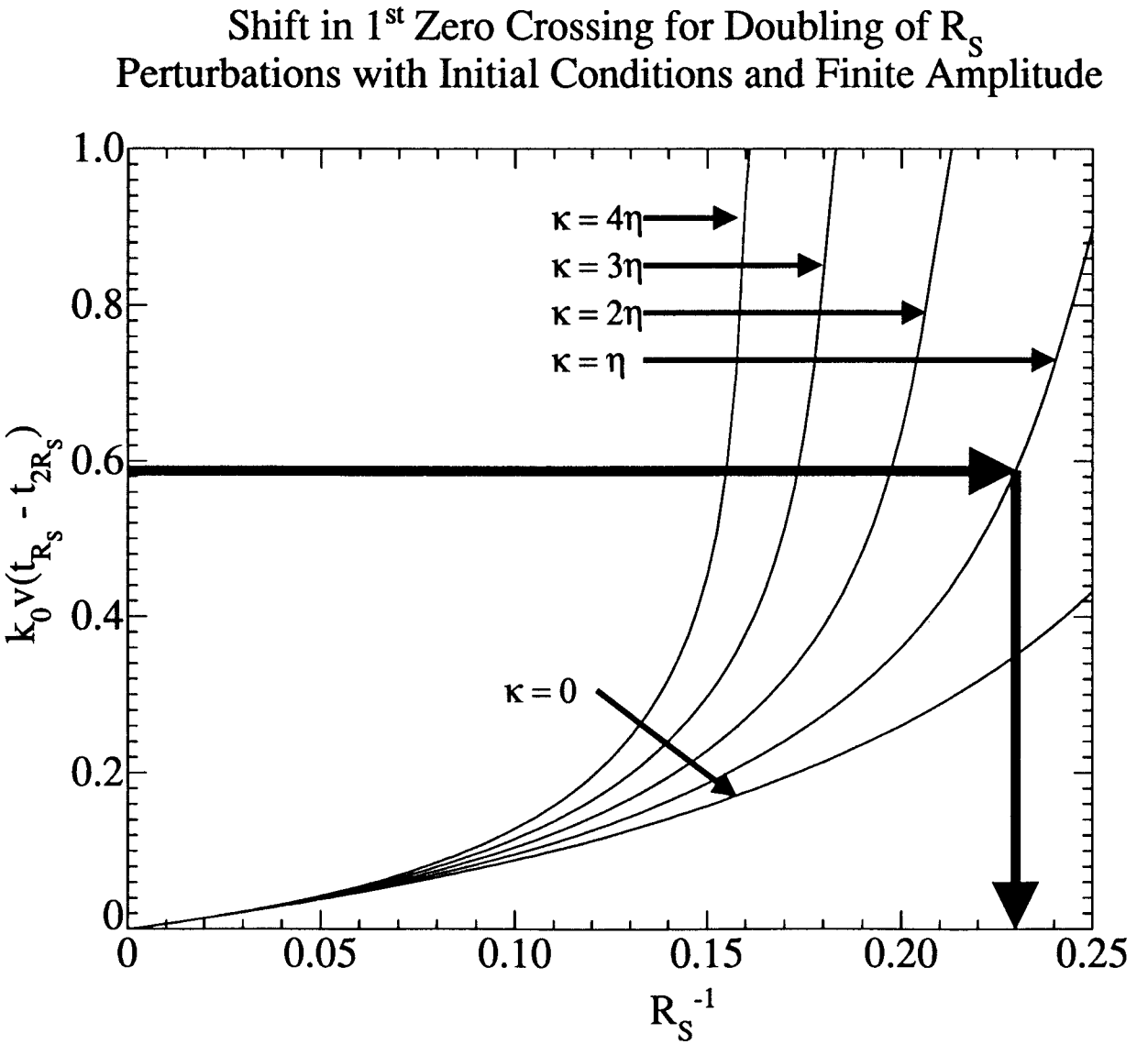
Shift in 1st Zero Crossing for Doubling of R_S
Perturbations with Initial Conditions and Finite Amplitude
$\kappa = 4\eta$
$\kappa = 3\eta$
$\kappa = 2\eta$
$\kappa = \eta$
$\kappa = 0$
$k_0 v(t_{R_S} - t_{2R_S})$
R_S^{-1}
1.0
0.8
0.6
0.4
0.2
0
0
0.05
0.10
0.15
0.20
0.25

Figure 10d.

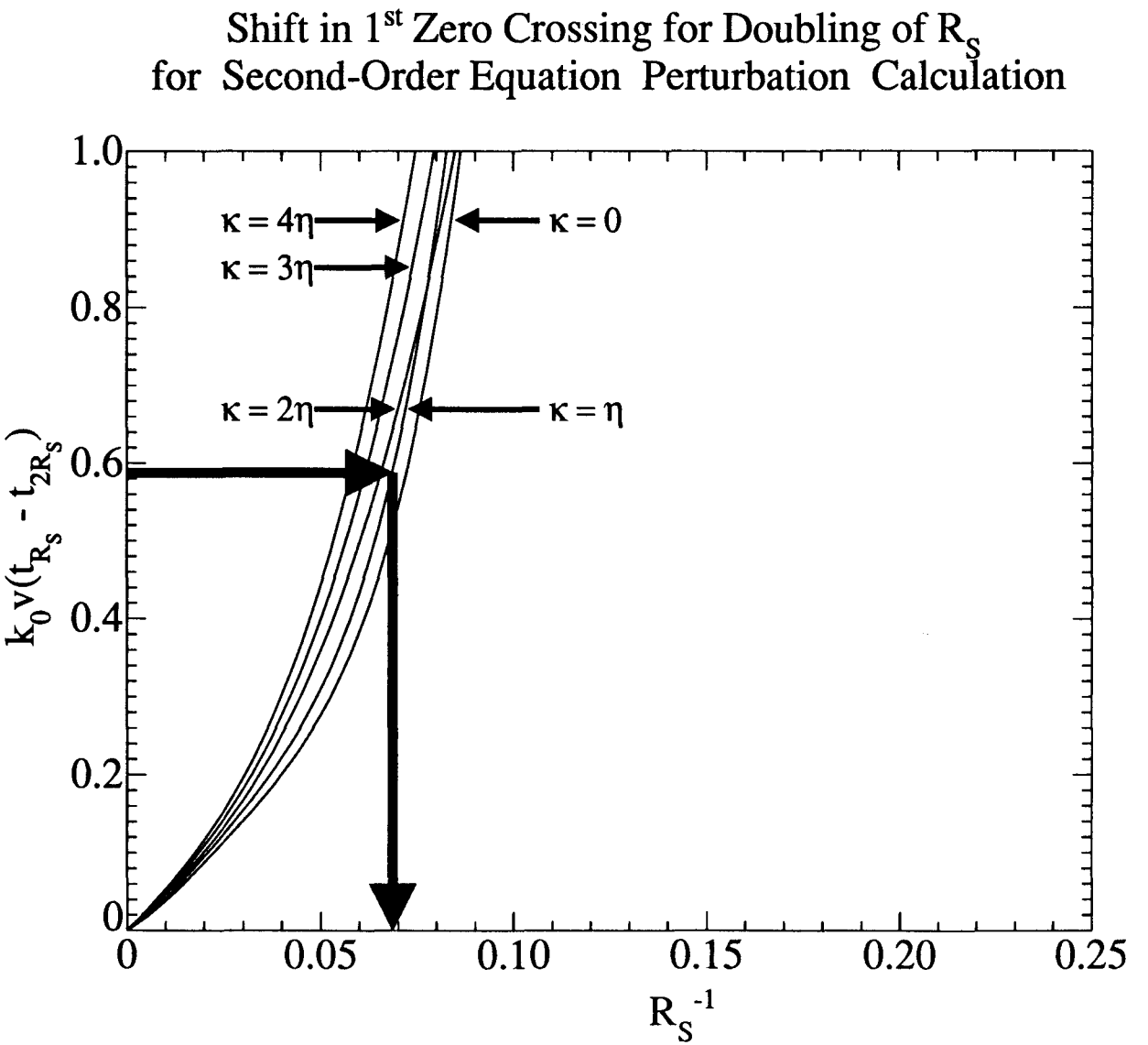
Shift in 1st Zero Crossing for Doubling of R_S
for Second-Order Equation Perturbation Calculation
$\kappa = 4\eta$
$\kappa = 3\eta$
$\kappa = 2\eta$
$\kappa = 0$
$\kappa = \eta$
$k_0 v(t_{R_S} - t_{2R_S})$
R_S^{-1}
1.0
0.8
0.6
0.4
0.2
0
0
0.05
0.10
0.15
0.20
0.25

calculated viscosities are substantially higher than other measurements and calculations (Fig. 2). One possible explanation for this many order of magnitude discrepancy is that some other dissipative mechanism may act on the shock front [Hamann and Linton, 1969]. One such mechanism is thermal conduction. Zaidel' [1967] noted that the combined equations of motion and continuity that govern this problem also, together with an equation of energy, describe the classical dissipation of sound [Landau and Lifshitz, 1959, pp. 298-302] by viscosity and thermal conductivity. This analysis predicts that the absorption coefficient for sound is proportional to

$$\frac{4}{3}\nu + \frac{\kappa}{\rho} + \alpha_P \gamma \chi T \,, \tag{143}$$

where κ is the bulk viscosity, α_P is the thermal expansivity at constant pressure, γ is the thermodynamic Grüneisen parameter, χ is the thermal diffusivity, and T is the shock temperature. Indeed, we have found the term $(\frac{4}{3}\nu+\frac{\kappa}{\rho})$ to be the relevant viscosity for that part of the induced fluid motion associated with sound waves. We might suppose that this association of parameters, including thermal conductivity, might effect the damping of the perturbed shock front. In this case, for the thermal diffusivity to be important $\alpha_P\gamma\chi T$ would need to have magnitude $O(\nu)$ to have a significant impact on the viscosity measurement.

In the weak shock limit, the width of the shock front is proportional to Eqn. 143 [Landau and Lifshitz, 1959, pp. 337-341]. The effective viscosity calculated from shock front profiles therefore includes both bulk viscosity and thermal diffusivity contributions. This grouping of terms describes only part of the viscous damping of shock perturbations: that part associated with sound waves. That part of the damping associated with entropy-vortex waves is dependent only on the shear viscosity (*cf.* Eqn. 81). Viscosities calculated from shock profiles should be comparable to those calculated from shock perturbation damping to the extent that the acoustic damping mechanism dominates and the entropy-vortex damping mechanism has negligible influence. Harris and Presles

[1981] estimate the viscosity of water at 0.58 GPa to be ≤ 0.6 poise by the shock profile method. If this is typical of stronger shocks as well, then thermal diffusivity cannot be responsible for the anomalously large viscosity estimates.

Mineev and Zaidel' [1968] attribute the large viscosity measured under these conditions to the high frequency of the perturbations relative to the relaxation time of the sample, *i.e.*, they propose $\tau \geq 1/\dot{\varepsilon}$ where $\dot{\varepsilon}$ is the strain rate. They estimate this strain rate to be:

$$\dot{\varepsilon} \approx k_0^2 v_0 \xi_0 , \tag{144}$$

which they calculate to be on the order of 0.1 MHz, corresponding to a characteristic time of 10 μs. Another measure of the characteristic frequency of perturbations comes from the acoustic frequency:

$$\Omega = c\sqrt{k_0^2 + \mathrm{Im}[\lambda_{acoustic}]^2} \tag{145}$$

evaluated at the poles of Eqn. 68. These poles are readily determined from the denominator of Eqn. 74 with the transformation Eqn. 72, and give a characteristic acoustic frequency of 4.8 MHz and time scale 0.22 μs with the parameters in Table III. If water has an anelastic absorption mode near 4.8 MHz, than sound waves will be attenuated as if by viscosity. The effective viscosity calculated by the method described above will therefore greatly overestimate the bulk and shear viscosities.

Harris and Presles [1981] suggested that the Sakharov *et al.* [1965] experiments appear to measure shock front related viscosity. Indeed, our analysis does suggest that the viscosity at the shock boundary does have a greater influence over the damping than does the viscosity in the bulk of the shocked fluid. Figure 5a shows the shock front contributions (Eqns. 86b, 86c) and volume contributions (Eqns. 86d, 86e, 86f) to the viscous perturbation (IC neglected). Clearly the magnitude of the BC term is comparable to that of the bulk, and more importantly it is of opposite sign. This calculation suggests that a viscosity at the surface of magnitude 10^4 poise, and a viscosity in the volume of magnitude 10^{-2} poise would explain the experimental results while allowing for the

possibility that the shear viscosity could be as small as 10^{-2} poise.

If the material properties of the sample near the shock front were different than in the bulk, however, the surface viscosity might be much greater than the viscosity in the volume. Rice and Walsh [1957] recognized that the Hugoniot for water passes through (or very near) the field of ice VII stability (Fig. 11). More recent experiments by Al'tshuler *et al.* [1958] and analyses by Schroeder and McMaster [1973] suggest that water does actually freeze to ice VII on the Hugoniot, and melts at higher shock pressure. If this is true, then crystalline or partially crystalline water in (or near) the shock front could easily have a higher viscosity than the crystal-free liquid away from the front. This effect might influence the shock viscosity at higher pressure than the point at which ice VII melts on the water Hugoniot: ice VII formed on the Rayleigh path through the shock front might exist even if the final shock state were outside the field of ice VII stability. The existence of a phase transformation on the Rayleigh path would also have an adverse effect on the estimation of viscosity from the shock front profile.

Mineev and Savinov [1976] discussed the shock viscosity of water in relation to its phase diagram. They noted that the measured viscosity of water decreases by about a factor of 5 in the range 12-25 GPa, but remains on the order of 10^4 poise. This large viscosity was attributed to the existence of ice VII. They suggested that melting did not occur abruptly on the Hugoniot, but occurred gradually with increasing pressure. While it is possible that water remains in the two-phase region over an extended pressure interval, this interpretation is inconsistent with the experimental results of Al'tshuler *et al.* [1958] and the calculations of Schroeder and McMaster [1973] that indicate complete melting by 13 GPa. Our suggestion that the material properties near the shock front may dominate reconciles Mineev and Savinov's [1976] interpretation with the phase relations.

Figure 11: Phase diagram for water [Liu and Bassett, 1986; Pistorius *et al.*, 1963], and calculated Hugoniot temperature for water [Rice and Walsh, 1957]. More recent calculations by Schroeder and McMaster [1972] indicate that ice VII melts on the 20°C initial temperature Hugoniot at 13 GPa. The -10°C initial temperature Hugoniot is calculated to melt at 23.4 GPa. The shock temperature measurements of Kormer [1968] and Lyzenga *et al.* [1982] support the high melting temperature calculation of Schroeder and McMaster.

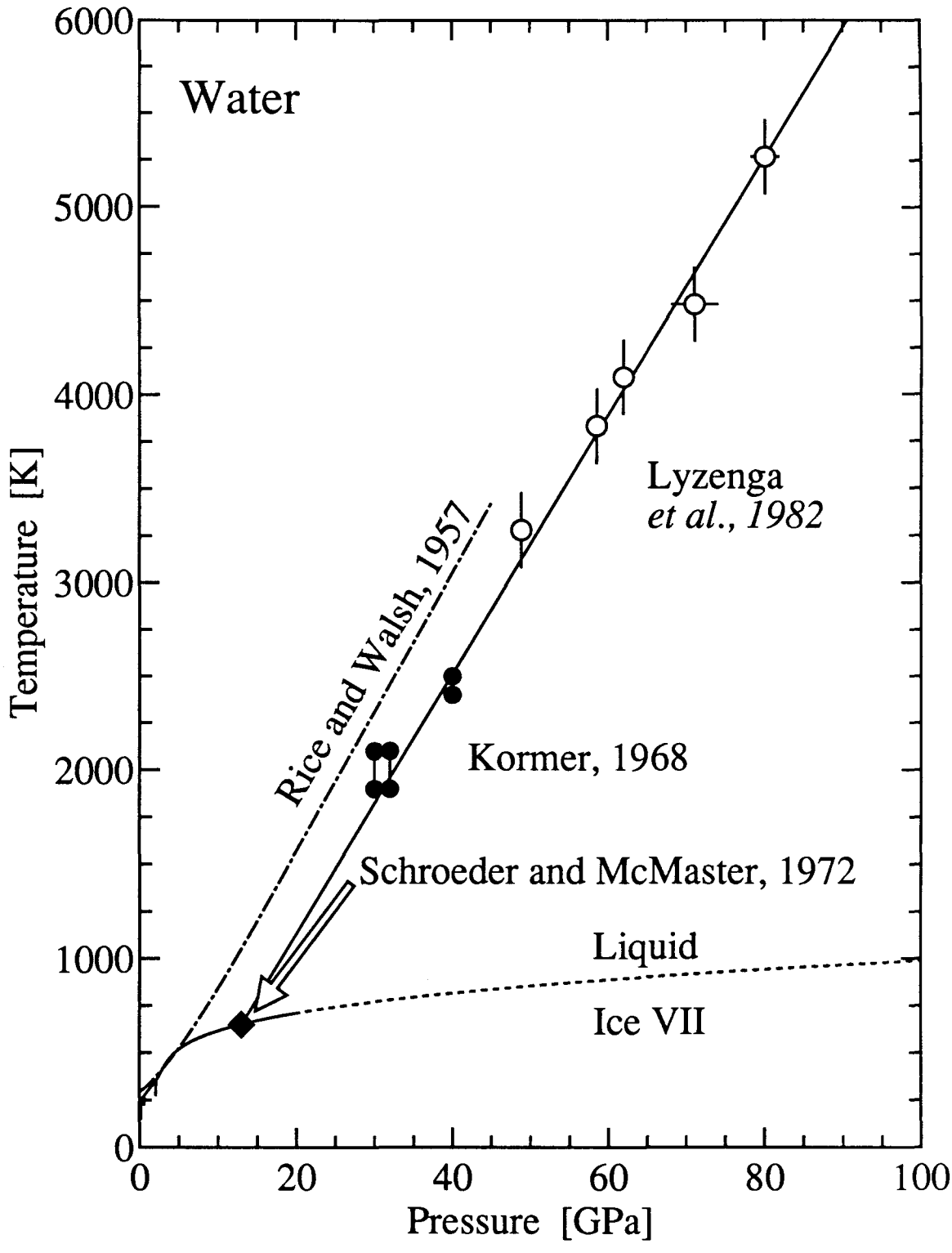
Water
Temperature [K]
Pressure [GPa]
6000
5000
4000
3000
2000
1000
0
0
20
40
60
80
100
Lyzenga
et al., 1982
Rice and Walsh, 1957
Kormer, 1968
Schroeder and McMaster, 1972
Liquid
Ice VII

Figure 11.

If water were partially crystallized near 15 GPa on the Hugoniot, then indirect viscosity measurements, *e.g.*, the electrical conductivity experiments [Hamann and Linton, 1969], might well predict a substantially lower viscosity than the oscillatory damping method. Even if ice VII existed at equilibrium with water behind the shock front, the existence of a fully interconnected melt network would give essentially the same conductivity measurement as a completely liquid system. Partially crystalline water behind the shock front would have an adverse effect on the viscous drag experiments [Al'tshuler *et al.*, 1977, 1986; Kim, 1984] as well, although these experiments should be insensitive to the material properties near the shock front itself.

13. Conclusions

We have expanded upon the analysis of Zaidel' [1967] for the damping of perturbations on a shock front. We have also clarified the assumptions implicit in the analysis, and explored the ramifications of these assumptions on the application of the method to analyzing experiments. We considered in detail (1) the effect of initial conditions, (2) finite shock amplitude, and (3) the validity of the viscous perturbation approach.

The controversial experiments on shocked water [Mineev and Zaidel', 1968] were reviewed. To the extent that we can analyze these experiments from the published descriptions, we conclude that the dissipative forces in the system are compatible with the viscosities calculated from the Zaidel' [1967] formulae. That this calculated viscosity may be apparent rather than real is suggested by the sensitivity of the calculation to the material properties in and near the shock front, and the prediction that water may be at least partially crystalline (ice VII) on the Rayleigh path. This explanation reconciles the Mineev and Zaidel' [1968] experiments with the viscosity estimates obtained from electrical conductivity measurements of dilute salt solutions.

If water has an anelastic absorption mode near 4.8 MHz, this too would lead to a gross overestimation of the viscosity. The importance of anelasticity might be tested experimentally by conducting these experiments with longer wavelength perturbations that give lower frequency compressional wave frequencies.

It important to note that the complete experimental measurements for $\phi(T)$ have not been published for any fluid, including water. Only the results for aluminum have been shown by Sakharov *et al.*, [1965] and Mineev and Savinov [1967]. In the case of aluminum, decreasing the Reynolds number shifts the first zero of ϕ to shorter times. This is qualitatively opposite to our calculations for water. Since only the magnitude, and not the sign, of this phase shift for water has been reported, it remains to be shown whether or not the analytic description of the experiment even qualitatively models the data. Until such a comparison can be made to demonstrate good agreement between the theory and experiment, these calculated viscosities must be regarded as provisional.

The oscillatory damping experiments were originally suggested as a method for determining shear viscosity at high pressure. We have shown that the bulk viscosity (and by inference, thermal conductivity) influence the damping as well. These viscosities are coupled, and cannot be decoupled experimentally by independent adjustment of either the perturbation wavenumber, k_0, or amplitude, ξ_0. The shear and bulk contributions have different phases, however, so precise measurement of $\phi(t)$ could, at least in principle, be analyzed for both shear and bulk viscosities. Such an analysis would be quite sensitive to the IC, however, and the approximations considered here may prove inadequate for this purpose.

Preliminary calculations with the full second-order Navier-Stokes equations for viscous compressible flow indicate that shock instabilities may occur even when the Kontorovich-D'yakov thermodynamic stability criteria are satisfied. These rheological instabilities may manifest them-

selves as turbulence behind the shock front, and might be responsible for the rapid dynamic mixing that is observed in shock-mediated chemical reactions.

We are grateful to D.W. Schwendeman for his invaluable assistance with the mathematical analysis in §5, and R.F. Svendsen, Jr., for very helpful discussions regarding the formulation of boundary conditions. We also thank Professors D.J. Stevenson and W.I. Newman (UCLA) for their thoughtful comments and suggestions.

References

Al'tshuler, L.V., A.A. Bakanova, and R.F. Trunin, Phase transformations of water compressed by strong shock waves, *Sov. Phys. Doklady, 3*, 761-763, 1958.

Al'tshuler, L.V., G.I. Kanel', and B.S. Chekin, New measurements of the viscosity of water behind a shock wave front, *Sov. Phys. JETP, 45*, 348-350, 1977.

Al'tshuler, L.V., G.S. Doronin, and G.Kh. Kim, Viscosity of shock-compressed fluids, *J. Appl. Mech. Tech. Phys. (Eng. Transl.), 27*, 887-894, 1986.

Angell, C.A., P.A. Cheeseman, and S. Tamaddon, Pressure enhancement of ion mobilities in liquid silicates from computer studies to 800 kilobars, *Science, 218*, 885-887, 1982.

Bakanova, A.A., V.N. Zubarev, Yu.N. Sutulov, and R.F. Trunin, Thermodynamic properties of water at high pressures and temperatures, *Sov. Phys. JETP, 41*, 544-548, 1976.

Bellman, R.E., R.E. Kalaba, and J.A. Lockett, *Numerical Inversion of the Laplace Transform: Applications to Biology, Economics, Engineering, and Physics*, pp. 249, Elsevier, New York, 1966.

Bland, D.R., On shock structure in a solid, *J. Inst. Maths Applics, 1*, 56-75, 1965.

Boslough, M.B., Shock-induced chemical reactions in nickel-aluminum powder mixtures: Radiation pyrometer measurements, *Chem. Phys. Lett., 160*, 618-622, 1989.

Boslough, M.B., A thermochemical model for shock-induced reactions (heat detonations) in solids, *J. Chem. Phys., 92*, 1839-1848, 1990.

Bottinga, Y., and D.F. Weill, The viscosity of magmatic silicate liquids: A model for calculation, *Am. J. Sci., 272*, 438-475, 1972.

Brey, L.A., G.B. Schuster, and H.G. Drickamer, High pressure studies of the effect of viscosity on fluorescence efficiency in crystal violet and auramine O, *J. Chem. Phys., 67*, 2648-2650, 1977.

D'yakov, S.P., Investigation of the problem of stability of shock waves in arbitrary media, *Zh. Eksp. Teor. Fiz. (Russian), 27*, 288-295, 1954.

Förster, Th., and G. Hoffmann, Die viskositätsabhängigkeit der fluoreszenzquantenausbeuten einiger farbstoffsysteme, *Z. Physik. Chem. NF, 75*, 63-76, 1971.

Fowles, G.R., and A.F.P. Houwing, Instabilities of shock and detonation waves, *Phys. Fluids, 27*, 1982-1990, 1984.

Freeman, N.C., A theory of the stability of plane shock waves, *Proc. Roy. Soc. Lond. A, 288*, 341-

362, 1955.

Fujii, T., and I. Kushiro, Melting relations and viscosity of abyssal tholeiite, *Carnegie Inst. Wash. Yearb., 76*, 461-465, 1977a.

Fujii, T., and I. Kushiro, Density, viscosity, and compressibility of basaltic liquid at high pressures, *Carnegie Inst. Wash. Yearb., 76*, 419-424, 1977b.

Godunov, S.K., A.A. Deribas, I.D. Zakharenko, and V.I. Mali, Investigation of the viscosity of metals in high-velocity collisions, *J. Appl. Mech. Tech. Phys. (Eng. Transl.), 12*, 114-118, 1971.

Hamann, S., and M. Linton, The viscosity of water under shock compression, *J. Appl. Phys., 40*, 913-914, 1969.

Harris, P., and H.N. Presles, Reflectivity of a 5.8 kbar shock front in water, *J. Chem. Phys., 74*, 6864-6866, 1981.

Huston, A.L., B.L. Justus, and A.J. Campillo, Direct measurement of the viscosity of glycerol under laser driven shock compression: fluorescence lifetime changes in crystal violet, *Chem. Phys. Lett., 122*, 617-621, 1985.

Istrakov, A.G., and V.B. Librovich, The effect of transport properties in the stability of a plane flame front, *PMM Appl. Math. Mech. (Eng. Transl.), 30*, 541-557, 1966.

Kanzaki, M., K. Kurita, T. Fujii, T. Kato, O. Shimomura, and S. Akimoto, A new technique to measure the viscosity and density of silicate melts at high pressure, in *High-Pressure Research in Mineral Physics*, edited by M. Manghnani and Y. Syono, pp. 195-200, American Geophysical Union, Washington, D.C., 1987.

Kim, G.Kh., Viscosity measurements for shock-compressed water, *J. Appl. Mech. Tech. Phys. (Eng. Transl.), 26*, 692-695, 1984.

Knittle, E., and R. Jeanloz, Melting curve of $(Mg,Fe)SiO_3$ perovskite to 96 GPa: Evidence for a structural transition in lower mantle melts, *Geophys. Res. Lett., 16*, 421-424, 1989.

Kontorovich, V.M., Concerning the stability of shock waves, Sov. Phys. JETP, 6, 1179-1180, 1957.

Kormer, S.B., Optical study of the characteristics of shock-compressed condensed dielectrics, *Sov. Phys. Uspekhi, 11*, 229-254, 1968.

Kushiro, I., Changes in viscosity and structure of melt of $NaAlSi_2O_6$ composition at high pressures, *J. Geophys. Res., 81*, 6347-6350, 1976.

Kushiro, I., H.S. Yoder, and B.O. Mysen, Viscosities of basalt and andesite melts at high pressures, *J. Geophys. Res., 81*, 6351-6356, 1976.

Kushiro, I., Phase transformations in silicate melts under upper-mantle conditions, in *High-Pressure Research Applications in Geophysics*, edited by M.H. Manghnani and S.I. Akimoto, pp. 25-37, Academic Press, New York, 1977.

Kushiro, I., Viscosity and structural changes of albite ($NaAlSi_3O_8$) melt at high pressures, *Earth Planet. Sci. Lett., 41*, 87-90, 1978a.

Kushiro, I., Viscosity change of GeO_2 melt with pressure as a model of SiO_2 melt, *Carnegie Inst. Wash. Yearb., 77*, 672-674, 1978b.

Kushiro, I., Density and viscosity of hydrous calc-alkaline andesite magma at high pressures, *Carnegie Inst. Wash. Yearb., 77*, 675-677, 1978c.

Kushiro, I., Viscosity, density, and structure of silicate melts at high pressures, and their petrological applications, in *Physics of Magmatic Processes*, edited by R.B. Hargraves, pp. 93-120, 1980.

Kushiro, I., Viscosity of partial melts in the upper mantle, *J. Geophys. Res., 91*, 9343-9350, 1986.

Landau, L.D., and E.M. Lifshitz, *Fluid Mechanics*, pp. 536, Pergamon Press, New York, 1959.

Liebermann, L.N., The second viscosity of liquids, *Phys. Rev. 2, 75*, 1415-1422, 1949.

Liu, L., and W.A. Bassett, Elements, Oxides, Silicates: High-Pressure Phases with Implications for the Earth's Interior, pp. 250, Oxford University Press, New York, 1986.

Lyzenga, G.A., T.J. Ahrens, W.J. Nellis, and A.C. Mitchell, The temperature of shock-compressed water, *J. Chem. Phys., 76*, 6282-6286, 1982.

Mineev, V.N., and E.V. Savinov, Viscosity and melting point of aluminum, lead, and sodium chloride subjected to shock compression, *Sov. Phys. JETP, 25*, 411-416, 1967.

Mineev, V.N., and E.V. Savinov, Relationship between the viscosity and possible phase transformations in shock-compressed water, *Sov. Phys. JETP, 41*, 656-657, 1976.

Mineev, V.N., and R.M. Zaidel', The viscosity of water and mercury under shock loading, *Sov. Phys. JETP, 27*, 874-878, 1968.

Mitchell, A.C., and W.J. Nellis, Equation of state and electrical conductivity of water and ammonia shocked to the 100 GPa (1 Mbar) pressure range, *J. Chem. Phys., 76*, 6273-6281, 1982.

Pistorius, C.W.F.T., M.C. Pistorius, J.P. Blakey, and L.J. Admiraal, Melting curve of ice VII to 200 kbar, *J. Chem. Phys., 38*, 600-602. 1963.

Rayleigh, Lord, Aerial plane waves of finite amplitude, *Proc. Roy. Soc. Lond. A, 84*, 247-284, 1910.

Rice, M.H., and J.M. Walsh, Equation of state of water to 250 kilobars, *J. Chem. Phys., 26*, 824-830, 1957.

Rigden, S.M., T.J. Ahrens, and E.M. Stolper, Shock compression of molten silicate: Results for a model basaltic composition, *J. Geophys. Res., 93*, 367-382, 1988.

Sakharov, A.D., R.M. Zaidel', V.N. Mineev, and A.G. Oleinik, Experimental investigation of the stability of shock waves and the mechanical properties of substances at high pressures and temperatures, *Sov. Phys. Doklady, 9*, 1091-1094, 1965.

Scarfe, C.M., B.O. Mysen, and D. Virgo, Changes in viscosity and density of melts of sodium disilicate, sodium metasilicate, and diopside composition with pressure, *Carnegie Inst. Wash. Yearb., 78*, 547-551, 1979.

Schlichting, H., *Boundary-Layer Theory, Seventh Ed.*, pp. 817, McGraw-Hill, New York, 1979.

Schroeder, R.C., and W.H. McMaster, Shock-compression freezing and melting of water and ice, *J. Appl. Phys., 44*, 2591-2594, 1973.

Swan, G.W., G.E. Duvall, and C.K. Thornhill, On steady wave profiles in solids, *J. Mech. Phys. Solids, 21*, 215-227, 1973.

Swegle, J.W., and D.E. Grady, Shock viscosity and the prediction of shock wave rise times, *J. Appl. Phys., 58*, 692-701, 1985.

Truesdell, C., and R.A. Toupin, The classical field theories, in *Handbuch der Physik, Vol. III/1*, edited by S. Flügge, pp. 226-793, Springer-Verlag, Berlin, 1960.

Walden, P., Über organische lösungs- und ionisierungsmittel III: Innere reibung und deren zusammenhang mit dem leitvermögen, *Z. Physik. Chem., 55*, 207-249, 1906.

Woodcock, L.V., C.A. Angell, and P. Cheeseman, Molecular dynamics studies of the vitreous state: Simple ionic systems and silica, *J. Chem. Phys., 65*, 1565-1577, 1976.

Yakusheva, O.B., V.V. Yakushev, and A.N. Dremin, Formation of particles of sulphur in solutions of sodium thiosulphate behind fronts of shock waves, in *Combustion and Explosion*, pp. 544-548, Izdat. Nauk., 1972.

Zaidel', R.M., Shock wave from a slightly curved piston, *PMM Appl. Math. Mech. (Eng. Transl.), 24*, 316-327, 1958.

Zaidel', R.M., Development of perturbations in plane shock waves, *J. Appl. Mech. Tech. Phys. (Eng. Transl.), 8*, 30-39, 1967.

Chapter 3: The Equation of State of Molybdenum at 1400°C[†]

[†] Published in *Journal of Applied Physics, 63*, 4469-4475, 1988.

Shock compression data to 96 GPa for pure molybdenum, initially heated to 1400°C, are presented. Finite strain analysis of the data gives a bulk modulus at 1400°C, K_{0S}, of 244±2 GPa and its pressure derivative, K'_{0S}, of 4. A fit of shock velocity to particle velocity gives the coefficients of $U_S=c_0+s\,U_P$ to be c_0=4.77±0.06 km/s and s=1.43±0.05. From the zero pressure sound speed, c_0, a bulk modulus of 232±6 GPa is calculated that is consistent with extrapolation of ultrasonic elasticity measurements. The temperature derivative of the bulk modulus at zero pressure, $\partial K_{0S}/\partial T|_P$, is approximately -0.012 GPa/K. A thermodynamic model is used to show that the thermodynamic Grüneisen parameter is proportional to the density and independent of temperature. The Mie-Grüneisen equation of state adequately describes the high temperature behavior of molybdenum under the present range of shock loading conditions.

1. Introduction

The equation of state (EOS) of molybdenum (Mo) at high pressures is being used as a calibration standard to relate absolute pressure-density data to diamond anvil compression data [Mao *et al.*, 1978]. Both shock and particle velocity have been measured for Mo shocked with a nuclear explosive [Regan *et al.*, 1977] to obtain Hugoniot data to 2.0 TPa. Mo is thus well calibrated along the room temperature (or "principal") Hugoniot, yet theoretical arguments are necessary to extend the shock EOS to neighboring regions of P-V-T space. The present study is the first study of the absolute EOS of any metal at significantly high initial temperatures. A 1400°C Mo Hugoniot has been measured that calibrates models for this P-V-T extrapolation.

One of the research efforts of the experimental geophysics group at Caltech is the study of molten silicates under shock loading conditions. These experiments, developed by Rigden *et al.* [1984; 1988], employ a Mo sample assembly that both contains the sample at temperatures in excess

of 1400°C, and acts as a furnace by coupling to a radio frequency power source. A flyer plate, propelled by a gun, impacts the first surface of the heated Mo container, and the subsequent shock wave traverses the Mo driver plate, then the silicate sample, and finally the Mo cover. The transit time of the shock wave through the sample and cover combination is recorded with a rotating prism streak camera. A direct impedance match solution [Ahrens, 1987] for this composite sample assembly requires knowledge of the shock behavior of either the molten sample or the heated Mo. Since the former is the objective of these experiments, the latter must either be calculated or experimentally determined. Rigden *et al.* [1984; 1988] calculated the high temperature shock behavior of Mo from its known principal Hugoniot with a Mie-Grüneisen extension of the Birch-Murnaghan EOS [Birch, 1952].

In order to verify these calculations, we undertook an experimental study of the dynamic loading properties of Mo at 1400°C, the temperature to which Rigden *et al.* heated their molten anorthite-diopside eutectic composition. In addition to their direct relevance to our shock wave studies of molten silicates, our new results on hot Mo give more general insights into the high temperature and pressure equations of state of metals.

2. Experimental Procedure

Dynamic shock compression of hot Mo was achieved using the Caltech 40 mm powder gun [Ahrens, 1987]. The experimental procedure is similar the that used by Rigden *et al.* [1984; 1988] for the shock measurement of the EOS of molten silicates.

Molybdenum of 99.95% purity, specification ABL-2 from Amac Specialty Metals, Cleveland, was used. The samples were machined from this polycrystalline stock into a single piece driver plate-sample combination as shown in Figure 1. A 2 mm thick, 45 mm diameter disk of Mo acts as

the driver plate, and a 3.6 mm thick, 13.5 mm diameter disk of Mo, coaxial to the driver plate, is the sample.

The Mo samples were supported by a 6.4 mm thick plate of fibrous Al_2O_3 ceramic at a distance of approximately 1 mm from a three-turn water-cooled copper coil. This coil, attached to a 10 kW radio frequency source, acted as an induction heater. Temperatures in excess of 1800°C could be achieved with this configuration. At 1400°C, the temperature can be stabilized to within one-half degree. A 100%Pt-90%Pt 10%Rh thermocouple was pressed into a well in the sample to record its preheating temperature. Light reflected from the free surface of the sample and driver was turned by a mirror in the tank to a port at the side of the tank. This reflected light was subsequently focused onto the slit of a continuous writing streak camera. This streak record was used to record the shock transit time within the sample. A xenon flash lamp operating at 10-15 kV was used to illuminate the sample during the experiment.

The flyer plates were 2.4 mm thick, 32 mm diameter disks of either tungsten or 2024 aluminum mounted in a Lexan projectile. The velocity of the projectile was recorded with a double exposure X-ray shadowgraph. The X-ray exposure occurred immediately prior to impact. As a backup device, the time taken for the projectile to cross the known distances between three lasers that cross the flight path is measured. Projectile velocities were between 1.5 and 2.5 km/s.

The measured quantities in our experiment are the sample and flyer plate density, initial sample temperature, the shock transit time in the sample, and the velocity of impact.

3. Results and Discussion

The shock pressure, P_H, and sample density, ρ_{HS}, were calculated from the Rankine-Hugoniot equations for stress and mass conservation across the flyer plate-driver/sample interface. Sample

Figure 1: Schematic cross section of the experimental setup. A molybdenum driver plate (a) and sample (b) are machined as a single piece. The sample is suspended in a fibrous Al_2O_3 ceramic plate (c) adjacent to a copper induction coil (d). Preheat temperatures are recorded by the 100%Pt-90%Pt 10%Rh thermocouple (e) that is pressed into the sample. A tungsten or 2024 aluminum flyer plate (f) is pressed into a Lexan projectile (g) with O-rings (h) to help retain the muzzle gasses.

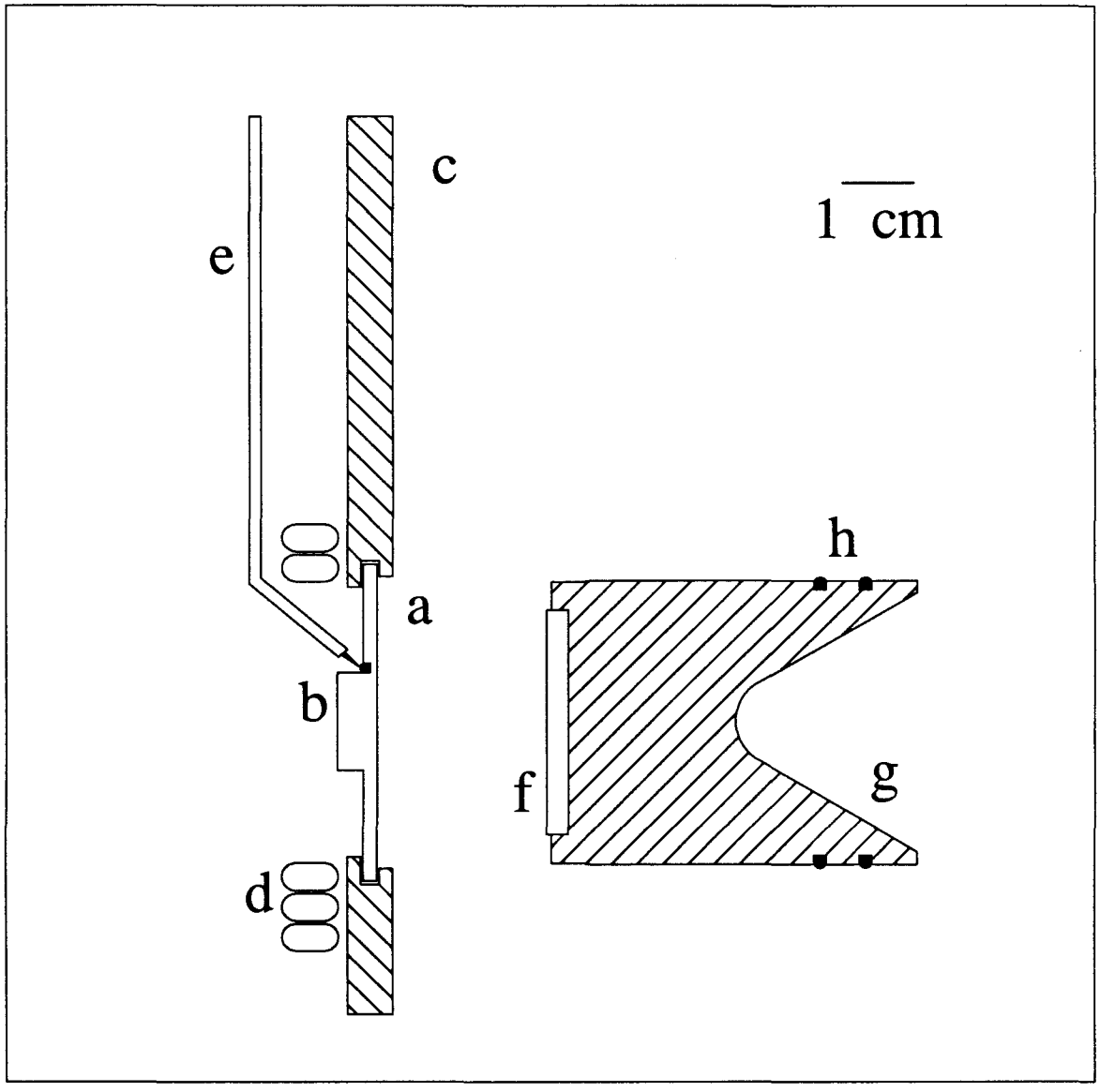

Figure 1.

thickness and initial density are not directly measured, but calculated from their measured room temperature values, the sample preheat temperature, and the linear thermal expansion data in Table I. The shock states with their estimated RMS errors are given in Table II.

Our analysis of these results is presented in parts. First, we demonstrate that our final shock states are solid and not liquid. Second, we determine the isentropic bulk modulus and its pressure derivative for Mo at 1400°C with both a finite strain model and the shock EOS. Third, we compare our shock data with the theoretical predictions of the Mie-Grüneisen EOS and show that the Grüneisen parameter varies in proportion to density. Fourth and finally, we compare our data with elasticity measurements to discriminate between three possible interpretations of our data.

Shock State: Solid versus *Liquid*

The calculated melting temperature for Mo is at least 1000 K higher than the calculated shock temperatures of our experiments at a given shock pressure. Our final shock states therefore represent solid Mo in all cases.

The Rankine-Hugoniot equations can be used to determine the pressure (P), volume per unit mass (V), and internal energy per unit mass (E) along the Hugoniot. A constitutive relationship is necessary to relate these state variables to the temperature (T). The Mie-Grüneisen equation is a useful constitutive relationship for this purpose and has a strong theoretical foundation [Eliezer *et al.*, 1986].

The thermodynamic Grüneisen parameter, $\gamma \equiv -\partial \ln T/\partial \ln V|_S$, relates internal energy and pressure according to the Mie-Grüneisen equation, $\partial P/\partial E|_V = \gamma/V$. The Grüneisen parameter is assumed to be a function of volume according to:

Table I. Parameters used in data reduction

	c_0 (km/s)	s	ρ_0 (Mg/m^3)
W	4.029 [a]	1.237 [a]	19.224 [a]
2024 Al	5.328 [a]	1.338 [a]	2.785 [a]
Mo	5.14 [b]	1.22 [b]	10.2201 [c]

$$\Delta L/L_0 = 4.697\times10^{-6}(T-293) + 9.756\times10^{-10}(T-293)^2 + 9.403\times10^{-14}(T-293)^3$$

for Mo from 293 to 1545 K, ±4%, and

$$\Delta L/L_0 = 7.60\times10^{-3} + 7.583\times10^{-6}(T-1545) + 1.329\times10^{-9}(T-1545)^2 + 1.149\times10^{-12}(T-1545)^3$$

for Mo from 1545 to 2800 K, ±5% [d]

$$\gamma_{0,Mo} = 1.52$$ [e]

$$Cp = 34.139 - 4.4926\times10^{-3}T + 3.7012\times10^{-6}T^2 - \frac{1.5722\times10^2}{\sqrt{T}} \text{ J mol}^{-1}\text{ K}^{-1}$$

for Mo from 298 to 1800 K [f]

[a] McQueen, 1969.
[b] Marsh, 1980.
[c] Straumanis and Shodhan, 1968.
[d] Touloukian *et al.*, 1970.
[e] McQueen *et al.*, 1970.
[f] Robie *et al.*, 1978.

Table II. Experimental Results

Shot No.	Flyer	ρ_{298K} (Mg/m^3)	T_0 (K)	V_{imp} (km/s)	U_S (km/s)	U_P (km/s)	P_H (GPa)	ρ_H (Mg/m^3)	T_H[a] (K)
707	W	10.206±0.002	1667	1.456±0.007	5.960±0.119	0.883±0.008	52.3±1.1	11.68±0.05	1887±532
716	W	10.206±0.002	1673	1.527±0.006	6.115±0.047	0.919±0.004	55.9±0.5	11.70±0.02	2602±222
725	W	10.210±0.002	1671	2.030±0.010	6.516±0.049	1.219±0.009	79.0±0.8	12.24±0.03	3101±367
736	2024 Al	10.207±0.002	1674	1.995±0.008	5.525±0.041	0.538±0.004	29.5±0.3	11.02±0.02	1864±174
741	W	10.212±0.002	1674	2.368±0.008	6.788±0.021	1.414±0.006	95.6±0.5	12.57±0.02	3721±253

[a] Temperatures calculated with q = 1.

$$\frac{d \ln \gamma}{d \ln V} \equiv q, \tag{1}$$

where q is assumed to be constant, and it is further assumed that the temperature dependence of γ lies solely in the temperature dependence of the volume.

Recognizing that $\partial E/\partial T|_V = C_V$, the heat capacity at constant volume, temperature and pressure are related by $\partial T/\partial P|_V = V/(\gamma C_V)$. Integration of this equation along a path of constant volume requires a reference P-T point at the volume of interest. It is convenient to use the principal isentrope as a reference curve since pressure and temperature are readily calculated for any specified volume. The principal isentrope is a path of constant entropy that, like the principal Hugoniot, passes through the 1 bar, 20°C point.

Along an isentrope, the temperature is readily calculated [Ahrens, 1979] from the definition of γ:

$$T_S = T_0 \exp\left[\frac{\gamma_0}{q}\left[1-\left[\frac{V}{V_0}\right]^q\right]\right] \qquad q \neq 0 \tag{2a}$$

$$T_S = T_0\left[\frac{V_0}{V}\right]^{\gamma_0} \qquad q = 0, \tag{2b}$$

where the subscript S denotes the isentropic state, and V_0, T_0, and γ_0 are the volume, temperature, and Grüneisen parameter at zero pressure, 25°C, respectively.

Pressure along an isentrope may be calculated from the third-order Birch-Murnaghan equation:

$$P_S = \frac{3}{2} K_{0S}\left[\left[\frac{V_0}{V}\right]^{7/3} - \left[\frac{V_0}{V}\right]^{5/3}\right]\left[1-\frac{3}{4}(4-K'_{0S})\left[\left[\frac{V_0}{V}\right]^{2/3}-1\right]\right], \tag{3}$$

where K_{0S} is the isentropic bulk modulus at zero pressure and K'_{0S} is its pressure derivative.

Using the isentrope as a reference curve, the temperature of a point on the Hugoniot, T_H, may be calculated from:

$$T_H = T_S + \frac{V_H(P_H - P_S)}{\gamma C_V} , \tag{4}$$

where the subscript H denotes a point on the Hugoniot. It has been assumed for simplicity (justification follows) that the heat capacity may be taken as a constant. The isentrope temperature, T_S, and pressure, P_S, and the Grüneisen parameter, γ, in Eqn. 4 are calculated at the Hugoniot volume, V_H.

The shock temperatures achieved in our experiments were calculated with Eqns. 1, 2, 3, and 4 using values of V_H and P_H (Table II) calculated from the Rankine-Hugoniot equations. Specifically, the Grüneisen parameter is calculated at V_H with Eqn. 1, and the isentrope pressure, P_S, and temperature, T_S, are calculated using Eqns. 2 and 3 with $V = V_H$. The Hugoniot pressure, P_H, and volume, V_H, are used with these isentrope points in Eqn. 4 to calculate the Hugoniot temperature, T_H.

A general temperature-pressure relationship for the Hugoniot can be calculated in the same manner by using an appropriate constitutive relationship for P_H as a function of V_H. The Mie-Grüneisen formulation for this relationship is developed is a subsequent section of the discussion.

The melting point of Mo at high pressures may be estimated by Lindemann's rule, given by Gilvarry [1956] as:

$$\left.\frac{\partial \ln T}{\partial \ln V}\right|_M = 2\left[\frac{1}{3} - \gamma_D\right] , \tag{5}$$

where the subscript M designates melting. γ_D is the Debye model for the Grüneisen parameter, $\gamma_D \equiv -d \ln \Theta_D / d V$, where Θ_D is the Debye temperature. We evaluate Eqn. 5 with the approximation that the Debye model Grüneisen parameter is equal to the thermodynamic Grüneisen parameter, which assumes that the Debye model is valid for Mo and that $T \gg \Theta_D$. The Debye temperature for Mo is 380 K [Hoch, 1975], and the melting temperature at zero pressure is 2893 K [Hultgren *et al.*, 1963], thus the latter assumption is valid. Because we are principally concerned with temperatures in excess of the Debye temperature, we make the additional assumption that $C_V = 3R$, where R is the gas constant. Combining Eqns. 1 and 5 with the assumption $\gamma \approx \gamma_D$ and integrating, we get the result:

$$T_M = T_{0M}\left[\frac{V_M}{V_{0M}}\right]^{2/3} \exp\left[\frac{2\gamma_0(V_{0M}^q - V_M^q)}{q\, V_0^q}\right] \qquad q \neq 0 \tag{6a}$$

$$T_M = T_{0M}\left[\frac{V_M}{V_{0M}}\right]^{2\left\{\frac{1}{3}-\gamma_0\right\}} \qquad q = 0\,, \tag{6b}$$

where V_M and T_M are the temperature and corresponding volume of the solid along the melting curve. $V_M = V_{0M}$ and $T_M = T_{0M}$ at the zero pressure melting point. V_0 is the volume at which $\gamma = \gamma_0$.

The pressure, P_M, at which melting occurs for a particular T_M and V_M may again be calculated with the aid of the Mie-Grüneisen equation. Rearranging Eqn. 4 and changing subscripts (M for H):

$$P_M = P_S + \frac{\gamma C_V (T_M - T_S)}{V_M}. \tag{7}$$

To evaluate Eqn. 7, the isentrope points P_S and T_S and the Grüneisen parameter γ are calculated at $V = V_M$.

A check of the internal consistency of these calculations can be made by computing the melting temperature at zero pressure by simultaneous solution of Eqns. 1, 2, 3, 6, and 7. The calculated temperature exceeds the known value by about 200 K when q=1.

The shock temperatures, calculated with q=1, are shown with the calculated melting curve for Mo in Figure 2. The calculated melting curve for Mo exceeds the calculated experimental shock temperatures by over 1000 K in all cases. It is evident that our experimental points are well within the field of solid stability as judged by the Lindemann's rule calculation. The Lindemann's rule melting curve (L in Fig. 2) is in good agreement with the 34±4 K/GPa slope of the fusion (SGM) determined by Shaner *et al.* [1977]. The Lindemann's rule curve differs sizably, however, from the experimental measurements (VF) of Vereshchagin and Fateeva [1977] to 8 GPa. Although these calculations are sensitive to q, the conclusion that our shock states are all within the field of solid stability is firm for q as high as 3.

Further evidence that our samples remained solid is provided by the measurement of the bulk modulus from the shock data. As shown in the next section, the isentropic bulk modulus of 1400°C Mo is between 225 and 244 GPa. This is similar to the room temperature value of 261 GPa for solid Mo that we calculate from the principal Hugoniot data [Marsh, 1980]. If the samples melted, the bulk modulus would be expected to drop by as much as a factor of two [Kamb, 1968]. The small drop in bulk modulus suggests that the samples remained solid.

Equation of State

The shock wave data for hot Mo, tabulated in Table I, were analyzed with a Eulerian finite strain expansion model [Birch, 1978] adapted for Hugoniot data analysis [Jeanloz and Ahrens, 1980; Heinz and Jeanloz, 1984; Ahrens and Jeanloz, 1987]. With this model, P-V data along a Hugoniot

Figure 2: Mo phase diagram. Calculations based on our data are represented by diamond symbols with 1-σ error bars. The curves are: (L) Lindemann's rule melting curve calculation, (VF) experimental melting curve to 8 GPa of Vereshchagin and Fateeva [1977], (SGM) Clausius-Clapeyron melting slope measured by Shaner *et al.* [1977], (PH) calculated curve for the principal Hugoniot, and (HT) calculation for the 1400°C Hugoniot. These curves were calculated with q=1.

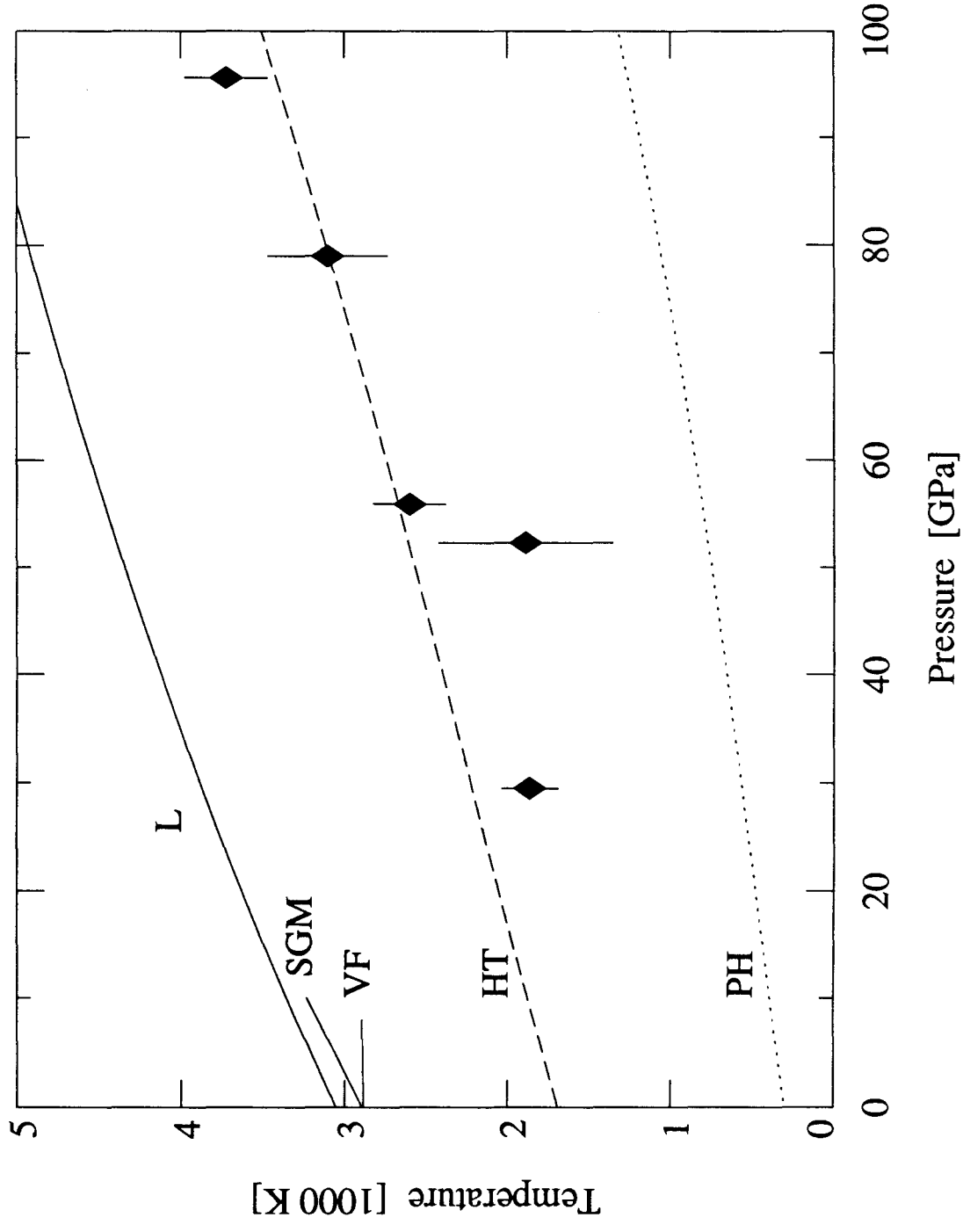
Temperature [1000 K]
Pressure [GPa]
L
SGM
VF
HT
PH
0
1
2
3
4
5
0
20
40
60
80
100

Figure 2.

is mapped into a strain (f) - normalized isentropic pressure (F) plane, wherein the finite strain expansion for pressure may be linearized. This method of analysis is equivalent to fitting the P-V data (corrected to an isentrope) to the Birch-Murnaghan EOS. This transformation is accomplished by:

$$f = \frac{\left[V_0/V\right]^{2/3} - 1}{2} \tag{8}$$

and

$$F_{HS} = \frac{1 - 0.5\gamma[R(1+2f)^{1.5} - 1]}{3f(1+2f)^{1.5}[1+(2-1.5\gamma)f]} P_H, \tag{9}$$

where $R \equiv V_{00}/V_0$, and V_{00} is the actual initial volume of the sample including any porosity. The subscript HS designates that the Hugoniot state has been transformed into an isentrope by means of Eqn. 9. The thermodynamic Grüneisen parameter is assumed to be a function of volume alone according to Eqn. 1. In the absence of phase changes, F and f are related by

$$F_{HS} = K_{0S}(1 - 2\xi_S f_{3H} + 4\zeta_S f_{4H}^2 + \cdots), \tag{10}$$

where

$$f_{3H} = \frac{f[1+(2-\gamma)f]}{1+(2-1.5\gamma)f}, \tag{11}$$

$$f_{4H}^2 = \frac{f^2[1+(2-0.75\gamma)f]}{1+(2-1.5\gamma)f}, \tag{12}$$

$$\xi_S = \frac{3}{4}(4-K'_{0S}), \tag{13}$$

and,

$$\zeta_S = \frac{3}{8}\left[K_{0S}K''_{0S} + K'_{0S}(K'_{0S}-7) + \frac{143}{9}\right]. \tag{14}$$

K_{0S}, K'_{0S}, and K''_{0S} are the zero pressure isentropic bulk modulus, and its first and second derivatives with respect to pressure at constant entropy. The subscript 0 designates the initial zero-pressure state. The bulk modulus and its derivatives are calculated by multiple linear regression [Press *et al.*, 1986] with Eqn. 10. The independent variables are f_{3H} and f_{4H}^2, and the dependent variable is F_{HS}.

The experimental data are presented in the f-F plane in Figure 3. The error and scatter of the data are exaggerated in the f-F projection, as noted by Birch [1978]. These data were calculated with the assumption that q=1, for reasons that will be explained later. Another common assumption for q is that q=0, or γ=constant [Bassett *et al.*, 1968; Anderson, 1987]. These calculations are, however, insensitive to our assumed value of q; values from 0.0 to 10.0 do not change the results. Following Heinz and Jeanloz [1984], the least squares fitting of the data to Eqn. 10 uses weighting according to the 1-σ RMS experimental errors on the assumption that these errors are normally distributed, consequently the data point for shot #707, which has the greatest error, carries little weight in the fit.

A zero-order fit, or simple average (shown as the horizontal dashed line in Fig. 3), gives K_{0S}=244±2 GPa, and K'_{0S}=4 and K''_{0S}=-0.016 GPa^{-1} from Eqns. 13 and 14 respectively. A first-order fit (shown as the dotted line in Fig. 3) gives K_{0S}=225±8 GPa and K'_{0S}=4.76±0.33. K''_{0S} is -0.023 GPa^{-1} from Eqn. 14. Although the data are strongly suggestive of a linear relationship with positive slope, such a linear fit to our data is not statistically justifiable at a reasonable confidence level (>90%). In addition, it will be shown below that such a fit is not reconcilable with the 1 bar elasticity data on Mo.

An alternative method for calculating K_{0S} is to fit the data in the particle velocity (U_P) - shock velocity (U_S). plane [Ahrens, 1987]. Particle and shock velocity are related by:

$$U_S = c_0 + s U_P , \tag{15}$$

Figure 3: Finite strain representation of the experimental data with 1-σ errors. The f and F values were calculated with q=1. Zero-order (dashed line) and first-order (dotted line) fits in the f-F plane are plotted with the fit from the U_P-U_S plane (solid line; see Fig. 4.).

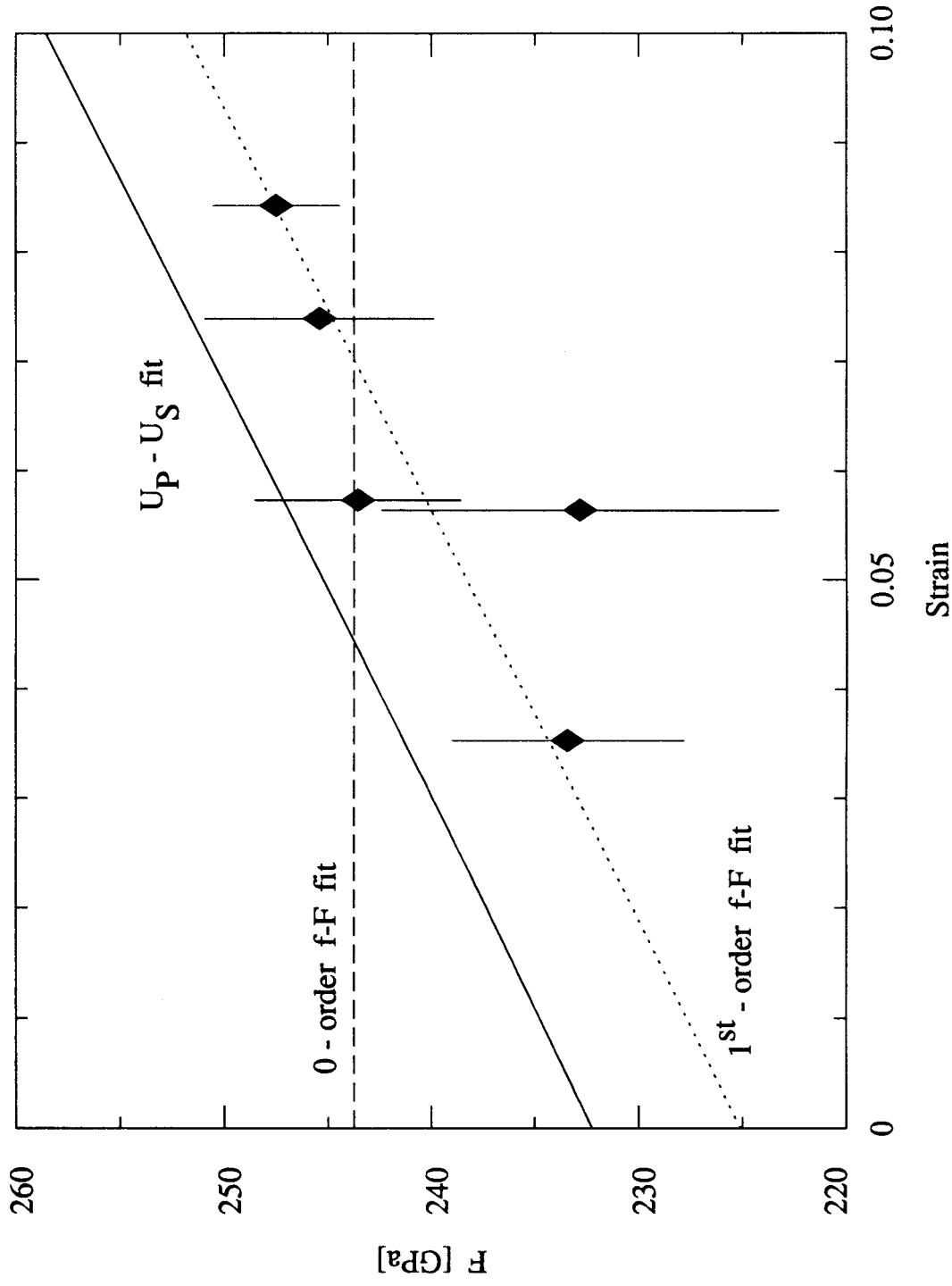
260
250
240
230
220
F [GPa]
0
0.05
0.10
Strain
$U_P - U_S$ fit
0 - order f-F fit
1st - order f-F fit

Figure 3.

where

$$c_0=\sqrt{K_{0S}V_0} \tag{16}$$

and

$$s=\frac{1}{4}\left(1+K'_{0S}\right). \tag{17}$$

The best fit to Eqn. 15 is shown as the solid line in Figure 4, and the values of K_{0S} and K'_{0S} determined from this fit are used in calculating the solid curve in Figure 3. This fit gives c_0=4.77±.06 km/s and s=1.43±0.5, from which K_{0S}=232±6 GPa and K'_{0S}=4.7±.2 are calculated.

These two calculations, although related [Jeanloz and Grover, 1988], are not interchangeable. A linear U_P–U_S relationship is identical to a first-order f-F fit only when $18s\gamma_0=162s^2-360s+215$ [Jeanloz and Grover, 1988]; a condition that Mo fails to obey both on the principal Hugoniot and on the 1400°C Hugoniot. The U_P–U_S fit is consistently offset from the f-F data in Figure 3. For the purpose of calculating an impedance match the U_P–U_S fit is preferred. On the other hand, in calculating a Birch-Murnaghan isentrope, the f-F fit is preferred. These fits overlap within their 2-σ errors.

These bulk modulus calculations may be compared with their cold counterparts computed from principal Hugoniot data [Marsh, 1980]. These principal Hugoniot data are shown in the U_P–U_S and f-F projections in Figures 4 and 5 respectively. Since no experimental errors are reported in Marsh [1980], these data were fit without statistical weighting; *i.e.*, with the assumption that all points have equal error. n Figure 5 the U_P–U_S best fit parameters are used in calculating the solid curves, and the zero- and first-order fits of the f-F data are plotted as the dashed and dotted curves, respectively. We calculate K_{0S} = 261 GPa and K'_{0S}=4 from the zero-order f-F fit and K_{0S}=272 GPa and K'_{0S}=3.71 from the first-order f-F fit. The U_P–U_S fit gives c_0=5.14 km/s and s=1.22 or K_{0S}=270 GPa and K'_{0S}=3.88. As with our data, only the zero-order fit of these data is statistically justifiable.

Figure 4: Particle velocity versus shock velocity for Mo at 1400°C (large diamond symbols), and 25°C (small hexagonal symbols). The lines are least squares best fits.

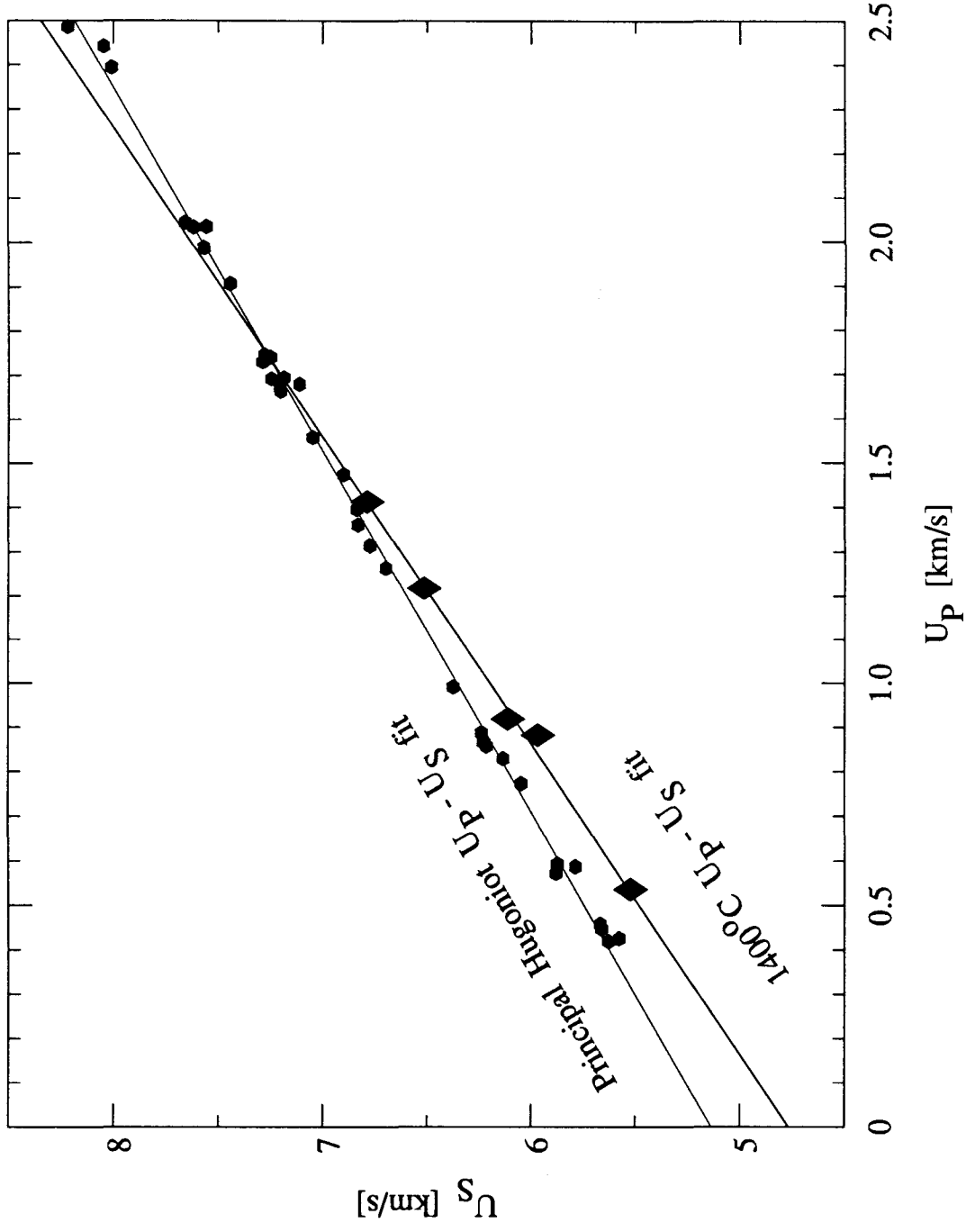
U_S [km/s]
8
7
6
5
0
0.5
1.0
1.5
2.0
2.5
U_P [km/s]
Principal Hugoniot U_P - U_S fit
1400°C U_P - U_S fit

Figure 4.

Figure 5: Finite strain expansion representation of principal Hugoniot data in Marsh [1980]. Zero-order (dashed line) and first-order (dotted line) fits in the f-F plane are plotted with the fit from the U_P-U_S plane (solid line; see Fig. 4).

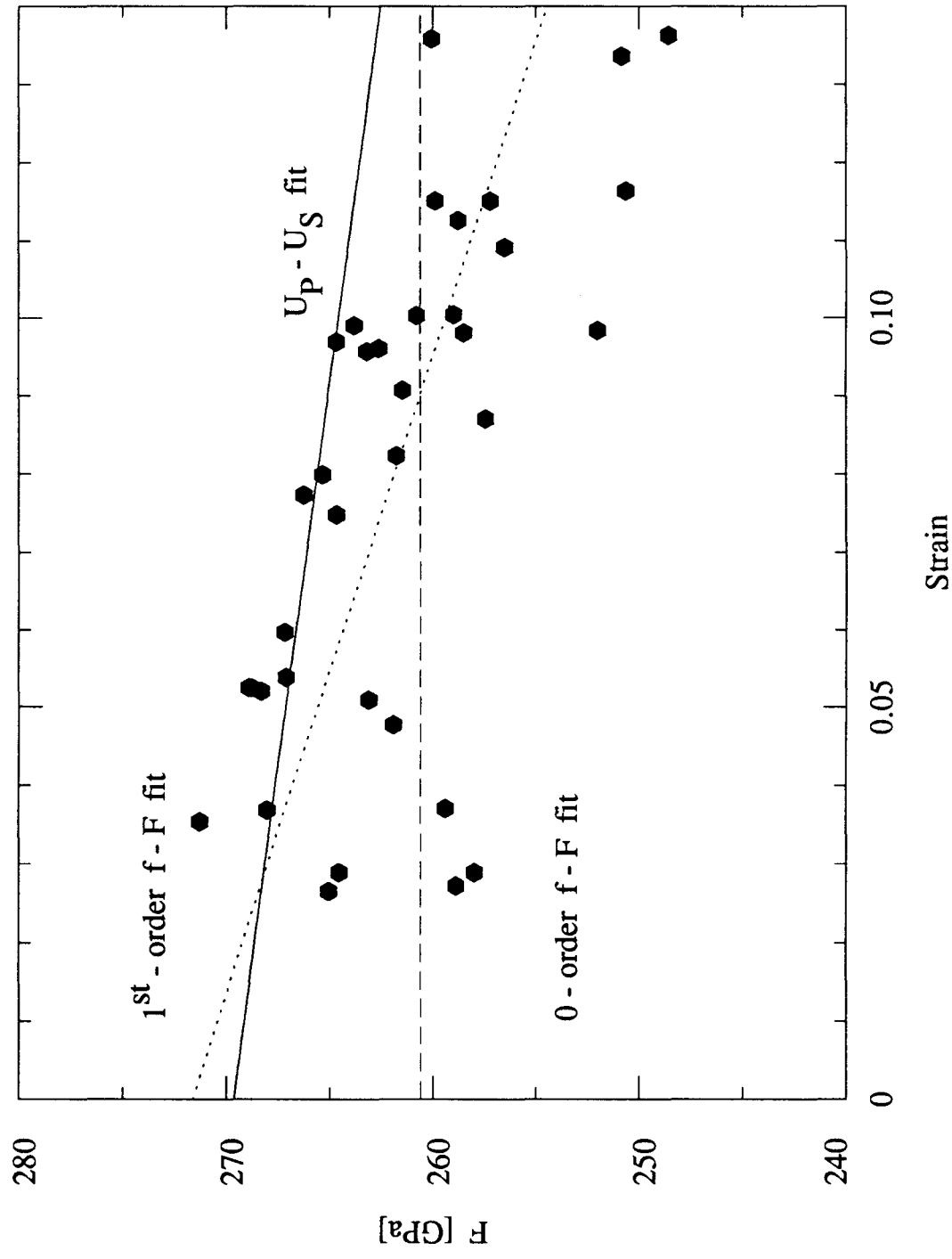
280
270
260
250
240
F [GPa]
0
0.05
0.10
Strain
$U_P - U_S$ fit
1^{st} - order f - F fit
0 - order f - F fit

Figure 5.

From a comparison of these data sets, we conclude that Mo is somewhat more compressible at higher temperatures. No firm conclusions may be drawn concerning its pressure derivative; however, the first-order fits would suggest that Mo becomes less compressible more rapidly at higher temperatures. This is consistent with our expectations since the two Hugoniot curves should be asymptotic at very high shock pressures.

These calculated moduli are independent of our assumptions regarding γ; that is, if we let q=0, or γ=constant, the resulting fit parameters do not vary within their error bars. Similarly, by neglecting the data of shot #707, which has anomalously high errors, the results are unchanged within the calculated errors.

Mie-Grüneisen Equation of State

The experimental data may be compared with a thermodynamic model by computing the Hugoniot for a heated sample. The cold or principal Hugoniot, designated by subscript C, and the high temperature Hugoniot, designated by subscript T, are related by the Mie-Grüneisen EOS at a constant shock volume, V_H by:

$$P_{HT} = \frac{P_{HC}\left(\frac{V_{0C}-V_H}{2} - \frac{V_H}{\gamma}\right) - \int_{T_{0C}}^{T_{0T}} C_p dT}{\frac{V_{0T}-V_H}{2} - \frac{V_H}{\gamma}}. \qquad (18)$$

The initial volume of the preheated sample is calculated from its cold volume and the preheat temperature from the linear expansion data. Shock and particle velocities of the preheated samples may be calculated from:

$$U_S = V_{0T}\sqrt{(P_{HT}-P_0)/(V_{0T}-V_H)} \tag{19}$$

and

$$U_P = \sqrt{(P_{HT}-P_0)(V_{0T}-V_H)}. \tag{20}$$

The cold Hugoniot P-V-U_p relationships are given by the shock EOS [Ahrens, 1987]:

$$P_{HC} = \frac{U_P}{V_{0C}}(c_0+sU_P) \tag{21}$$

and

$$V_{HC} = \frac{c_0+(s-1)U_P}{c_0+sU_P} V_{0C}, \tag{22}$$

where c_0, the zero-pressure sound speed, is given by Eqn. 16, and s is given by Eqn. 17.

The 1400°C Hugoniot for Mo, calculated from Eqns. 16 through 22, is plotted in the V-P and U_P-P planes in Figures 6 and 7 respectively. The calculated 1400°C Hugoniot is also shown in the temperature-pressure plane in Figure 2. For comparison, the principal Hugoniot is also plotted in Figures 6 and 7. In these figures, the best-fit 1400°C Hugoniot is plotted as a thin solid curve, and the 1400°C theoretical Mie-Grüneisen curve, with γ/V constant (q=1) is plotted as a dashed line. The scatter of the data is significantly smaller in these projections than in the f-F projection. It is evident from these figures that the Mie-Grüneisen EOS models the experimental data quite well. The data refinement procedures of Rigden *et al.* [1984; 1988], which used this model to describe Mo at high T and P, are supported by our experiments.

Since Eqn. 19 is sensitive to q, q may be used as a fit parameter to minimize the difference between the Mie-Grüneisen calculation and our experimental data. A value of $q\approx1$ yields the best fit. We suggest therefore, that $q\approx1$, and consequently that the Grüneisen parameter varies approximately in proportion to density. This agrees with the experimental determination [Boehler, 1983] of

Figure 6: 1400°C Mo experimental data in the V-P plane. The curve labeled "fit" is calculated with the best-fit U_P–U_S parameters. The "M-G" curve is calculated with the Mie-Grüneisen equation with q=1. "PH" is the principal Hugoniot for comparison.

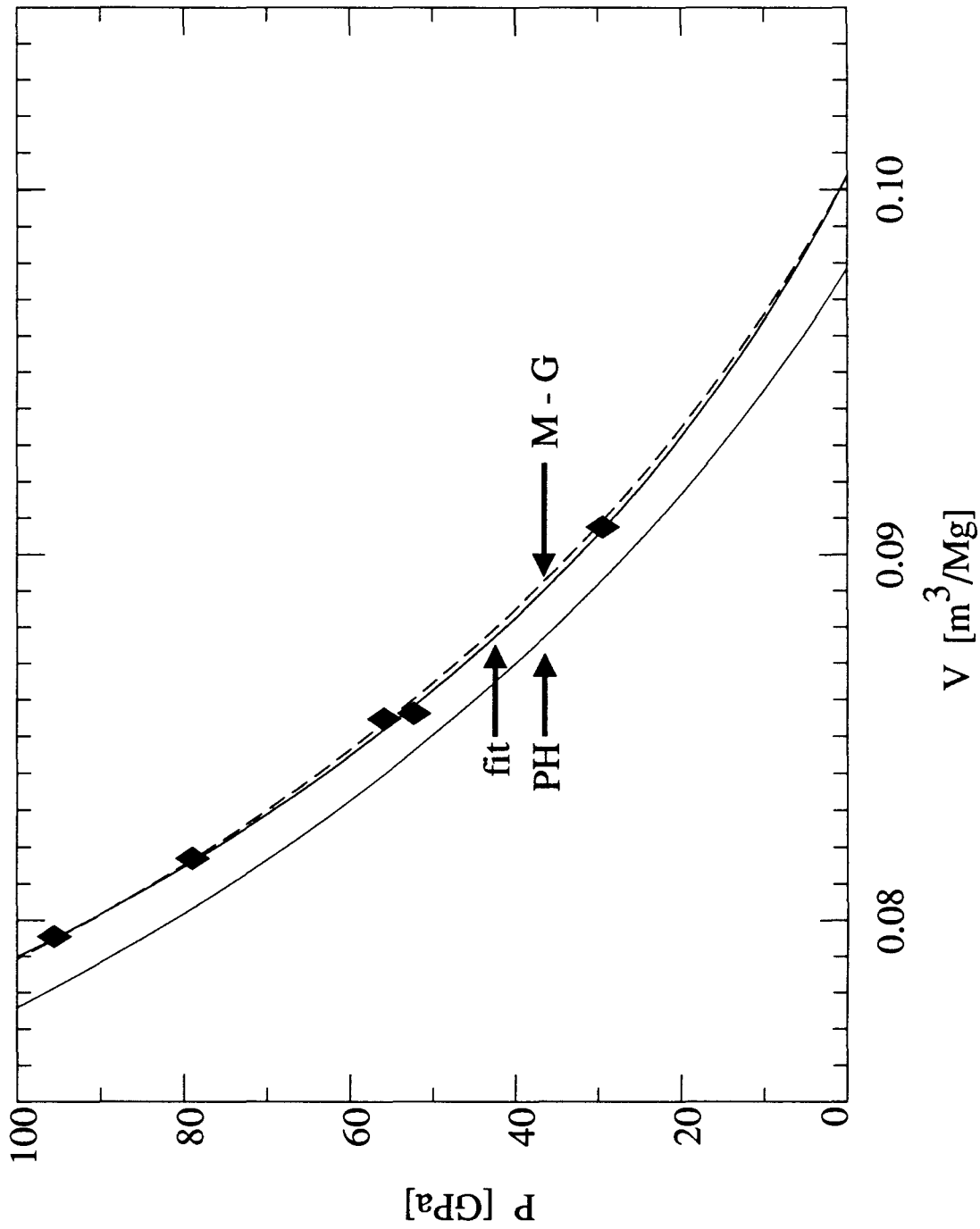

Figure 6.

Figure 7: 1400°C Mo experimental data in the U_P–P plane. Labels correspond to Figure 6.

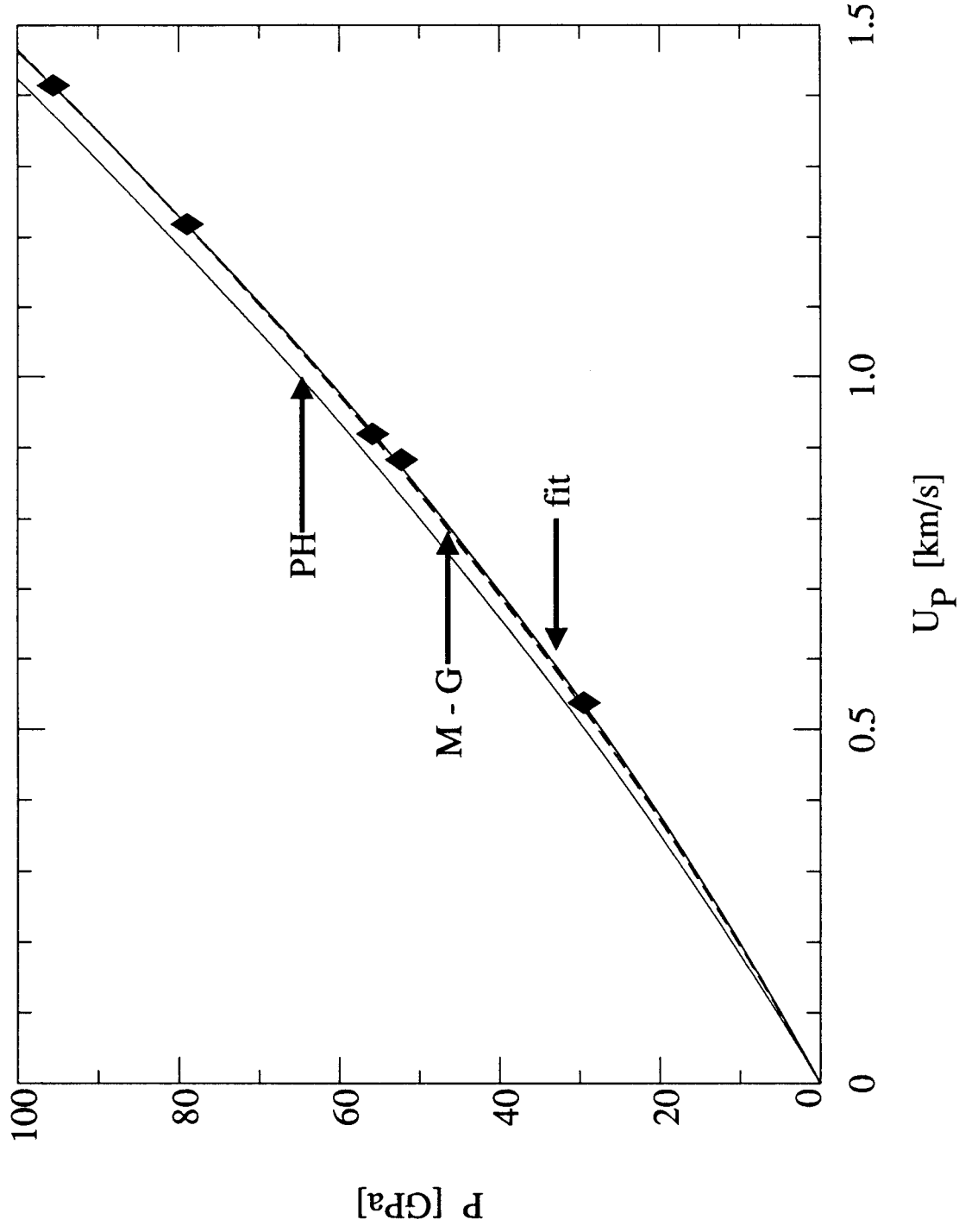

Figure 7.

$q \approx 1$ for Li, Na, and K.

Extrapolation of Ultrasonic Elasticity Measurements

With q constrained to be ≈ 1, we may now employ a thermodynamic model of q to discriminate between our three model calculations of K_{0S} and K'_{0S}. Bassett *et al.* [1968] derived the following thermodynamic expression for the parameter q:

$$q = 1 - \frac{(1+\gamma\alpha T)}{\alpha K_S}\left.\frac{\partial K_S}{\partial T}\right|_P - \left.\frac{\partial K_S}{\partial P}\right|_T + \gamma. \tag{23}$$

This expression does not assume that γ is a function of volume alone, *i.e.*, q is not required to be constant, but rather allows for a temperature dependence as well. More common formulations for γ assume γ to be a function of volume alone [Anderson, 1967; 1987]. By way of the approximation $K'_{0S} \approx \partial K_S/\partial P|_T$:

$$\left.\frac{\partial \ln K_{0S}}{\partial T}\right|_P = \frac{\alpha\left[1-q-K'_{0S}+\gamma_0\left(\frac{V}{V_0}\right)^q\right]}{1+\alpha T\gamma_0\left(\frac{V}{V_0}\right)^q} \tag{24}$$

the isentropic bulk modulus may be calculated as a function of temperature for an assumed constant value of q. V and α are both temperature dependent quantities, thus Eqn. 24 must be numerically integrated. Volume is calculated directly from the thermal expansion data in Table I, and the volumetric coefficient of thermal expansion, $\alpha \equiv \partial \ln V/\partial T|_P$, is calculated from the linear expansion relationships by

$$\alpha = 3\frac{\partial}{\partial T}\ln\left(1+\frac{\Delta L}{L_0}\right)\Bigg|_P. \tag{25}$$

K'_{0S} is not known as a function of temperature, however the zero-order f-F fits of both the principal and 1400°C Hugoniot data suggest that $K'_{0S}\approx 4$, and is therefore independent of temperature. Although not statistically significant, the first-order f-F fits (dotted lines of Figs. 3 and 5) suggest that $K'_{0S}(25°C)<4$ and $K'_{0S}(1400°C)>4$, thus by approximating $K'_{0S}=4$ Eqn. 24 may overestimate K_{0S} at a given temperature. For simplicity we use the approximation $K'_{0S}=4$ in Eqn. 24.

Figure 8 shows a compilation of elasticity data for K_{0S} to 973°C. Our three candidate values of K_{0S} at 1673 K are also included. The diamond symbols represent the values of K_{0S} calculated from the U_P–U_S best fit and the zero- and first-order f-F fits of our data. The data of Featherston and Neighbours [1963], triangles in Figure 8, are believed to be erroneous because of impurities in their samples [Berg *et al.*, 1985]. The more recent data of Dickinson and Armstrong [1967] are favored over the earlier data of Bolef and de Klerk [1962] for our calculations. The principal Hugoniot data reported by Marsh [1980], the hexagonal symbol, is in accord with the elasticity data of Dickinson and Armstrong. This value was calculated from the zero-order fit of the principal Hugoniot data in the f-F projection.

Eqn. 24 provides a functional form upon which to extrapolate the elasticity data to 1400°C. Integration of Eqn. 24 requires a single reference datum. We use the K_{0S} point derived from the principal Hugoniot data because it is in good agreement with the elasticity data, and because it was computed in the same manner as our data.

Curves of constant q, calculated with Eqn. 24, are plotted in Figure 8. Within reported errors, q values from 1 to 5 satisfy the elasticity measurements of Dickinson and Armstrong. Because curves of constant q satisfy the data within their reported errors, no temperature dependence in the Grüneisen parameter is indicated except through the temperature dependence of V. A curve of q=1.5 fits the elasticity data within their reported errors and agrees with our zero-order f-F fit

Figure 8: Ultrasonic bulk modulus measurements and high temperature shock moduli. Triangles, squares, and circles denote the elasticity values of Featherston and Neighbours [1963], Dickinson and Armstrong [1967], and Bolef and de Klerk [1962] respectively. The hexagonal symbol is calculated from the principal Hugoniot data in Marsh [1980] as the average F value in Figure 5. The diamond symbols designate the various interpretations of the 1400°C shock data. The solid curves are calculated with Eqn. 24 for constant values of q from 1 to 4 using the value based on the principal Hugoniot data as a reference point.

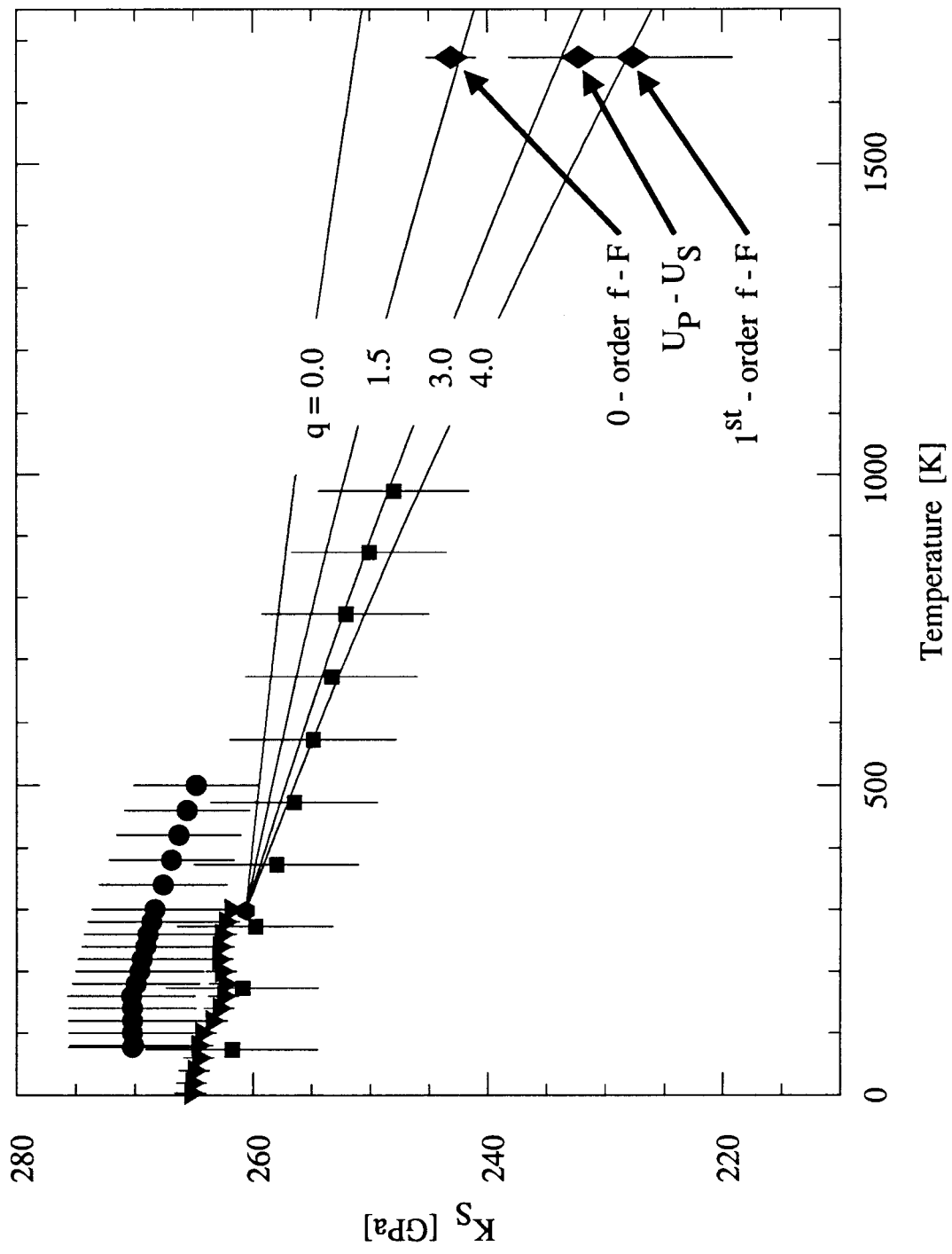
280
260
240
220
K_S [GPa]
0
500
1000
1500
Temperature [K]
q = 0.0
1.5
3.0
4.0
0 - order f - F
U_P - U_S
1st - order f - F

Figure 8.

datum. The q=4.0 curve also falls within the errors of the elasticity data and agrees with the first-order datum. Our U_P–U_S determination falls near q=3.0.

Since we suggested earlier that q≈1, we conclude based on Figure 8 that only the zero-order fit of Figure 3 can lead to an internally consistent view of the behavior of Mo initially heated to 1400°C. The other fits presented in Figure 3 would, in order to be consistent with the ultrasonic and principal Hugoniot data, require much higher values of q, which would lead to significant deviations between the calculated experimental temperatures and calculated Hugoniot temperature in the P-T plane (Fig. 2). Our best choices for K_{0S} and K'_{0S} are thus 244±2 GPa and 4. We note that although Mo becomes more compressible at higher temperatures, it is less compressible than would have been predicted on the basis of linear extrapolation of the ultrasonic elasticity measurements alone.

We note, however, that this discrimination by q values is ambiguous when 2-σ errors are allowed, that is all of the three candidate K_{0S} and K'_{0S} values overlap with 2-σ error bars. This worst case uncertainty amounts to only about 5% uncertainty in K_{0S}, and 10% uncertainty in K'_{0S}.

Although the U_P–U_S best fit determination is not consistent with q=1 (*i.e.*, as shown in Fig. 8, if K_{0S}(1400°C) = 232 GPa, then q≈3), it is nevertheless best for the purpose of calculating an impedance match.

4. Conclusions

1) New data on the dynamic compression of preheated molybdenum is presented. A zero-order fit to the finite strain model indicates a bulk modulus, K_{0S}, of 244±2 GPa, and its pressure derivative, K'_{0S}, of 4 at 1400°C. Higher order fits give values of K'_{0S} greater than 4, and are consistent with the finite strain expansion analysis, but are not statistically significant and are inconsistent with extrapolation of the ultrasonic data. The temperature derivative of K_{0S} at zero pressure

is thus approximately -0.012 GPa/K. The Hugoniot parameters for Mo at 1400°C are c_0=4.77±0.06 km/s and s=1.43±0.05.

2) The Mie-Grüneisen EOS has been demonstrated to be a good model for the shock behavior of Mo at high temperatures.

3) Our data suggest that the Grüneisen parameter is proportional to density, and no evidence is found for a temperature dependence in γ. If this suggestion is correct, the zero-order fit to the finite strain model is favored.

We thank M. Long and E. Gelle for their expert technical assistance with the preparation and execution of the shock experiments. L. Young polished some of the Mo samples. Discussion and review by D. J. Stevenson was very helpful. We appreciate the use of the 10 kW RF heater provided by L. T. Silver. This work was funded by NSF grants EAR-86-18545 and EAR-85-08969. Contribution number 4510, Division of Geological and Planetary Sciences, California Institute of Technology, CA.

References

Ahrens, T.J., Equation of state of iron sulfide and constraints on the sulfur content of the earth, *J. Geophys. Res., 84*, 985-998, 1979.

Ahrens, T.J., Shock wave techniques for geophysics and planetary physics, in *Methods of Experimental Physics, 24 part A*, edited by C.G. Sammis and T.L. Henyey, pp. 185-235, Academic Press, New York, 1987.

Ahrens, T.J., and R. Jeanloz, Pyrite: Shock compression, isentropic release, and composition of the earth's core, *J. Geophys. Res., 92*, 10363-10375, 1987.

Anderson, D.L., A seismic equation of state, *Geophys. J. R. Astr. Soc., 13*, 9-30, 1967.

Anderson, D.L., A seismic equation of state II: Shear properties and thermodynamics of the lower mantle, *Phys. Earth Planet. Inter., 45*, 307-323, 1987.

Bassett, W.A., T. Takahashi, H. Mao, and J.S. Weaver, Pressure-induced phase transformation in NaCl, *J. Appl. Phys., 39*, 319-325, 1968.

Berg, L., G. Czack, E. Koch, and J. Wagner, *Gmelin Handbook of Inorganic Chemistry, 8th Edition, Molybdenum Supplemental Volume A 2a* , pp. 379, Springer-Verlag, New York, 1985.

Birch, F., Elasticity and constitution of the earth's interior, *J. Geophys. Res., 57*, 227-286, 1952.

Birch, F., Finite strain isotherm and velocities for single-crystal and polycrystalline NaCl at high pressures and 300 K, *J. Geophys Res., 83*, 1257-1268, 1978.

Boehler, R., Melting temperature, adiabats, and Grüneisen parameter of lithium, sodium, and potassium versus pressure, *Phys. Rev. B, 27*, 6754-6762, 1983.

Bolef, D.I. and J. de Klerk, Elastic constants of single-crystal Mo and W between 77 and 500 K, *J. Appl. Phys., 33*, 2311-2314, 1962.

Dickinson, J.M., and P.E. Armstrong, Temperature dependence of the elastic constants of molybdenum, *J. Appl. Phys., 38*, 602-606, 1967.

Eliezer, S., A. Ghatak, and H. Hora, *An Introduction to Equations of State: Theory and Applications*, pp. 366, Cambridge University Press, New York, 1986.

Featherston, F.H., and J.R. Neighbours, Elastic constants of tantalum, tungsten, and molybdenum, *Phys. Rev, 130*, 1324-1333, 1963.

Gilvarry, J.J., Grüneisen's law and the fusion curve at high pressure, *Phys. Rev., 102*, 317-325, 1956.

Heinz, D.L., and R. Jeanloz, The equation of state of the gold calibration standard, *J. Appl. Phys.*, *55*, 885-893, 1984.

Hoch, M., in *Thermodyn. Nucl. Mater., Proc. Symp., 4th 1974*, **2**, pp. 113, IAEA, Vienna, 1975.

Hultgren, R., R.L. Orr, P.D. Anderson, and K.K. Kelley, *Selected Thermodynamic Properties of Metals and Alloys*, John Wiley, New York, 1963.

Jeanloz, R., and T.J. Ahrens, Equations of state of FeO and CaO, *Geophys. J. R. Astr. Soc.*, *62*, 505-528, 1980.

Jeanloz, R., and R. Grover, Birch-Murnaghan and U_S–U_P equations of state, in *Proceedings of the American Physical Society Topical Conference on Shock Waves in Condensed Matter, Monterey, California, 20-23 July, 1987*, edited by S.C. Schmidt and N.C. Holmes, pp. 69-72, Plenum, New York, 1988.

Kamb, B., Ice polymorphism and the structure of water, in *Structural Chemistry and Molecular Biology*, pp. 507-542, edited by A. Rich and N. Davidson, W.H. Freeman, San Francisco, 1968.

McQueen, R.G., memo of May 1, 1969.

McQueen, R.G., S.P. Marsh, J.W. Taylor, J.N. Fritz, and W.J. Carter, The equation of state of solids from shock wave studies, in *High Pressure Impact Phenomena*, edited by R. Kinslow, pp. 294-417, Academic Press, New York, 1970.

Marsh, S.P., *LASL Shock Hugoniot Data*, pp. 658, University of California Press, Berkeley, 1980.

Mao, H.K., P.M. Bell, J.W. Shaner, and D.J. Steinberg, Specific volume measurements of Cu, Mo, Pd, and Ag and calibration of the ruby R_1 fluorescence pressure gauge from 0.06 to 1 Mbar, *J. Appl. Phys.*, *49*, 3276-3283, 1978.

Press, W.H., B.P. Flannery, S.A. Teukolsky, and W.T. Vetterling, *Numerical Recipes*, Cambridge University Press, New York, 1986.

Regan, C.E. III., M.G. Silbert, and B.C. Diven, Shock compression of molybdenum to 2.0 TPa by means of a nuclear explosion, *J. Appl. Phys.*, *48*, 2860-2870, 1977.

Rigden, S.M., T.J. Ahrens, and E.M. Stolper, Densities of liquid silicates at high pressures, *Science*, *226*, 1071-1074, 1984.

Rigden, S.M., T.J. Ahrens, and E.M. Stolper, Shock compression of molten silicate: Results for a model basaltic composition, *J. Geophys. Res.*, *93*, 367-382, 1988.

Robie, R.A., B.S. Hemingway, and J.R. Fisher, *Thermodynamic Properties of Minerals and Related Substances at 298.15 K and 1 bar (10^5 pascals) pressure and at higher temperatures*, U.S. Geol. Survey Bull., 1452, Washington D.C., 1978.

Shaner, J.W., G.R. Gathers, and C. Minichino, Thermophysical properties of liquid tantalum and molybdenum, *High Temp. — High Pressures, 9*, 331-343, 1977.

Straumanis, M.E., and R.P. Shodhan, Lattice constants, thermal expansion coefficients, and densities of molybdenum and the solubility of sulfur, selenium, and tellurium in it at 1100°C, *Z. Metallkde., 59*, 492-495, 1968.

Touloukian, V.S., R.K. Kirby, R.E. Taylor, and P.D. Desai, *Thermal Expansion of Metallic Elements and Alloys*, pp. 208-218, Plenum, New York, 1970.

Vereshchagin, L.F., and N.S. Fateeva, Melting temperatures of refractory metals at high pressures, *High Temp. — High Pressures, 9*, 619-628, 1977.

Appendix 1: Error Propagation

The analysis of an individual molten silicate shock experiment requires that a set of 9 algebraic formulae (Eqns. 1-9, Chapter 1) be solved simultaneously. This solution is only approximate, however, since results from a series of experiments are needed to find the c_{0s} and s_s parameters required for the sample-cover impedance matche. A complete reduction of the experimental data for a series of N individual experiments therefore requires the simultaneous solution of 9N+2 equations: Eqns. 1-9, Chapter 1, for each experiment, and 2 regression equations to determine c_{0s} and s_s. Rather than solving 110 simultaneous equations for our 12 experiments, we used an iterative approach. Beginning with assumed values for c_{0s} and s_s, we could analyze each experiment with 9 equations. The second step of this iterative procedure was to calculate new updated values of c_{0s} and s_s.

This iterative approach cannot be used in the calculation of propagated errors. If we computed errors in U_{ss} and U_{ps} including error contributions from c_{0s} and s_s, and then used these quantities in a weighted least squares fit to recalculate both c_{0s} and s_s and their formal errors, then the errors would increase without bound with successive iterations. To properly calculate the propagated errors, a minimum of 6N+2 (Eqns. 1-6, below, and two additional equations for c_{0s} and s_s) linear equations must be solved simultaneously to determine the uncertainties in c_0 and s together with N uncertainties in U_{ss}, U_{ps}, P_s, and ρ_s. Although this approach would be rigorous, it is not particularly instructive because the relative importance of various measurements cannot readily be determined. Because the contributions of c_{0s} and s_s to the uncertainty in each individual experiment are small, we can decouple the 6N+2 simultaneous equations into N sets of 6 simultaneous equations, 6 equations per experiment.

In the following error analysis we will consider the contribution of the error in our measurements, and in the uncertainty in the calculated value ρ_{0s}, to the error in U_{ss}, U_{ps}, P_s, and ρ_s. Individual experiments will be analyzed separately by ignoring the contribution of c_{0s} and s_s.

The minimum six equations which must be solved simultaneously to determine U_{ss}, U_{ps}, P_s, and ρ_s are: the flyer-driver impedance match (Eqn. 2, Chapter 1)

$$\rho_{0d}U_{pd}(c_{0d} + s_dU_{pd}) = \rho_{0f}(V_{imp} - U_{pd})(c_{0f} + s_f(V_{imp} - U_{pd})) , \tag{1}$$

the driver-sample impedance match (Eqn. 5, Chapter 1)

$$\rho_{0s}U_{ps}U_{ss} = \rho_{0d}(2U_{pd} - U_{ps})(c_{0d} + s_d(2U_{pd} - U_{ps})) , \tag{2}$$

the sample-cover impedance match (Eqn. 7, Chapter 1)

$$\rho_{0c}U_{pc}(c_{0c} + s_cU_{pc}) = \rho_{0s}(2U_{ps} - U_{pc})(c_{0s} + s_s(2U_{ps} - U_{pc})) , \tag{3}$$

the equation for the total shock wave transit time (Eqn. 1 with Eqns. 3 and 8, Chapter 1)

$$tt = \frac{x_s}{U_{ss}} + \frac{x_d}{c_{0d} + s_dU_{pd}} + \frac{x_c}{c_{0c} + s_cU_{pc}} , \tag{4}$$

and the equations of stress and mass conservation for the sample (Eqns. 5 and 6, Chapter 1)

$$P_s = \rho_{0s}U_{ss}U_{ps} , \tag{5}$$

$$\rho_s = \rho_{0s}\frac{U_{ss}}{U_{ss} - U_{ps}} , \tag{6}$$

In these equations, the dependent variables are U_{pd}, U_{pc}, U_{ps}, U_{ss}, P_s, and ρ_s. We will consider V_{imp}, tt, x_d, x_s, x_c, and ρ_{0s} to be independent variables that contribute error to the determination of the dependent variables. The remaining parameters are considered as exact constants.

The sensitivity of the dependent variables to changes in the independent variables is determined by the partial derivative. Because these equations are coupled, however, the partial derivatives cannot be immediately determined. The differential forms of Eqns. 1-6 are linear, however, and can be decoupled with a simple matrix equation:

$$\begin{bmatrix} dU_{ss} \\ dU_{ps} \\ dP_s \\ d\rho_s \\ dU_{pd} \\ dU_{pc} \end{bmatrix} = \mathbf{E} \times \begin{bmatrix} dV_{imp} \\ dtt \\ dx_d \\ dx_s \\ dx_c \\ d\rho_{0s} \end{bmatrix} , \tag{7}$$

where **E** is a 6×6 matrix of partial derivatives. The matrix **E** is given by:

(8)

$$\begin{bmatrix} 0 & 0 & 0 & 0 & \rho_{0d}(c_{0d}+2s_dU_{pd})+\rho_{0f}(c_{0f}+2s_f(V_{imp}-U_{pd})) & 0 \\ \rho_{0s}U_{ps} & \rho_{0s}U_{ss}+\rho_{0d}(c_{0d}+2s_d(2U_{pd}-U_{ps})) & 0 & 0 & -2\rho_{0d}(c_{0d}+2s_d(2U_{pd}-U_{ps})) & 0 \\ 0 & -2\rho_{0s}(c_{0s}+2s_s(2U_{ps}-U_{pc})) & 0 & 0 & 0 & \rho_{0c}(c_{0c}+2s_cU_{pc})+\rho_{0s}(c_{0s}+2s_s(2U_{ps}-U_{pc})) \\ \frac{x_s}{U_{ss}^2} & 0 & 0 & 0 & \frac{s_dx_d}{U_{sd}^2} & \frac{s_cx_c}{U_{sc}^2} \\ -\rho_{0s}U_{ps} & -\rho_{0s}U_{ss} & 1 & 0 & 0 & 0 \\ \frac{\rho_{0s}U_{ps}}{(U_{ss}-U_{ps})^2} & -\frac{\rho_{0s}U_{ss}}{(U_{ss}-U_{ps})^2} & 0 & 1 & 0 & 0 \end{bmatrix}^{-1}$$

$$\times \begin{bmatrix} \rho_{0f}(c_{0f}+2s_f(V_{imp}-U_{pd})) & 0 & 0 & 0 & 0 & 0 \\ 0 & 0 & 0 & 0 & 0 & \frac{-P_s}{\rho_{0s}} \\ 0 & 0 & 0 & 0 & 0 & \frac{P_c}{\rho_{0s}} \\ 0 & -1 & \frac{1}{U_{ss}} & \frac{1}{U_{sd}} & \frac{1}{U_{sc}} & 0 \\ 0 & 0 & 0 & 0 & 0 & \frac{P_s}{\rho_{0s}} \\ 0 & 0 & 0 & 0 & 0 & \frac{\rho_s}{\rho_{0s}} \end{bmatrix} \equiv \mathbf{E}\,.$$

The rows of **E** correspond to the differential forms of Eqns. 1-6, in order. The partial derivative of any dependent variable with respect to any independent variable can be found from the appropriate element of the matrix **E**. If errors are assumed to be normally distributed (Gaussian), then the variance in a dependent variable, X_i, is related to the variance of the independent variables, χ_j, according to:

$$\sigma_{X_i}^2 = \sum_j \left[\frac{\partial X_i}{\partial \chi_j}\right]^2 \sigma_{\chi_j}^2 = \sum_j \left[E_{i,j}\right]^2 \sigma_{\chi_j}^2 \,. \tag{9}$$

If we form a new matrix $\mathbf{E}^2$ such that $E^2_{i,j} = (E_{i,j})^2$, then the variances in the dependent variables can be readily calculated from:

$$\begin{bmatrix} \sigma^2_{U_{ss}} \\ \sigma^2_{U_{ps}} \\ \sigma^2_{P_s} \\ \sigma^2_{\rho_s} \\ \sigma^2_{U_{pd}} \\ \sigma^2_{U_{pc}} \end{bmatrix} = \mathbf{E}^2 \times \begin{bmatrix} \sigma^2_{V_{imp}} \\ \sigma^2_{tt} \\ \sigma^2_{x_d} \\ \sigma^2_{x_s} \\ \sigma^2_{x_c} \\ \sigma^2_{\rho_{0s}} \end{bmatrix} . \tag{10}$$

The relative magnitude of the $\mathbf{E}^2$ matrix elements shows their relative importance in the experiments. This matrix is presented for shot #755, which is near the median of the shock pressure range of our experiments:

(11)

$$\begin{bmatrix} \sigma^2_{U_{ss}} \\ \sigma^2_{U_{ps}} \\ \sigma^2_{P_s} \\ \sigma^2_{\rho_s} \\ \sigma^2_{U_{pd}} \\ \sigma^2_{U_{pc}} \end{bmatrix}_{755} = \begin{bmatrix} 1.10\times10^{-2} & 48.3 & 1.34 & 1.94 & 1.46 & 8.88\times10^{-4} \\ 0.586 & 0.119 & 3.31\times10^{-3} & 4.81\times10^{-3} & 3.61\times10^{-3} & 7.88\times10^{-3} \\ 102. & 399. & 11.0 & 16.1 & 12.1 & 26.3 \\ 0.636 & 4.68 & 0.130 & 0.189 & 0.141 & 1.61 \\ 0.221 & 0. & 0. & 0. & 0. & 0. \\ 0.105 & 7.33\times10^{-3} & 2.03\times10^{-4} & 2.95\times10^{-4} & 2.21\times10^{-4} & 7.14\times10^{-3} \end{bmatrix} \times \begin{bmatrix} \sigma^2_{V_{imp}} \\ \sigma^2_{tt} \\ \sigma^2_{x_d} \\ \sigma^2_{x_s} \\ \sigma^2_{x_c} \\ \sigma^2_{\rho_{0s}} \end{bmatrix} ,$$

where all velocities are in units of Km/s or mm/μs, time is measured in μs, distances in mm, and densities in g/cc.

This equation was used in the evaluation of errors for shot #755, and analogous equations (calculated from Eqn. 8) were used for the other experiments. These errors are reported in Table III, Chapter 1.

To illuminate the relative importance of the various error terms, it is necessary to scale Eqn. 11. Defining $\varepsilon_{X_i} \equiv \sigma_{X_i}/X_i$, a scaled uncertainty, Eqn. 11 can be rewritten:

(12)

$$\begin{bmatrix} \varepsilon^2_{U_{ss}} \\ \varepsilon^2_{U_{ps}} \\ \varepsilon^2_{P_s} \\ \varepsilon^2_{\rho_s} \\ \varepsilon^2_{U_{pd}} \\ \varepsilon^2_{U_{pc}} \end{bmatrix}_{755} = \begin{bmatrix} 2.30\times10^{-5} & 1.33 & 8.12\times10^{-4} & 0.995 & 3.39\times10^{-2} & 6.80\times10^{-5} \\ 1.13 & 4.68\times10^{-2} & 2.86\times10^{-5} & 3.50\times10^{-2} & 1.19\times10^{-3} & 3.46\times10^{-2} \\ 1.10 & 0.878 & 5.36\times10^{-4} & 0.657 & 2.24\times10^{-2} & 0.649 \\ 0.105 & 0.169 & 1.04\times10^{-4} & 0.127 & 4.32\times10^{-3} & 0.896 \\ 1.10 & 0. & 0. & 0. & 0. & 0. \\ 0.959 & 2.08\times10^{-2} & 1.27\times10^{-5} & 1.56\times10^{-2} & 5.32\times10^{-4} & 0.172 \end{bmatrix} \times \begin{bmatrix} \varepsilon^2_{V_{impp}} \\ \varepsilon^2_{tt} \\ \varepsilon^2_{x_d} \\ \varepsilon^2_{x_s} \\ \varepsilon^2_{x_c} \\ \varepsilon^2_{\rho_{0s}} \end{bmatrix} .$$

A 10% error in the transit time, tt, therefore contributes 4% error to ρ_s ($\sqrt{0.169\times(0.10)^2}=0.04$) and contributes nothing to the error in U_{pd} as expected. The relative importance of the measured values is different for each dependent variable. The transit time is the most important term for U_{ss} and the second most important for U_{ps}. The flyer plate velocity is the most important term for U_{ps}, but this term is unimportant for U_{ss}. Neither U_{ps} nor U_{ss} rely heavily on ρ_{0s}, thus the bulk sound speed and K'_{0S} are not strongly dependent on the initial density calculation. The bulk modulus, $K_{0S}=\rho_{0S}c^2_{0s}$, however, is strongly dependent on this calculated value.

Appendix 2: Thermodynamic Description of Shock Waves

In this Appendix I present an outline of the thermodynamics that describe the shock Hugoniot. Elucidation of thermodynamic properties from shock experiments requires that the locus of shock states be thermodynamically defined. From such a definition one may obtain thermodynamic data from the shock equation of state, *e.g.*, $U_S = c_0 + sU_P$. In the absence of elastic effects, the intercept c_0 is interpreted as the low pressure sound speed, and the slope s is related to the isentropic pressure derivative of the isentropic bulk modulus by $K'_S = 4s-1$. That this interpretation has a rigorous thermodynamic basis is implicit in the literature, but I am aware of no derivations of these equations that are free of model assumptions, *e.g.*, specific parameterizations such as the Birch-Murnaghan equation of state, and assumptions regarding the pressure and temperature dependence of the Grüneisen parameter. No such model assumptions are used in the following derivations, however chemical equilibrium will be assumed in the discussion of multiphase systems.

The approach used here is to write a system of differential equations that, taken together, describe the thermodynamic state of the system along the locus of shock states. Before considering the Hugoniot states, the temperature and pressure partial derivatives of K_S and K'_S are derived. I then derive the equations for the Hugoniot of a single-phase system. The extention of this derivation to an equilibrium two-phase single-component system is also presented.

1. Partial Derivatives of K_S and K'_S

Temperature and pressure vary simultaneously along the Hugoniot. In order to determine, for example, the derivative of the bulk modulus taken along the Hugoniot, it is convient to determine expressions for the temperature and pressure partial derivatives of the bulk modulus. The derivative of the bulk modulus along the Hugoniot is then readily determined from these quantities and the simultaneous changes in pressure and temperature on the Hugoniot. Accordingly, I will begin by

deriving expressions for the temperature and pressure partial derivative of K_S and K'_S ($\partial K_S/\partial P|_S$).

The isentropic bulk modulus is defined by:

$$K_S \equiv -V \left.\frac{\partial P}{\partial V}\right|_S , \tag{1}$$

and its temperature partial derivative can be determined from the ratio of Jacobian determinants:

$$\left.\frac{\partial K_S}{\partial T}\right|_P = \frac{\begin{vmatrix} (\partial K_S/\partial V)_S & (\partial K_S/\partial S)_V \\ (\partial P/\partial V)_S & (\partial P/\partial S)_V \end{vmatrix}}{\begin{vmatrix} (\partial T/\partial V)_S & (\partial T/\partial S)_V \\ (\partial P/\partial V)_S & (\partial P/\partial S)_V \end{vmatrix}} . \tag{2}$$

The terms in this expression are:

$$\left.\frac{\partial P}{\partial V}\right|_S = -\frac{K_S}{V} , \tag{3}$$

$$\left.\frac{\partial P}{\partial S}\right|_V = \frac{\gamma T}{V} , \tag{4}$$

$$\left.\frac{\partial T}{\partial V}\right|_S = -\frac{\gamma T}{V} , \tag{5}$$

$$\left.\frac{\partial T}{\partial S}\right|_V = \frac{T}{C_V} , \tag{6}$$

$$\left.\frac{\partial K_S}{\partial V}\right|_S = \left.\frac{\partial P}{\partial V}\right|_S \left.\frac{\partial K_S}{\partial P}\right|_S = -\frac{K_S K'_S}{V} , \tag{7}$$

and

$$\left.\frac{\partial K_S}{\partial S}\right|_V = \left.\frac{\partial}{\partial S}\right|_V \left[-V \left.\frac{\partial P}{\partial V}\right|_S\right] = -V \left.\frac{\partial}{\partial S}\right|_V \left.\frac{\partial P}{\partial V}\right|_S \tag{8}$$

$$= -V \left.\frac{\partial}{\partial V}\right|_S \left.\frac{\partial P}{\partial S}\right|_V = -V \left.\frac{\partial}{\partial V}\right|_S \frac{\gamma T}{V} = \frac{\gamma T}{V}(1 + \gamma - q) ,$$

where q is defined by:

$$q \equiv \left.\frac{\partial \ln\gamma}{\partial \ln V}\right|_S . \tag{9}$$

Substituting these terms into the determinant expression, and reducing the expression with $\gamma C_P = \alpha V K_S$ and $C_P = C_V(1 + \alpha\gamma T)$, gives the result:

$$\left.\frac{\partial K_S}{\partial T}\right|_P = -\alpha K_S(K'_S + q - \gamma - 1) . \tag{10}$$

To get the pressure derivative, $\partial K_S/\partial P|_T$, use

$$\left.\frac{\partial}{\partial P}\right|_T = \left.\frac{\partial}{\partial P}\right|_S + \frac{\left[\frac{\partial S}{\partial P}\right]_T}{\left[\frac{\partial S}{\partial T}\right]_P} \left.\frac{\partial}{\partial T}\right|_P \tag{11}$$

$$= \left.\frac{\partial}{\partial P}\right|_S - \frac{\gamma T}{K_S} \left.\frac{\partial}{\partial T}\right|_P$$

$$\left.\frac{\partial K_S}{\partial P}\right|_T = K'_S(1+\alpha\gamma T) - \alpha\gamma T(\gamma + 1 - q) . \tag{12}$$

The derivatives of K'_S are evaluated in the same manner. First determine the partial derivatives:

$$\left.\frac{\partial K'_S}{\partial V}\right|_S = -\frac{K_S K''_S}{V} \tag{13}$$

$$\left.\frac{\partial K'_S}{\partial S}\right|_V = \left.\frac{\partial}{\partial S}\right|_V \left[-\frac{V}{K_S} \left.\frac{\partial K_S}{\partial V}\right|_S\right] = -\frac{V}{K_S^2} \left.\frac{\partial K_S}{\partial S}\right|_V \left.\frac{\partial K_S}{\partial V}\right|_S - \frac{V}{K_S} \left.\frac{\partial}{\partial V}\right|_S \left.\frac{\partial K_S}{\partial S}\right|_V . \tag{14}$$

Eqn. 14 is solved by noting that:

$$\left.\frac{\partial}{\partial S}\right|_V = \frac{T}{C_V} \left.\frac{\partial}{\partial T}\right|_P + \frac{\gamma T}{V} \left.\frac{\partial}{\partial P}\right|_T . \tag{15}$$

Substituting the results from Eqns. 10 and 12 into Eqn. 15 one obtains:

$$\left.\frac{\partial K_S}{\partial S}\right|_V = \frac{\gamma T}{V}(\gamma + 1 - q) , \tag{16}$$

and substituting this result into Eqn. 14 gives

$$\left.\frac{\partial K'_S}{\partial S}\right|_V = \frac{\alpha T}{C_P}\left[K'_S(\gamma+1-q) + (q-1)(1+\gamma) - q'V\right] , \tag{17}$$

where

$$q' \equiv \left.\frac{\partial q}{\partial V}\right|_S . \tag{18}$$

Substituting Eqns. 13 and 17 into a Jacobian determinant expression for $\partial K'_S/\partial T|_P$ analogous to Eqn. 2 one obtains:

$$\left.\frac{\partial K'_S}{\partial T}\right|_P = -\alpha\left[K_S K''_S - \gamma q + Vq' - (K'_S - 1)(1+\gamma-q)\right] , \tag{19}$$

and $\partial K'_S/\partial P|_T$ is readily determined from Eqn. 11:

$$\left.\frac{\partial K'_S}{\partial P}\right|_T = K''_S(1+\alpha\gamma T) - \frac{\alpha\gamma T}{K_S}\left[\gamma q - Vq' + (K'_S - 1)(1+\gamma-q)\right] . \tag{20}$$

2. Single-Phase Hugoniot

The thermodynamic properties of a shocked single-phase system are found by writing the total derivatives of volume and internal energy:

$$dV = -V\beta_T dP + V\alpha dT \tag{21}$$

$$dE = V(P\beta_T - \alpha T)dP + (C_P - \alpha VP)dT , \tag{22}$$

and the Rankine-Hugoniot relationship for internal energy in a Hugoniot state:

$$E = E_0 + \tfrac{1}{2}(P+P_0)(V_0 - V) \tag{23}$$

$$2dE = (V_0 - V)dP - (P+P_0)dV . \tag{24}$$

Eqns. 21, 22, and 24 are three equations in four unknowns (dE, dT, dP, and dV). Selecting dP as an independent parameter and dividing these equations by dP, one arrives at a set of three coupled equations in three unknowns. In matrix form, these equations are:

(25)

$$\begin{vmatrix} 0 & 1 & -\alpha V \\ 1 & 0 & (\alpha VP - C_P) \\ 2 & (P+P_0) & 0 \end{vmatrix} \times \begin{vmatrix} dE/dP \\ dV/dP \\ dT/dP \end{vmatrix} = \begin{vmatrix} -V\beta_T \\ V(P\beta_T - \alpha T) \\ (V_0 - V) \end{vmatrix} .$$

The solution to this matrix equation is given by the following three equations:

$$\frac{dT}{dP} = \frac{(V_0-V) + 2V\alpha T - (P-P_0)V\beta_T}{2C_P - (P-P_0)\alpha V} \tag{26}$$

$$= \frac{2\gamma C_P T - V(P-P_0)(1+\alpha\gamma T) + K_S(V_0-V)}{C_P[2K_S - \gamma(P-P_0)]}$$

$$\frac{dV}{dP} = \frac{V\left[(V_0-V)\alpha + 2V\alpha^2 T - 2\beta_T C_P\right]}{2C_P - (P-P_0)\alpha V} \tag{27}$$

$$= \frac{\gamma(V_0-V) - 2V}{2K_S - \gamma(P-P_0)}$$

$$\frac{dE}{dP} = \frac{C_P(V_0-V) + (P+P_0)V[\beta_T C_P - \alpha^2 T] - PV(V_0-V)\alpha}{2C_P - (P-P_0)\alpha V} \tag{28}$$

$$= \frac{V(P+P_0) + (V_0-V)(K_S + \gamma P)}{2K_S - \gamma(P-P_0)}$$

From Eqn. 27 one can write an expression for the Hugoniot bulk modulus:

$$K_H = -V \left.\frac{dP}{dV}\right|_{Hugoniot} = \frac{V[2K_S - \gamma(P-P_0)]}{2V - \gamma(V_0-V)} . \tag{29}$$

In the limit of zero compression, one obtains from this the result:

$$\lim_{\substack{P\to P_0 \\ V\to V_0}} K_H = K_S , \tag{30}$$

thus the Hugoniot bulk modulus and the isentropic bulk modulus are identical in the limit of zero compression. The total pressure derivative of the Hugoniot bulk modulus is:

$$K'_H \equiv \frac{dK_H}{dP} = \tag{31}$$

$$\frac{V\left[2K_S K'_S(1+\alpha\gamma T)(2V-\gamma(V_0-V)) + K_S(V_0-V)(2K_S\gamma_P+2\gamma+\gamma^2) + 2K_S\alpha\gamma T(V(2q-2-\gamma)+\gamma(V_0-V)(2+\gamma-q)) - (P-P_0)V_0\gamma^2(1+\alpha\gamma T) - K_S(P-P_0)V\gamma_P\right]}{K_S\left[2V-\gamma(V_0-V)\right]^2}$$

$$+ \frac{V\left[2K_S\alpha(2V-\gamma(V_0-V))(1-q-K'_S) - 2K_S(V_0-V)(\alpha\gamma(1+\gamma)-\gamma_T) + 2K_S V\alpha\gamma + (P-P_0)V_0\alpha\gamma^2 - 2(P-P_0)V\gamma_T\right]}{\left[2V-\gamma(V_0-V)\right]^2}\frac{dT}{dP}$$

where q is given by Eqn. 9, and γ_P and γ_T are the pressure and temperature partial derivatives of γ. The derivative dT/dP is given by Eqn. 26. The limit of K'_H is:

$$\lim_{P\to P_0,\ V\to V_0} K'_H = K'_S\ , \tag{32}$$

thus the pressure derivative of the Hugoniot bulk modulus is identical to the isentropic pressure derivative of the isentropic bulk modulus in the limit of zero compression.

Now in terms of shock velocity, U_S, and particle velocity, U_P, pressure and volume can be written as:

$$P = P_0 + \frac{U_P U_S}{V_0} \tag{33}$$

$$V = V_0\left(1 - \frac{U_P}{U_S}\right) \tag{34}$$

From these relationships, the Hugoniot bulk modulus and its pressure derivative can be written:

$$K_H = \frac{U_S}{V_0}(U_S-U_P)\left[\frac{U_S+U_P U'_S}{U_S-U_P U'_S}\right] \tag{35}$$

(36)

$$K'_H = \frac{U_S^3(4U'_S-1) + U_P U_S^2(2U_S U''_S-3U'_S-2(U'_S)^2) + U_P^2 U_S(3(U'_S)^2-2(U'_S)^3-2U_S U''_S) + U_P^3(U'_S)^3}{(U_S+U_P U'_S)(U_S-U_P U'_S)^2}\ ,$$

where U'_S is dU_S/dU_P and U''_S is d^2U_S/dU_P^2. The limits of these quantities are:

$$\lim_{U_P\to 0,\ U_S\to c_0} K_H = K_S = \frac{c_0^2}{V_0}\ , \tag{37}$$

and

$$\lim_{U_P \to 0,\ U_S \to c_0,\ U'_S \to \infty} K'_H = K'_S = 4s-1 \ . \tag{38}$$

From these limits one can identify the terms in the power series

$$U_S = c_0 + sU_P + \cdots \tag{39}$$

with isentropic properties: c_0 is the sound speed, and s is $(K'_S+1)/4$. This correspondence between the U_S-U_P coefficients and the isentropic properties has long been known [Ruoff, 1967], but I are aware of no derivations of these equations that are independent of model assumptions. Ruoff [1967], for example, assumed a specific form (Birch-Murnaghan) for the isentropic compression curve, and made further assumptions regarding the P and T depencence of γ. That such assumptions are not required is important since it emphasizes the rigorous thermodynamic foundation of the shock wave method.

3. Shock Equation of State Centered on a Principal Hugoniot State

When a shocked sample impacts a second higher impedance material, the sample experiences a second shock. The c^{HP} and s^{HP} parameters for the reshock equation of state, $U_S = c^{HP} + s^{HP}U_P$, can be obtained from expressions derived above.

c^{HP} is the sound speed of the sample at its principal Hugoniot state. This quantity is related to the high pressure bulk modulus, $K_S = (c^{HP})^2/V$, which can be written in terms of the Hugoniot bulk modulus, K_H, with Eqn. 29. Writing K_H in terms of the principal Hugoniot equation of state parameters with Eqn. 35, and assuming a linear principal Hugoniot shock equation of state for simplicity, the high pressure sound speed, c^{HP}, is given by Eqn. 13, Chapter 1.

The quantity s^{HP} is $(K'_S+1)/4$ evaluated at the principal Hugoniot state. Writing K'_S in terms

of K'_H and K_S with Eqn. 31, writing this expression in terms of principal Hugoniot parameters with Eqns. 35 and 36, and assuming a linear principal Hugoniot shock equation of state, one obtains Eqn. 14, Chapter 1.

4. Two-Phase One-Component Hugoniot

Assume volume additivity for the two phases, *i.e.*, that the phases will mix mechanically. The specific volume of the system, V^S, can then be written in terms of the specific volumes of the component phases, V^I and V^{II}, and the mass fraction of phase II, X^S_{II}:

$$V^S = (1-X^S_{II})V^I + X^S_{II}V^{II} , \tag{40}$$

$$(1-X^S_{II})dV^I + X^S_{II}dV^{II} + (V^{II}-V^I)dX^S_{II} - dV^S = 0 . \tag{41}$$

The volumes of the individual phases change as:

$$\alpha^I V^I dT - V^I \beta^I_T dP - dV^I = 0 , \tag{42}$$

and

$$\alpha^{II} V^{II} dT - V^{II} \beta^{II}_T dP - dV^{II} = 0 , \tag{43}$$

where β^i_T is $1/K^i_T$, the inverse of the isothermal bulk modulus for phase i.

The entropies of the individual phases change as:

$$\frac{C^I_P}{T} dT - \alpha^I V^I dP - dS^I = 0 , \tag{44}$$

and

$$\frac{C^{II}_P}{T} dT - \alpha^{II} V^{II} dP - dS^{II} = 0 , \tag{45}$$

and the internal energy of the component phases, E^I and E^{II}, change as:

$$(C^I_P - P\alpha^I V^I)dT + (PV^I\beta^I_T - T\alpha^I V^I)dP - dE^I = 0 , \tag{46}$$

and

$$(C_P^{II}-P\alpha^{II}V^{II})dT + (PV^{II}\beta_T^{II}-T\alpha^{II}V^{II})dP - dE^{II} = 0 . \quad (47)$$

With the assumption of simple mechanical mixing, the internal energy of the mixture is:

$$E^S = (1-X_{II}^S)E^I + X_{II}^S E^{II} \quad (48)$$

$$(1-X_{II}^S)dE^I + X_{II}^S dE^{II} + (E^{II}-E^I)dX_{II}^S - dE^S = 0 . \quad (49)$$

Chemical equilibrium between phases I and II can be represented with the Gibbs-Duhem equation, which, for this simple one-component system, is given by the Clausius-Clapeyron equation.

$$(S^{II}-S^I)dT - (V^{II}-V^I)dP = 0 \quad (50)$$

All states on the Hugoniot can be characterized by the Rankine-Hugoniot relationship for internal energy.

$$E^S - E_0^S = \tfrac{1}{2}(P + P_0)(V_0^S - V^S) \quad (51)$$

$$2dE^S + (P+P_0)dV^S - (V_0^S-V^S)dP = 0 \quad (52)$$

I have written 10 independent equations in 11 unknowns. Let us select pressure as the independent variable. Dividing all differential equations by dP then gives 10 equations in 10 unknowns. This system of equations can be expressed in matrix form:

(53)

$$\begin{vmatrix} C_P^I/T & 0 & 0 & 0 & 0 & 0 & -1 & 0 & 0 & 0 \\ C_P^{II}/T & 0 & 0 & 0 & 0 & 0 & 0 & 0 & 0 & -1 \\ \alpha^I V^I & 0 & 0 & 0 & 0 & -1 & 0 & 0 & 0 & 0 \\ \alpha^{II} V^{II} & 0 & 0 & 0 & 0 & 0 & 0 & 0 & -1 & 0 \\ (C_P^I - P\alpha^I V^I) & 0 & 0 & 0 & -1 & 0 & 0 & 0 & 0 & 0 \\ (C_P^{II} - P\alpha^{II} V^{II}) & 0 & 0 & 0 & 0 & 0 & 0 & -1 & 0 & 0 \\ 0 & 0 & -1 & (V^{II}-V^I) & 0 & (1-X_{II}^S) & 0 & 0 & X_{II}^S & 0 \\ 0 & -1 & 0 & (E^{II}-E^I) & (1-X_{II}^S) & 0 & 0 & X_{II}^S & 0 & 0 \\ (S^{II}-S^I) & 0 & 0 & 0 & 0 & 0 & 0 & 0 & 0 & 0 \\ 0 & 2 & (P+P_0) & 0 & 0 & 0 & 0 & 0 & 0 & 0 \end{vmatrix} \times \begin{vmatrix} dT/dP \\ dE^S/dP \\ dV^S/dP \\ dX_{II}^S/dP \\ dE^I/dP \\ dV^I/dP \\ dS^I/dP \\ dE^{II}/dP \\ dV^{II}/dP \\ dS^{II}/dP \end{vmatrix} = \begin{vmatrix} \alpha^I V^I \\ \alpha^{II} V^{II} \\ V^I \beta_T^I \\ V^{II} \beta_T^{II} \\ V^I(T\alpha^I - P\beta_T^I) \\ V^{II}(T\alpha^{II} - P\beta_T^{II}) \\ 0 \\ 0 \\ (V^{II}-V^I) \\ (V_0^S - V^S) \end{vmatrix}$$

The solutions to this set of coupled equations are given below.

4.1. Temperature

$$\frac{dT}{dP} = \frac{V^{II}-V^I}{S^{II}-S^I} \tag{54}$$

The temperature change throughout the two-phase region is equal to the Clausius-Clapeyron slope of the reaction boundary. Entropy-dominated transitions (*e.g.*, solid-liquid phase transitions) will therefore experience modest temperature changes in the two-phase region. In contrast, temperature will change very rapidly in volume-dominated transitions (*e.g.*, solid-solid phase boundaries). Temperature measurement in a shock experiment will be useful in identifying volume-dominated reaction boundaries, but will be less useful in identifying entropy-dominated reactions.

4.2. Reaction Coordinate

$$\frac{dX_{II}^S}{dP} = \frac{2C_P^S \frac{dT}{dP} + (P-P_0)V^S\beta_T^S - \alpha^S V^S\left[2T + (P-P_0)\frac{dT}{dP}\right] - (V_0^S - V^S)}{(S^I-S^{II})\left[2T - (P-P_0)\frac{dT}{dP}\right]}, \tag{55}$$

where

$$C_P^S = (1-X_{II}^S)C_P^I + X_{II}^S C_P^{II}\,, \tag{56}$$

$$V^S\beta_T^S = (1-X_{II}^S)V^I\beta_T^I + X_{II}^S V^{II}\beta_T^{II}\,, \tag{57}$$

and

$$V^S\alpha^S = (1-X_{II}^S)V^I\alpha^I + X_{II}^S V^{II}\alpha^{II}\,. \tag{58}$$

Eqn. 55 may also be written as:

$$\frac{dX_{II}^S}{dP} = \frac{-\left.\frac{\partial}{\partial P}\right|_{X_{II}^S}\left[2E^S - (P+P_0)(V_0^S-V^S)\right]}{\left.\frac{\partial}{\partial X_{II}^S}\right|_P\left[2E^S - (P+P_0)(V_0^S-V^S)\right]}\,. \tag{59}$$

One can also write

$$\frac{dT}{dP} = \left.\frac{dT}{dP}\right|_{X_{II}^S} + \frac{dX_{II}^S}{dP}\left.\frac{dT}{dX_{II}^S}\right|_P\,, \tag{60}$$

or

$$\frac{dX_{II}^S}{dP} = \frac{\frac{dT}{dP} - \left.\frac{dT}{dP}\right|_{X_{II}^S}}{\left.\frac{dT}{dX_{II}^S}\right|_P}\,, \tag{61}$$

where dT/dP is given by Eqn. 54, and $dT/dP|_X$ is given by Eqn. 26, and $dT/dX_{II}^S|_P$ is given by

$$\left.\frac{dT}{dX_{II}^S}\right|_P = \left(\left.\frac{dE}{dX_{II}^S}\right|_P\right)\Big/\left(\left.\frac{dE}{dT}\right|_P\right) = \frac{2\Delta H - (P-P_0)\Delta V}{2C_P^S - (P-P_0)\alpha^S V^S}\,. \tag{62}$$

The rate, in terms of pressure, at which the two-phase region is traversed is proportional to the difference in PT slope between the single-phase Hugoniot and the Clausius-Clapeyron reaction boundary. In general, one can consider the single-phase Hugoniot to have a relatively shallow PT slope. Porous samples may be quite steep, however. Solid-solid reactions, characterized by steep Clapeyron slopes, will be traversed rapidly by the Hugoniot. Solid-liquid reactions, having

shallower Clapeyron slopes, will be crossed more slowly by the Hugoniot. Temperature measurements in the two-phase region may be used to determine the Clapeyron slope of a congruently melting solid since the two-phase region will be largest in this case.

4.3. U_S–U_P Relation

The U_S–U_P relationships can be determined from the identity

$$\frac{dU_S}{dU_P} = V_0^S \frac{dP}{dE} - \frac{V_0}{2} \frac{(P-P_0)}{(E^S-E_0^S)} . \tag{63}$$

This expression can be written as:

$$\frac{dU_S}{dU_P} = \frac{V_0^S(P+P_0)(V_0^S-V^S) - V_0^S(P-P_0)\left[\left.\frac{\partial E}{\partial P}\right|_{x_{II}^S} + (E^{II}-E^I)\frac{dX_{II}^S}{dP}\right]}{(P+P_0)(V_0^S-V^S)\left[\left.\frac{\partial E}{\partial P}\right|_{x_{II}^S} + (E^{II}-E^I)\frac{dX_{II}^S}{dP}\right]} , \tag{64}$$

where the terms containing dX_{II}^S/dP represent the perturbation to the single-phase solution.

Reference

Ruoff, A.L., Linear shock-velocity — particle-velocity relationship, *J. Appl. Phys.*, *38*, 4967-4980, 1967.

Appendix 3: The Natural Occurrence of Hydroxide in Olivine

Phys Chem Minerals (1987) 14:461–472

PHYSICS AND CHEMISTRY OF MINERALS

The Natural Occurrence of Hydroxide in Olivine

Gregory H. Miller[1], George R. Rossman[1], and George E. Harlow[2]
[1] Division of Geological and Planetary Sciences*, California Institute of Technology, Pasadena, CA 91125, USA
[2] Department of Mineral Sciences, American Museum of Natural History, New York, New York 10024-5192, USA

Abstract. Polarized infrared (IR) spectra of olivine single crystals from 17 different localities show a tremendous variability in both mode and abundance of hydroxide (OH) incorporation. Kimberlitic olivines contain the most total OH at an estimated concentration level of 976 H/10^6Si, whereas olivines from basalts contain the least at 3 H/10^6Si. Olivines of metamorphic and hydrothermal origin have widely varying concentration levels intermediate between those of basalts and kimberlites. Over 30 distinct OH absorption bands have been identified. Most of these bands are not unique to individual localities but may be found in samples from several different localities. Pleochroism is consistent among localities, but relative band intensities vary. No evidence is found for molecular H_2 in olivine.

Hydrous minerals have been identified in olivine by their characteristic OH absorption bands. Serpentine is commonly found and is clearly distinguishable from intrinsic OH. Talc is present in one sample. Prominent OH bands at 3572 and 3525 cm^{-1} are attributed to humite group minerals.

San Carlos, Arizona, olivines annealed in the presence of H_2O develop absorption bands which are found in natural samples, however the OH absorption spectra of these annealed olivines are not identical to those of any single natural crystal. Sharp-band OH abundances in annealed samples are an order of magnitude lower than the maximum measured in natural specimens. The mechanical properties determined from these annealed olivines may not be directly applicable to mantle olivine because both the OH sites and concentrations are different.

Introduction

The occurrence of hydroxide (OH) in olivine, a nominally anhydrous silicate, has received a great deal of attention in recent geochemical and geophysical literature because of (1) the effect of OH on mineral deformation and its impact on mantle rheology (Justice and Graham 1982, Kirby 1983, Chopra and Paterson 1984, Mackwell et al. 1985, Karato et al. 1986, and Kohlstedt 1986), (2) the well known role of volatiles on the evolution of igneous rocks, and (3) the crystal chemical interest in the specific modes of incorporation of hydrogen bearing defects in anhydrous minerals (Beran and Putnis 1983, Freund and Oberheuser 1986). Despite the great ammount of work on OH in olivine, there are a number of fundamental questions which remain to be answered. These include:

1. How much OH occurs in natural olivines? What is the range of concentrations, and how do concentrations relate to the geologic conditions of the olivine's formation and subsequent history?
2. How is OH incorporated into olivine? How many distinct sites are there, and how do they vary with geologic occurrence?
3. Do the annealed olivines used in deformational studies contain OH in the same sites as natural olivines, and are the concentration levels achieved by annealing comparable to those found in natural samples?

A survey of a broad range of large crystals of natural olivine (peridot) as well as annealed San Carlos, Arizona, olivine was conducted to address these questions. *Infrared* (IR) spectroscopy was used to detect the presence of OH by its characteristic absorption bands near 3700 cm^{-1}, and to detect molecular water by its characteristic bending plus stretching combination mode at 5240 cm^{-1}.

Experimental Procedure

Thirty four olivine crystals from seventeen localities were studied. The localities, geologic occurrence, and available references for the samples are summarized in Table 1. Because of the low OH concentrations encountered in natural specimens a minimum thickness of 1 mm was required for most samples. Only inclusion and fracture free portions of the samples, as judged by optical microscopy, were used for spectroscopy where possible. Sample dimensions and observations of fractures and inclusions are summarized in Table 2.

Samples 7, 8, 9, and 22 were oriented by morphology, and orientations were verified with polarized IR reflectance spectra in the range of 1200 cm^{-1} to 400 cm^{-1}. Other specimens were oriented by X-ray diffraction using either Laue or precession methods, and faces normal to crystallographic axes were cut and polished.

Spectra were obtained with a Nicolet 60SX Fourier transform IR spectrophotometer. The 60SX uses a Michelson interferometer calibrated with a He-Ne laser. The optic bench and sample compartment of the 60SX is continuously purged with H_2O- and CO_2-free air. Spectra were collected with either a silicon carbide source, KBr beamsplitter, liquid nitrogen cooled HgCdTe detector, and AgBr polarizer; or a tungsten source, CaF_2 beamsplitter, liquid nitrogen

* Contribution number 4362

Table 1. Localities and geologic occurrences of olivines surveyed

Sample number	Locality	Occurence, comments	Reference number
1	Norway[a]	metamorphic	GRR #949
2	Norway	metamorphic	CIT #15089a
3	Norway	metamorphic	CIT #15089b
4	Unknown, East Africa	rift basalt xenolith	GRR #1000
5	Zabargad Isl., Egypt[b]	hydrothermal	GRR #999a
6	Zabargad Isl., Egypt	hydrothermal	GRR #999b
7	Zabargad Isl., Egypt	hydrothermal	CIT #12012
8	Zabargad Isl., Egypt	hydrothermal	GRR #889
9	Monastery Farm, Winburg, South Africa[c]	kimberlite xenolith	GRR #1006, BMNH #84361
10	Emali, Kenya[d]	rift basalt xenolith, brown	GRR #1004
11	Emali, Kenya	rift basalt xenolith, green	GRR #1005
12	Angola		GRR #1002
13	Angola		GRR #1003
14	Toowoomba Range, Queensland, Australia	basalt xenolith	GRR #1008, BMNH #1913,93
15	Vesuvius, Italy	1776 eruption leucitite basalt	GRR #1007, BNMH #1934.74
16	Morales, Mexico	basalt	GRR #1001-1
17	Kingiti, Tanzania	basalt	GRR #1348, AMNH #98601-2
18	Sri Lanka		GRR #1346, AMNH #G98660
19	Nosy Mitsio, Madagascar[e]	basalt	GRR #1353, MNHN #11950-2
20	Cheviot Hills, Hughenden, Queensland, Australia	basalt xenolith	GRR #1355, BGS #36015
21	Hebei Pr., China[f]	basalt	GRR #1349, AMNH #98152
22	Unknown, Sri Lanka		GRR #914, HVD #107027
23	San Carlos, Arizona[g]	basalt xenolith	GRR #998a
24	San Carlos, Arizona	basalt xenolith	GRR #997
25	San Carlos, Arizona	basalt xenolith	GRR #998b
26	San Carlos, Arizona	basalt xenolith	GRR #1022a
27	San Carlos, Arizona	basalt xenolith	GRR #1022b
28	San Carlos, Arizona	basalt xenolith	GRR #1022c
29	San Carlos, Arizona	basalt xenolith	GRR #1022d
30	San Carlos, Arizona	basalt xenolith	GRR #1022e
31	San Carlos, Arizona	annealed 1073 K, 8.9 kbar, 4×10^5 s	GRR #932
32	San Carlos, Arizona	not annealed, same crystal as 31	GRR #933
33	San Carlos, Arizona	annealed 1273 K, 3.5 kbar, 10^4 s	GRR #1283
34	Kimberley, South Africa	Kimberlite xenolith	GRR #920, HVD #12531

AMNH = American Museum of Natural History
BMNH = British Museum of Natural History
BGS = British Geological Survey
CIT = California Institute of Technology
HVD = Harvard Mineralogic Museum
MNHN = Muséum National d'Histoire Naturelle (Paris)

[a] Brueckner 1977
[b] Clocchiatti et al. 1981, Wilson 1976
[c] Whitelock 1973
[d] Suwa et al. 1975, Bank and Saul 1972
[e] Lacroix 1922
[f] Keller and Fuquan 1986
[g] Koivula 1981, Frey and Prinz 1978

cooled InSb detector, and $LiIO_3$ polarizer. The former configuration is optimized for the range 2000-400 cm^{-1}, and the latter for 7000-2000 cm^{-1}. Spectra were collected with either 1, 2, or 4 cm^{-1} resolution. Typically 1024 scans were averaged for each spectrum. Spectra were obtained for each sample with [100] (E||a, 4.76 Å), [010] (E||b, 10.23 Å), and [001] (E||c, 5.99 Å) polarizations (space group Pbnm).

OH concentration was estimated using the molar absorptivity correlation of Paterson (1982) based on the molar absorptivity of OH in glasses and quartz. Total OH concentrations were determined by summing the concentrations determined from three orthogonal polarizations using an orientation factor, γ, of 1 for each polarization. This enables the total OH concentration to be determined with greater precision than would be possible if a single spectrum were resolved into component bands, and an orientation factor assigned to each component.

Cryogenic spectra were obtained using an evacuated liquid nitrogen cryostat with Al_2O_3 (0001) windows.

The spectra presented in this paper were collected at room temperature unless noted otherwise.

Annealed San Carlos olivine crystals were examined to compare natural and artificial OH defects. Sample 31 was prepared by Andreas Kronenberg at the USGS, Menlo

Table 2. Microscopic features

Sample	k	Thickness (mm)	Special features
1		8.39*	(010) lilly pad fractures, veils of unidentified material
	[001]	12.10	(010) lilly pad fractures, veils of unidentified material
2	[100]	7.56	healed fractures, veils of unidentified material
	[001]	9.02	clear
3	[100]	7.36	veils of unidentified material
	[001]	10.88	clear
4	[100]	24.09	clear
	[010]	7.97	clear
5	[100]	3.49	few unidentified dark inclusions
	[010]	4.80	several unidentified dark inclusions
6	[100]	3.57	clear
	[001]	7.78	cluster of (010) fractures
7	[100]	3.7	etch pits on surface
	[010]	8.0	etch pits on surface
8	[100]	4.7	etch pits on surface
	[010]	2.3	etch pits on surface
9	[010]	3.98	few inclusions elongated on [001]
	[001]	4.96	few inclusions elongated on [001]
10	[010]	3.79	clear, dark color
	[001]	5.56	clear, dark color
11	[100]	6.41	clear
	[010]	4.13	clear
12	[100]	5.87	clear
	[010]	7.37	clear
13	[100]	6.98	clear
	[001]	6.07	clear
14	[100]	4.71	clear
	[010]	2.76	clear
15	[100]	4.59	dark color, few inclusions elongated subparallel [100]
	[010]	2.65	dark color, few inclusions elongated subparallel [100]
16	[100]	2.29	clear
	[010]	3.58	clear
17	[100]	5.59	clear
	[001]	5.75	clear
18	[100]	8.79	clear
	[001]	2.30	clear
19	[100]	5.21	clear, dark color
	[010]	3.31	clear, dark, color
20	[100]	6.52	(010) lilly pad fractures
	[010]	2.81	clear
21	[100]	7.99	many healed fractures, negative crystals
	[010]	9.27	many healed fractures, negative crystals
22	[100]	7.45	surface etch pits
	[010]	10.14	surface etch pits
23	[010]	8.04	clear
	[001]	18.49	fractures and (010) lilly pad fractures
24	[100]	25.06	clear, dark color
	[010]	9.53	dark color, (010) fractures with veils of unidentified material
25	[010]	2.71	clear
	[001]	4.24	clear
26	[010]	2.96	clear
27	[010]	2.96	clear
28	[010]	2.96	clear
29	[010]	2.96	clear
30	[010]	2.96	clear
31	[100]	4.07	unfilled fractures, primarily (010)
	[010]	2.96	unfilled fractures, primarily (010)
32	[100]	4.07	clear
	[010]	2.97	clear
33	[010]	3.25	clear
	[001]	3.30	clear
34	[100]	8.14	turbid, submicroscopic inclusions?
	[010]	5.02	turbid, submicroscopic inclusions?

* k is 29° inclined from [010] in (001)

Park. The sample was packed in a mixture of brucite, periclase, and water, and sealed in a gold foil capsule. The capsule was annealed at 800° C, 8.9 kbar water pressure, for 4×10^5 s (≈ 5 days). The experimental technique is identical to that reported in Kronenberg et al. (1986), with the exception that a SiO_2 disc was not used.

Sample 33 was prepared by Steve Mackwell at Cornell. The sample was annealed at 1000° C at 3.5 kbar for 10^4 s (≈ 3 h) in the presence of water (Mackwell, pers. comm.). The oxygen fugacity was regulated by a magnetite/wustite buffer.

Results and Discussion

The two halves of Figure 1 form a composite of seventeen normalized OH spectra in [100] polarization which demonstrates a number of features. First, there is a wide range in OH speciation as shown by the diversity and multiplicity of bands. Second, OH abundances, as estimated from normalized absorbance (see Table 3) vary greatly. Olivines range from essentially "dry", e.g., Angola and San Carlos (Fig. 1q and 1p), to comparatively "wet", e.g., Kimberley (Fig. 1a). Third, spectral complexity tends to increase with total OH content. Fourth, each locality has a characteristic OH spectrum which is readily distinguishable from other localities. These spectra are reproducible; the spectra for olivine from San Carlos, and Zabargad Island, Egypt are consistent with the published spectra of other workers (e.g., Mackwell et al. 1985, Beran and Putnis 1983, and Freund and Oberheuser 1986) with the exception of a band at 4200 cm^{-1} discussed later in this section.

The variability observed within a single locality is small with respect to the variability among different localities. Figure 2 is a composite of four Zabargad [100] spectra which shows the variability observed within a single locality. In general, the same bands are always seen in samples from a single locality, though their absolute and relative amplitudes may vary by as much as a factor of 4 in extreme cases (San Carlos). Total OH abundances vary by over a factor of 3 for dry localities (San Carlos, and Angola), wetter crystals (Zabargad, Kenya, and Norway) show much less variability at about 20%. In spite of the difference in OH abundance, San Carlos samples demonstrate similar variability to the Zabargad samples.

Sample 34 from the Kimberley kimberlite is unusual in that the broad underlying absorption (Figure 1a) is due to liquid water. Liquid water is characterized by a broad absorption at 3420 cm^{-1} and a bending plus stretching combination mode at 5240 cm^{-1} (Fig. 3) which is absent in dry samples. Upon cooling the crystal to 77 K, no ice band was observed (3200 cm^{-1}). When molecular water domains are sufficiently small, e.g., a few molecules, ice may not form even at 77 K. The molecular water in Kimberley olivines may be present in these small domains, thereby precluding the formation of ice. This water probably exists in submicroscopic fluid inclusions.

The broad absorption extending from 3700 to 3200 cm^{-1} in the spectrum of the Hebei Province, olivine (Fig. 1d) is also due to fluid inclusions. The water combination mode was observed at 5240 cm^{-1}. This sample is full of healed fractures which form arrays of small fluid bubbles. No inclusion-free path was available in the sample. Beam paths which pass through inclusion rich regions show more molecular water absorption than do paths in inclusion poor

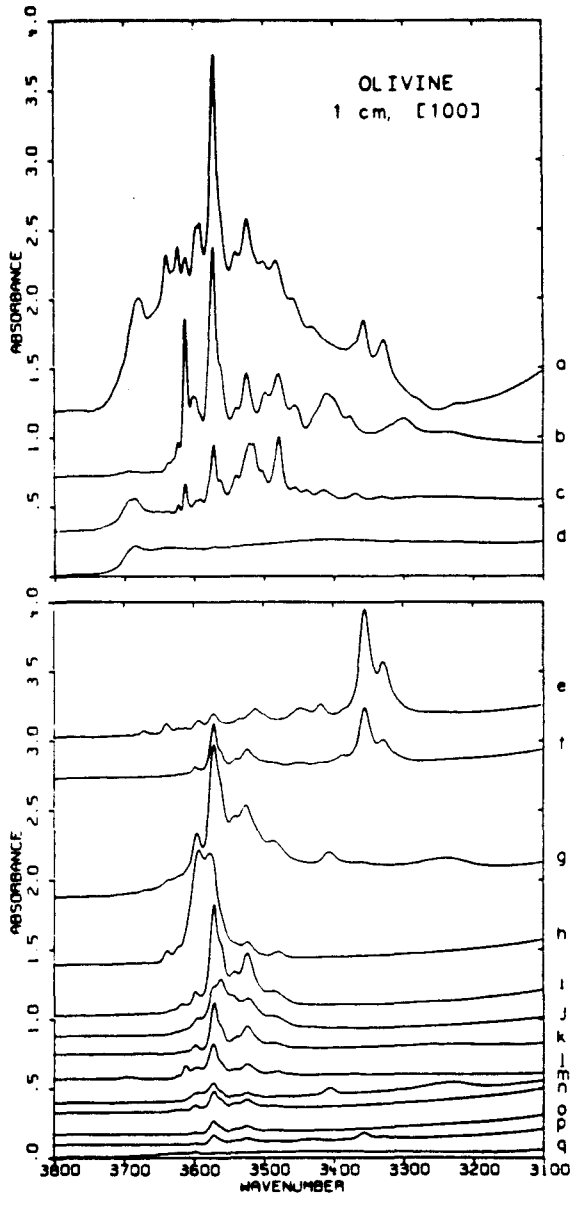

Fig. 1. Representative OH absorption spectra for the localities in Table 1. All the spectra are polarized [100], and thicknesses are normalized to 1 cm. Localities and sample numbers are: (a) Kimberley, 34; (b) Winburg, 9; (c) Norway, 3; (d) China, 21; (e) Kenya, 11; (f) Mexico, 16; (g) Vesuvuius, 15; (h) Tanzania, 17; (i) Sri Lanka, 18; (j) Madagascar, 19; (k) E. Africa, 4; (l) Sri Lanka, 22; (m) Zabargad, 5; (n) Cheviot Hills, Australia, 20; (o) Toowoomba Range, Australia, 14; (p) San Carlos, 23; (q) Angola, 12

regions, supporting the idea that the detected molecular water resides along healed fractures. A fracture-free olivine from Hebei, China, (not included in Table 1) was run unoriented and unpolarized. This sample had no measurable OH absorption.

A broad underlying absorption from molecular water

Table 3. Estimated hydrogen abundances

Sample	Location	H abundance		Occurence
		H/10⁶Si	by weight	
34	Kimberley, South Africa, including molecular water	976	6.64 ppm	Kimberlite
1	Norway	344	2.34	Metamorphic
34	Kimberley, South Africa, no molecular water	263	1.79	Kimberlite
9	Monastery, South Africa	261	1.78	Kimberlite
2	Norway	220	1.50	Metamorphic
3	Norway	204	1.39	Metamorphic
17	Kingiti, Tanzania	195	1.33	Basalt
21	Hebei Pr., China	134	912 ppb	Basalt
15	Vesuvius, Italy	127	864	Basalt
11	Emali, Kenya	98.0	667	Basalt
18	Sri Lanka	69.8	475	
16	Morales, Mexico	62.5	425	Basalt
10	Emali, Kenya (alterred)	54.8	373	Basalt
19	Madagascar	52.4	356	Basalt
22	Sri Lanka	41.4	282	Metamorphic
33	Annealed San Carlos	37.8	257	Annealed
4	East Africa	30.0	204	Basalt
5	Zabargad, Egypt	27.3	186	Hydrothermal
31	Annealed San Carlos	19.4	132	Annealed
20	Cheviot Hills, Australia	11.2	76.2	Basalt
23	San Carlos, Arizona	9.40	63.9	Basalt
14	Toowoomba, Australia	8.29	56.4	Basalt
12	Angola	5.94	40.4	Basalt
24	San Carlos, Arizona	2.83	19.3	Basalt

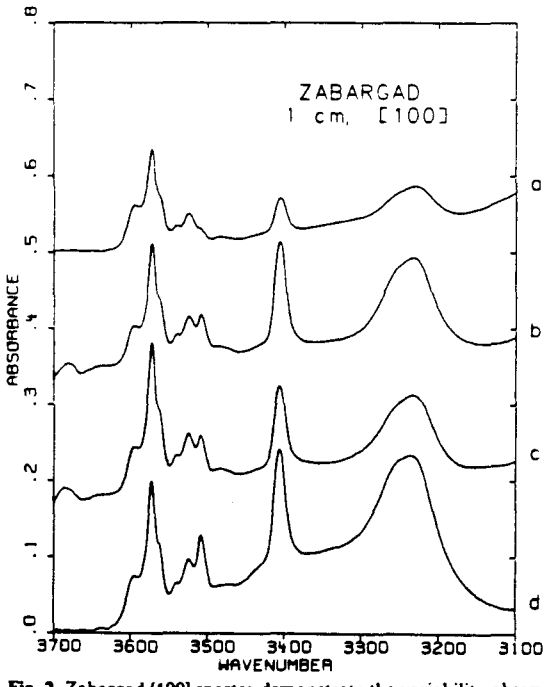

Fig. 2. Zabargad [100] spectra demonstrate the variability observed for individual localities. Thicknesses normalized to 1 cm. Samples: (a) 5, (b) 6, (c) 7, (d) 8

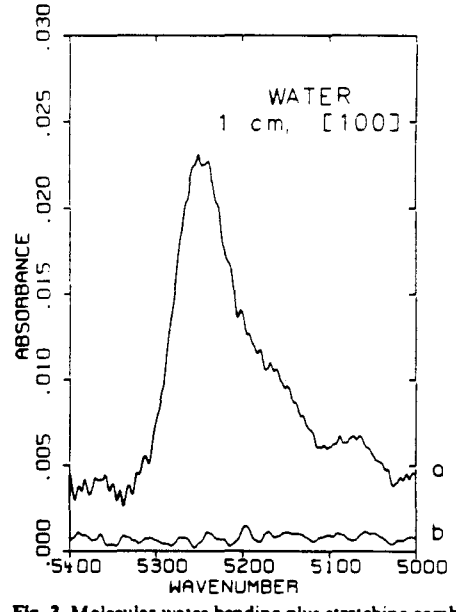

Fig. 3. Molecular water bending plus stretching combination mode at 5240 cm^{-1} for (a) Kimberley sample 34, and baseline (b) for Kingiti, Tanzania, sample 17. Both spectra have [100] polarization and have been normalized to 1 cm thickness

may also be present in Figures 2d and 1q; however no combination mode was observed due to the low concentrations present in the samples and the intrinsically low absorptivity of the combination mode.

Freund and Oberheuser (1986) report an absorption band near 4200 cm^{-1} which they attribute to molecular hydrogen in association with an oxygen-oxygen bond. Figure 4 shows an unpolarized (100) transmission spectrum of an olivine from Zabargad, Egypt, from 4400 to 4000 cm^{-1} with a reproduction of Freund and Oberheuser's re-

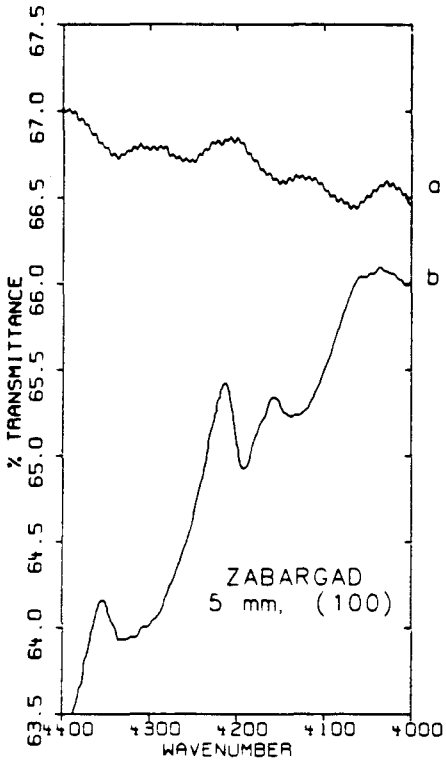

Fig. 4. Unpolarized (100) transmission spectra of Zabargad, Egypt, olivine. Sample thicknesses are 5 mm. (a) Sample 5 run in this laboratory and normalized to 5 mm thickness. The periodic oscillations are interference fringes. No bands near 4200 cm^{-1} are observed. (b) Reproduced from Freund and Oberheuser (1986). They attribute the band at 4200 cm^{-1} to molecular hydrogen in a noncentrosymmetric lattice site

ported molecular hydrogen band. Our sample has been normalized to Freund and Oberheuser's 5 mm thickness. The periodic oscillations in our data are due to inference fringes. We have observed no bands near 4200 cm^{-1} in spectra of the four Zabargad crystals in Table 1, nor have any such bands been found for any of the crystals examined in this study.

Despite the differences among localities, there are striking similarities and consistencies. Most bands can be identified in spectra from several localities, and some are present in all of the spectra examined (e.g., Figure 1: 3572 $cm,^{-1}$). None of the readily recognizeable OH absorption bands intrinsic to olivine are unique to any single sample or locality. Detailed examination of the spectra, particularly of the 77 K spectra, reveals some minor bands which are either unique or indistinguishable in other specimens because of band overlaps or very low absorptivities. These bands may be members of complex multiplets which contain the more common bands, and are seen only when the trace and minor element chemistries vary in such a way as to make them more prominent.

The pleochroism of the bands (e.g., Table 4 and Fig. 9) is the same in all crystals. Olivine thus seems to have a discrete set of OH defect sites. Differences arise because total OH and relative site occupancy are variable among localities, as observed by Beran and Putnis (1983).

Macroscopic and Microscopic Observations

The samples in Table 1 were examined both macroscopically and microscopically to determine the extent of internal fracturing and surface etching, to identify included minerals and fluid inclusions, and to identify any other unique properties of the crystals which may have bearing on their spectroscopy. These features are described in Table 2. Only features which might have impact on the IR spectra are shown. No mention is made of fractured samples, for example, which had clear fracture-free windows for spectroscopy. Submicroscopic features (<1 μm) such as microfractures and inclusions, if present, were not in sufficient quantity to cause discernible scattering (except for Kimberly sample 34).

Samples 1, 2, 3, 5, 6, 9, 15, 20, 21, 23, 24, and 31 have fractures and/or inclusions which interfere with the IR beam in one or more propagation directions, **k**. The effect of these features on the IR spectra in the regions of interest can be determined, in some cases, by using a single polarization with two propagation directions. Sample 3, for example, has a clear beam path when **k**||**c** but the beam passes through veils of an unidentified material when **k**||**a**. The **E**||**b** polarization can be used with either propagation vector. If the **E**||**b** **k**||**a** and **E**||**b** **k**||**c** spectra (after normalization to a common thickness) are different, then the unidentified veils are considered responsible for the differences. Conversely, if the spectra are identical, then the unidentified veils had no measurable effect on the IR spectra. When only subtle differences are observed, sample misorientation may be responsible for the differences rather than the inclusions.

When a clear path is not available in the crystal, a qualitative estimate of the impact of the inclusions may still be possible by comparing relatively inclusion-rich and inclusion-poor paths. This technique was used for samples 1, 5, 9, 15, 21, and 31 for which there were no inclusion-free paths.

A multiplet of bands at 3709, 3685, and 3645 cm^{-1} in samples 1, 2, and 3 is correlated with the fractured regions of the samples. These bands are attributed to serpentine, as discussed in the following section. The broad absorption centered at 3420 cm^{-1} in sample 21 is attributed to molecular water. The strength of the molecular water absorption in this crystal is strongly correlated to fracture density. Samples 5, 6, 9, 15, 20, 23, 24, and 31 have no bands which appear to be correlated with fractures or inclusions.

The effect of surface etch pits (e.g., samples 7, 8, and 22) can be assessed in a similar manner. Again we use a common polarization with two different propagation vectors, and we require that the thickness of the sample in the two propagation directions is different. The two beams traverse the same thickness of surface layer, but different thicknesses of bulk sample. After normalization to a common thickness, the bulk sample thicknesses are identical and the surface layer thicknesses are different. The spectra will differ only if the surface layer had a measurable absorption. Spectra of samples 7, 8, and 22 had no contribution from surface etch pits.

Three saples have unusual color. Pleochroism for the three principal directions (α = E||**b**, β = E||c, and γ = E||a)

are presented in Munsell notation (Munsell Book of Color, 1976) and named in accordance with the National Bureau of Standards Circular 440 (Judd and Kelly 1976). Emali, Kenya (#10) $\alpha = 5YR\ 6/12$ (strong orange), $\beta = 1Y\ 8.5/10$ (light orange brown), and $\gamma = 5YR\ 7/12$ (strong orange); Vesuvius, Italy (#15) $\alpha = 2.5Y\ 7/10$ (strong yellow), $\beta = 10YR\ 8/8$ (light orange brown), and $\gamma = 7.5Y\ 9/5$ (pale greenish yellow); and Nosy Mitsio, Madagascar (#19) $\alpha = 10YR\ 7/10$ (strong orange yellow), $\beta = 7.5YR\ 5/10$ (strong yellowish brown), and $\gamma = 10YR\ 6/7$ (dark orange yellow).

Each of these unusually colored samples has unique OH spectra, as do all of the samples in Table 1. The colored samples have neither abundances nor speciation peculiarities which set them apart from the other samples. We conclude that the factors responsible for the unusual colors have no apparent common influence on OH.

Included Hydrous Minerals

In addition to intrinsic OH defects and fluid inclusions, OH may become incorporated into olivine as an included hydrous phase. There is sufficient complexity in the OH spectra of olivine such that no single hydrous mineral, nor even any simple assemblage of hydrous minerals can account for the variety of absorption bands which we see. While there is little doubt that serpentine, for instance, could account for some of the narrow band absorption near 3700 cm^{-1}, serpentine alone cannot account for the bulk of the OH absorption. The majority of the absorption bands from 3200 cm^{-1} to 4000 cm^{-1} do not have both positions and half-widths which are consistent with common hydrous minerals likely to be associated with olivine. If, on the one hand, a large hydrous mineral crystal were included in olivine it would cause an OH absorption band indistinguishable from that of the isolated hydrous mineral. If, on the other hand, only a few unit cells of the hydrous phase were present in the olivine crystal, then the OH absorption of the hydrous phase might be shifted in position, and its width changed by the crystal field of the olivine host. In this latter limiting case, OH spectra alone may not be able to distinguish between OH intrinsic to olivine and OH in unit cell sized domains of hydrous phase inclusions. The OH spectra of hydrous phases are generally characteristic, so coincidence of olivine OH bands and hydrous mineral bands should be interpreted as evidence of inclusion of the hydrous phase in the olivine. Conversely, if no common associated hydrous phase corresponds to an OH band, that band is considered intrinsic to olivine as a modification of its structure.

Included hydrous phases could be primary igneous phlogopite or alteration products such as serpentine. Figure 5a shows the characteristic absorption of serpentine, which can be seen in several olivines as well (e.g., Figs. 5b, and 1a, c, d, l) at 3709, 3685, and 3645 cm^{-1}. Figure 6a shows the absorption of talc, which is similar to that of other trioctahedral magnesian layered silicates. The same bands were found in the brown olivine from Emali, Kenya (Fig. 6b) at 3678 and 3662 cm^{-1}. No other bands observed in the olivine spectra unambiguously correspond with common hydrous mineral spectra, however a strong case may be made for the humite group minerals.

It has been suggested that the humite group minerals, being structurally similar to olivine as well as being hy-

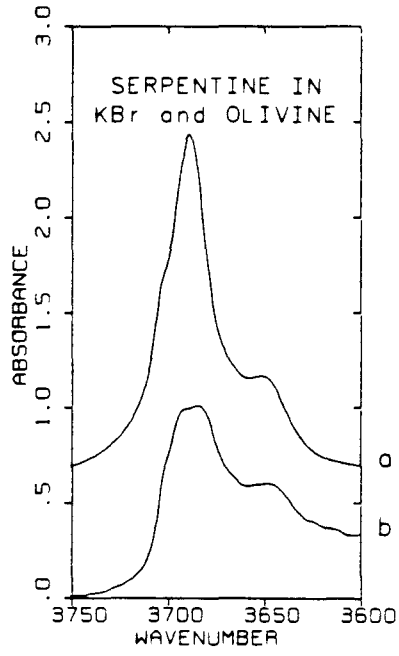

Fig. 5. The OH absorption of (a) lizardite plus chrysotile in KBr pellet superimposed upon (b) sample 1 from Norway in [001] polarization

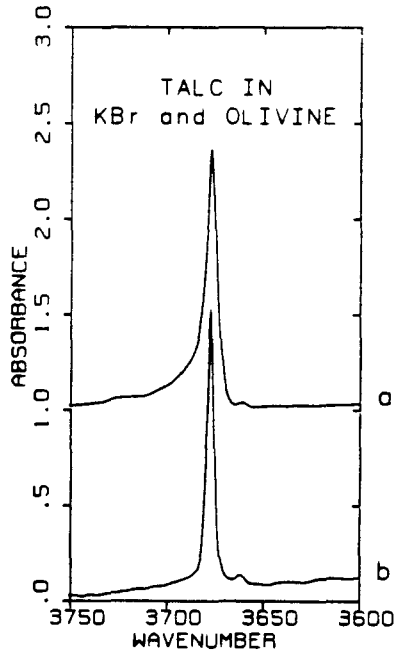

Fig. 6. The OH absorption of (a) talc in KBr pellet superimposed upon (b) OH band in brown sample from Emali, Kenya (#10). This band is not present in the green sample (#11, see Fig. 1e) from this locality. Similar absorption bands are seen in other magnesian trioctahedral layered silicates

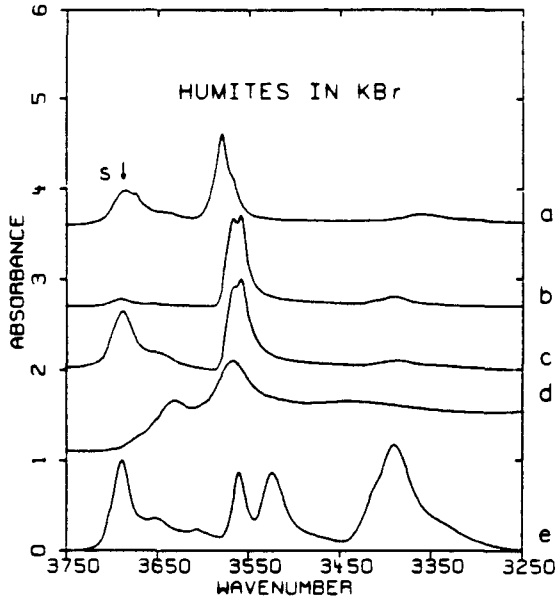

Fig. 7. Humite group minerals: (a) norbergite, (b) chondrodite, (c) humite, (d) clinohumite, and (e) titanian clinohumite. Samples were run as KBr pellets. The absorption bands near 3700 cm^{-1} are due to serpentine (s)

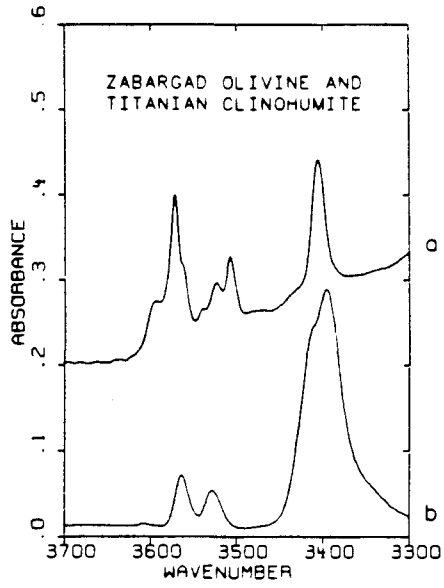

Fig. 8. Spectra of (a) 1 cm thick Zabargad olivine (sample 8) in [100] polarization superimposed upon (b) 5 μm thick titanian clinohumite run unpolarized in optic axis orientation

drous, may account for many of the OH bands. Spectra of the humite minerals norbergite, chondrodite, humite, clinohumite, and titanian clinohumite are shown in Figure 7. These spectra were obtained from KBr pellets containing the powdered humites. The samples contain some serpentine which gives rise to the absorption bands near 3700 cm^{-1}. KBr powder spectra are broader than single crystal spectra, so the humite band widths measured in Figure 7 are upper bounds for the single crystal band widths.

The OH vectors of the magnesian humites are subparallel to [100] (Yamamoto 1977, Fujino and Takeuchi 1978), as are many of the olivine OH vectors (we use the olivine-based orientation for the humite minerals, see Ribbe, 1982, p. 241). The OH doublet is centered at 3580, 3559, 3558, and 3568 cm^{-1} for norbergite, chondrodite, humite, and clinohumite respectively. The doublet is split and shifted variably with minor element variations as clearly demonstrated by addition of Ti (Fig. 7e). The bands at 3391 cm^{-1} are most prominent in the titanian clinohumite spectra, but are found in the other humite spectra as well. No precise (± 1 cm^{-1}) correspondence is found between the humite spectra and the olivine spectra, however the prominent E||a bands at approximately 3572 and 3525 cm^{-1} are likely candidates for humite bands. These bands fall within the range of absorption wavenumbers covered by the humites, and exhibit the expected orientation. These bands are seen in most of the olivines in this survey, as can be readily seen in Figure 1. Additionally, the Zabargad olivines and the Monastery kimberlite olivine (samples 5 through 8, and 9) show an absorption at 3412 cm^{-1}, which roughly corresponds with the 3391 cm^{-1} titanian clinohumite band.

Figure 8 shows the [100] IR spectra of Zabargad olivine sample 8, normalized to 1 cm thickness, with a spectrum of titanian clinohumite from Moses Rock, Utah, normalized to 5 μm and run in optic axis orientation. Note the close correspondence of the 3572, 3525, and 3412 cm^{-1} bands. We find this compelling evidence that either titanian clinohumite is present in this sample, or that an OH defect environment exists in this sample which is chemically similar to that of titanian clinohumite.

The humite group minerals can be represented as $nMg_2SiO_4 \cdot Mg(OH,F)_2$, where $n = 1, 2, 3$, and 4 for norbergite, chondrodite, humite, and clinohumite respectively. Taylor and West (1928) and Bragg and Claringbull (1965) hypothesized that higher members of the series ($n > 4$) might occur. While these higher members have not been found as natural crystals, faults in natural humites consisting of even-n ($n = 6, 8, 10$, and higher) lamellae have been observed by White and Hyde (1982) in natural magnesian humites.

Although no regular unit cell sized lamellae of humite group minerals have been observed in natural olivine ($n = \infty$), larger (several micron sized) intergrowths of titanian clinohumite and olivine were observed by McGetchin et al. (1970) in kimberlite at the Moses Rock dike, Utah. Kitamura et al. (1987) have found humite group layers in olivine from Buell Park, Arizona. Other occurrences of humites in association with olivine are cited in Ribbe (1982). An OH abundance of 147 H/10^6Si or 1 ppm H would correspond to an approximate $n = 14200$ composition or one norbergite unit for each 14199 olivine units. Rare humite lamellae faults in olivine could account for the OH abundance in natural olivine near 3570 cm^{-1}, and the pleochroism of OH in olivine at this wavenumber is consistent with this possibility.

If a humite mineral is responsible for the 3572 and 3525 cm^{-1} OH absorptions in olivine, then the wavenumber differences between these bands in olivine and the similarly positioned bands in humites may be due to the

Table 4. Pleochroism and calculated OH dipole orientations from 77 K spectra of monastery kimberlite olivine (sample 9)

Band cm^{-1}	Width cm^{-1}	Pleochroism	OH angle with		
			[100]	[010]	[001]
3637	6	a>>b=c	0°	90°	90°
3623	4	a>>b=c	0	90	90
3615	5	a>b>>c	12	78	90
3607	7	a>b>>c	16	74	90
3602	8	a>c>b	30	90	60
3600	28	a>>b=c	0	90	90
3594	6	a>c>b	26	90	64
3576	11	a>c>b	30	73	66
3582	5	b>>a=c	90	0	90
3565	8	a>c>b	46	64	55
3559	7	b>>a=c	90	0	90
3554	19	b=c>>a	90	45	45
3550	6	b>>a=c	90	0	90
3542	32	a>c>>b	30	90	60
3529	10	a>c>b	37	74	58
3499	11	a>c>b	40	73	55
3483	12	a>b=c	35	66	66
3473	10	c>>a=b	90	90	0
3462	10	c>>a=b	90	90	0
3455	11	a>c>b	38	66	63
3433	10	a>c>b	36	77	58
3414	10	a>>b=c	0	90	90
3404	35	a>c>b	44	73	51
3390	12	c>b>a	90	73	17
3377	14	a>c>b	45	78	47
3364	12	b>>a=c	90	0	90
3346	20	a>c>b	46	75	48
3319	23	a>c>b	37	82	55
3287	31	a>c>b	37	68	62
3263	40	c>>a=b	90	90	0
3236	10	a>>b=c	0	90	90
3225	42	c>b>>a	90	56	34

olivine dominated crystal field energy around the humite, or simply different minor element chemistry. Alternatively, there may exist OH sites in olivine which are chemically similar to those of humites.

OH Crystallographic Sites

OH dipole orientations may be calculated from the [100], [010], and [001] polarized spectra alone. These calculations are subject to the combined errors of crystal orientation, polarizer orientation, and subgrain alignment. Table 4 shows these calculated angles for a number of the OH bands which were resolved in the 77 K spectra of Figure 9. Note that the majority of the bands are inclined toward [100].

Accurate measurement of the pleochroism of the bands requires deconvolution of the spectra into spectral components. While the theoretical band shape of an individual absorber is Lorentzian, the anharmonicity of the OH potential, coupled molecular motions, and the chemical inhomogeneity of the sample cause line broadening (Aines 1984). We found that a Gaussian band shape adequately described the sharp-band OH absorptions in olivine. Room temperature OH bands tend to be broader than those measured at 77 K, and what often appears to be a single band at room temperature may become resolvable as several closely spaced bands at 77 K. Spectrum fitting was thereby facilitated by using cryogenic spectra to improve resolution by

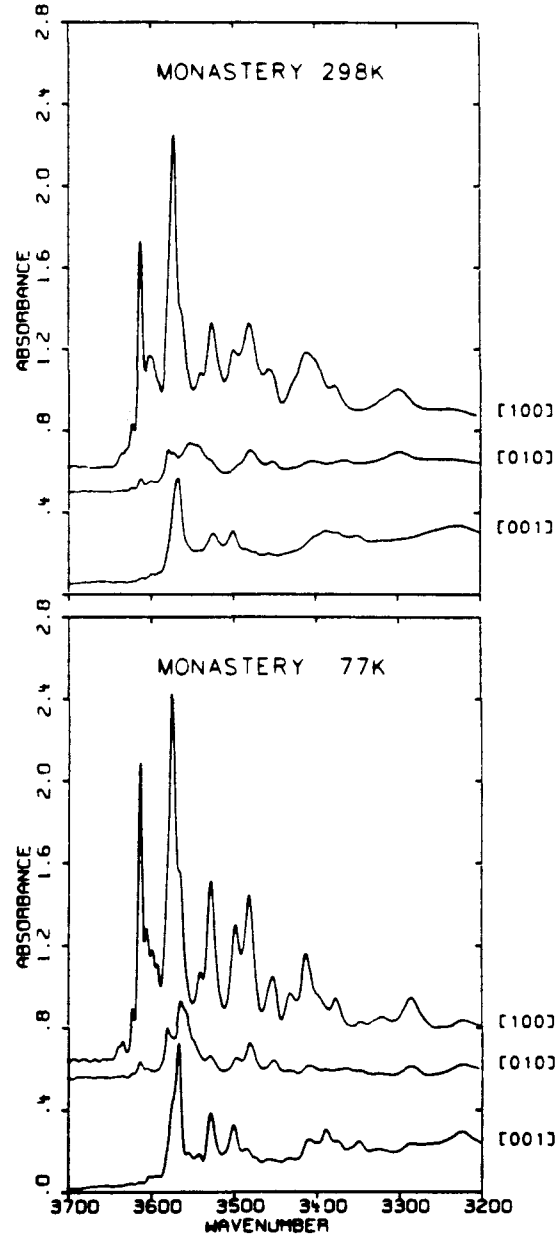

Fig. 9. Pleochroism of the OH absorption for Monastery kimberlite sample at 298 K and 77 K. Thicknesses have been normalized to 1 cm

narrowing the bands and by shifting them differentially. Even with this improved resolution many bands overlap and are distinguishable only as shoulders and asymmetries in other bands.

Note the trend towards increased full width at half height with decreasing wavenumber. Exceptions to this trend may be due to unresolvable overlapping bands.

In ideal olivine, and in other orthorhombic minerals, any IR spectrum will be a linear combination of the E||a,

E||b, and E||c spectra. It is imposible, therefore, for an absorption maximum to occur other than in one of the principal optic directions when the propagation direction is along a principal optic direction if the absorber shares the orthorhombic symmetry of its crystal host. This has been described mathematically by Strens et al. (1982), and shown experimentally in the absorption figures of Beran and Putnis (1983) for OH in Zabargad olivine. Freund and Oberheuser (1986) report that, in a (100) spectrum of Zabargad olivine, the intensity of the bands at 3614, 3591, and 3567 cm^{-1} showed a maximum at 35° off the [010] axis. This suggests that the OH absorbers responsible for these bands do not conform to the orthorhombic symmetry of olivine, and must therefore be due to mechanical inclusions which fortuitously share a common alignment. In accord with the measurements of Beran and Putnis we have found absorption maxima only in principal directions (when light is propagated along a principal direction), which implies that these OH absorbers are in sites controlled by the symmetry of olivine. Accurate determination of the OH dipole orientation is critical for determining the OH crystallographic sites. Site determination is in turn important for understanding the influence of OH upon the mechanical and rheological properties of olivine.

The details of H incorporation in olivine are not known. Beran and Putnis (1983) attempted to determine the atomic site of H in the olivine lattice using OH absorption figures. While their models quantitatively fit the direction of the OH dipole with good accuracy, the absorption wavenumbers which we calculated using the model of Nakamoto et al. (1955) do not agree with their site assignments. It is important to recognize that the structural positions of the major (stoichiometric) atoms will likely differ from their X-ray determined values in the environment of a point defect. This fact introduces uncertainty in the absorption figure models of Beran and Putnis and makes application of Nakamoto's model difficult.

Perhaps the most likely factors which regulate the number and types of OH absorbers in olivine are the trace elements. Kats' (1962) work on quartz showed that a tremendous variety of OH absorptions correlate with Al^{3+} substituted for Si^{4+}, and with alkali cation defects. Since OH is present at ppb to ppm concentrations in olivine, miniscule impurity levels (often below modern X-ray fluorescence and microprobe detection limits) may be responsible for controlling OH speciation.

Source of Hydroxide and Geologic Occurrence

OH in olivine is probably affected both by the conditions of crystallization and by later annealing, transport, and alteration. In order to relate the OH concentrations measured here with the OH concentrations in mantle and lower crustal olivines, it is necessary to assess the effects that metamorphic and alteration processes may have upon the crystal. These late stage processes may be very effective in changing primary OH concentration levels and speciation. The high diffusivity of hydrogen bearing species in olivine at magmatic temperatures (a conservative lower limit of 10^{-6} cm^2/s at 1100° C has been estimated by Mackwell et al. 1985) means that dramatic diffusive transport of hydrogen may occur even over the timescale of magmatic transport. Aines and Rossman (1985) have shown that OH in topaz and feldspar undergo site changes upon heating. Thus in addition to changing overall concentration, the thermal history will affect the site distribution, further obscuring the primary OH signature.

If magma transporting olivine xenocrysts was undersaturated in OH, then the olivine may have lost most of it original OH during it's residence in the magma. Olivines from xenoliths in basalts, like San Carlos, may have had one or two orders of magnitude greater OH abundance prior to being stoped off into the basaltic magma. Alternatively, the olivines transported in the vapor-rich kimberlites may have even gained OH from the magma, and certainly should have lost less of their original OH content than would the olivines from basalt. Thus the abundance of OH in olivines in the mantle may be quite different from the abundances which we can measure in olivines of mantle origin. The measured abundances in crystals from voluminous basaltic flows are almost certainly a lower limit for mantle olivine. The measured values for olivines in kimberlites would give a lower limit which is two orders of magnitude greater than that calculated from the basaltic olivines. Also, since the tectonic and geologic regimes for kimberlitic eruptions and basalt flows are different, the limits inferred from one may not be applicable to the other. Concentration profiles across large xenocrysts may be able to resolve the role of diffusive OH loss (or gain) during magmatic transport. This information is necessary to constrain the abundance of OH in olivines in the mantle prior to magmatic interaction.

The molecular water observed in the Kimberley sample may represent former OH, of the type normally found in olivine, which has subsequently exolved to form submicroscopic fluid inclusions. If this is the case, then a lower limit of 976 $H/10^6Si$ can be inferred for such mantle derived olivines. This is over an order of magnitude greater than the abundances of hydroxide which have been achieved in annealing experiments. The rheologic properties of the mantle, particularly where kimberlite diapirs form, may consequently be quite different than current experimentation indicates.

Annealed Olivine

The effect of OH on the rheologic properties of olivine is commonly studied by introducing OH into the olivine by annealing it in the presence of water. We have examined two crystals from San Carlos which were annealed for this purpose. Comparison of annealed with natural San Carlos olivine (Fig. 10) shows that new OH bands are created, and existing bands are enhanced. New bands detected at 298 K are at 3702, 3657, 3637, 3623, 3612, 3541, and 3524 cm^{-1}. A band at 3702 cm^{-1} (not shown in Fig. 9) is probably due to incipient serpentinization. The annealed olivine prepared by Mackwell was similar to that prepared by Kronenberg.

Note that the 3572 and 3524 cm^{-1} humite-like OH bands are the strongest features of the annealed olivine spectra.

The annealed samples had OH abundances of 19.4 (sample 31) and 37.8 $H/10^6Si$ (sample 33). Mackwell et al. (1985) report a maximum of 60 $H/10^6Si$ as sharp bands and 115 $H/10^6Si$ as broad bands in their annealed olivines. Justice and Graham (1982) report a maximum of 329 $H/10^6Si$ present as serpentine in their annealed olivines. These abundances are quite low compared with the maximum abundance observed in natural olivines of nearly 1000 $H/10^6Si$.

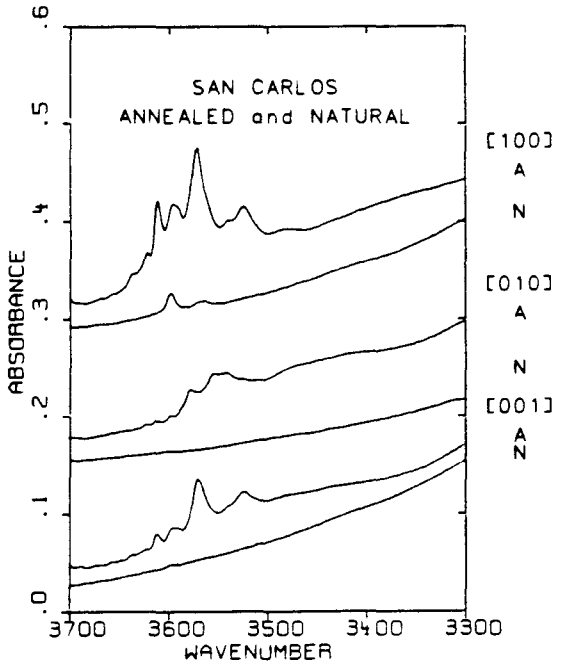

Fig. 10. Natural ("N", sample 23) and annealed ("A", sample 31) San Carlos olivine. Thicknesses normalized to 1 cm

Annealed San Carlos olivine differs from natural olivine in both OH abundance and speciation. While the OH bands of the annealed crystals are found in many of the natural crystals, many of the common natural bands (e.g, Fig. 1: 3356 and 3328 cm^{-1}) are not found in the annealed crystals. Since the effect of OH on the rheologic behavior of olivine is likely to depend upon both abundance and speciation, these annealed samples may not be representative of mantle olivine.

Conclusion

It is obvious that there is much work to be done to constrain the various effects of provenance and process on OH concentration and speciation in olivine. However, even with these limitations it is obvious that there is a greater range than previously measured. Kimberlitic and some metamorphic olivines show the greatest OH abundance whereas olivines from basalt xenoliths show the lowest.

Included hydrous minerals are distinguishable from olivine's intrinsic OH. Serpentine is commonly found and talc is found in one sample. Humite group minerals may be present as sparse until cell sized defects in olivine. The OH absorption bands at 3572 and 3525 cm^{-1} have both position and orientation consistent with humites.

Annealed San Carlos olivine has 6 OH bands not found in natural San Carlos olivine. These bands are observed in other natural olivines, but no single natural crystal has the same OH spectrum as the annealed samples. The sharp-band OH abundance in the annealed samples is low in comparison with the range of natural olivine OH abundances.

Acknowledgements. We wish to thank Peter Embry and the late John Fuller (British Museum of Natural History), Jacques Fabries (Muséum National d'Histoire Naturelle, Paris), Carl Francis (Harvard), Mike Gray (Culver City, CA), Roger Harding (British Geological Survey), Stein Jacobson (Harvard), Mary Johnson (Caltech, formerly Harvard), Peter Keller (Los Angeles County Museum), Masao Kitamura (Kyoto University, Kyoto, Japan), Andreas Kronenberg (Texas A&M, formerly at U.S.G.S Menlo Park), Steve Mackwell (Cornell), Lee Silver (Caltech), and Huang Zheng Zhi (Geological Museum, Beijing) for generously providing samples used in this study, and Sten Samson (Caltech) for his help with the Laue work. This work was funded by NSF grant EAR-83-13098.

References

Aines RD (1984) The significance of infrared band shapes and positions in hydrogen bonded systems. PhD Thesis, California Institute of Technology, Pasadena, California, pp 57–87

Aines RD, Rossman GR (1985) The high temperature behavior of trace hydrous components in silicate minerals. Am Mineral 70:1169–1179

Bank H, Saul J (1972) Schleifwürdige Olivine aus Kenya. Z Dtsch Gemmol Ges 21:216–218

Beran A, Putnis A (1983) A model of the OH positions in olivine, derived from infrared-spectroscopic investigations. Phys Chem Minerals 9:57–60

Bragg WL, Claringbull GF (1965) The crystaline state, vol IV: Crystal structures of minerals. G Bell and Sons, London, pp 175–178

Brueckner HK (1977) A crustal origin for eclogites and a mantle origin for garnet peridotites: strontium isotopic evidence from clinopyroxenes. Contrib Mineral Petrol 60:1–15

Chopra P, Paterson MS (1984) The role of water in the deformation of dunite. J Geophys Res 89:7861–7876

Clocchiatti R, Massare D, Jehanno C (1981) Origine hydrothermale des olivines gemmes de l'île de Zabargad (St. Johns) Mer Rouge, par l'étude de leurs inclusions. Bull Minéral 104:354–360

Freund F, Oberheuser G (1986) Water dissolved in olivine: a single-crystal infrared study. J Geophys Res 91:745–761

Frey FA, Prinz M (1978) Ultramafic and mafic nodules from San Carlos, Arizona: Mineralogy, petrology and chemistry. Earth and Planetary Science Letters 38:129–176

Fujino K, Takéuchi Y (1978) Crystal chemistry of titanian chondrodite and titanian clinohumite of high-pressure origin. Am Mineral 63:535–543

Judd DB, Kelly KL (1976) Color – universal language and dictionary of names. National Bureau of Standards special publication 440, pp 184

Justice M, Graham E (1982) The effect of water on high-temperature deformation in olivine. Geophys Res Lett 9:1005–1008

Karato S, Paterson MS, FitzGerald JD (1986) Rheology of synthetic olivine aggregates: influence of grain size and water. J Geophys Res 91:8151–8176

Kats A (1962) Hydrogen in alpha quartz. Philips Res Rep 17:133–195

Keller PC, Fuquan W (1986) A survey of the gemstone resources of China. Gems and Gemology 22:3–13

Kirby SH (1983) Rheology of the lithosphere. Rev Geophys Space Phys 21:1458–1487

Kitamura M, Kondoh S, Morimoto N, Miller GH, Rossman GR, and Putnis A (1987) Planar OH-bearing defects in mantle olivine. Nature (in press)

Kohlstedt DL (1986) Role of point defects in high-temperature deformation of olivine. International Mineralogical Association, Fourteenth General Meeting, Stanford, California, Abstract: Abstracts with Programs, 143

Koivula JI (1981) San Carlos peridot. Gems and Gemology 17:205–214

Kronenberg AK, Kirby SH, Aines RD, Rossman GR (1986) Solubility and diffusional uptake of hydrogen in quartz at high water pressures: implications for hydrolytic weakening. J Geophys Res 91:12723–12744

Lacroix A (1922) Minéralogie de Madagascar. Tome I. Géologie minéralogie descriptive. Challamel A (ed), Paris, pp 79–83

Mackwell SJ, Kohlstedt DL, Paterson MS (1985) The role of water in the deformation of olivine single crystals. J Geophys Res 90:11319–11333

McGetchin TR, Silver LT, Chodos AA (1970) Titanoclinohumite: a possible mineralogical site for water in the upper mantle. J Geophys Res 75:255–259

Munsell book of Color (1976) Macbeth Division of Kollmorgen Corporation, Baltimore

Nakamoto K, Margoshes M, Rundle RE (1955) Stretching frequencies as a function of distances in hydrogen bonds. J Am Chem Soc 77:6480–6486

Paterson MS (1982) The determination of hydroxyl by infrared absorption in quartz, silicate glasses and similar materials. Bull Minéral 105:20–29

Ribbe PH (1982) The humite series and Mn-analogs. In: Ribbe PH (ed) Reviews in mineralogy, vol 5, ed 2, Orthosilicates. Mineralogic Society of America, Washington, DC, pp 213–274

Strens RGJ, Mao HK, Bell PM (1982) Quantitative spectra and optics of some meteoritic and terrestrial titanian clinopyroxenes. In: Saxena SK (ed) Advances in physical geochemistry. Springer Verlag, New York, pp 327–346

Suwa K, Yusa Y, Kishida N (1975) Petrology of peridotite nodules from Ndonyuo Olnchoro, Samburu district, central Kenya. Phys Chem Earth 9:273–286

Taylor WH, West J (1928) The crystal structure of the chondrodite series. Proc R Soc London Ser A 117:517–532

White TJ, Hyde BG (1982) Electron microscope study of the humite minerals: I. Mg-rich specimens. Phys Chem Minerals 8:55–63

Whitelock TK (1973) The Monastery Mine kimberlite pipe. In: Nixon PH (ed) Lesotho kimberlites. Lesotho National Development Corporation, Maseru, South Africa, pp 214–237

Wilson WE (1976) Saint John's Island, Egypt. Mineral Rec 7:310–314

Yamamoto K (1977) The crystal structure of hydroxylchondrodite. Acta Crystallogr B33:1481–1485

Received November 11, 1986